Temperature-Dependent Extended Electron Energy Loss Fine Structure Measurements from K, L_{23}, and M_{45} Edges in Metals, Intermetallic Alloys, and Nanocrystalline Materials

Thesis by

James Kozo Okamoto

In Partial Fulfillment of the Requirements

for the Degree of

Doctor of Philosophy

California Institute of Technology

Pasadena, California

1993

(Defended May 6, 1993)

To my parents

and my wife

Acknowledgements

First and foremost, I would like to express my gratitude to my advisor, Professor Brent Fultz, for directing my research and providing me with constant support and encouragement. My research would not have begun without Brent's ideas, and it is a great pleasure to work in his group.

I would also like to acknowledge my deep indebtedness to Dr. Channing Ahn for teaching me the art of electron microscopy and the science of electron energy loss spectrometry. Channing gave this work a flying start by supervising my initial experiments and generously sharing his expertise with me.

I am appreciative to Carol Garland for facilitating my work on the electron microscope.

Finally, I would like to thank the various members of the Fultz group for their help, especially Dr. Douglas Pearson, Zheng-Qiang Gao, and Lawrence Anthony.

Financial support for this research was received from the United States Department of Energy under grant DE-FG03-86ER45270 and from a Leila Clark fellowship from Caltech. The Gatan model 666 parallel-detection EELS spectrometer was acquired through a grant from Caltech's Program in Advanced Technologies, supported by Aerojet, General Motors, and TRW. The transmission electron microscopy facility was largely supported by the National Science Foundation under grant DMR-8811795.

Abstract

This dissertation developed the extended energy loss fine structure (EXELFS) technique. EXELFS experiments using the Al K, Fe L_{23}, and Pd M_{45} edges in the elemental metals gave nearest-neighbor distances which were accurate to within ± 0.1 Å. In addition, vibrational mean-square relative displacements (MSRD) derived from the temperature dependence of the EXELFS compared favorably with predictions from published force constant models derived from inelastic neutron scattering data. Thus, information about "local" atomic environments can be obtained not only from K edges, but from L_{23} and M_{45} edges as well. This opens up most of the periodic table to possible EXELFS experiments.

The EXELFS technique was used to study the local atomic structure and vibrations in intermetallic alloys and nanocrystalline materials. EXELFS measurements were performed on Fe_3Al and Ni_3Al alloys which were chemically disordered by piston-anvil quenching and high-vacuum evaporation, respectively. Chemical short-range order was observed to increase as the as-quenched Fe_3Al and as-evaporated Ni_3Al samples were annealed *in-situ* at 300 C and 150 C, respectively. Temperature-dependent measurements indicated that local Einstein temperatures of ordered samples of Fe_3Al and Ni_3Al were higher than those of the corresponding disordered samples. Within a "pair" approximation, these increases in local Einstein temperatures for the ordered alloys corresponded to decreases in vibrational entropy per atom of 0.48 ± 0.25 k_B for Fe_3Al and 0.71 ± 0.38 k_B for Ni_3Al. In comparison, the decrease in configurational entropy per atom between perfectly disordered and ordered A_3B alloys is 0.56 k_B in the mean-field approximation. These results suggest that

including vibrational entropy in theoretical treatments of phase transformations would lower significantly the critical temperature of ordering for these alloys.

EXELFS investigations were also performed on nanocrystalline Pd and TiO_2. At 105 K, the MSRD in nanocrystalline Pd and TiO_2 were found to be greater than that in the corresponding large-grained materials by $1.8 \pm 0.3 \times 10^{-3}$ $Å^2$ and $1.8 \pm 0.4 \times 10^{-3}$ $Å^2$, respectively. Temperature-dependent measurements were inconclusive in measuring differences in local atomic vibrations between the nanocrystalline and large-grained materials.

Table of Contents

List of Figures

List of Tables

1 Historical Introduction

§1.1 and §1.2 review the history of electron energy loss spectrometry (EELS) and the history of extended x-ray absorption fine structure (EXAFS), respectively. §1.3 introduces extended electron energy loss fine structure (EXELFS) and discusses some practical differences between EXELFS and EXAFS. §1.4 schematically explains the physical origin of extended fine structure. §1.5 discusses applications of extended fine structure in materials science.

1.1 Electron Energy Loss Spectrometry (EELS)

The history of electron energy loss spectrometry dates back to the work of Franck and Hertz during the years 1914 to 1920. They showed that when a fast-moving electron collides with an atom or molecule in a gas, it bounces off with only a very small loss of kinetic energy, unless it has enough energy to raise the atom or molecule to an excited electronic state, or to ionize the atom or molecule.

The first report on the characteristic energy losses of electrons in solids was made by Becker in an abstract printed in 1924. In his abstract, Becker briefly described the energy distribution of electrons which were dispersed by a magnetic field onto photographic film after being reflected from solid targets. A more quantitative study on the energy losses of electrons reflected from the surface of a solid was published by Rudberg in 1930. Rudberg prepared samples of various metals and oxides *in-situ* by vacuum evaporation immediately before his measurements.

In 1941, Ruthemann was the first to publish the energy spectrum of electrons transmitted through thin solid specimens. In order to achieve

transmission, Ruthemann used incident electrons with energies of several keV. His energy-loss spectrum from a thin film of aluminum revealed a series of peaks which were later attributed by Bohm and Pines (1951) to multiple plasmon excitations. Ruthemann (1942) also recorded an energy loss spectrum from a thin film of collodion which showed the K shell ionization edge from carbon.

Since these early measurements of electron energy losses, electron energy loss spectrometry (EELS) has developed into an important technique for materials characterization. Electron energy loss spectrometers are now common analytical attachments to transmission electron microscopes. A comprehensive text on the subject of EELS in the electron microscope was published by Egerton in 1986. An up-to-date review of the applications of EELS in materials science was given in the book by Disko et al. (1992).

EELS is well-known as a highly sensitive tool for elemental microanalysis. There is no theoretical lower limit for the mass fraction one can detect with EELS (Kruit, 1986). Recently, Atwater and Ahn (1991) used EELS in the reflection geometry for the *in-situ* elemental analysis of semiconductor surfaces during molecular-beam epitaxy. Alternatively, instead of using the spectrometer to display a spectrum, the energy-selecting capabilities of the spectrometer can be combined with the imaging capabilities of the microscope to obtain energy-filtered images (Shuman and Somlyo, 1981).

Today, in addition to the capability of EELS for elemental microanalysis, there is an increasing awareness that EELS can provide information about the electronic and atomic structure of materials. Recently, Pearson et al. (1989) used EELS measurements of near-edge fine structure to determine the electronic occupancy of d states in transition metals. The present thesis uses

EELS measurements of extended fine structure to probe the local atomic structure in metals and alloys.

1.2 Extended X-ray Absorption Fine Structure (EXAFS)

The first reports of fine structure on the high-energy side of ionization edges were made by Fricke (1920) and Hertz (1920) using x-ray absorption measurements. The structure that they observed was confined to strong features within a few tens of electron volts (eV) of the edge onsets, in what today is called the "near-edge" regime. These near-edge features were readily attributed to bound excited electronic states using the theory of Kossel (1920). Later, as experimental methods improved, the fine structure was observed to extend up to several hundreds of eV past the edge. These "extended" oscillations, now called EXAFS (extended x-ray absorption fine structure), required a new physical explanation.

The first theory explaining the EXAFS was proposed by Kronig in 1931. Kronig suggested that the structure could be attributed to variations in the density of electronic states predicted by the zone theory of solids. This description became known as a long-range order (LRO) theory of EXAFS because it depended upon the periodicity of the solid. Kronig (1932) also proposed a short-range order (SRO) theory to explain the observation of EXAFS in molecules. SRO theories attributed EXAFS to variations in the final state wavefunction caused by backscattering of the photoelectron from neighboring atoms. Although LRO theories could not explain the EXAFS found experimentally in molecules and amorphous solids, for many years confusion existed as to which description, LRO or SRO, was appropriate (Azaroff, 1963).

The work of Sayers et al. (1971) elevated EXAFS from an obscure phenomenon to a useful structural tool. Using single-scattering SRO theory, they realized that a Fourier analysis of the EXAFS with respect to the photoelectron wave number should peak at distances corresponding to nearest-neighbor coordination shells of atoms. By separating the contributions from the various atomic shells, the Fourier analysis technique made possible the direct extraction of structural information. It suddenly became clear that EXAFS could be used as a quantitative probe of SRO.

Following the work of Sayers et al., rapid advances were made in the theory of EXAFS (Schiach, 1973; Stern, 1974; Ashley and Doniach, 1975; Lee and Pendry, 1975). It quickly became well-established that single-scattering SRO theory was an adequate description of EXAFS in most circumstances.

Meanwhile, the development of synchrotron radiation sources greatly improved the statistical quality of experimental EXAFS data (Kincaid and Eisenberger, 1975). Synchrotron sources became typically at least three orders of magnitude more intense than standard x-ray tube sources, and now they are even more intense.

These improvements in both theory and experiment made EXAFS a practical tool for probing the atomic structure of materials. Since then, a large number of EXAFS experiments have been performed. A recent review of EXAFS and its applications was given in the book edited by Koningsberger and Prins (1988).

1.3 Extended Electron Energy Loss Fine Structure (EXELFS)

Although the vast majority of extended fine structure measurements are presently being made using x-ray absorption, it is also possible to measure

extended fine structure using EELS (Ritsko et al., 1974; Leapman and Cosslett, 1976; Colliex et al., 1976; Kincaid et al., 1978; Teo and Joy, 1981). When extended fine structure is measured using EELS, the technique is called EXELFS (extended electron energy loss fine structure). Figure 1.1 contains the EELS spectrum from pure aluminum which clearly shows the EXELFS above the ionization edge.

EXAFS and EXELFS originate from the same physical mechanism; they are both caused by the backscattering of the excited electron from neighboring atoms. The difference is that EXAFS uses a photoabsorption process which completely transfers the x-ray photon energy to the excitation of the photoelectron, while EXELFS involves partial energy transfers from the high-energy incident electron beam. From this perspective, EXAFS is similar to an infrared absorption experiment, while EXELFS is more analogous to a Raman scattering experiment.

While EXAFS and EXELFS are basically the same physical phenomenon, there are many significant differences between the experimental techniques which are used to measure them. A list of important advantages and disadvantages of EXELFS vs. EXAFS is given in Table 1.1. Unlike EXAFS experiments which utilize x-rays from synchrotron or bremsstrahlung radiation sources, EXELFS experiments are usually performed using the electron beam in a transmission electron microscope (TEM). This makes it easy to combine EXELFS experiments with the imaging, diffraction, and analytical capabilities of the TEM. Other important advantages of the EXELFS technique are its increased spatial resolution and its ability to measure extended fine structure in elements with very low atomic number. Disadvantages of the EXELFS

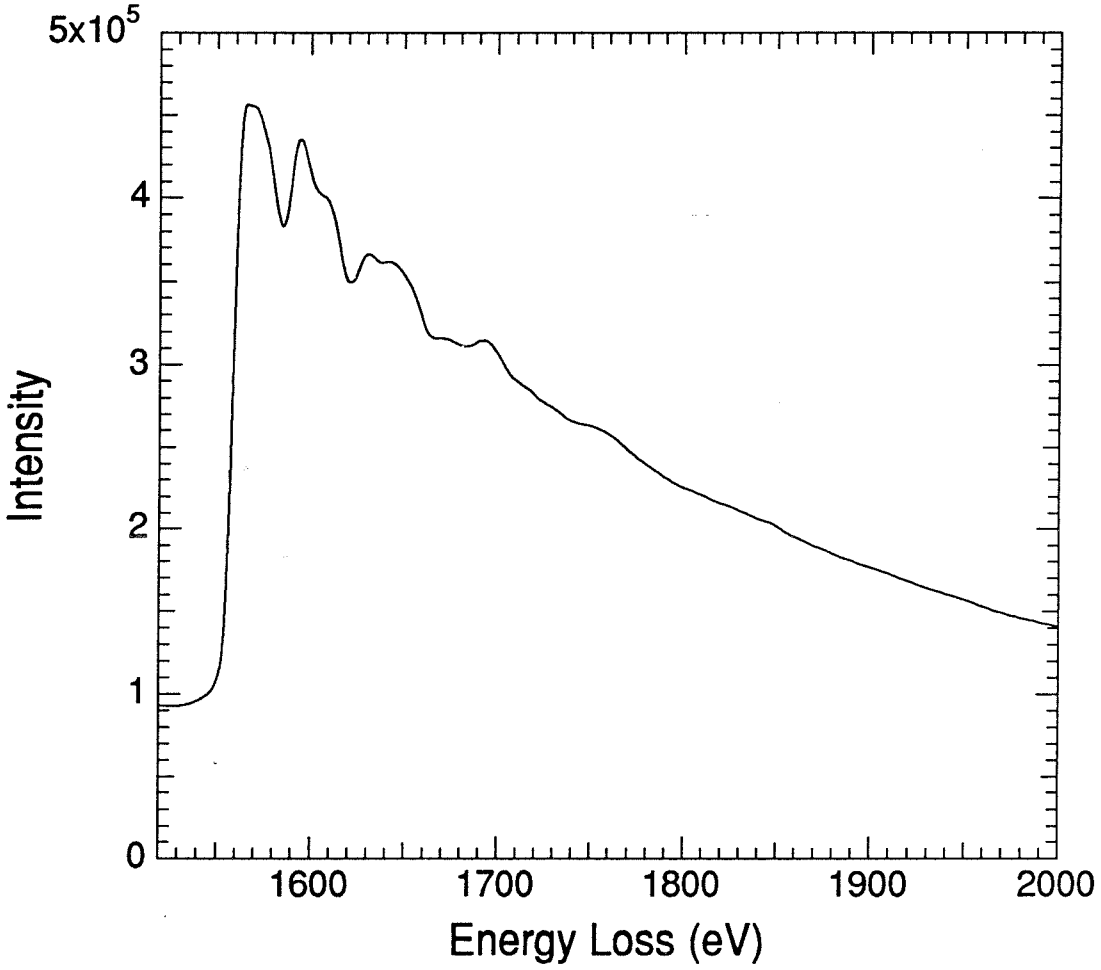

Figure 1.1. EELS measurement of Al K edge from foil of pure aluminum.

technique include a greater likelihood of overlapping edges and the need for very thin samples in order to avoid large multiple inelastic scattering effects.

Advantages of EXELFS vs. EXAFS

1. EXELFS can measure core edge fine structure in lower atomic number elements (edges < 5 keV) than EXAFS (edges > 3 keV).
2. Very small electron probes can be used, allowing inhomogeneous samples to be studied.
3. The instrumentation is more accessible and less expensive than synchrotron sources.
4. EXELFS can be combined with electron diffraction and imaging in the transmission electron microscope.

Disadvantages of EXELFS vs. EXAFS

1. Overlapping edges are more likely to limit the data range or complicate the analysis.
2. Samples must be very thin to limit multiple inelastic scattering effects.
3. The electron beam may heat the samples, but this is shown not to be a problem in §3.3.

Table 1.1. Important advantages and disadvantages of EXELFS vs. EXAFS.

Historically, EXELFS studies have been inhibited by the inherent inefficiency of serial detection systems. With serial detectors, EXELFS data have suffered from inadequate signal-to-noise ratios, resulting in very limited data ranges in k-space (Csillag et al., 1981). The recent development of parallel detectors has overcome this problem (Krivanek et al., 1987). Parallel detection of a spectrum with 1000 discrete data channels is, in principle,

roughly 1000 times more efficient than serial detection of the same spectrum would be.

Another factor inhibiting EXELFS studies has been their limitation mainly to K edges. K-edge EXELFS is easy to interpret because of its simple structure. L and M edges, on the other hand, are complicated by the variety of possible transitions. The present thesis shows that useful EXELFS information can be extracted from L_{23} (Leapman et al., 1982) and M_{45} edges, in spite of their more complicated structure. The use of L_{23}, M_{45} , and other similar edges opens up most of the periodic table to EXELFS investigations.

1.4 Physical Origin of Extended Fine Structure

Using single-scattering SRO theory, the origin of extended fine structure is illustrated schematically in Figure 1.2. The solid circles represent atomic cores, and the rings represent electron-wave crests. An electron is excited from the central atom core and can be thought of as an outgoing spherical wave (solid rings). Note that the phase of the outgoing wave in Figure 1.2 is defined so that there is a crest at the central atom core. The energy of the outgoing wave is the energy loss in excess of the ionization energy. Some of the outgoing wave is elastically scattered (dashed rings) from neighboring atoms. From Fermi's Golden Rule, we know that it is only the interference in the region of the initial state (i.e., at the central atom core) which changes the excitation probability, and hence modifies the edge shape. One can visualize the interference between outgoing and scattered waves at the central atom as varying periodically with the wavelength of the excited electron (i.e., with the distance between concentric rings in Figure 1.2). If constructive interference occurs at the central atom, as in Figure 1.2a, then the excitation probability

increases, creating positive extended fine structure. For destructive interference, shown in Figure 1.2b, the extended fine structure is negative. Extended fine structure is thus a quantum interference phenomenon dependent on the amplitude and phase of the backscattering from the local environment surrounding the ionized atom.

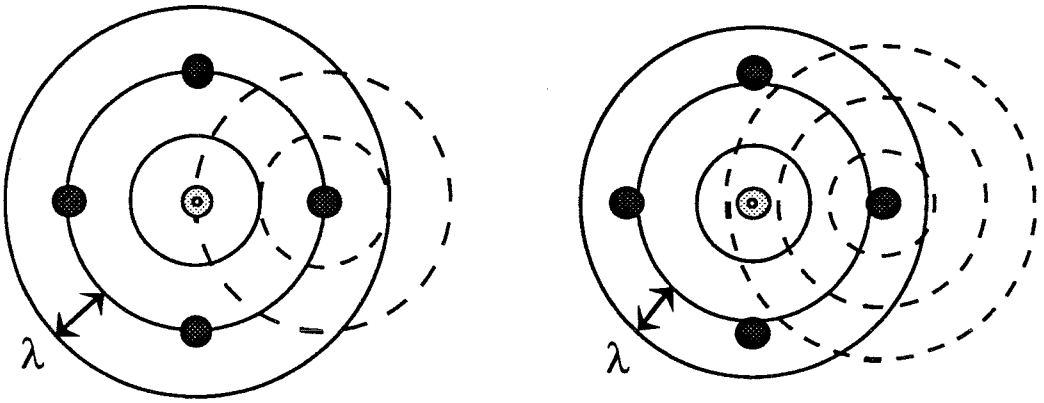

(a) constructive (b) destructive

Figure 1.2. Schematic illustration of (a) constructive and (b) destructive interference at the central atom.

1.5 Applications of EXELFS in Materials Science

Extended fine structure is useful because it can provide local information which is difficult to obtain by diffraction techniques. Because of their sensitivity to LRO, diffraction techniques are most powerful when applied to crystalline materials. In contrast, extended fine structure is sensitive only to SRO. Regardless of the amount of LRO in a material, extended fine structure can be used to determine the identities and positions of nearest-neighbor atoms surrounding the probe atom.

An important feature of extended fine structure is its ability to probe independently the environments of different atomic species. This feature makes

EXELFS appropriate for studies of the atomic structure of alloys, especially alloys with high concentrations of the probe species. To my knowledge, no EXELFS studies of dilute alloys have been made; such experiments would require extremely good signal-to-noise ratios, which are more easily achieved with EXAFS using a synchrotron source than with EXELFS. This thesis work shows, however, that EXELFS can be used to observe chemical short-range order (CSRO) in non-dilute alloys. Measurements are presented in §6.1 which show differences in CSRO between as-quenched and annealed alloys of Fe_3Al and Ni_3Al.

Extended fine structure measurements are sensitive to disorder in the local structure surrounding the probe atom. The disorder can be either structural or vibrational in origin. Historically, extended fine structure has been considered to be particularly suited to study the structural disorder in amorphous materials (Sayers et al., 1971). The primary goal of such studies is the determination of partial radial distribution functions (RDFs). The problem is that it is difficult to differentiate between a reduction in coordination number and an increase in disorder without assumptions about the partial RDFs in the first place (Lee et al., 1981). Thus, in order to determine partial RDFs from disordered systems, extended fine structure must be used in conjunction with other techniques, such as x-ray and neutron RDF studies. There have been many good reviews of the use of extended fine structure to study amorphous materials (Lee et al., 1981; Gurman, 1982; Hayes and Boyce, 1982; Stearns and Stearns, 1986; Crozier et al., 1988).

Recently the structural disorder in nanocrystalline materials has become a topic of interest (Gleiter, 1989). EXAFS measurements have been used to support the claim that the grain boundaries in some nanocrystalline materials

are highly disordered (Haubold et al., 1989). In this thesis work, EXELFS was used to investigate the structural disorder in nanocrystalline Pd and TiO_2. Results presented in §6.2 indicate greater amounts of structural disorder are present in the nanocrystalline Pd and TiO_2 than in large-grained materials.

Vibrational disorder results from the thermal vibrations of atoms in a material. Extended fine structure measurements of vibrational disorder are usually characterized with temperature-dependent mean-square relative displacement (MSRD) data. Temperature-dependent MSRD data can be fit to "local" Debye temperatures using the correlated Debye model (Beni and Platzman, 1976). Local Debye temperatures indicate the stiffness of bonds between the probe atom and its nearest-neighbor atoms. Data presented in §5.3 give local Debye temperatures for the elemental metals Al, Fe, and Pd, which correlate well with published force constant models derived from inelastic neutron scattering data.

The vibrational entropy of a material can be estimated by a weighted average of its local Debye temperatures. An important application of this thesis was the measurement of the differences in vibrational entropy between chemically disordered and ordered intermetallic alloys. EXELFS data presented in §6.1 indicate that the differences in vibrational entropy between chemically disordered and ordered alloys of Fe_3Al and Ni_3Al are almost as large as the entropy of mixing.

In summary, previous applications of EXELFS to materials science have been mostly meager and exploratory. This work is the first to apply the method to contemporary problems.

2 Electron-Atom Scattering Theory

This chapter discusses the electron-atom scattering theory that underpins the EXELFS technique. EXELFS utilizes both the inelastic and elastic scattering of electrons by atoms.

The inelastic scattering of fast electrons by atoms is reviewed in §2.1. §2.1.1 describes the kinematics of the problem. §2.1.2 outlines the calculation of ionization cross sections in the Born approximation. Lastly, §2.1.3 discusses the deconvolution of energy-loss spectra to remove multiple inelastic scattering.

The elastic scattering of electrons by atoms, and how it causes the extended fine structure phenomenon, is reviewed in §2.2. First, §2.2.1 determines the phase shifts and scattering amplitudes associated with elastic scattering. §2.2.2 then discusses the theory of extended fine structure. The equation used to interpret extended fine structure is presented, and its derivation is discussed in detail.

2.1 Inelastic Scattering of Fast Electrons

When electrons collide inelastically with atoms, the incident electrons may be classified as either "fast" or "slow" relative to the mean orbital velocity of the atomic electrons involved in the interaction. For example, incident electrons with 1 keV of kinetic energy are fast with respect to any ionizations of He (22 eV), but they are not fast with respect to the K-shell ionization of Al (1.56 keV). The expression for the scattering cross section of fast collisions may be factored into two distinct parts, one dealing with the incident electron only and the other dealing with the target only. Because the characteristics of the incident electron can be factored out, the study of fast collisions is effectively that of the scatterer properties (Inokuti, 1971).

Inelastic scattering occurs when the incident electron interacts with either outer-shell or inner-shell atomic electrons. Interaction with outer-shell electrons can result in either a single-electron excitation or a collective excitation of electrons in the specimen. In a single-electron excitation, a valence electron makes a transition to a delocalized higher-energy state (Figure 2.1b). A collective excitation can be described by the creation of a plasmon pseudoparticle which represents an oscillation of the valence-electron density. Interaction with an inner-shell electron results in the excitation of a core electron to a delocalized higher-energy state (Figure 2.1c). These inner-shell interactions cause the core edges observed in EELS, typically at energy losses of hundreds or thousands of eV.

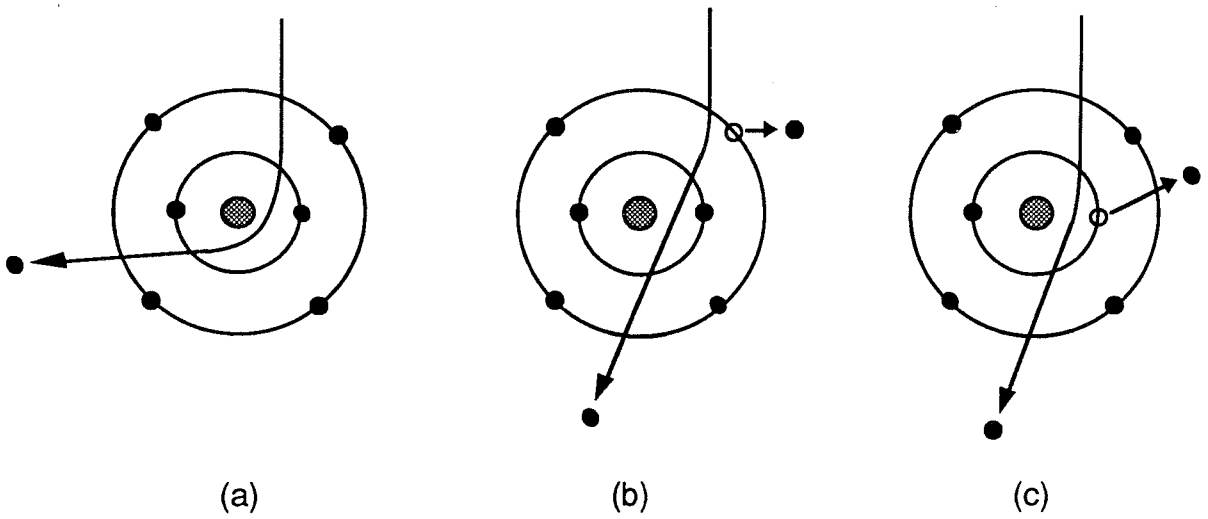

Figure 2.1. Classical picture of electron scattering by a single atom (carbon). Gray dots represent atomic nuclei. Black dots represent electrons. Rings represent classical electron orbitals. Lines represent electron trajectories. (a) Elastic scattering caused by Coulomb attraction of nucleus. Inelastic scattering from Coulomb repulsion by (b) outer- and (c) inner-shell electrons (After Egerton, 1986).

2.1.1 Kinematics

Consider the scattering of a fast electron from an atom. The momentum vectors of the electron before and after the collision are defined to be $\mathbf{p}_i = \hbar\mathbf{k}_i$ and $\mathbf{p}_f = \hbar\mathbf{k}_f$, respectively. By conservation of momentum, the momentum supplied to the atom is $\hbar\mathbf{q} = \hbar\mathbf{k}_i - \hbar\mathbf{k}_f$, where $\mathbf{q}$ is known as the scattering wavevector. The vector relationship between $\mathbf{q}$, $\mathbf{k}_i$, and $\mathbf{k}_f$ is illustrated in Figure 2.2. For inelastic scattering ($k_i \neq k_f$), the magnitude, q, of the scattering wavevector depends on both the scattering angle, θ, and the energy loss, E. The relationship between q, θ, and E is derived using conservation of both momentum and energy.

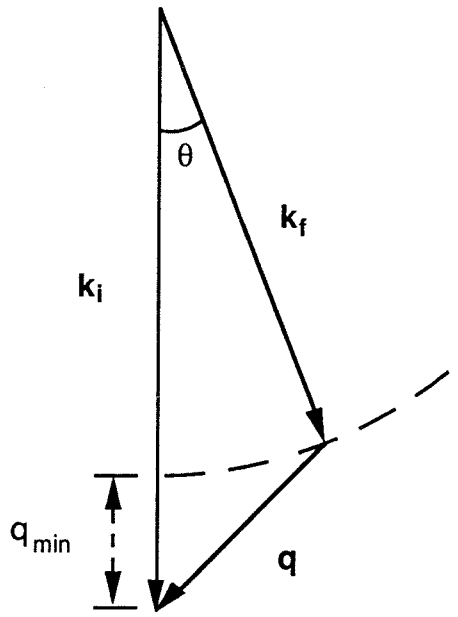

Figure 2.2. Vector relationship of $\mathbf{q}$, $\mathbf{k}_i$, and $\mathbf{k}_f$ due to conservation of momentum (After Egerton, 1986).

Applying the "law of cosines" to the vector triangle in Figure 2.2 gives

$$q^2 = k_i^2 + k_f^2 - 2k_ik_f\cos\theta \qquad (2.1a)$$

or

$$q^2 = (k_i - k_f)^2 + 4k_ik_f\sin^2\left(\theta/2\right) \tag{2.1b}$$

Conservation of energy gives

$$W_i - E = W_f \tag{2.2}$$

where W_0 and W_n are the total energies of the high-energy electron before and after the collision, respectively. From relativistic kinematics we know that the total energy of an electron is given by $W = [m_e^2c^4 + (\hbar k)^2c^2]^{1/2}$, where m_e is the rest mass of the electron, k is its wavevector, and c is the speed of light. Using this expression to substitute for W_0 and W_n in Equation (2.2) and solving for k_f^2 gives

$$k_f^2 = k_i^2\left(1 - \frac{2E}{p_iv_i} + \frac{E^2}{(p_ic)^2}\right) \tag{2.3}$$

where v_i is the speed of the incident electron. Using Equation (2.3) to substitute for k_f in Equation (2.1b) gives

$$q^2 = k_i^2\left\{\left[1-\left(1 - \frac{2E}{p_iv_i} + \frac{E^2}{(p_ic)^2}\right)^{1/2}\right]^2 + 4\sin^2\left(\theta/2\right)\left(1 - \frac{2E}{p_iv_i} + \frac{E^2}{(p_ic)^2}\right)^{1/2}\right\} \tag{2.4}$$

Equation (2.4) gives q as a function of q and E. Since typically beam energies are in the hundreds of keV while energy losses, E, are at most a few keV, we can assume that $E << p_i v_i < p_i c$. Therefore, we can make the approximation that

$$q^2 \cong k_i^2 \left[\left(\frac{E}{p_i v_i} \right)^2 + 4\sin^2(\theta/2) \right] \tag{2.5}$$

Furthermore, if $\theta << 1$, then

$$q^2 \cong k_i^2 \left[\theta_E^2 + \theta^2 \right] \tag{2.6}$$

where $\theta_E \equiv \frac{E}{p_i v_i}$. It is shown geometrically in Figure 2.2 that for a given energy loss, the minimum length, q_{min}, for the scattering wavevector is at $\theta = 0$. From Equation (2.6) we see that $q_{min} \cong k_i \theta_E$.

2.1.2 Ionization Cross Sections

Energy loss experiments, in effect, measure the energy-differential cross section, $d\sigma/dE$. In this section, the theoretical calculation of $d\sigma/dE$ for the ionization of an atom is reviewed.

In experiments, the scattered electrons are generally collected over a range of θ. For our calculations, however, it is more convenient to use q, rather than θ, as an independent variable. Therefore, we use Equation (2.6) to convert from θ to q. The energy-differential cross section, $d\sigma/dE$, is then obtained by integrating the double-differential cross section $\frac{d^2\sigma}{dqdE}$ over the appropriate range in q.

Within the framework of nonrelativistic one-electron wavefunctions, we assume that the collision affects only the wavefunction of the atomic electron directly involved in the transition. The Hamiltonian for the system is then

$$H = \frac{p^2}{2m_e} + \frac{p_a^2}{2m_e} + V(\mathbf{r_a}) + \frac{e^2}{|\mathbf{r}-\mathbf{r_a}|} \tag{2.7}$$

where p and p_a are the momenta for the incident and atomic electrons, $\mathbf{r}$ and $\mathbf{r_a}$ are their position vectors, and V is the atomic potential. The last term, $e^2/|\mathbf{r}-\mathbf{r_a}|$, is the interaction potential which perturbs the system during the collision.

Before and after the collision, the system is assumed to be in energy eigenstates of the unperturbed Hamiltonian, $|\mathbf{k_i}\rangle|n_0l_0\rangle$ and $|\mathbf{k_f}\rangle|nl\rangle$, respectively. $|\mathbf{k_i}\rangle$ and $|\mathbf{k_f}\rangle$ are the initial and final planewave states of the incident electron. $|n_0l_0\rangle$ is the ground state of the atomic electron, and $|nl\rangle$ are excited states of the atomic electron.

In the first Born approximation, in which the influence of the incident particle upon the atom is regarded as a sudden and weak perturbation, the differential cross section for the inelastic collision is

$$\frac{d\sigma}{d\Omega} = \frac{4e^4m_e^2k_f}{\hbar^4q^4k_i}\left|\sum_{nl}\langle nl|\exp(i\mathbf{q}\cdot\mathbf{r_a})|n_0l_0\rangle\right|^2 \tag{2.8}$$

where $d\Omega$ is the element of solid angle for the scattered electrons (Bethe, 1930; Inokuti, 1971). When the final states of the atomic electron are unbound continuum states, $|\varepsilon l\rangle$, rather than bound discrete states, $|nl\rangle$, the sum over the

final states is replaced with a density of final states, $\rho(\varepsilon)$, and we obtain a result which is differential with respect to energy:

$$\frac{d^2\sigma}{d\Omega dE} = \frac{4e^4 m_e^2 k_f}{\hbar^4 q^4 k_i} \rho(\varepsilon) \sum_l \left| \langle \varepsilon l | \exp(i\mathbf{q} \bullet \mathbf{r_a}) | n_0 l_0 \rangle \right|^2 \qquad (2.9)$$

Rewriting the element of solid angle with $d\Omega = 2\pi \sin\theta d\theta = \frac{2\pi q dq}{k_i k_f}$ gives the following expression for the cross section which is differential with respect to q and E:

$$\frac{d^2\sigma}{dqdE} = \frac{8\pi e^4 m_e^2}{\hbar^4 q^3 k_i^2} \rho(\varepsilon) \sum_l \left| \langle \varepsilon l | \exp(i\mathbf{q} \bullet \mathbf{r_a}) | n_0 l_0 \rangle \right|^2 \qquad (2.10)$$

The energy-differential cross section is obtained by integrating Equation (2.10) over q:

$$\frac{d\sigma}{dE} = \frac{8\pi e^4 m_e^2}{\hbar^4 k_i^2} \rho(\varepsilon) \sum_l \int_{q_{min}}^{q_{max}} \frac{1}{q^3} \left| \langle \varepsilon l | \exp(i\mathbf{q} \bullet \mathbf{r_a}) | n_0 l_0 \rangle \right|^2 dq \qquad (2.11)$$

The matrix elements in Equation (2.11) are evaluated by expanding the operator $\exp(i\mathbf{q}\cdot\mathbf{r_a})$ in terms of spherical Bessel functions. Integrals over angular coordinates are expressed as Wigner 3-j coefficients leaving a radial integral to be evaluated numerically (Manson, 1972; Leapman, et al., 1980).

2.1.3 Deconvolution of Multiple Inelastic Scattering

This section reviews the deconvolution of energy-loss spectra to remove multiple inelastic scattering. Multiple inelastic scattering can drastically affect the

overall shape of an ionization edge. Although deconvolution is reviewed here, deconvolution is not necessarily required prior to EXELFS analysis. As shown in §4.3, if the sample is reasonably thin, EXELFS oscillations are not radically altered by multiple inelastic scattering.

While the probability of a transmitted electron causing more than one inner-shell ionization is generally negligible, there is a significant chance that one or more outer-shell excitations will occur in addition to the inner-shell ionization. These additional outer-shell excitations change the observed shape of the inner-shell edge. The edge that we measure is basically a convolution of the low-loss distribution with the single inelastic scattering profile of the edge.

The effects of multiple inelastic scattering are commonly removed by Fourier-transform methods of deconvolution. There are two schemes for Fourier deconvolution: the Fourier-log method and the Fourier-ratio method. First, let us discuss the Fourier-log method (Johnson and Spence, 1974). Assuming independent scattering events that follow Poisson statistics, the measured intensity in an energy loss spectrum, I(E), can be expressed as

$$I(E) = Z(E) * \left[\delta(E) + \frac{1}{I_o} S(E) + \frac{1}{2! I_o^2} S(E) * S(E) + \ldots \right] \qquad (2.12)$$

where Z(E) is the zero-loss peak, I_o is the area under the zero-loss peak, $\delta(E)$ is a unit area delta function, S(E) is the single scattering distribution, and * denotes convolution. Taking the Fourier transform of Equation (2.12) and solving for the Fourier transform of the single scattering distribution gives

$$S'(\upsilon) = I_o \ln\left(\frac{I'(\upsilon)}{Z'(\upsilon)} \right) \qquad (2.13)$$

where primes denote the Fourier transforms.

Taking the inverse Fourier transform of Equation (2.13), in principle, gives the single scattering intensity which is unbroadened by the instrumental resolution. In practice, however, I'(υ) contains noise, and the noise begins to dominate the signal at high frequencies. Dividing I'(u) by Z'(u) preferentially amplifies the high-frequency noise because Z'(υ) generally falls with increasing υ. Thus, the direct use of Equation (2.13) results in the extreme amplification of high-frequency noise in a spectrum. This noise amplification can be reduced by multiplying S'(υ) by a "reconvolution" function g(υ) which has unit area and falls rapidly with increasing υ (Egerton, 1986). g(υ) is basically a υ-space filter.

Note that some ambiguity exists in Equation (2.13) because the logarithm of a complex number is a multivalued function. In particular, $\ln(z) = \ln(r) + i\theta + i2\pi n$, where $z = r \exp(i\theta)$ and n may be any integer. In practice, this ambiguity becomes a problem only when the sample thickness, t, is about π times greater than the mean free path for inelastic scattering, λ (Spence, 1979).

The second method for spectrum deconvolution, Fourier-ratio method, divides the energy-loss spectrum into the low-loss and core-loss regions. First, the pre-edge background is subtracted to isolate the core edge. Deconvolution is then accomplished by dividing the Fourier transform of the core edge by that of the low-loss region. Unlike the Fourier-log method, which deconvolutes an entire EELS spectrum, the Fourier-ratio method can remove multiple inelastic scattering only from core edges.

In theory, deconvolution with respect to energy alone assumes that all of the scattered electrons have been collected. In practice, only those electron scattered within the spectrometer entrance aperture are collected. However, recently Egerton and Wang (1989) have shown that the effect of the collection

aperture on deconvolution is relatively limited. Another assumption of the previous deconvolution procedures is that the thickness of the sample is constant. Johnson and Spence (1974) calculated that very little unwanted multiple inelastic scattering would remain after the deconvolution of a slightly wedge-shaped sample.

2.2 Elastic Scattering

An important difference between inelastic and elastic scattering is that inelastic scattering is incoherent while elastic scattering is coherent. Because of its coherency, elastic scattering results in interference effects. Diffraction is one example of an interference effect caused by elastic scattering. Extended fine structure is another.

Extended fine structure is an interference phenomenon caused by the elastic scattering of an ionized electron by neighboring atomic cores. When an electron is ionized from an isolated atom, the final state can be represented by an outgoing electron-wave with spherical symmetry. In condensed matter, however, the final state is perturbed by backscattering from the surrounding environment. Elastically backscattered electron-waves coherently modify the amplitude of the outgoing wave in the region of the initial atomic state, thus changing the probability of excitation in the first place.

2.2.1 Phase Shifts and Scattering Amplitudes

In order to study quantitatively the extended fine structure phenomenon, we must first understand phase shifts and scattering amplitudes. The following discussion of phase shifts largely follows the one in Cohen-Tannoudji et al., (1977). In a central (i.e., spherically symmetric) potential V(r), there exists

stationary states with well-defined angular momentum, i.e., eigenstates common to the H, $\mathbf{L}^2$, and L_z, where H is the Hamiltonian, and $\mathbf{L}$ is the orbital angular momentum of the particle. The wave functions associated with these states are called partial waves. Partial waves can be written as $\varphi_{klm}(r,\theta,\phi)$, where $\hbar^2k^2/2m_e$, $l(l+1)\hbar^2$, and $m\hbar$ are respectively the eigenvalues of H, $\mathbf{L}^2$, and L_z. The angular dependence of the partial wave $\varphi_{klm}(r,\theta,\phi)$ is always given by the spherical harmonic $Y_{lm}(\theta,\phi)$. However, the radial dependence of the partial wave is influenced by the central potential V(r).

Consider the case where we are dealing with a free particle, i.e., V(r) = 0. The stationary states with well-defined angular momentum are then called free spherical waves $\varphi^{(0)}_{klm}(r,\theta,\phi)$. Free spherical waves are given by

$$\varphi^{(0)}_{klm}(r,\theta,\phi) = \sqrt{\frac{2k^2}{\pi}}\, j_l(kr)\, Y_{lm}(\theta,\phi) \qquad (2.14)$$

where $j_l(kr)$ is a spherical Bessel function. The asymptotic behavior of $j_l(kr)$ is given by

$$j_l(kr) \underset{kr\to\infty}{\sim} -\frac{\exp(-ikr)\exp(il\pi/2) - \exp(ikr)\exp(-il\pi/2)}{2ikr} \qquad (2.15)$$

Therefore, the free spherical wave $\varphi^{(0)}_{klm}(r,\theta,\phi)$ behaves asymptotically as the superposition of an incoming wave exp(-ikr)/r and an outgoing wave exp(ikr)/r, where the phase difference between the two waves is equal to $l\pi$.

Assuming that V(r) = 0 for $r > r_0$, the partial wave $\varphi_{klm}(r,\theta,\phi)$ also behaves asymptotically as the superposition of an incoming wave exp(-ikr)/r and an outgoing wave exp(ikr)/r, with a phase difference between the two waves.

However, the phase difference of the partial wave is not the same as that of the free spherical wave. The potential V(r) introduces an additional phase shift $2\delta_l(k)$ which is the only difference between the asymptotic behavior of $\varphi_{klm}(r,\theta,\phi)$ and that of $\varphi^{(0)}_{klm}(r,\theta,\phi)$. The phase shift $2\delta_l(k)$ depends on both the orbital angular momentum of the wave, through l, and the energy of the wave, through k.

The phase shift can be interpreted in the following way. Suppose we have an incoming spherical wave $Y_{lm}(\theta,\phi)\exp(-ikr)/r$. This incoming wave is perturbed when it enters the zone of influence of the potential V(r). After turning back and leaving the zone of influence, it is transformed into an outgoing wave which has accumulated a phase shift of $2\delta_l(k)$ relative to the free outgoing wave that would have resulted if V(r) had been zero. The additional phase factor $\exp[i2\delta_l(k)]$ summarizes the total effect of the potential on the particle.

Next, we show how these phase shifts can be used to calculate the scattering amplitude of a beam of particles with energy $\hbar^2k^2/2m_e$ from the central potential V(r). The problem is illustrated in Figure 2.3. Initially, before a particle in the beam reaches the influence of V(r), it is represented by the plane wave state exp(ikz). When the plane wave collides with V(r), the structure and evolution of the wave are modified in a complicated way. Nevertheless, when the wave leaves the influence of V(r) it once again takes on a simple form. It becomes split into a transmitted plane wave exp(ikz) which continues to propagate along the z-direction and a scattered wave represented by $f(\theta,k)\exp(ikr)/r$. $f(\theta,k)$ is called the scattering amplitude. Thus, for the steady-state configuration described above, the stationary scattering state $\psi(r,\theta)$ will have asymptotic behavior of the form:

$$\psi(r,\theta) \underset{r\to\infty}{\sim} \exp(ikz) + f(\theta,k)\exp(ikr)/r \qquad (2.16)$$

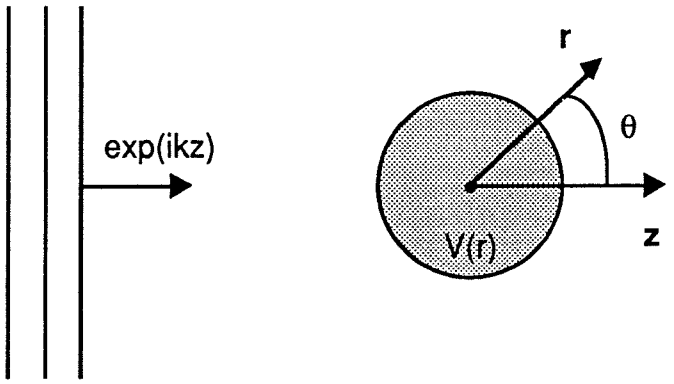

(a) before collision

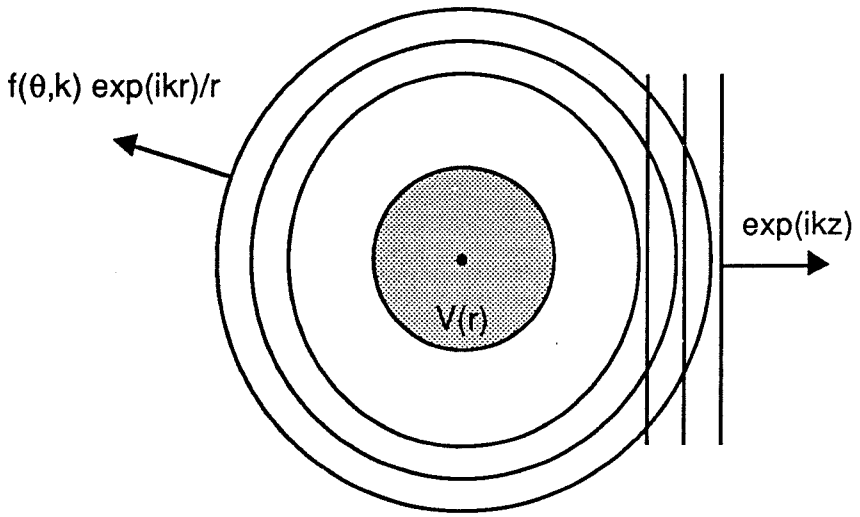

(b) after collision

Figure 2.3. Scattering of plane-wave packet from central potential (After Cohen-Tannoudji et al., 1977).

When V(r) is identically zero, $\psi(r,\theta)$ reduces to the plane wave exp(ikz). The plane wave exp(ikz) can be expanded in terms of free spherical waves:

$$\exp(ikz) = \sqrt{\frac{\pi}{2k^2}} \sum_{l=0}^{\infty} i^l \sqrt{4\pi(2l+1)}\, \varphi_{kl0}^{(0)}(r,\theta) \qquad (2.17)$$

Note that because the plane wave is symmetric with respect to rotations around the z-axis, its expansion includes only those free spherical waves with m = 0. If we slowly turn on the potential V(r), then we intuitively expect that the free spherical waves $\varphi_{kl0}^{(0)}(r,\theta)$ will slowly turn into the corresponding partial waves $\varphi_{kl0}(r,\theta)$. Therefore, in general, the stationary scattering state $\psi(r,\theta)$ can be expanded in terms of partial waves:

$$\psi(r,\theta) = \sqrt{\frac{\pi}{2k^2}} \sum_{l=0}^{\infty} i^l \sqrt{4\pi(2l+1)}\, \varphi_{kl0}(r,\theta) \qquad (2.18)$$

Using the fact that, except for the additional phase shifts $2\delta_l(k)$, the asymptotic behavior of partial waves is identical to that of free spherical waves, we find:

$$\psi(r,\theta) \underset{r\to\infty}{\sim} -\sum_{l=0}^{\infty} i^l \sqrt{4\pi(2l+1)}\, Y_{l0}(\theta) \left[\frac{e^{-ikr} e^{il\pi/2} - e^{ikr} e^{-il\pi/2} e^{i2\delta_l(k)}}{2ikr} \right] \qquad (2.19)$$

Rewriting the phase factor $e^{2i\delta_l(k)} = 1 + 2i\, e^{i\delta_l(k)} \sin \delta_l(k)$, rearranging the terms, and recognizing the asymptotic expansion of the plane wave exp(ikz):

$$\psi(r,\theta) \underset{r\to\infty}{\sim} \exp(ikz) + \frac{\exp(ikr)}{r} \frac{1}{k} \sum_{l=0}^{\infty} \sqrt{4\pi(2l+1)}\, e^{i\delta_l(k)} \sin \delta_l(k)\, Y_{l0}(\theta) \qquad (2.20)$$

By comparing Equation (2.20) with Equation (2.16), we arrive at an expression for the scattering amplitude $f(\theta,k)$ in terms of the phase shifts $\delta_l(k)$:

$$f(\theta,k) = \frac{1}{k}\sum_{l=0}^{\infty}\sqrt{4\pi(2l+1)}\; e^{i\delta_l(k)} \sin\delta_l(k)\; Y_{l0}(\theta)$$
$$= \frac{1}{k}\sum_{l=0}^{\infty}(2l+1)\; e^{i\delta_l(k)} \sin\delta_l(k)\; P_l(\cos\theta) \qquad (2.21)$$

where $P_l(\cos\theta)$ are the Legendre polynomials. Finally, note that because $f(\theta,k)$ is a complex function, it is often expressed in polar notation:

$$f(\theta,k) = |f(\theta,k)|\exp[i\eta(\theta,k)] \qquad (2.22)$$

2.2.2 Theory of Extended Fine Structure

The physical origin of extended fine structure was briefly explained in §1.4. This section contains a more quantitative discussion of the theory.

Because the dipole rule does not strictly hold for EXELFS, transitions to any angular-momentum channel are possible. However, for small scattering angles the dipole approximation is generally valid. The dipole rule states that if l_0 is the angular-momentum quantum number of the initial state, then only transitions to final states with angular-momentum quantum numbers $l_0 \pm 1$ are allowed. Furthermore, as shown by calculations of partial energy-differential cross sections presented in chapter 4, the transition to $l_0 + 1$ dominates over that to $l_0 - 1$. The dominance of the l_0 to $l_0 + 1$ channel allows us to interpret EXELFS in polycrystalline or amorphous materials with the following equation:

$$\chi(k)=(-1)^{l_0+1}\sum_j \frac{|f_j(\pi,k)|\; S(k)}{kR_j^2}\; e^{-2R_j/\lambda(k)}\; e^{-2\sigma_j^2k^2}\; \sin[2kR_j + \eta_j(\pi,k) + 2\delta_{l_0+1}(k)] \qquad (2.23)$$

$\chi(k)$ represents the extended fine structure oscillations normalized to the non-oscillatory intensity of the ionization edge. l_0 is the angular-momentum quantum number of the initial state. The summation over j is over all atoms neighboring the central (ionized) atom. The distance from the central atom to neighboring atom j is denoted by R_j. $|f_j(\pi,k)|$ and $\eta_j(\pi,k)$ are respectively the amplitude and phase shift of the backscattered wave. $2\delta_l(k)$ is the central atom phase shift. The factor S(k) approximately takes into account many-body effects such as "shake up/off" processes at the central atom. The factor $\exp[-2R_j/\lambda(k)]$ is a phenomenological term which accounts for the finite lifetime of the excited state, where $\lambda(k)$ is the inelastic mean free path of the ionized electron. Finally, the term $\exp(-2\sigma_j^2k^2)$ is a Debye-Waller type factor due to vibrations between atoms, where σ_j^2 is the mean-square relative displacement (MSRD) between the central atom and neighboring atom j.

Equation (2.23) is basically the same as "the EXAFS equation" which is commonly used to interpret EXAFS oscillations. The most serious approximation made in Equation (2.23) is the plane-wave approximation. The plane-wave or small-atom approximation assumes that the outgoing spherical wave can be approximated by a plane wave in the vicinity of the scattering atom. This approximation is valid if the effective size of the scattering atom is much smaller than its distance from the center atom. At high k, say $k > 4$ Å^{-1}, this is generally true because the electron penetrates deeply into the atom before scattering. However, at low k the effective size of the atom can be about the same as the interatomic distance. Therefore, in the low k region the curvature of the outgoing wave and the finite size of the scattering atom must be taken into account. Theories of extended fine structure that do not use the plane-wave approximation are called curved-wave theories.

Another approximation made in Equation (2.23) is the single-scattering approximation. The single-scattering approximation assumes that the outgoing wave scatters only once from neighboring atoms before being combined with the unscattered wave. Multiple-scattering processes are neglected. Like the plane-wave approximation, the single-scattering approximation is valid in the high-k region, again say $k > 4$ Å^{-1}. This is because scattering amplitudes generally decrease with increasing k. In principle, multiple scattering should not have any effect on extended fine structure oscillations from first nearest-neighbor (1nn) atoms surrounding the center atom. This is because multiple-scattering path lengths are always longer than the single-scattering path lengths to and from 1nn atoms.

Since both the plane-wave and single-scattering approximations are valid at high k, the use of Equation (2.23) is restricted to the high-k region. It is this restriction that is responsible for the "extended" in the phrase "extended fine structure."

We now present a derivation of Equation (2.23). This derivation closely follows that of Boland et al. (1982), except that we focus on EXELFS rather than EXAFS. Although many other derivations of Equation (2.23) are published (Stern, 1974; Ashley and Doniach, 1975; Lee and Pendry, 1975; Lee, 1976), the derivation by Boland et al. is especially clear. For an efficient curved-wave theory of extended fine structure, see either Gurman et al. (1984) or Schaich (1984).

Since this thesis is concerned with EXELFS, we start with the energy-differential cross section which is given by Equation (2.11). In the dipole approximation, the matrix element in Equation (2.11) reduces to $\langle \varepsilon(l_0 \pm 1) | \mathbf{q} \cdot \mathbf{r_a} | n_0 l_0 \rangle$, where $\mathbf{q}$ is the scattering wavevector, $\mathbf{r_a}$ is the position

vector of the atomic electron which undergoes the transition, $|n_0 l_0\rangle$ is the initial state, and $|\varepsilon(l_0+1)\rangle$ are final states of energy ε. The matrix element is then of the same form as that for x-ray absorption. Fortunately, the dipole approximation is generally valid for the experiments performed in this thesis. A simple condition for the validity of the dipole approximation is that $qr_{max} << 1$, where q is the magnitude of the scattering wavevector and r_{max} is the radial extent of the initial core wavefunction. Consider our experiments on the Al K edge which are performed using 200 keV incident electrons and collection angles of roughly 5 mrad. For these experiments, $q \cong 1$ Å^{-1} and $r_{max} \cong 0.1$ Å, so $qr_{max} \cong 0.1 << 1$. The validity of the dipole approximation for our experiments is shown more precisely in §A.1. §A.1 calculates the cross sections for excitation into the various angular momentum channels and shows that dipole transitions to $l_0 \pm 1$ dominate over non-dipole transitions.

Moreover, as mentioned previously, calculations of partial energy-differential cross sections presented in chapter 4 show that the $l_0 + 1$ transition dominates over all others. Therefore, the matrix element further reduces to $\langle\varepsilon(l_0+1)|\mathbf{q}\bullet\mathbf{r_a}|n_0 l_0\rangle$. To simplify our notation, we now substitute **r** for $\mathbf{r_a}$, $|i\rangle$ for $|n_0 l_0\rangle$, and $|f\rangle$ for $|\varepsilon(l_0+1)\rangle$. In this notation, the energy-differential cross section can be written as

$$\frac{d\sigma}{dE} = \frac{8\pi e^4 m_e^2}{\hbar^4 k_i^2}\,\rho(\varepsilon)\,\ln\left(\frac{q_{max}}{q_{min}}\right)\left|\langle f|\hat{\mathbf{q}}\bullet\mathbf{r}|i\rangle\right|^2 \qquad (2.24)$$

where q_{max} is the maximum scattering wavelength experimentally collected.

The initial and final states of the system are both eigenfunctions of the Hamiltonian H:

$$H = -\frac{\hbar^2}{2m}\nabla_r^2 + U(r) + V(\mathbf{r}) \qquad (2.25)$$

where U(r) is the attractive atomic potential primarily felt by the electron in its initial state, and V(**r**) is the total scattering potential seen by the final-state electron. We represent V(**r**) with a muffin-tin potential, i.e., a sum of nonoverlapping, spherically symmetric potentials centered around each atomic site of the alloy. The potential of the center atom seen by the final-state electron is that of a "relaxed" ion with a core hole. This is because the transit time for the ejected electron to travel to a neighboring atom and back is much shorter than the lifetime of the core hole, but it is generally much longer than the relaxation time for the remaining core electrons (Teo, 1986).

In particular, we consider the scattering from two neighbors about an atom. This problem is illustrated in Figure 2.4. The atom undergoing ionization is at the center of the coordinate system and is labeled "c." The two neighbors labeled "a" and "b" are located respectively at $\mathbf{R_a}$ and $\mathbf{R_b}$.

To calculate the matrix element in Equation (2.24), it is necessary to find the initial and final states. These states must be eigenfunctions of H. At the large negative energy corresponding to the initial state, the scattering potential V(**r**) may be ignored. The resulting Hamiltonian has eigenfunctions which are the usual core wavefunctions obtained from atomic structure calculations.

For final-state electrons of sufficiently high energy, the attractive atomic potential U(r), which determined the initial state, becomes negligible. The resulting Schrödinger equation for the final state is as follows:

$$(\varepsilon - H^0)\,|f\pm\rangle = V\,|f\pm\rangle \qquad (2.26)$$

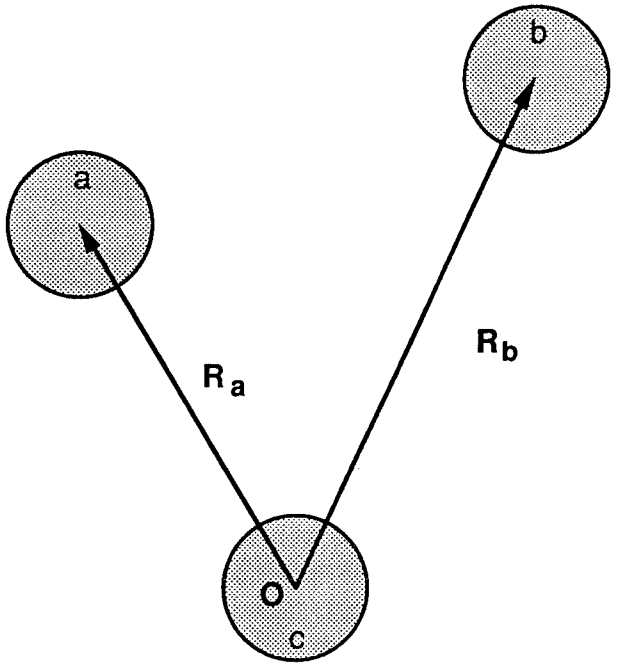

Figure 2.4. Schematic illustration of the final state potential V(**r**) (After Boland et al., 1982).

where H^0 is the free-particle Hamiltonian. This equation is inverted to give the Lippman-Schwinger equation:

$$\begin{aligned} |f\pm\rangle &= |k\rangle + G_0^{\pm}\, V\, |f\pm\rangle \\ &= |k\rangle + G_0^{\pm}\, T^{\pm}\, |k\rangle \end{aligned} \qquad (2.27)$$

where $\langle r|k\rangle$ are the normalized eigenfunctions of H^0. Because we want $\langle r|k\rangle$ to correspond to the outgoing asymptote of the scattering process, we use the minus form of the free-particle Green and T operators.

The full T operator can be expanded in terms of operators t_j associated with the individual scattering centers located at $\mathbf{r} = \mathbf{R_j}$.

$$T = \sum_{j \neq c} t_i + \sum_{j \neq m} t_j G_0 t_m + \sum_{j \neq m, m \neq n} t_j G_0 t_m G_0 t_n + \ldots \qquad (2.28)$$

Note that successive scattering by the same potential is not permitted. The first-order terms in the expansion correspond to single-scattering processes, second-order terms to double-scattering processes, and so on. Figure 2.5 diagrams the zero-scattering, single-scattering , and double-scattering processes for our three atom system. Note that the free-particle Green functions represent free propagation between two neighboring atom potentials.

One might assume that only processes (a) through (c) would be used in the single-scattering approximation of extended fine structure. That assumption, however, would be incorrect. In addition to zero-scattering and single-scattering processes, the correct single-scattering approximation also includes some select double-scattering processes as well. In particular, (d) and (e) in Figure 2.5 represent double-scattering processes for which the second scattering center is the center atom potential. In such processes, the scattering path lengths to the center atom are identical with those of the single-scattering processes (b) and (c), respectively. Since it is the path length back to the center atom which is important for extended fine structure, (d) and (e) must also be included in the single-scattering approximation.

Thus, in the single-scattering formalism, the terms corresponding to diagrams (a) through (e) in Figure 2.5 are substituted into the matrix element of Equation (2.24):

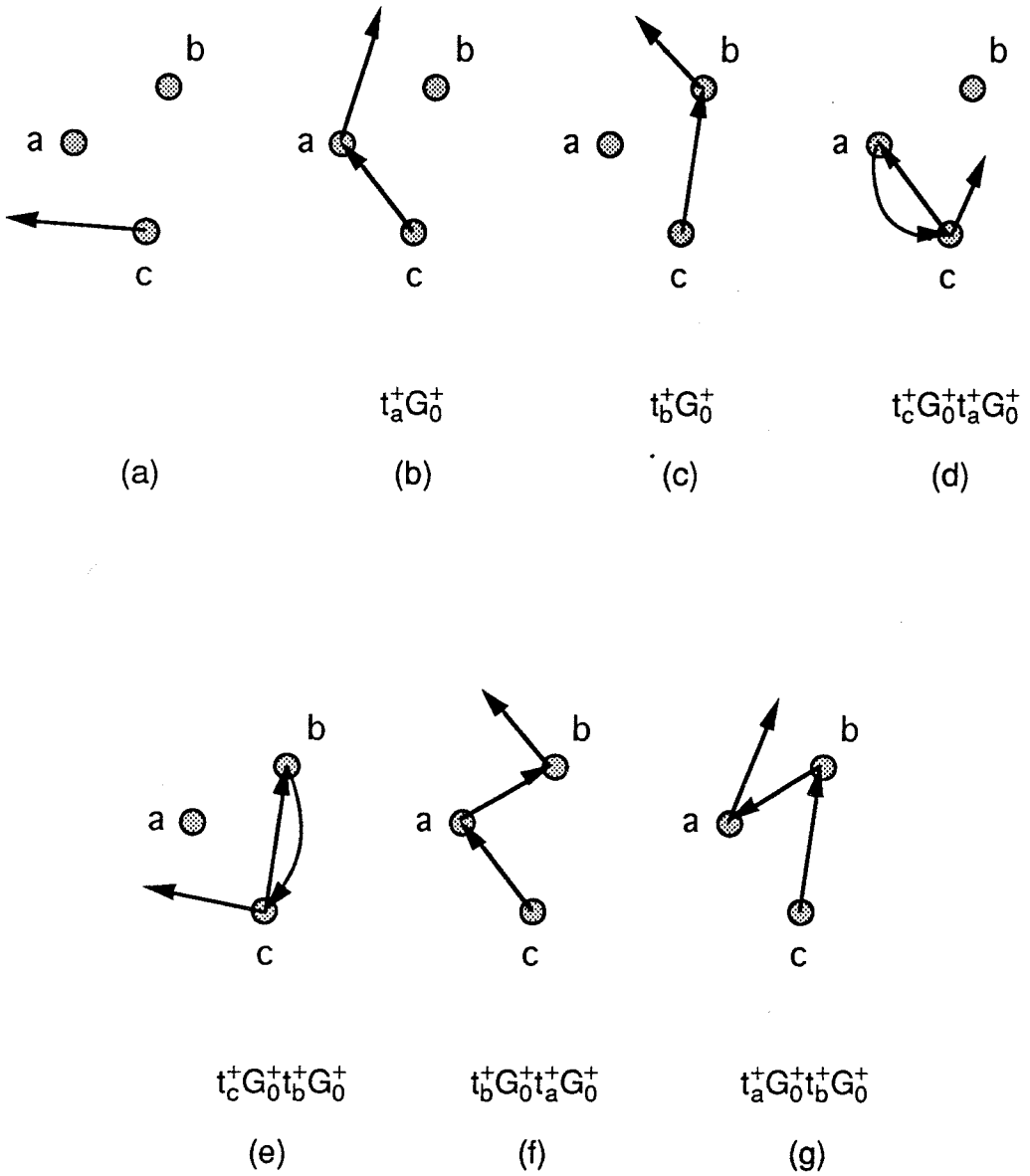

Figure 2.5. Diagrammatic representations of (a) zero-scattering, (b-c) single-scattering, and (d-g) double-scattering processes for three-atom system (After Boland et al., 1982).

$$\langle f-|\hat{\mathbf{q}}\bullet\mathbf{r}|i\rangle = \langle k|\hat{\mathbf{q}}\bullet\mathbf{r}|i\rangle + \sum_j \langle k|t_j^+ G_0^+ \hat{\mathbf{q}}\bullet\mathbf{r}|i\rangle + \sum_j \langle k|t_c^+ G_0^+ t_j^+ G_0^+ \hat{\mathbf{q}}\bullet\mathbf{r}|i\rangle \qquad (2.29)$$

where, of course, we have taken the complex conjugate of Equation (2.27). To proceed further, we must determine the effective values at the origin of all the matrix elements in the right-hand side of Equation (2.29).

The first matrix element on the right-hand side of Equation (2.29) is responsible for the unscattered outgoing electron and can be evaluated using the addition theorem for spherical harmonics to become of the form:

$$\langle k|\hat{\mathbf{q}}\bullet\mathbf{r}|i\rangle = M(k)\ \hat{\mathbf{k}}\bullet\hat{\mathbf{q}} \qquad (2.30)$$

where
$$M(k) = (2\pi)^{-3/2} 4\pi(-i)\int_0^\infty j_1(kr)\langle r|i\rangle r^3 dr \qquad (2.31)$$

and $\hat{\mathbf{k}}$ is the direction of propagation of the electron as it originally leaves the center atom. Intuitively, the term $\hat{\mathbf{k}}\bullet\hat{\mathbf{q}}$ makes sense because it means that the electron is most likely to be ejected in the direction of the scattering vector. Boland et al. (1982) determines M(k) explicitly for the case where $\langle r|i\rangle$ is a hydrogenic wave function.

The single-scattering and double-scattering terms can be expanded:

$$\sum_j \langle k|t_j^+ G_0^+ \hat{\mathbf{q}}\bullet\mathbf{r}|i\rangle = \sum_j \int \langle k|t_c^+|r_1\rangle\langle r_1|G_0^+|r\rangle \hat{\mathbf{q}}\bullet\mathbf{r}\langle r|i\rangle dr dr_1 \qquad (2.32)$$

$$\sum_j \langle k|t_c^+ G_0^+ t_j^+ G_0^+ \hat{\mathbf{q}}\bullet\mathbf{r}|i\rangle =$$

$$\sum_j \int \langle k|t_c^+|r_3\rangle\langle r_3|G_0^+|r_2\rangle\langle r_2|t_j^+|r_1\rangle\langle r_1|G_0^+|r\rangle \hat{\mathbf{q}}\bullet\mathbf{r}\langle r|i\rangle dr dr_1 dr_2 dr_3 \qquad (2.33)$$

Assuming that the scattering potentials are due mostly to the core electrons which are very close to the center of the atoms, the free-particle Green function may be approximated using:

$$\langle r_1|G_0^+|r\rangle = -\frac{m}{2\pi\hbar^2}\frac{\exp(ik|\mathbf{r}_1-\mathbf{r}|)}{|\mathbf{r}_1-\mathbf{r}|} \cong -\frac{m}{2\pi\hbar^2}\frac{\exp[i\mathbf{k}_j\bullet(\mathbf{r}_1-\mathbf{r})]}{R_j} \qquad (2.34)$$

where $\mathbf{k}_j = k\hat{\mathbf{R}}_j$ is the wavevector of the outgoing electron as it heads towards atom j. Equation (2.34) is equivalent to the plane-wave or small-atom approximation. Boland et al. (1982) shows that substituting Equation (2.34) into Equations (2.32) and (2.33) allows one to perform the space integrals, with the results:

$$\sum_j \langle k|t_j^+ G_0^+ \hat{\mathbf{q}}\bullet\mathbf{r}|i\rangle = -\sum_j \frac{m(2\pi)^2}{\hbar^2}\frac{1}{R_j}M(k)\left(\hat{\mathbf{q}}\bullet\hat{\mathbf{R}}_j\right)\left\langle k\left|t_j^+\right|k_j\right\rangle \qquad (2.35)$$

$$\sum_j \langle k|t_c^+ G_0^+ t_j^+ G_0^+ \hat{\mathbf{q}}\bullet\mathbf{r}|i\rangle = \sum_j \frac{m^2(2\pi)^4}{\hbar^4}\frac{1}{R_j^2}M(k)\left(\hat{\mathbf{q}}\bullet\hat{\mathbf{R}}_j\right)\left\langle k\left|t_c^+\right|k_j'\right\rangle\left\langle k_j'\left|t_j^+\right|k_j\right\rangle \qquad (2.36)$$

where $\mathbf{k}_j' = -k\hat{\mathbf{R}}_j$ is the wavevector of the backscattered electron.

The matrix element $\left\langle k\left|t_j^+(\mathbf{R}_j)\right|k_j\right\rangle$ represents the scattering of the electron by an atom at $\mathbf{R}_j$. We can relate $\left\langle k\left|t_j^+(\mathbf{R}_j)\right|k_j\right\rangle$ to $\left\langle k\left|t_j^+(\mathbf{0})\right|k_j\right\rangle$, which represents the same scattering problem but is centered at the origin:

$$\left\langle k\left|t_j^+(\mathbf{R}_j)\right|k_j\right\rangle = \exp\left[i(\mathbf{k}_j-\mathbf{k})\bullet\mathbf{R}_j\right]\left\langle k\left|t_j^+(\mathbf{0})\right|k_j\right\rangle \qquad (2.37)$$

Because we are dealing only with elastic scattering, the matrix elements $\left\langle k\left|t_j^+(\mathbf{0})\right|k_j\right\rangle$ may be expressed in terms of the scattering amplitude $f_j(\theta_j,k)$:

$$\left\langle k\left|t_j^+(\mathbf{0})\right|k_j\right\rangle = \frac{-\hbar^2}{m(2\pi)^2} f_j(\theta_j,k) \tag{2.38}$$

where θ_j is the angle between $\hat{\mathbf{k}}_j$ and $\hat{\mathbf{k}}$.

Equations (2.35) and (2.36) may now be rewritten:

$$\sum_j \langle k|t_j^+ G_0^+ \hat{\mathbf{q}}\bullet\mathbf{r}|i\rangle = \sum_j \frac{1}{R_j} M(k)\left(\hat{\mathbf{q}}\bullet\hat{\mathbf{R}}_j\right) f_j(\theta_j,k)\exp\left[ikR_j\left(1-\cos\theta_j\right)\right] \tag{2.39}$$

$$\sum_j \langle k|t_c^+ G_0^+ t_j^+ G_0^+ \hat{\mathbf{q}}\bullet\mathbf{r}|i\rangle = \sum_j \frac{1}{R_j^2} M(k)\left(\hat{\mathbf{q}}\bullet\hat{\mathbf{R}}_j\right) f_c(\pi-\theta_j,k) f_j(\pi,k)\exp(2ikR_j) \tag{2.40}$$

The complete matrix element of Equation (2.24) is the sum of the three terms Equations (2.30), (2.39), and (2.40) corresponding respectively to the unscattered outgoing electron, single scattering by neighboring atoms, and secondary scattering by the center atom:

$$\left|\langle f-|\hat{\mathbf{q}}\bullet\mathbf{r}|i\rangle\right|^2 = \left|M(k)\hat{\mathbf{k}}\bullet\hat{\mathbf{q}} + \sum_j \langle k|t_j^+ G_0^+ \hat{\mathbf{q}}\bullet\mathbf{r}|i\rangle + \sum_j \langle k|t_c^+ G_0^+ t_j^+ G_0^+ \hat{\mathbf{q}}\bullet\mathbf{r}|i\rangle\right|^2 \tag{2.41}$$

Equation (2.41) emphasizes the interference nature of the extended fine structure phenomenon in which the probability amplitude for ionization is given by the sum of the amplitudes of three independent scattering processes. Such a sum is required due to the indistinguishability of the individual events; the ejection of the electron in some direction $\hat{\mathbf{k}}$ upon ionization is indistinguishable from a process

whereby the ejected electron scatters off of an adjacent atom into the same direction $\hat{\mathbf{k}}$.

The development above treats a single ionization event. Experimentally, however, a large number of such ionizations will occur, and the ejected electrons will be scattered into many directions $\hat{\mathbf{k}}$. In order to compute the average energy-differential cross section of such a macroscopic system, it is necessary to average over all such directions $\hat{\mathbf{k}}$ in Equation (2.41):

$$\frac{d\sigma}{dE} \propto \int \left| \langle f - |\hat{\mathbf{q}} \bullet \mathbf{r}| i \rangle \right|^2 \frac{d\Omega_k}{4\pi}$$

$$= \int \left| M(k)\left(\hat{\mathbf{k}} \bullet \hat{\mathbf{q}}\right) + \sum_j \langle k | t_j^+ G_0^+ \hat{\mathbf{q}} \bullet \mathbf{r} | i \rangle + \sum_j \langle k | t_c^+ G_0^+ t_j^+ G_0^+ \hat{\mathbf{q}} \bullet \mathbf{r} | i \rangle \right|^2 \frac{d\Omega_k}{4\pi} \quad (2.42)$$

The four lowest order terms in R_j in this spherical average are evaluated in Boland et al. (1982) with the results:

$$\int |M(k)|^2 \left(\hat{\mathbf{k}} \bullet \hat{\mathbf{q}}\right)^2 \frac{d\Omega_k}{4\pi} = \frac{1}{3} |M(k)|^2 \quad (2.43)$$

$$\int 2\,\mathrm{Re}\left[M^*(\hat{\mathbf{k}} \bullet \hat{\mathbf{q}}) \sum_j \langle k | t_j^+ G_0^+ \hat{\mathbf{q}} \bullet \mathbf{r} | i \rangle \right] \frac{d\Omega_k}{4\pi} =$$

$$-|M|^2 \sum_j \frac{\left(\hat{\mathbf{q}} \bullet \hat{\mathbf{R}}_j\right)^2}{kR_j^2} \mathrm{Im}\left\{ \exp\left(2ikR_j\right) f_j(\pi, k) + f_j(0, k) \right\} \quad (2.44)$$

$$\int \left| \sum_j \langle k | t_j^+ G_0^+ \hat{\mathbf{q}} \bullet \mathbf{r} | i \rangle \right|^2 \frac{d\Omega_k}{4\pi} = |M|^2 \sum_j \frac{\left(\hat{\mathbf{q}} \bullet \hat{\mathbf{R}}_j\right)^2}{R_j^2} \int \left| f_j\left(\theta_j, k\right) \right|^2 \frac{d\Omega_k}{4\pi} \quad (2.45)$$

$$\int 2\mathrm{Re}\left[M^{*}(\hat{\mathbf{k}}\bullet\hat{\mathbf{q}})\sum_{j}\langle k|t_c^{+}G_0^{+}t_j^{+}G_0^{+}\hat{\mathbf{q}}\bullet\mathbf{r}|i\rangle \right]\frac{d\Omega_k}{4\pi} =$$

$$(-1)^{l_0+1}|M|^2\sum_{j}\frac{\left(\hat{\mathbf{q}}\bullet\hat{\mathbf{R}}_j\right)^2}{kR_j^2}\mathrm{Im}\left\{\left[\exp\left(2i\delta_{l_0+1}\right)-1\right]f_j(\pi,k)\exp\left(2ikR_j\right)\right\} \qquad (2.46)$$

In summing the above expressions, the forward-scattering term $f_j(0,k)$ in Equation (2.44) cancels with Equation (2.45) because of the optical theorem. The rest of Equation (2.44) cancels with part of Equation (2.46). Thus, the macroscopic energy-differential cross section is of the form:

$$\frac{d\sigma}{dE} \propto \frac{1}{3}|M|^2+(-1)^{l_0+1}|M|^2\sum_{j}\frac{1}{kR_j^2}\left(\hat{\mathbf{q}}\bullet\hat{\mathbf{R}}_j\right)^2\mathrm{Im}\left[f_j(\pi,k)\exp\left(2ikR_j+2i\delta_{l_0+1}\right)\right] \qquad (2.47)$$

Equation (2.47) gives the energy-differential cross section for ionization from the initial state $|n_0l_0\rangle$ into the final states $|\varepsilon(l_0+1)\rangle$. By convention, extended fine structure oscillations are normalized to $\frac{1}{3}|M|^2$:

$$\chi(k)=\frac{\frac{d\sigma}{dE}-\frac{1}{3}|M|^2}{\frac{1}{3}|M|^2}$$

$$=(-1)^{l_0+1}\sum_{j}\frac{3}{kR_j^2}\left(\hat{\mathbf{q}}\bullet\hat{\mathbf{R}}_j\right)^2\left|f_j(\pi,k)\right|\sin\left[2kR_j+\eta_j(\pi,k)+2\delta_{l_0+1}(k)\right] \qquad (2.48)$$

where the scattering amplitude $f_j(\pi,k)$ has been decomposed according to Equation (2.22).

If the sample has no angular dependence, such as a polycrystalline material with no preferred orientation or an amorphous solid, then Equation (2.48) should be averaged over all directions $\hat{\mathbf{R}}_j$. Averaging in three dimensions:

$$\frac{\int\left(\hat{\mathbf{q}}\bullet\hat{\mathbf{R}}_j\right)^2 d\Omega_{R_j}}{4\pi}=\frac{1}{3} \tag{2.49}$$

Therefore, for samples with no angular dependence, Equation (2.48) becomes

$$\chi(k) = (-1)^{l_0+1}\sum_j \frac{1}{kR_j^2}\left|f_j(\pi,k)\right|\sin\left[2kR_j+\eta_j(\pi,k)+2\delta_{l_0+1}(k)\right] \tag{2.50}$$

With Equation (2.50) we have derived the basic form of Equation (2.23). However, Equation (2.23) also contains three additional factors.

The first factor S(k) is an amplitude reduction factor due to many-body effects during the excitation of the central atom. Equation (2.50) simply assumes that a single electron is excited from a core state to the continuum. In reality, the (Z – 1) "bystander" electrons may also be excited in so-called shake-up (excitation to a bound state) and shake-off (excitation to continuum) processes. When these additional excitations occur, the final state consists of the ionized electron and a partially relaxed ion with (Z – 1) electrons. In these cases, the ionized electron ends up a kinetic energy less than ($E - E_0$). This tends to "wash out" the extended fine structure signal since shake-up and shake-off processes generally have broad energy spectra (Teo, 1986). Shake-up and shake-off processes do not turn on until the excess energy is several times the binding energies of the outer electrons. Thus, $S(k) \approx 1$ for low k values and $S(k) < 1$ for k

greater than about 5 $Å^{-1}$. It has been shown that generally $0.6 < S(k) < 0.8$ for k greater than about 7 $Å^{-1}$ (Martin and Davidson, 1977; Stern et al., 1980).

The second factor $\exp[-2R_j/\lambda(k)]$, where $\lambda(k)$ is the inelastic mean free path of the ejected electron, is an exponential damping term which approximates the inelastic losses due to the excitation of other electrons or plasmons in the neighboring environment. Actually, this exponential term can only roughly approximate these inelastic losses. A more general expression would be $L_j(k)L_m(k,R_j)L_c(k)$, where $L_j(k)$ represents inelastic losses due to electrons on the neighboring atom, $L_c(k)$ losses due to electrons on the central atom, and $L_m(k,R_j)$ losses due to the electronic medium in between the two (Eisenberger and Lengeler, 1980). Within the exponential damping approximation, $\lambda(k)$ can be roughly approximated by

$$\lambda(k) = C\left[\left(\frac{D}{k}\right)^4 + k^n\right] \tag{2.51}$$

where C and D are constants, $1 \le n \le 2$, λ is in Å, and k is in $Å^{-1}$. For elemental materials, $C \approx 1$ and $D \approx 3$ (Powell, 1974; Penn, 1976; Seah and Dench, 1979; Teo, 1986).

The third factor $\exp(-2\sigma_j^2 k^2)$, where σ_j^2 is the mean-square relative displacement (MSRD) between the central atom and neighboring atom j, is a Debye-Waller type factor which is used to account for disorder in the interatomic distance between the two atoms. Generally speaking, σ_j^2 has two components:

$$\sigma_j^2 = \sigma_{j,vib}^2 + \sigma_{j,struct}^2 \tag{2.52}$$

where $\sigma^2_{j,vib}$ is due to vibrational disorder and $\sigma^2_{j,struct}$ is due to structural or static disorder. Changes in the vibrational MSRD $\sigma^2_{j,vib}$ can be measured by varying the temperature of the sample. Theoretical calculations of vibrational MSRD using various models are discussed in Chapter 5.

Chapter 3 Instrumentation and Experimental Procedures

This chapter discusses the instrumentation and experimental procedures used for the measurements in this dissertation. §3.1 reviews specimen preparation techniques. §3.2 discusses the characterization of alloys and nanocrystalline materials. §3.3 describes the equipment used to control the temperature of the specimens and calculates the amount of electron beam heating during a typical experiment. Finally, §3.4 describes the parallel-detection electron energy loss spectrometer and outlines the procedure which was used to mitigate its channel-to-channel gain variations.

3.1 Specimen Preparation

Specimen preparation began with elemental metals of at least 99.99% purity. Alloys of Fe_3Al and Ni_3Al were synthesized from the elemental metals using an Edmund-Buehler arc-melting apparatus. The apparatus melts metals on a water-cooled copper hearth in an argon atmosphere. Since the mass losses after melting were negligible, the stoichiometry of the alloys was assumed to be that of the initial mixture of elements. The stoichiometry was also checked by energy-dispersive x-ray (EDX) analysis and EELS.

Foils of the elemental metals Al, Fe, and Pd were prepared by cold rolling. Foils of chemically disordered Fe_3Al were prepared using an Edmund-Buehler piston-anvil quenching (splat cooling) apparatus. The apparatus levitates and melts a small piece of metal in an argon atmosphere using a radio frequency power supply connected to a conical copper coil. When the radio frequency current to the coil is stopped, the molten droplet falls, and two copper disks are triggered to rapidly quench the droplet into a foil. Figure 3.1 depicts schematically the piston-anvil quenching apparatus.

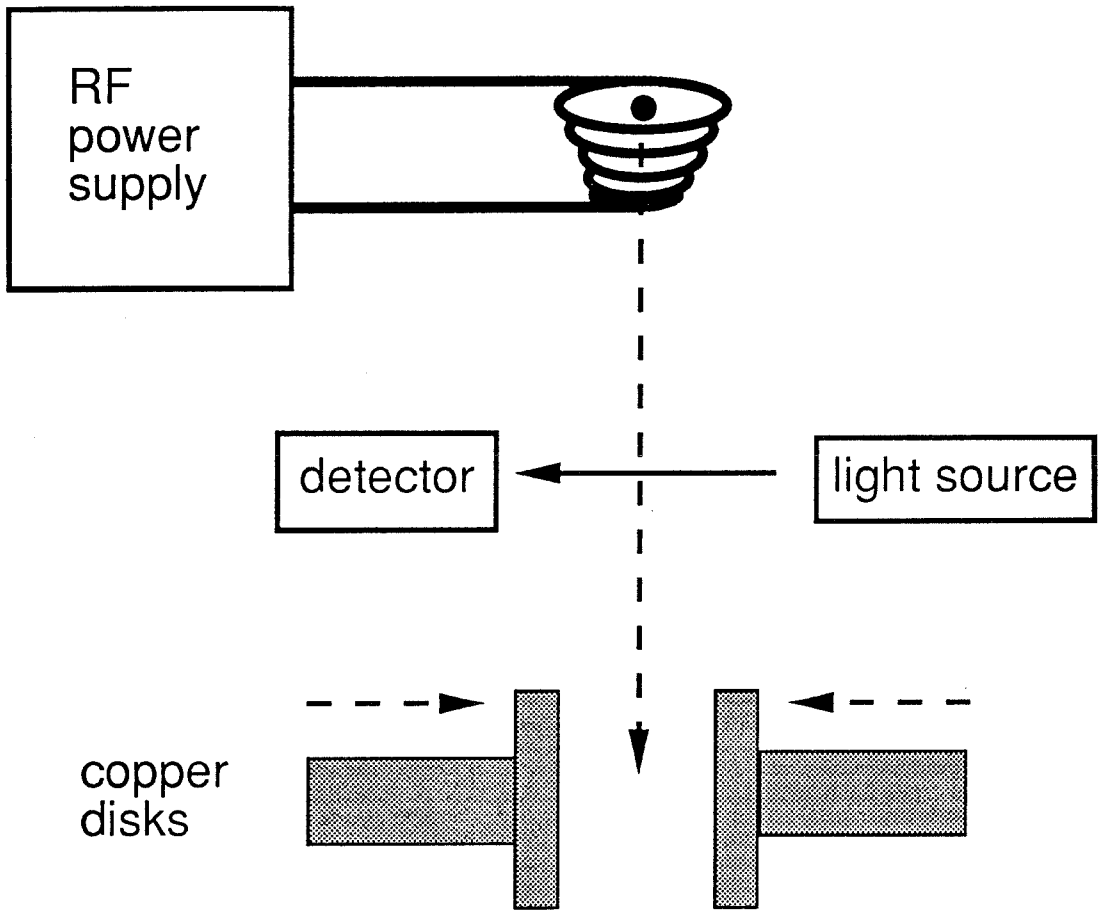

Figure 3.1. Schematic illustration of piston-anvil quenching apparatus (After Pearson, 1992).

For my energy loss experiments, it was necessary to have specimens which were thin enough to be transparent to the 200 keV electrons in the transmission electron microscope. Specimens approximately 1000 Å or less in thickness were required. The Al, Fe, Pd, and Fe_3Al foils were thinned using a Fishione twin-jet electropolisher. The specimen is mounted between two jets of electrolyte, and a voltage is applied across the electropolishing cell. When it is necessary to cool the electropolishing solution below room temperature, the apparatus is immersed in a bath of methanol cooled by liquid nitrogen. A light source and a photo-detector are used to stop polishing at the moment of perforation (Schoone and Fischione, 1966). Table 3.1 lists the conditions at which the specimens were successfully electropolished.

Specimen	Electrolytic Solution	Temperature
Al	30% nitric acid, 70% methanol	-30 C
Fe	20% perchloric acid, 80% methanol	-30 C
Pd	20% perchloric acid, 80% acetic acid	+20 C
Fe_3Al	20% perchloric acid, 80% methanol	-30 C

Table 3.1. Electrolytic solutions and approximate polishing temperatures used to prepare thin foils of Al, Fe, Pd, and Fe_3Al.

Chemically disordered Ni_3Al was prepared in a Denton Vacuum model 502 high vacuum evaporator. A piece of the arc-melted Ni_3Al ingot was placed in a tungsten wire basket. In high vacuum, current was run through the tungsten wire until the Ni_3Al was evaporated onto substrates of either rock salt or copper. The substrates were at room temperature. Figure 3.2 schematically depicts the high vacuum evaporator. Thin films approximately 1000 Å thick were floated in

water off the rock salt substrates onto copper TEM grids. Larger quantities of Ni_3Al were scraped off the copper substrates. Some of the thin films of Ni_3Al were annealed at 300 C in a heating holder of the TEM to develop $L1_2$ order.

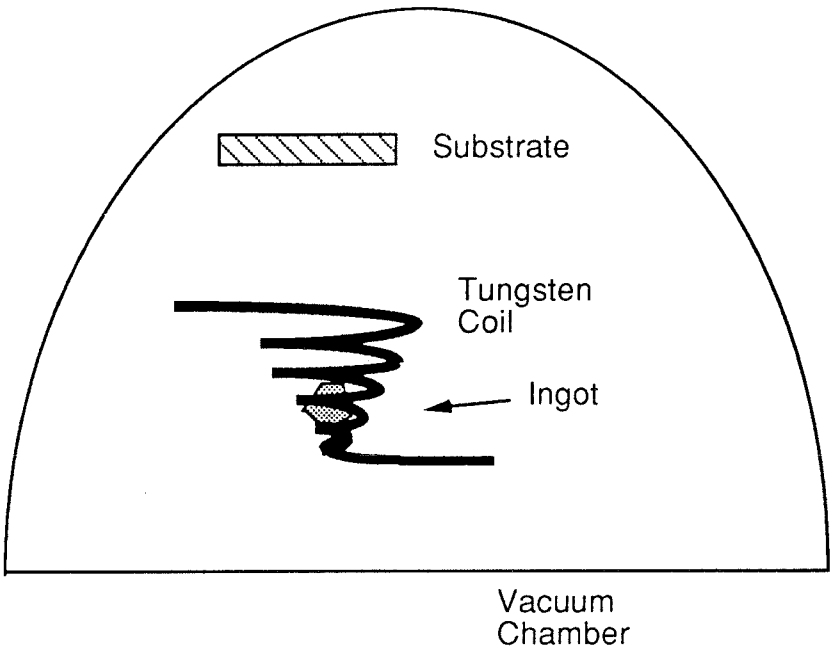

Figure 3.2 Schematic illustration of high-vacuum evaporator.

Nanocrystalline Pd was also prepared using the high vacuum evaporator. Thin films of Pd were evaporated onto substrates of rock salt at room temperature and subsequently floated in water onto copper TEM grids. Some of the thin films of Pd were annealed at 600 C to develop larger grains.

I also used a partially compacted powder of Pd nanocrystals synthesized by inert gas condensation. Pd was evaporated into He gas. A holey carbon TEM grid was held at the temperature of liquid nitrogen to collect some of the particles. The powder was partially compacted in atmosphere at room temperature using a hand-powered compaction device (courtesy Z.Q. Gao).

The preparation of TiO_2 samples started with the evaporation of thin films of Ti metal onto rock salt substrates. The Ti metal was then oxidized by heating the substrates in air in a furnace at 500 C. At 500 C, the shiny film of Ti metal transformed into a transparent film of TiO_2. Some of the films of TiO_2 were subsequently sealed in an evacuated quartz tube and annealed for 30 minutes at 850 C to develop larger grain sizes. To make TEM samples, the rock salt substrates were placed in water and the thin films of TiO_2 were floated onto copper TEM grids.

3.2 Characterization of Alloys and Nanocrystalline Materials

Gao and Fultz (1993) performed x-ray diffractometry measurements on the Fe_3Al foils prepared by piston-anvil quenching. They found an absence of superlattice peaks in the as-quenched foils. This indicated that the Fe_3Al did not have significant amounts of B2 or $D0_3$ long-range order. Figure 3.3 presents the growth of the $(\frac{1}{2}\frac{1}{2}\frac{1}{2})$ and (100) superlattice peaks as the Fe_3Al samples were annealed for increasing times at 300 C.

Gao and Fultz also performed Mössbauer spectrometry measurements on the Fe_3Al foils. Two of their Mössbauer spectra are presented in Figure 3.4. These spectra are basically composed of overlapping sextets of peaks which are caused by the nuclear Zeeman effect. The distribution of ^{57}Fe hyperfine magnetic fields (HMF) are obtained from these spectra using the method of Le Caër and Dubois (Le Caër and Dubois, 1979). The HMF distributions from an Fe_3Al sample as it was annealed for increasing times at 300 C are shown in Figure 3.5. The numbers of the peaks in Figure 3.5 correspond to the number of Al atoms in the 1nn shell of an ^{57}Fe atom. The intensities of these peaks correspond approximately to the probability of each 1nn environment. As the

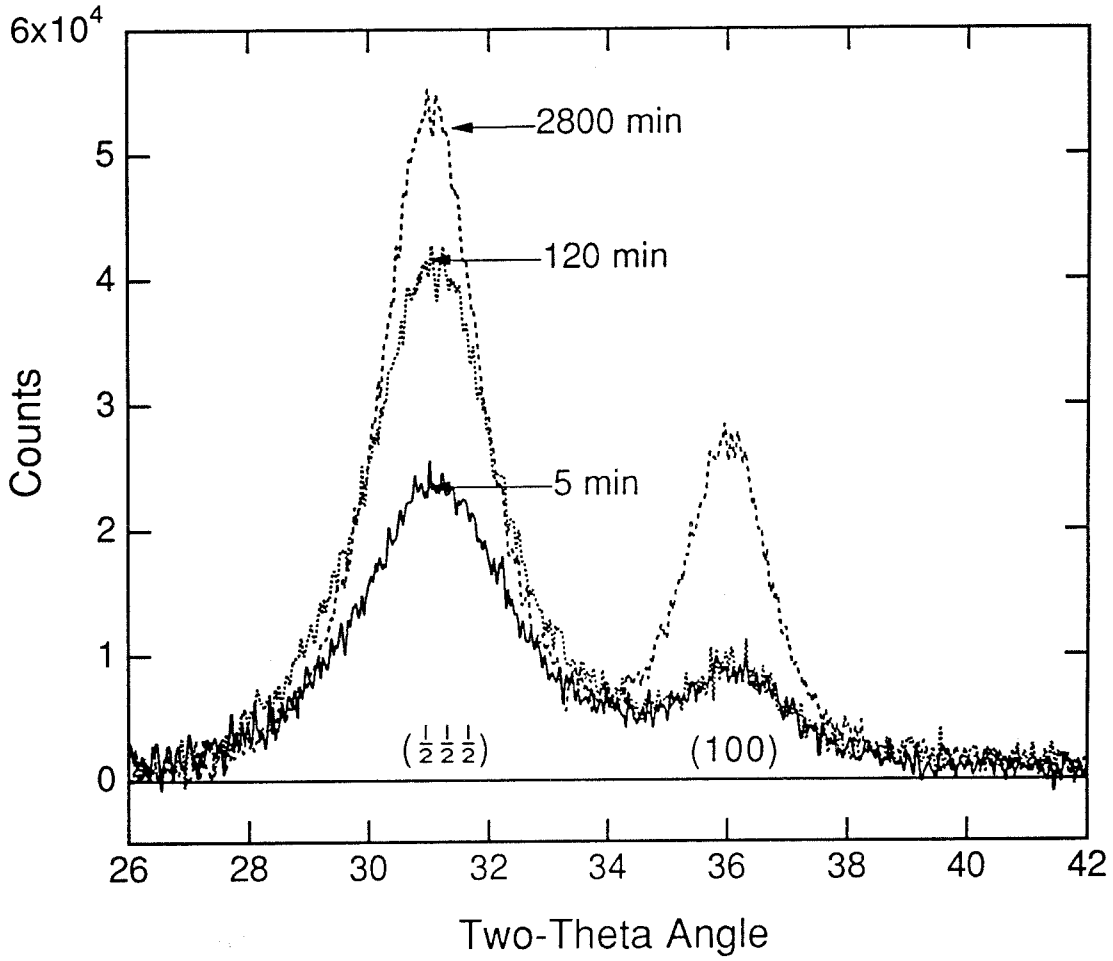

Figure 3.3. Growth of superlattice diffraction peaks in initially piston-anvil quenched Fe_3Al annealed at 300 C (Gao and Fultz, 1993).

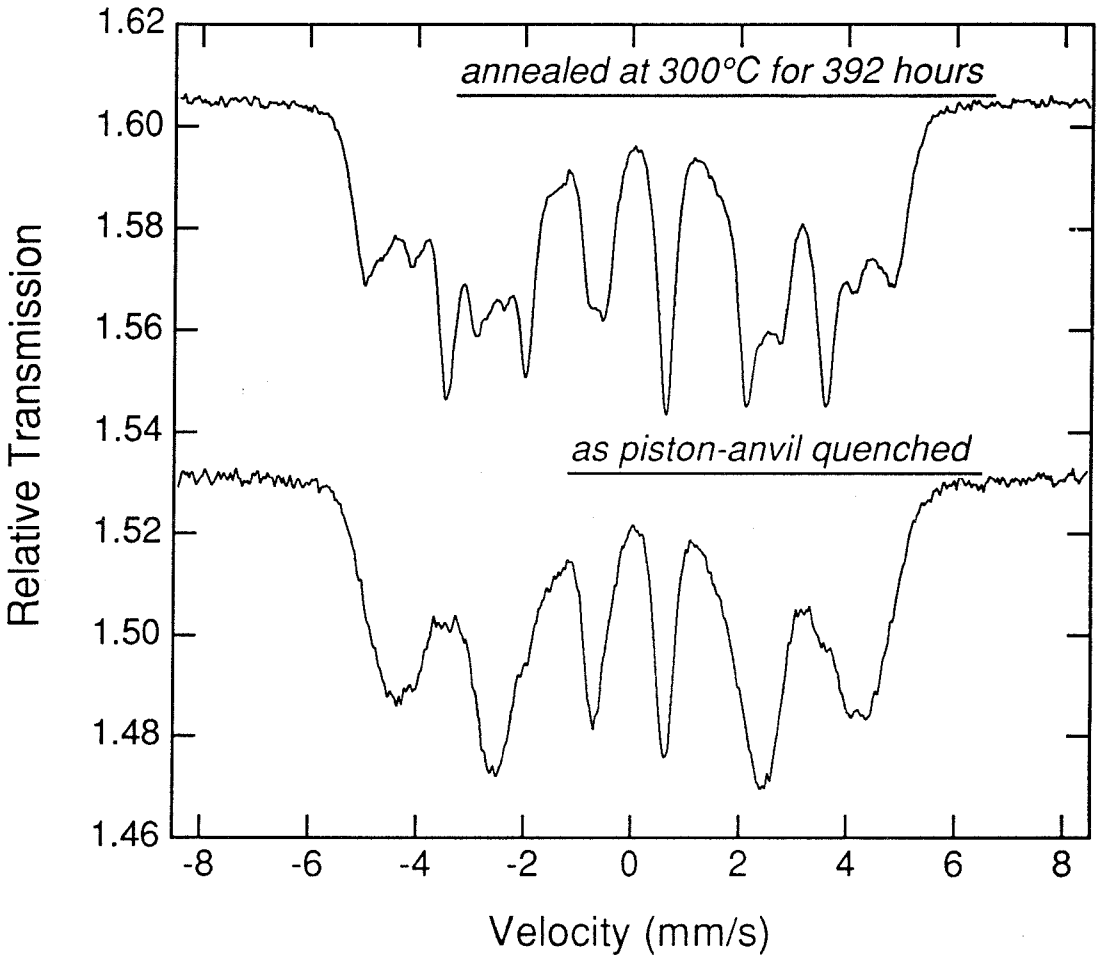

Figure 3.4. Mössbauer spectra of Fe_3Al as-quenched and after annealing at 300 C for 392 hours (Gao and Fultz, 1993).

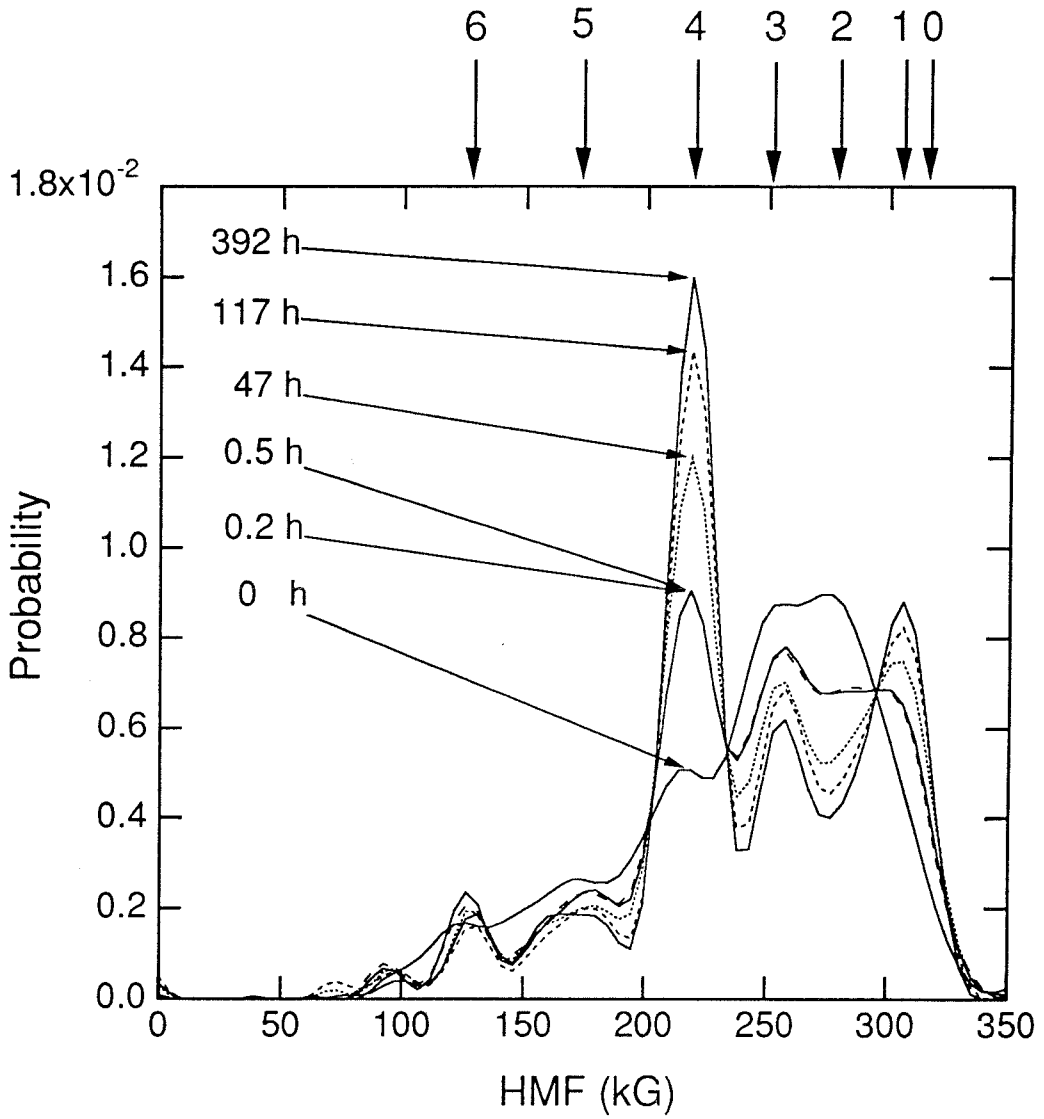

Figure 3.5. Hyperfine magnetic field distributions for Fe_3Al as piston-anvil quenched and after annealing at 300 C for various times. Numbers at top of figure identify resonances from ^{57}Fe atoms with different numbers of Al neighbors (Gao and Fultz, 1993).

sample is annealed, there is significant growth in the peaks corresponding to four and zero 1nn Al atoms. These changes in the local environment of Fe atoms are consistent with the DO_3 ordered structure.

The evaporated Ni_3Al was shown to be both stoichiometric and chemically disordered by the x-ray diffractometry, calorimetry, and energy-dispersive x-ray analysis performed by Harris et al. (1991). Figure 3.6 compares the x-ray diffraction patterns of the as-evaporated and annealed material. Average grain sizes of approximately 5 nm were determined using x-ray diffractometry data and transmission electron microscopy dark field images. The differential scanning calorimetry (DSC) traces of the as-evaporated material are displayed in Figure 3.7. The DSC traces show an initial exothermic relaxation beginning near 100 C and a larger exothermic relaxation starting near 300 C. Harris et al. found that the large relaxation near 300 C is due to both long-range ordering and grain growth. They speculated that the relaxation near 100 C might be due to chemical short-range ordering.

Transmission electron microscopy was performed on the thin films of Pd. Figure 3.8 presents a typical bright and dark field image pair and a diffraction pattern from the as-evaporated material. The images indicate an average grain size of roughly 5 nm. Figure 3.9 displays the x-ray diffraction measurement of the (111) peak from the as-evaporated Pd. A simple Scherrer analysis of the line broadening gives a grain size of 6.5 nm.

Some of these thin films of Pd were annealed *in situ* in the heating holder of the electron microscope. Rapid growth of the grains was observed when the annealing temperature reached approximately 550 C. Figures 3.10 displays a bright and dark field image pair and a diffraction pattern from an annealed film

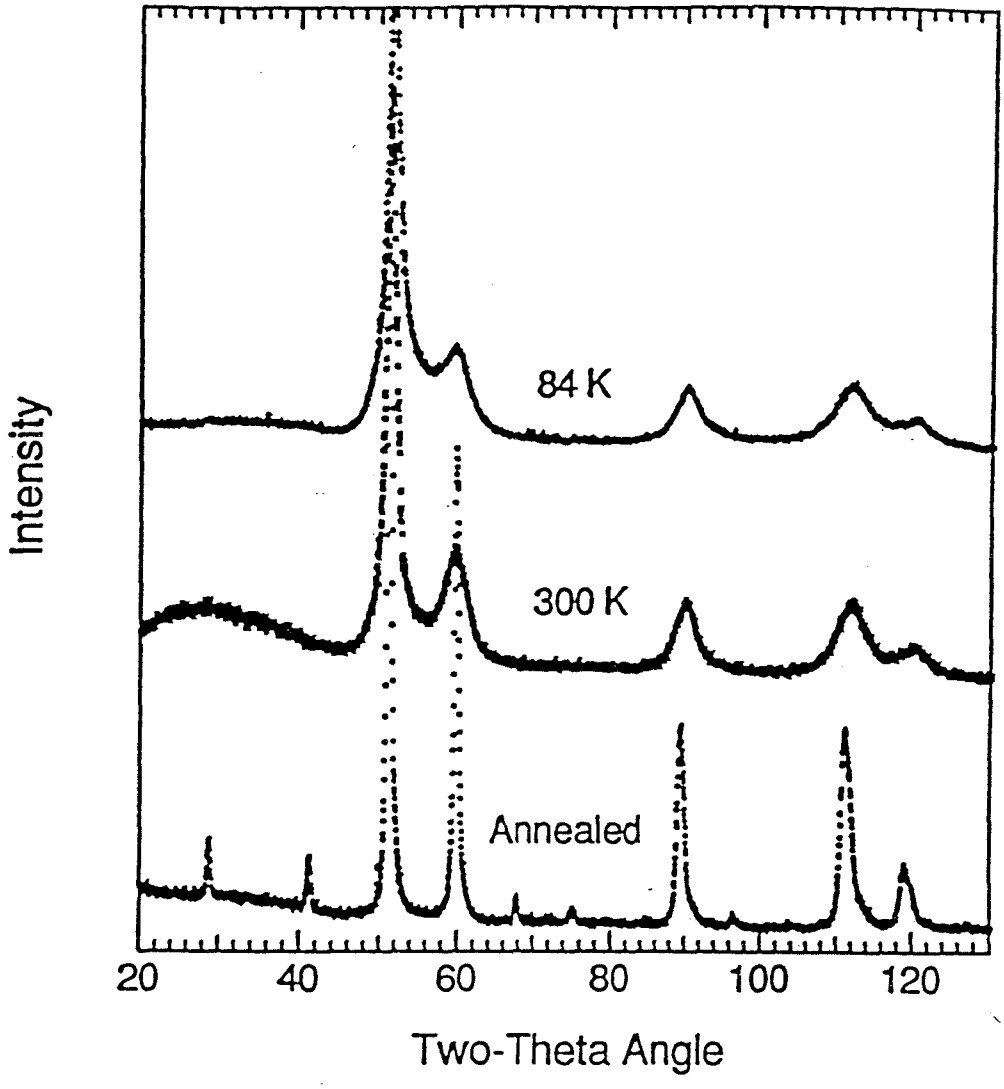

Figure 3.6. X-ray diffraction patterns from Ni_3Al material as-evaporated onto 84 K substrates, onto 300 K substrates, and from material annealed in the DSC to 550 C (Harris et al., 1991).

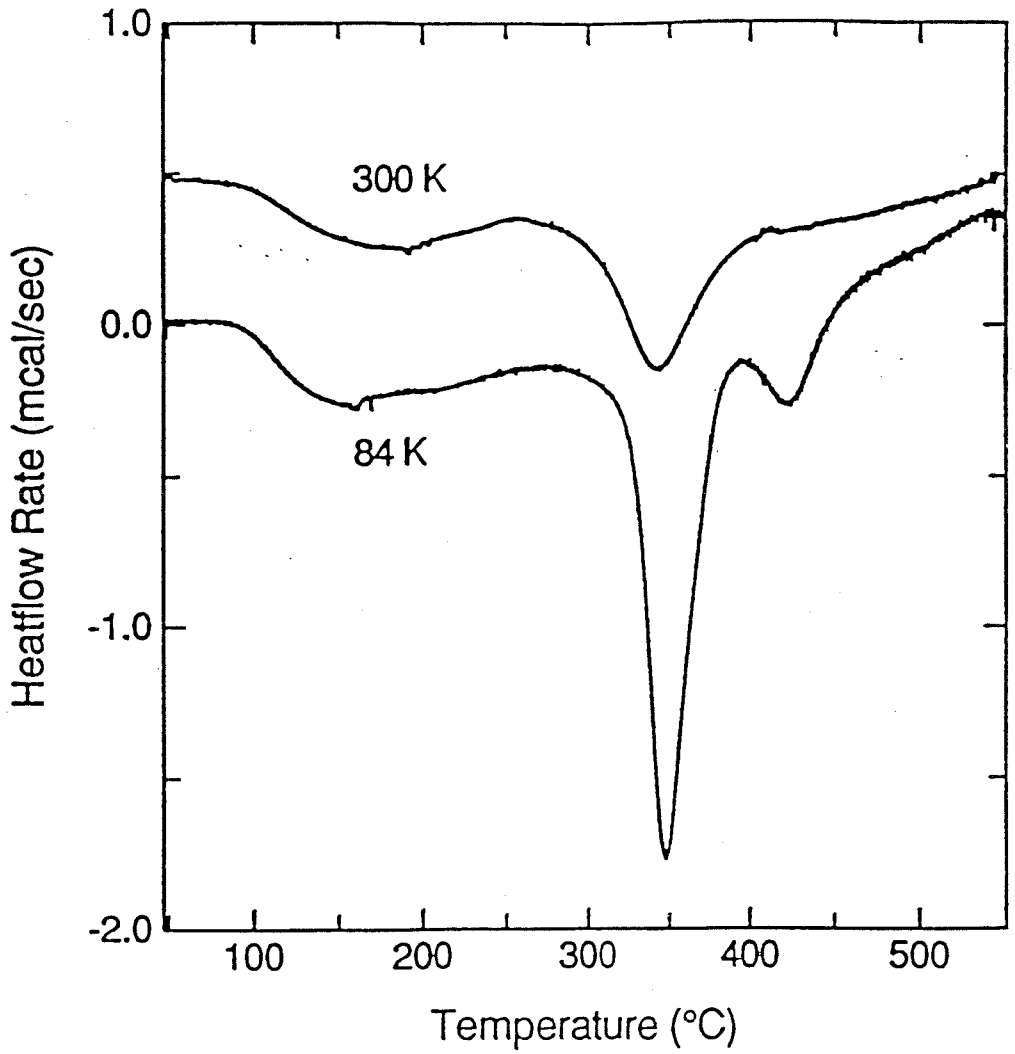

Figure 3.7. DSC traces for Ni_3Al material evaporated onto 300 K and 84 K substrates. 5.7 mg of material was used for the upper trace, 8.7 mg of material for the lower trace (Harris et al., 1991).

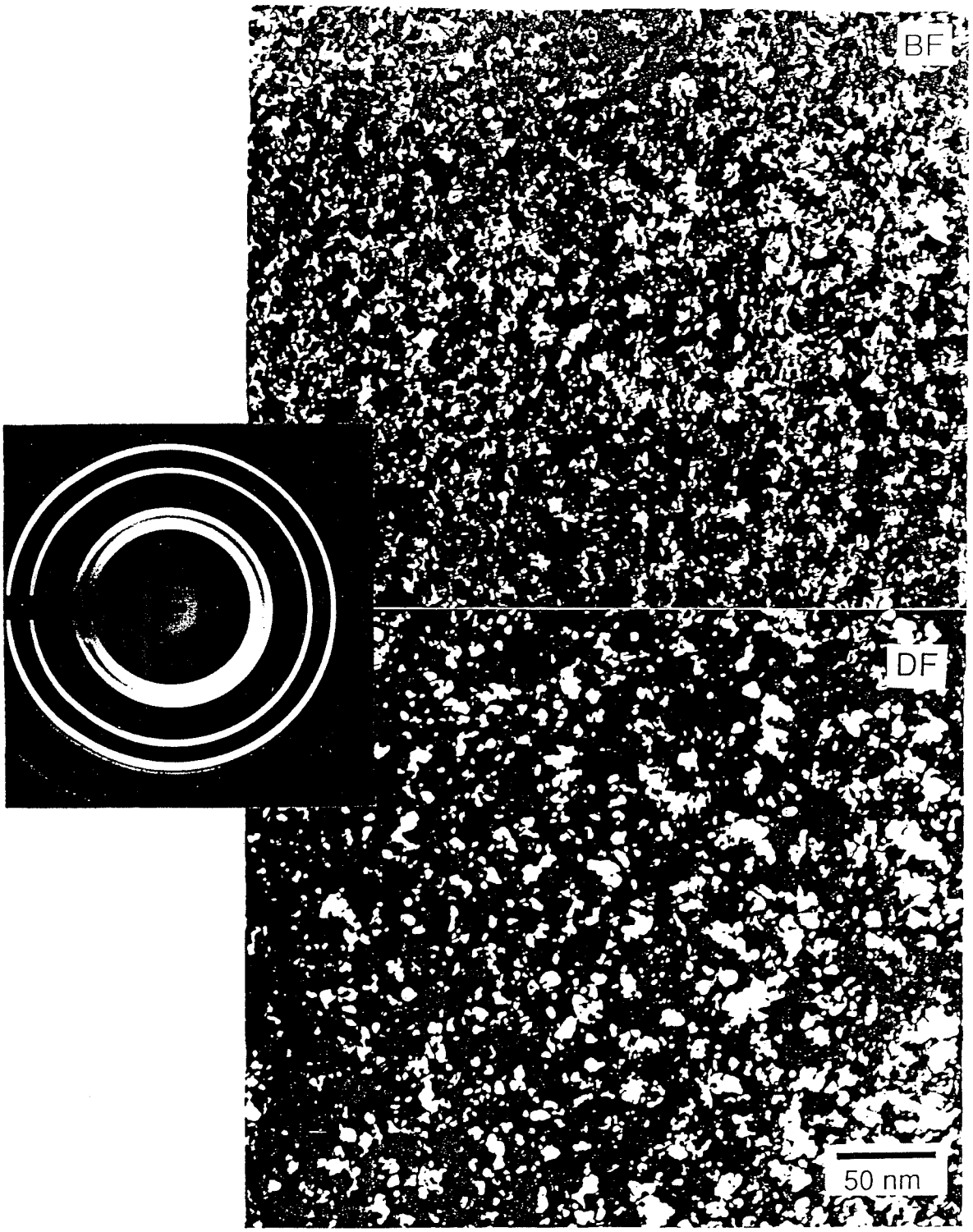

Figure 3.8. Bright field (BF) and dark field (DF) image pair and diffraction pattern from as-evaporated thin film of Pd. DF image taken using portion of (111) diffraction ring.

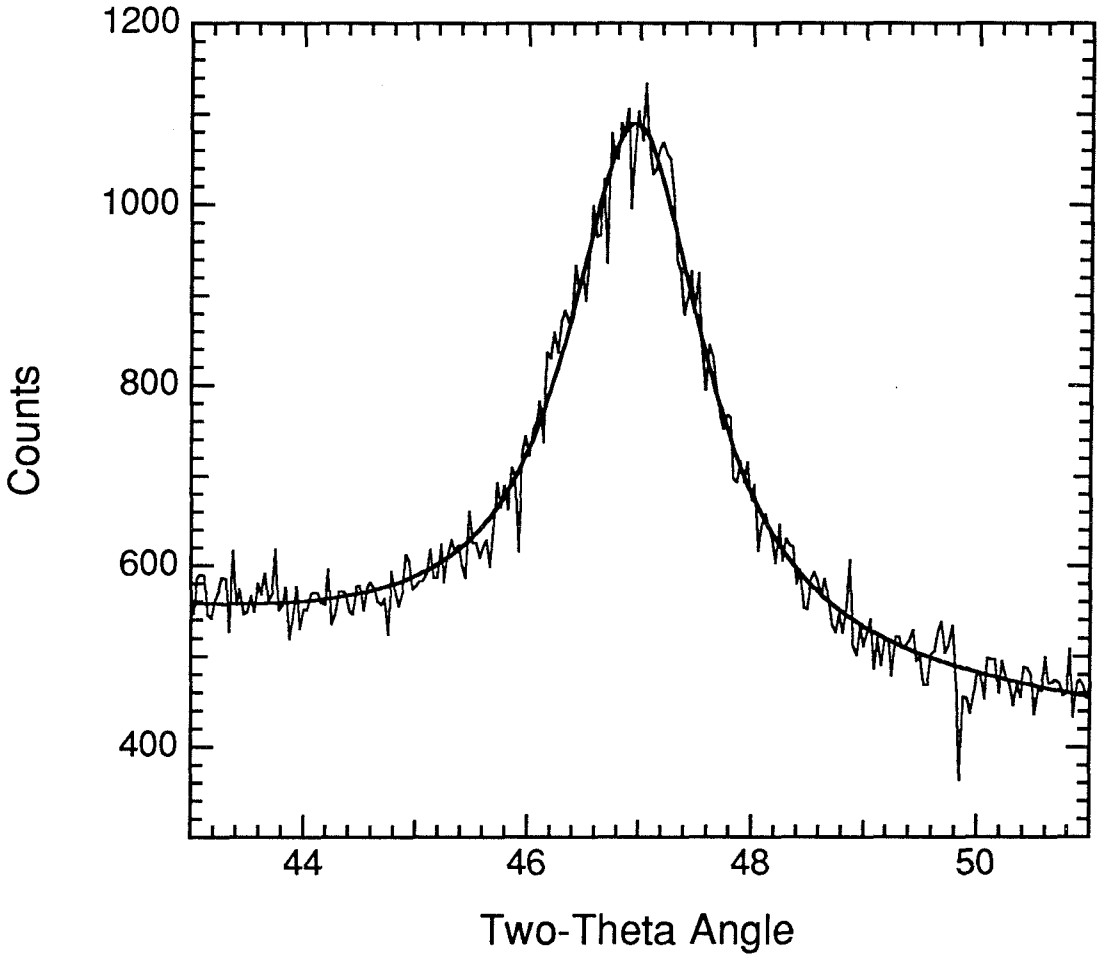

Figure 3.9. X-ray diffraction measurement of (111) peak from as-evaporated Pd. Smooth line is Lorentzian fit to lineshape.

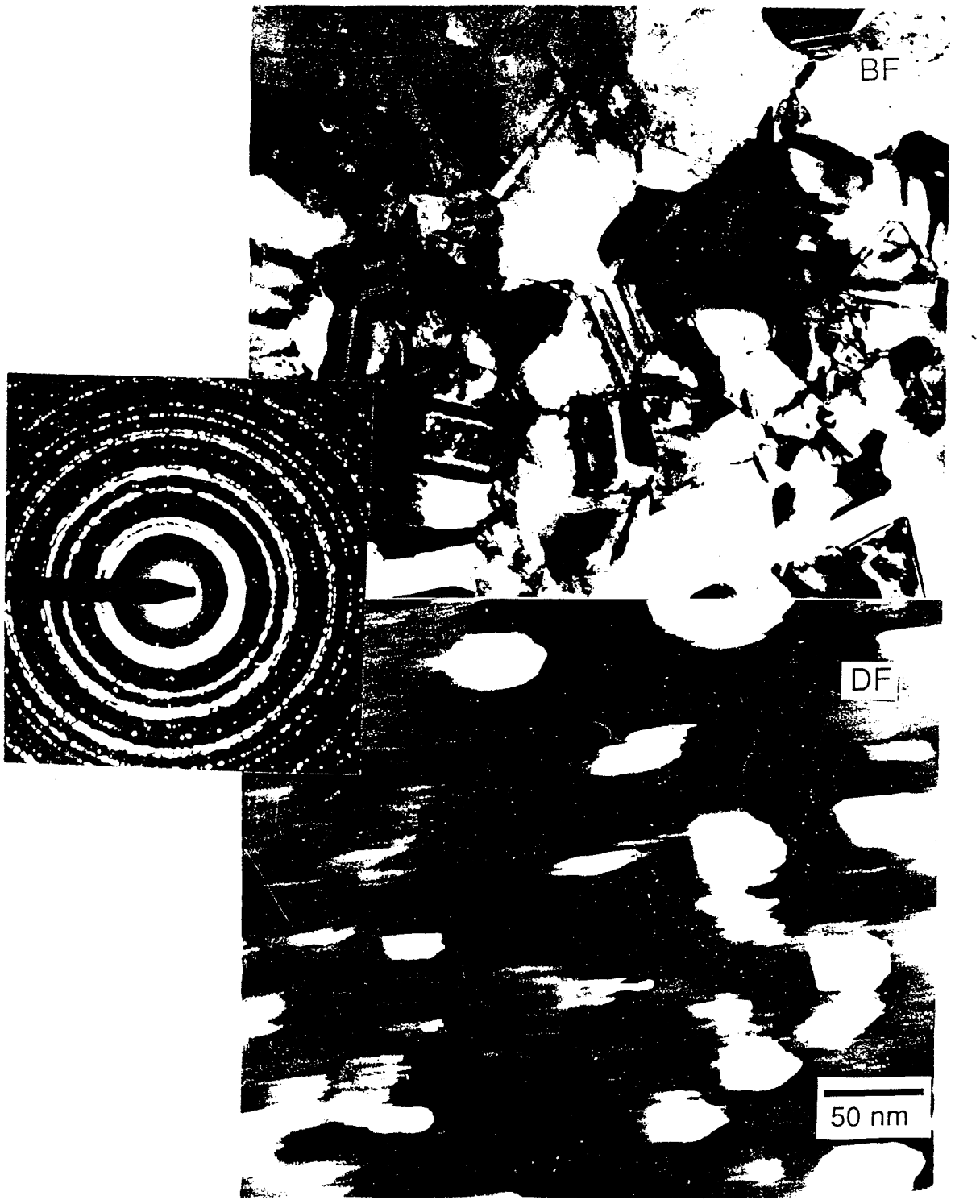

Figure 3.10. Bright field (BF) and dark field (DF) image pair and diffraction pattern from thin film of Pd after annealing at up to 550 C. DF image taken using portion of (111) diffraction ring. Streaking in DF image due to sample drift in microscope.

of Pd. The images show that the average grain size in the annealed films is approximately 30 nm.

Transmission electron microscopy of the partially compacted powder of Pd nanocrystals, prepared by inert gas condensation, showed that the material had an average grain size of roughly 6 nm. Figure 3.11 gives the bright and dark field image pair.

Transmission electron microscopy was also performed on the thin films of TiO_2. Figure 3.12 presents a typical bright and dark field image pair and a diffraction pattern from the as-prepared material. Analysis of the diffraction pattern indicates that the as-prepared thin films of TiO_2 are dominated by the rutile phase but also contain some of the anatase phase. The images show that the as-prepared film has an average grain size of roughly 7 nm.

After some of the thin films of TiO_2 were annealed at 900 C for 11 hours, transmission electron microscopy was again performed. A bright and dark field image pair and a diffraction pattern from the annealed material are presented in Figure 3.13. Analysis of the diffraction pattern indicates the presence only of the rutile phase. The images show that the grains have grown to an average size of approximately 20 nm. This grain growth is consistent with that seen in TiO_2 prepared by the gas-condensation method after annealing at temperatures above 800 C (Siegel et al., 1988).

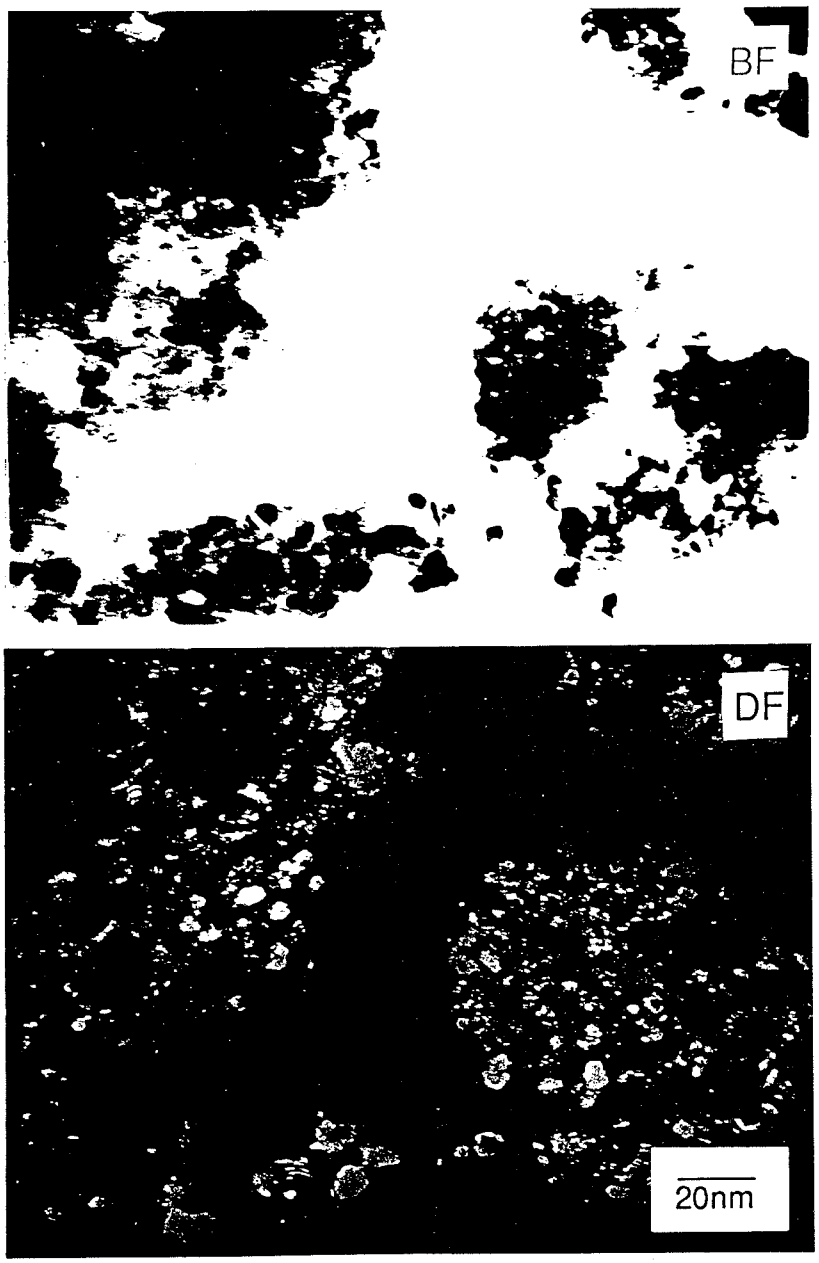

Figure 3.11. Bright field (BF) and dark field (DF) image pair from partially compacted powder of Pd nanocrystals.

Figure 3.12. Bright field (BF) and dark field (DF) image pair and diffraction pattern from as-prepared thin film of TiO_2.

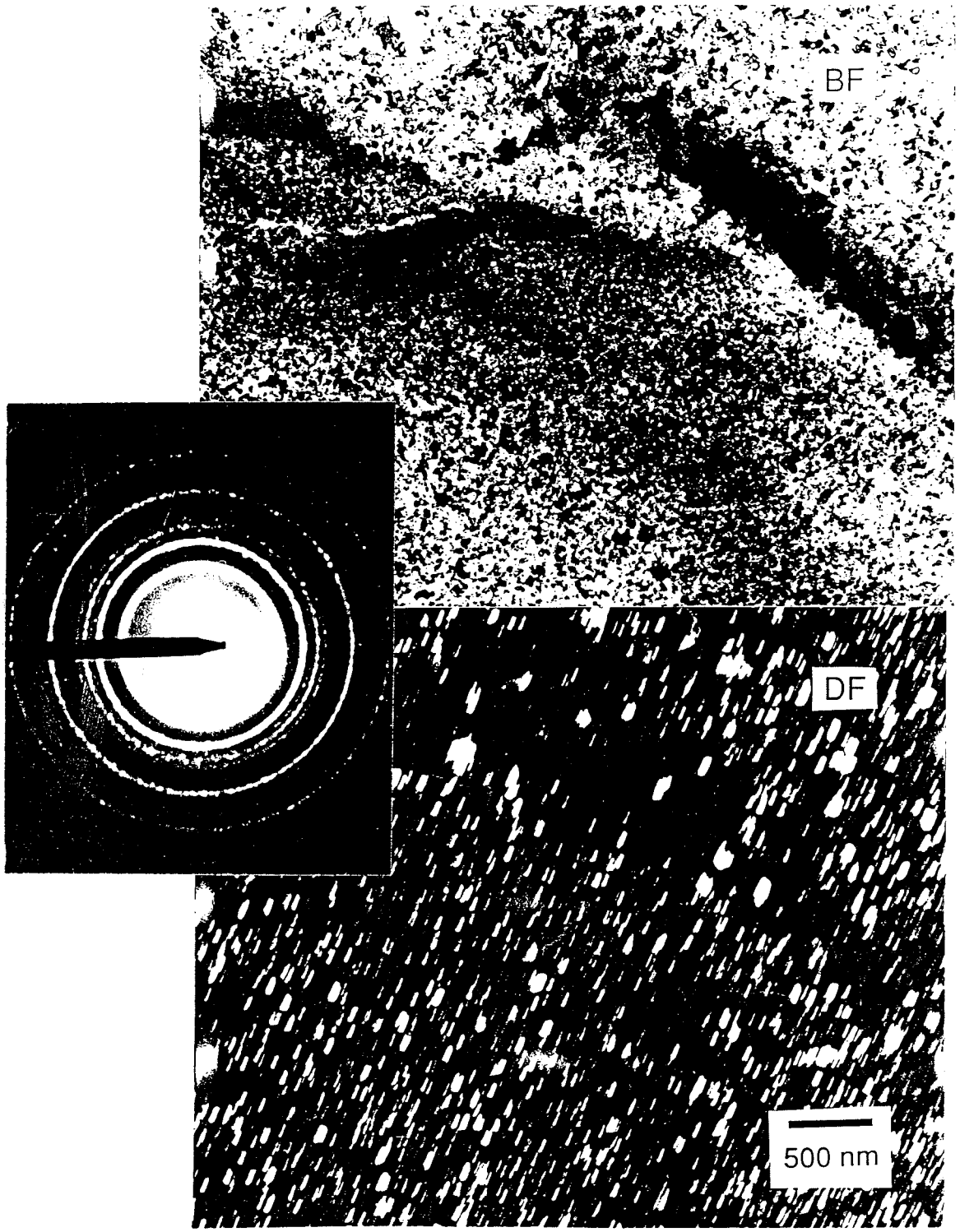

Figure 3.13. Bright field (BF) and dark field (DF) image pair and diffraction pattern from thin film of TiO_2 after annealing at 900 C for 11 hours. Streaking in DF image due to sample drift in microscope.

3.3 Control of Specimen Temperature

During the EXELFS measurements a liquid nitrogen (LN_2) cooled substrate holder with a heating element was used to control the temperature of the specimens. The holder, Gatan model 636, is depicted in Figure 3.14. It has a temperature range of approximately -175 C to +150 C. Intermediate temperatures are maintained by the feedback-controlled heating of a copper transfer rod between the specimen and the LN_2 reservoir. A silicon diode is used to sense the temperature at the specimen cradle.

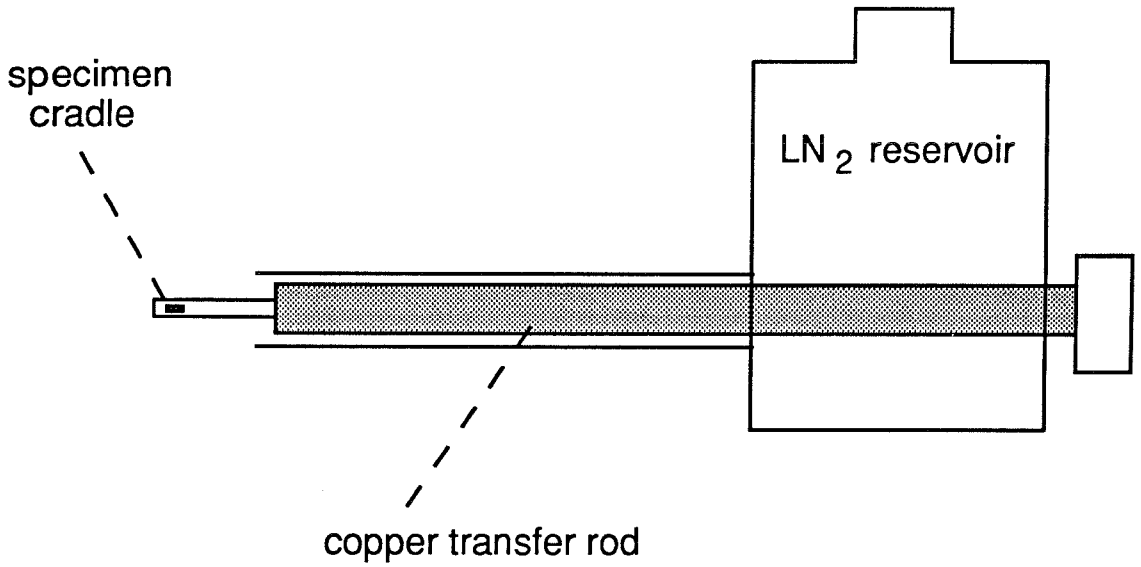

Figure 3.14. Schematic diagram of liquid nitrogen cooled substrate holder for transmission electron microscopy.

The substrate holder measures the temperature at the edge of the specimen. The temperature of the material being sampled may be higher due to heating from the electron beam. The amount of beam heating may be estimated as follows: Consider the specimen to be a self-supporting film of uniform thickness τ and thermal conductivity κ that, for simplicity, lies over a

copper support grid with a circular hole of radius r_{grid}. Assume that the electron beam has a uniform current density of J_o and falls on a circular area of radius r_{beam} which is centered over the hole in the grid. Furthermore, assume that the copper grid is held at temperature T_{grid} by the temperature control unit of the substrate holder. The situation is illustrated in Figure 3.15.

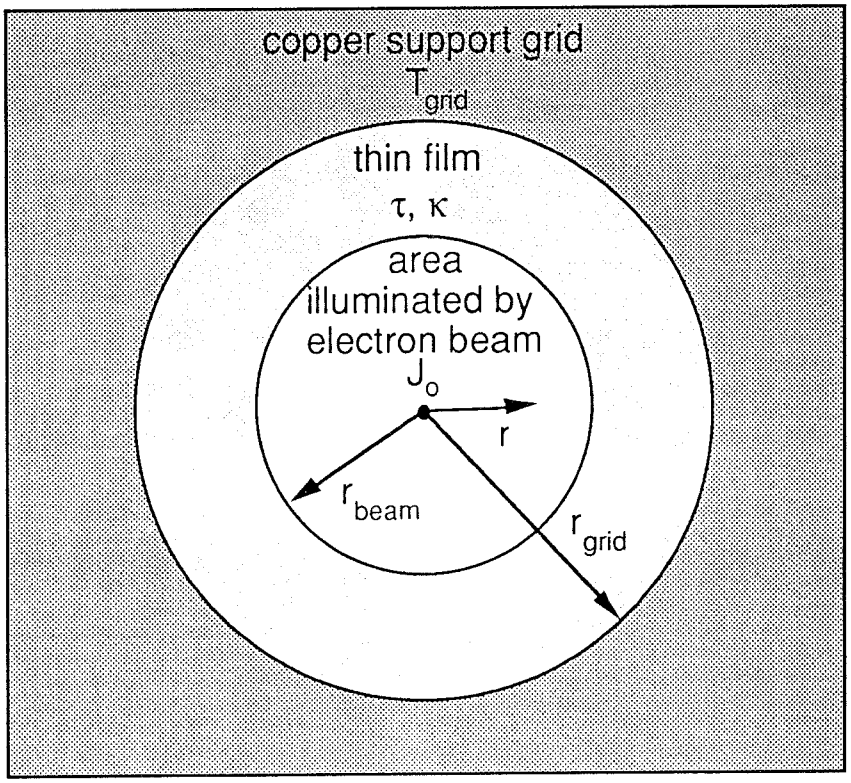

Figure 3.15. Diagram of the hypothetical situation used to estimate increases in sample temperature due to heating from the electron beam.

Assume that the film is thin enough so that the problem becomes two-dimensional. In other words, temperature varies in the plane of the film, but it is constant within the thickness of the film. Furthermore, the problem actually becomes one-dimensional because of its circular symmetry. Our goal is to determine the radial distribution of the temperature T(r).

Through inelastic collisions, the electron beam acts as a heat source. Assuming that all energy lost by the beam is eventually converted to heat within the thin film, the amount of heating per unit area is given by

$$s(r) = s_0 = J_0 \int_0^\infty P(E)dE \qquad , \text{if } r \le r_{beam}$$

$$= 0 \qquad , \text{if } r_{beam} < r \qquad (3.1)$$

where P(E) is the energy-loss probability distribution, and $\int_0^\infty P(E)dE$ gives the average energy loss for an electron transmitted through the sample. Of course, P(E) is determined from EELS measurements.

Assuming thermal equilibrium, the three-dimensional heat diffusion equation becomes Poisson's equation, which has solutions that are well-known from electrostatics. The appropriate analog of Gauss's Law for heat diffusion is

(heat flux out of surface S) = (heat generated within surface S) (3.3)

where S is any closed surface. Applying Equation (3.3) to cylindrical surfaces appropriate to the problem gives

$$\left(-\kappa \frac{dT(r)}{dr}\right)(2\pi r\tau) = s_0(\pi r_{beam}^2) \qquad , \text{if } r_{beam} < r \le r_{grid} \qquad (3.4)$$

and

$$\left(-\kappa \frac{dT(r)}{dr}\right)(2\pi r\tau) = s_0(\pi r^2) \qquad , \text{if } r \le r_{beam} \qquad (3.5)$$

Equations (3.4) and (3.5) depend on the assumption that no heat transfer occurs due to convection or radiation from the top and bottom surfaces of the thin film. Applying the boundary condition $T(r_{grid}) = T_{grid}$ allows us to solve for T(r):

$$T(r) = T_{grid} + \frac{s_0 r_{beam}^2}{2\kappa\tau} \ln\left(\frac{r_{grid}}{r}\right) \quad , \text{if } r_{beam} < r \le r_{grid}$$

$$= T_{grid} + \frac{s_0 r_{beam}^2}{2\kappa\tau} \ln\left(\frac{r_{grid}}{r_{beam}}\right) + \frac{s_0}{4\kappa\tau}\left(r_{beam}^2 - r^2\right) \quad , \text{if } r \le r_{beam} \qquad (3.6)$$

Reasonable values for the EXELFS experiments in this thesis are r_{grid} = 20 μm, r_{beam} = 10 μm, $s_o = 0.16 \frac{W}{cm^2}$, $\kappa = 1 \frac{W}{cm\,K}$ (metal) or $0.05 \frac{W}{cm\,K}$ (ceramic), and τ = 0.1 μm. To obtain the value for s_o, Equation (3.1) was applied using $J_o = 2 \times 10^{16} \frac{1}{sec\,cm^2}$ and $\int_0^\infty P(E)dE$ = 50 eV = 8×10^{-18} J, as determined from a typical low-loss spectrum.

Figure 3.16 shows the result of substituting these values into Equation (3.6). The increase in temperature is seen to be negligible, even for the ceramic thin film. The calculated effect of beam heating is so small because the electron beam is rather spread-out during the EXELFS measurements. If, for instance, r_{beam} were ten times smaller, then the increase in temperature due to beam heating would be about 100 times larger. In contrast, the increase in temperature is less sensitive to changes in the current density, J_o, the thermal conductivity of the sample, κ, or the distance from the grid, r_{grid}. Changes in sample thickness, τ, should have almost no effect on the temperature because the average energy loss, $\int_0^\infty P(E)dE$, is proportional to τ.

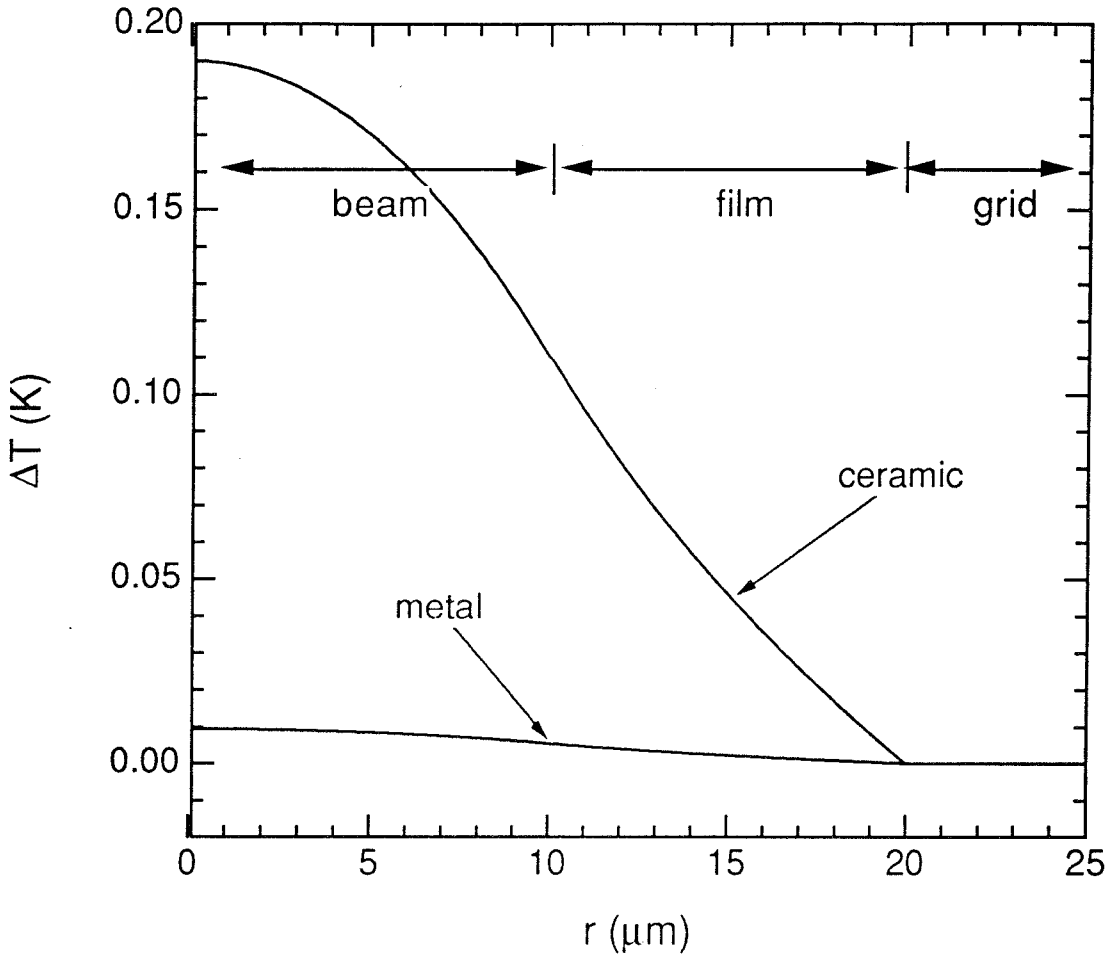

Figure 3.16. Change in temperature due to electron beam heating as function of radial distance using Equation (3.6) for thin film sample illustrated in Figure 3.15. Values used for parameters in Equation (3.6) are given on p. 63.

3.4 Parallel-Detection EELS (PEELS)

The experiments in this thesis were performed using a Gatan PEELS model 666 mounted beneath a Philips TEM model EM430. The experimental configuration is schematically illustrated in Figure 3.17.

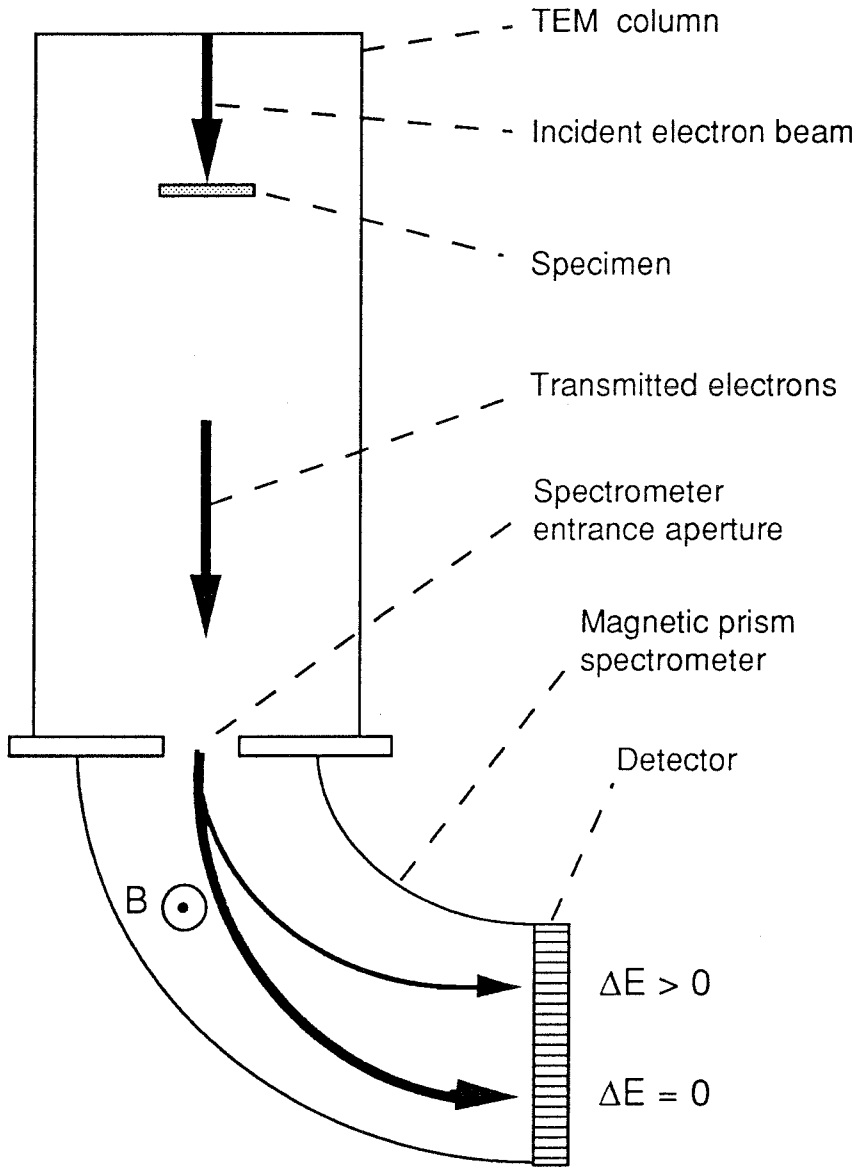

Figure 3.17. Schematic of electron energy loss spectrometer attached to bottom of TEM.

EELS measurements can be made with the TEM in either its imaging or diffraction mode. Measurements in this thesis were made using the TEM diffraction mode, and this mode is diagrammed in Figure 3.18. In this mode, a diffraction pattern is visible on the microscope viewing screen, and the spectrometer entrance aperture collects the electrons which are scattered within the collection semi-angle β. β is determined by the diameter of the spectrometer entrance aperture d, and the camera length of the microscope L.

$$\tan(\beta) = \frac{d/2}{L} \tag{3.7}$$

The Gatan PEELS is a magnetic-prism spectrometer which utilizes a one-dimensional array of photodiodes to record the electron energy-loss spectrum in parallel. Figure 3.19 schematically illustrates the spectrometer.

The transmitted electron beam enters the magnetic prism through the spectrometer entrance aperture. The shape of the magnetic sector allows for bending of about 90 °. Bending of the electron beam occurs because electrons travel in circular orbits within a perpendicular magnetic field. The radius of curvature of the circular orbits is given by

$$R = \frac{\gamma m_e}{eB} v \tag{3.8}$$

where $\gamma = \left(1 - \frac{v^2}{c^2}\right)^{-1/2}$ is a relativistic factor, m_e is the rest mass of an electron, e is the electronic charge, B is the strength of the magnetic field, and v is the velocity of the electron.

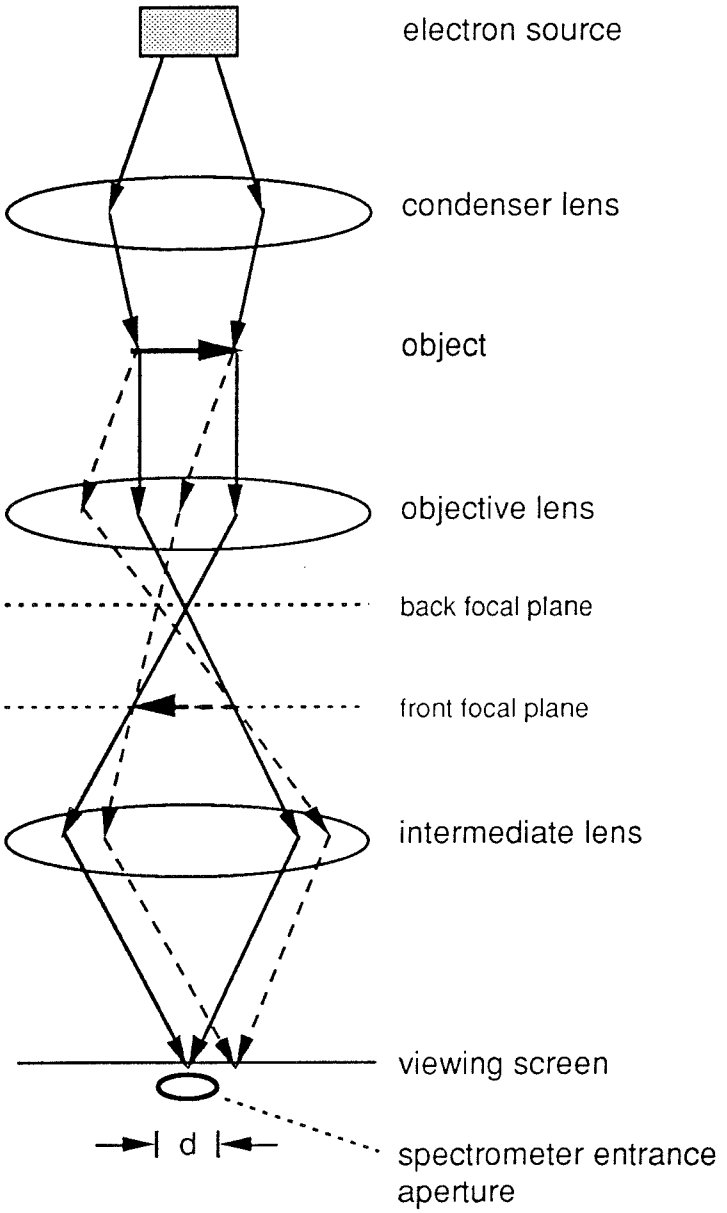

Figure 3.18. Ray diagram of TEM operating in diffraction mode.

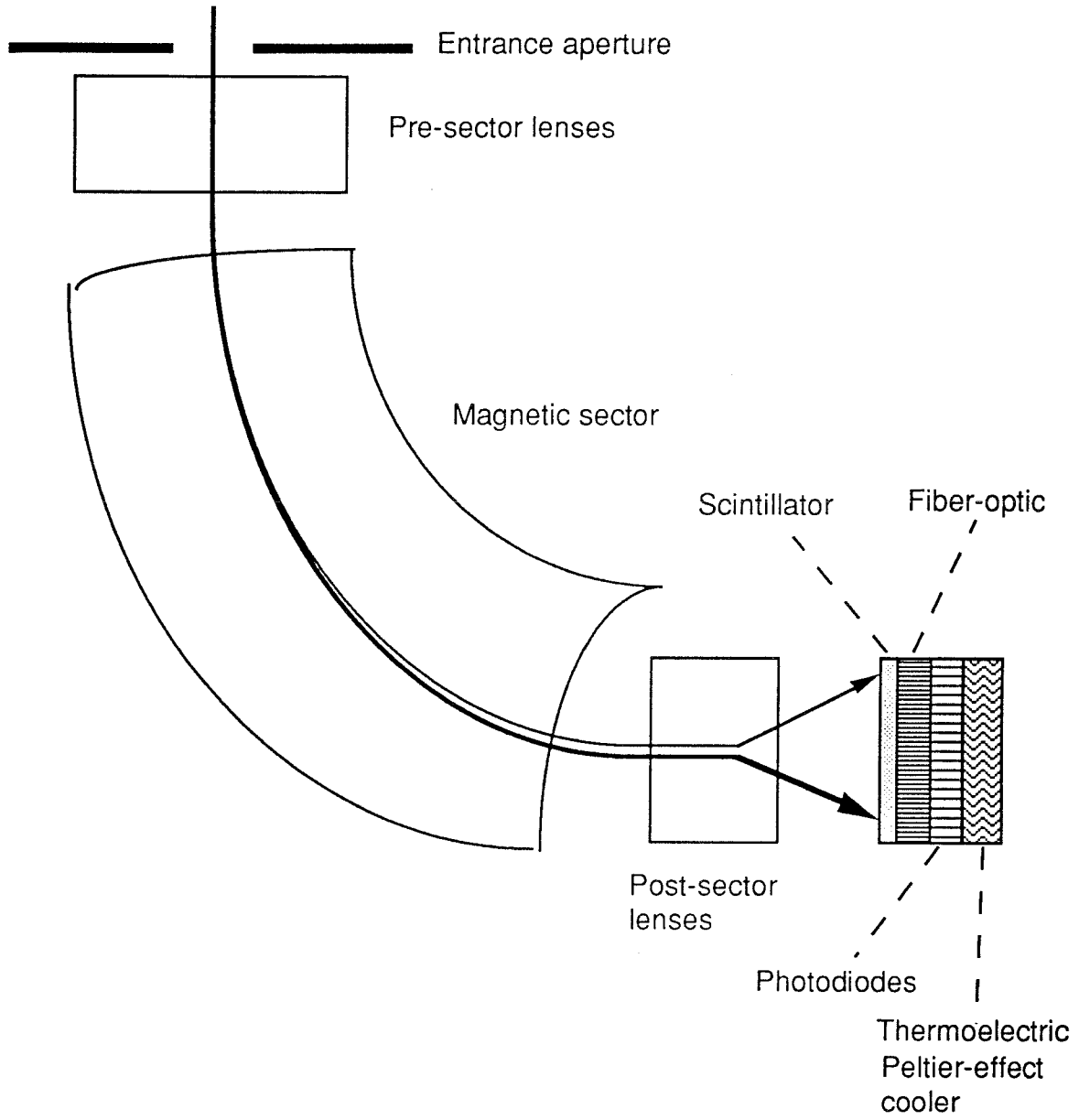

Figure 3.19. Schematic of PEELS spectrometer.

The strength of the perpendicular magnetic field, B, can be set so that the electrons with the zero-loss velocity v_o are bent onto the detector. Electrons with velocities lower than v_o will have smaller R and so leave the magnetic prism with a slightly larger deflection angle. This is the source of the dispersion in the spectrometer. The dispersion is magnified with the use of post-sector quadrupole lenses.

The magnified spectrum of electrons falls on the detector and is converted to light by a scintillator disk. A fiber-optic plate channels the light onto the active area of a linear photodiode array. The linear photodiode array consists of 1024 independent channels, each one with an active area 25 μm high and 2.5 mm wide. The total active area is 25 mm high and 2.5 mm wide. The back of the array is cooled by a thermoelectric cooler.

Although the collection of EELS core loss data is relatively efficient when compared to the collection of energy-dispersive x-ray (EDX) emission data, the EXELFS oscillations superposed on these core losses are comparatively weak, only a few percent of the signal amplitude. Consequently, data of high statistical quality are required.

EXELFS data from serial detectors generally suffers from inadequate signal-to-noise ratios, resulting in very limited data ranges in k-space (Csillag et al., 1981). The advent of parallel detectors has greatly improved the statistical quality of EELS data (Krivanek et al., 1987). Unfortunately, the EXELFS signal is often overwhelmed by the gain variations of the linear photo-diode arrays used in parallel detectors.

Fortunately, there are ways to mitigate the effects of these variations in gain. A particularly effective method involves dividing by a gain calibration spectrum followed by gain averaging over many data channels (Shuman and

Kruit, 1985). Figure 3.20 shows a gain calibration spectrum collected in the so-called "uniform illumination mode" of a Gatan model 666 parallel EELS detector. Gain averaging involves collecting several spectra, each shifted by a few data channels, as illustrated in Figure 3.21. These spectra are then aligned using a feature in the data as a marker, and subsequently added together. Gain averaging over a large energy range is particularly important in obtaining reliable EXELFS data to large momentum transfers, because detector uniformity over a larger energy range is required.

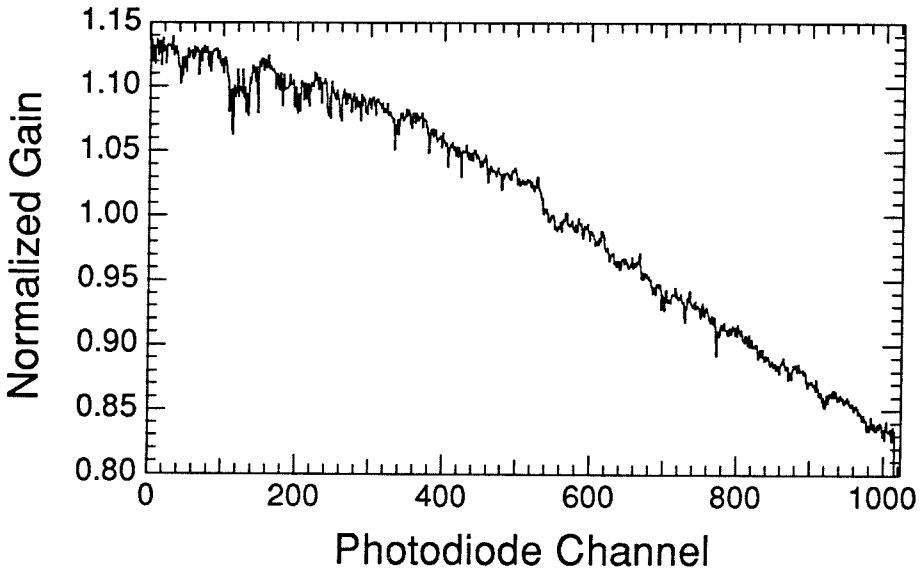

Figure 3.20. Typical gain calibration spectrum. Note offset of vertical axis.

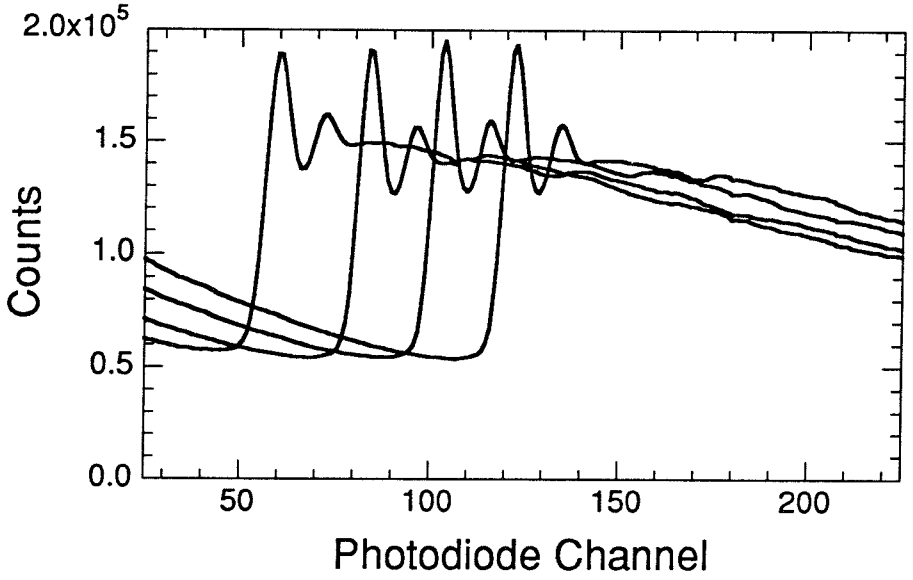

Figure 3.21. Illustration of gain averaging for Fe L_{23} edge. Although only 4 spectra, each shifted by about 20 channels, are shown, gain averaging in this thesis is actually performed using about 20 spectra, each shifted by about 3 channels.

Chapter 4 EXELFS Analysis of K, L_{23}, and M_{45} Edges

In this chapter the analysis and interpretation of the EXELFS data are discussed. §4.1 describes the procedures used to isolate, normalize, and Fourier filter the EXELFS oscillations for K edges. §4.2 describes how these procedures can be extended to L_{23} and M_{45} edges. §4.3 discusses the effect of multiple inelastic scattering on EXELFS.

4.1 Basic Analytical Procedures

The EXELFS signal, χ, is the oscillatory part of the edge intensity, $\Delta J(E)$, normalized to the non-oscillatory part, $J_o(E)$:

$$\chi(E) = \frac{J(E) - J_o(E)}{J_o(E)} = \frac{\Delta J(E)}{J_o(E)} \qquad (4.1)$$

where J(E) is the experimental edge intensity, and $J_o(E)$ is the smooth edge intensity which would be observed in the absence of backscattering. In principle, J(E) and $J_o(E)$ should both be single inelastic scattering intensities (Egerton, 1986). However, as discussed in §4.3, if the sample is sufficiently thin, EXELFS analysis can be performed without prior deconvolution of the EELS data.

Subtraction of the pre-edge background removes counts that are not due to the particular atomic edge of interest. One method commonly used in EELS for performing such background subtraction involves fitting an energy range preceding the edge to a power-law energy dependence, AE^{-B}, where A and B are the parameters (Egerton, 1986). The power law is then extrapolated through the edge, as shown in Figure 4.1 for the Al K edge of Al metal. Ideally, this determines the general shape of the normalizing intensity $J_o(E)$, which is

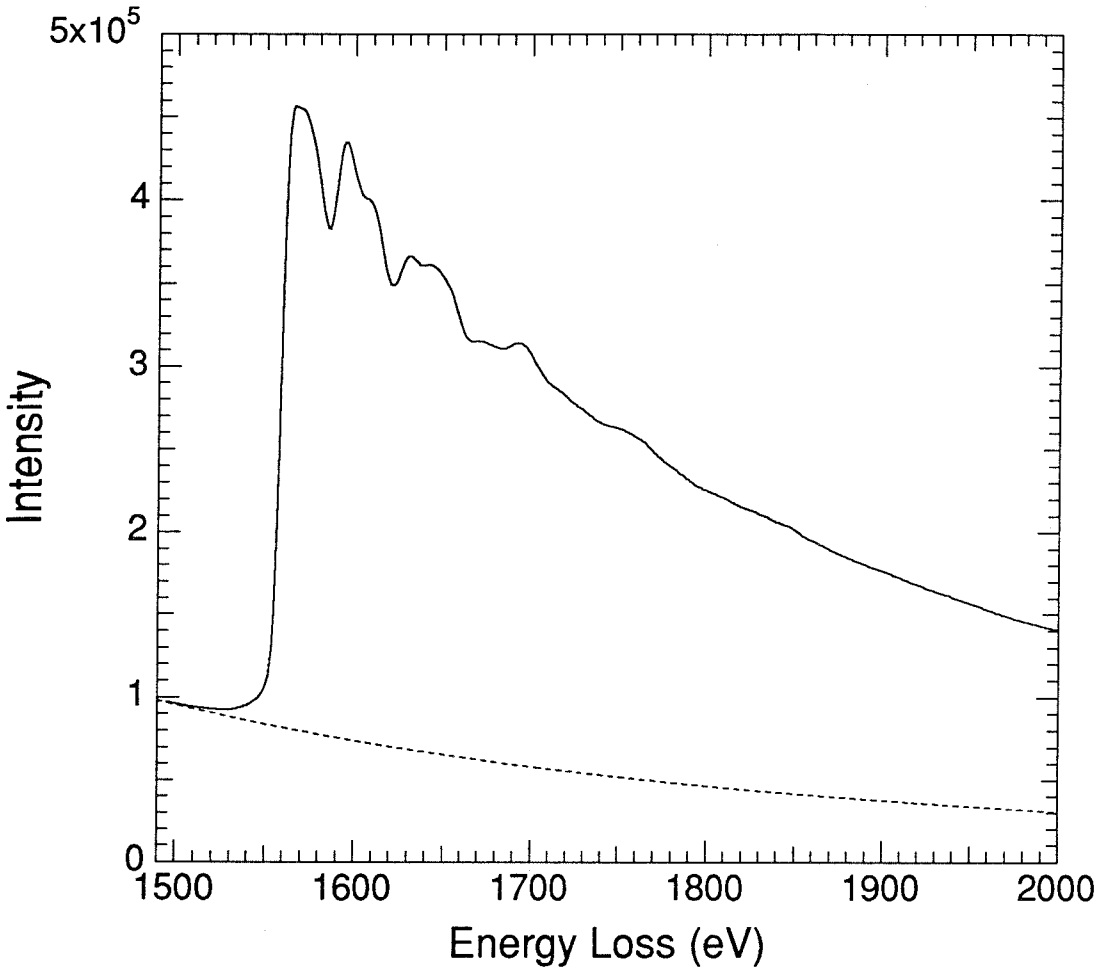

Figure 4.1. Power-law extrapolation (broken line) to remove pre-edge background for Al K edge of Al metal. Spectrum was not deconvoluted. Sample thickness about 0.4 times mean free path for inelastic scattering.

the denominator in Equation (4.1). Unfortunately, the power-law extrapolation into the extended region is not always accurate. It is especially inaccurate when the ratio of the edge jump to the background is much less than one.

Instead of determining the general shape of $J_o(E)$ by subtracting the pre-edge background, a more robust alternative is to use background subtraction simply to define the height of the edge jump, while assuming a theoretical form for the energy dependence of $J_o(E)$ (Sayers and Bunker, 1988). Such an approach was used in this thesis to determine the normalizing intensity $J_o(E)$. Theoretical ionization cross sections, as calculated in §A.1, were used for the energy dependence of $J_o(E)$.

In principle, the edge onset energy E_o is the minimum energy needed to free the core electron. E_o is known to be affected by the chemistry of a material. Unfortunately, there is no unique way to determine E_o from the experimental spectrum. Fortunately, in the analysis of extended fine structure, it is not usually necessary to know the exact value of E_o. Any reasonable choice for E_o is usually sufficient. It is important, however, to be consistent about the choice of E_o when comparing the fine structure between chemically similar compounds.

Once E_o is determined, transformation from energy loss, E, to the wavevector of the outgoing electron, k, is accomplished by the equation

$$E - E_o = \frac{\hbar^2 k^2}{2m_e} = (3.81\ \text{Å}^2\ \text{eV})\ k^2 \qquad (4.2)$$

From Equation (4.2), it is apparent that the choice of E_o affects the positions of the extended fine structure oscillations in k-space. This is especially true in the low-k regime but is less important in the high-k regime.

The most popular method for isolating the oscillating intensity $\Delta J(E)$ from the rest of the core edge is a polynomial spline fit. A polynomial spline function is composed of a series of consecutive intervals, each containing a polynomial of some order. The intervals are "tied together" by making the function and its first derivative continuous across the boundaries or "knots" (Sayers and Bunker, 1988). If the spline intervals and the orders of their polynomials are chosen well, a spline fit can remove the low frequency components due to the smooth atomic edge shape, without affecting the higher frequency EXELFS signal. Too many intervals or a polynomial of too high an order will result in the removal of part of the EXELFS oscillations. Not enough intervals or too low an order results in a large peak in the low-r region (r below about 1.0 Å) in the Fourier transform (Teo, 1986).

In k-space, the EXELFS oscillations have periods which are approximately π/R_{1nn} or less, where R_{1nn} is the 1nn interatomic spacing in the material. Figure 4.2 compares two periods of a sinusoidal oscillation with a cubic polynomial. Clearly, the cubic polynomial does not have enough degrees of freedom to simulate well the behavior of the sinusoid over two periods. Therefore, a reasonable first attempt may be to use a cubic spline fit with knots spread about $2\pi/R_{1nn}$ apart in k-space. Figure 4.3 presents a spline fit to the Al K edge of Al metal. Figure 4.4 displays the resultant EXELFS interference function $\chi(k)$, which was normalized by using the method described previously to determine $J_o(E)$.

Recall from §2.2.2 that $\chi(k)$ is interpreted in the plane-wave approximation using Equation (2.23):

$$\chi(k)=(-1)^{l_o+1}\sum_j \frac{|f_j(\pi,k)|\,S_j(k)}{kR_j^2}\,e^{-2R_j/\lambda(k)}\,e^{-2\sigma_j^2k^2}\,\sin[2kR_j+\eta_j(\pi,k)+2\delta_{l_o+1}(k)] \quad (2.23)$$

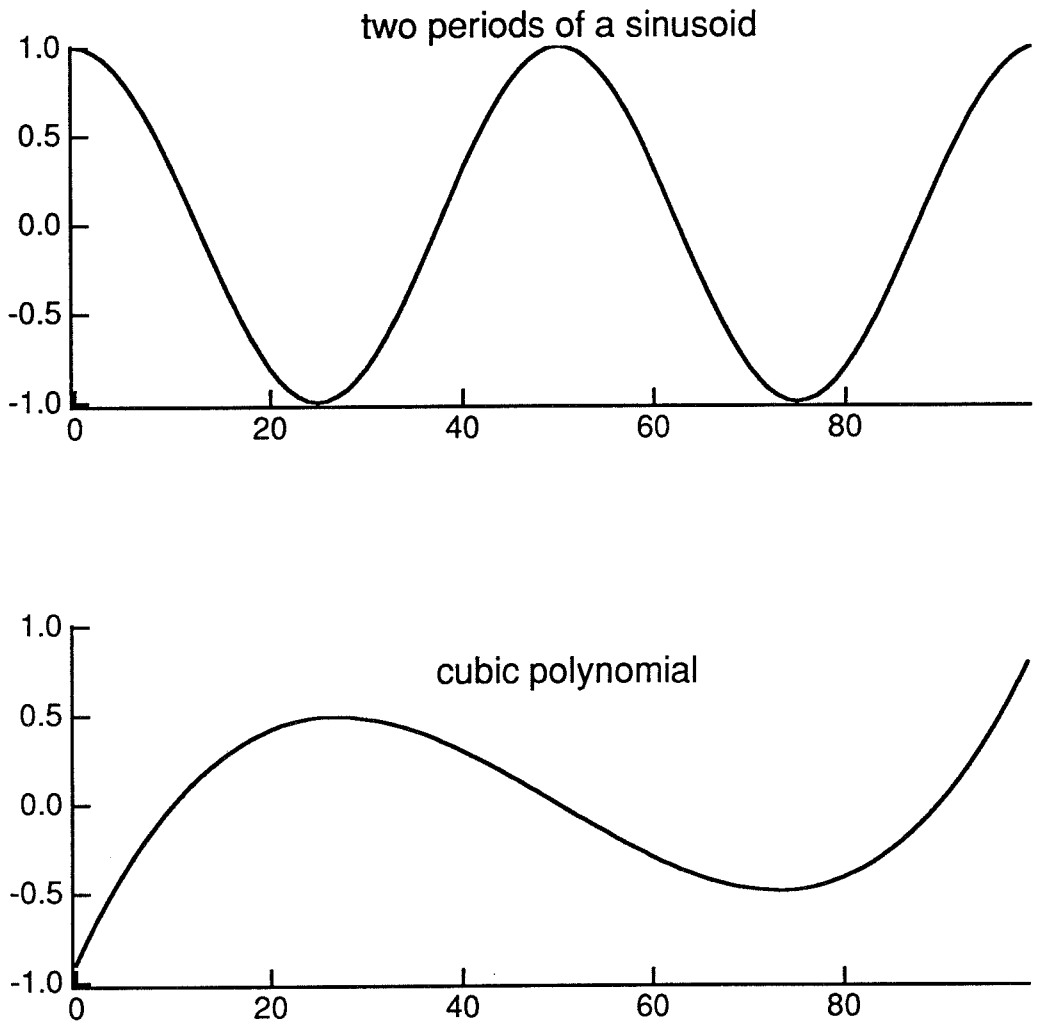

Figure 4.2. Comparison between two periods of a sinusoid and a cubic polynomial.

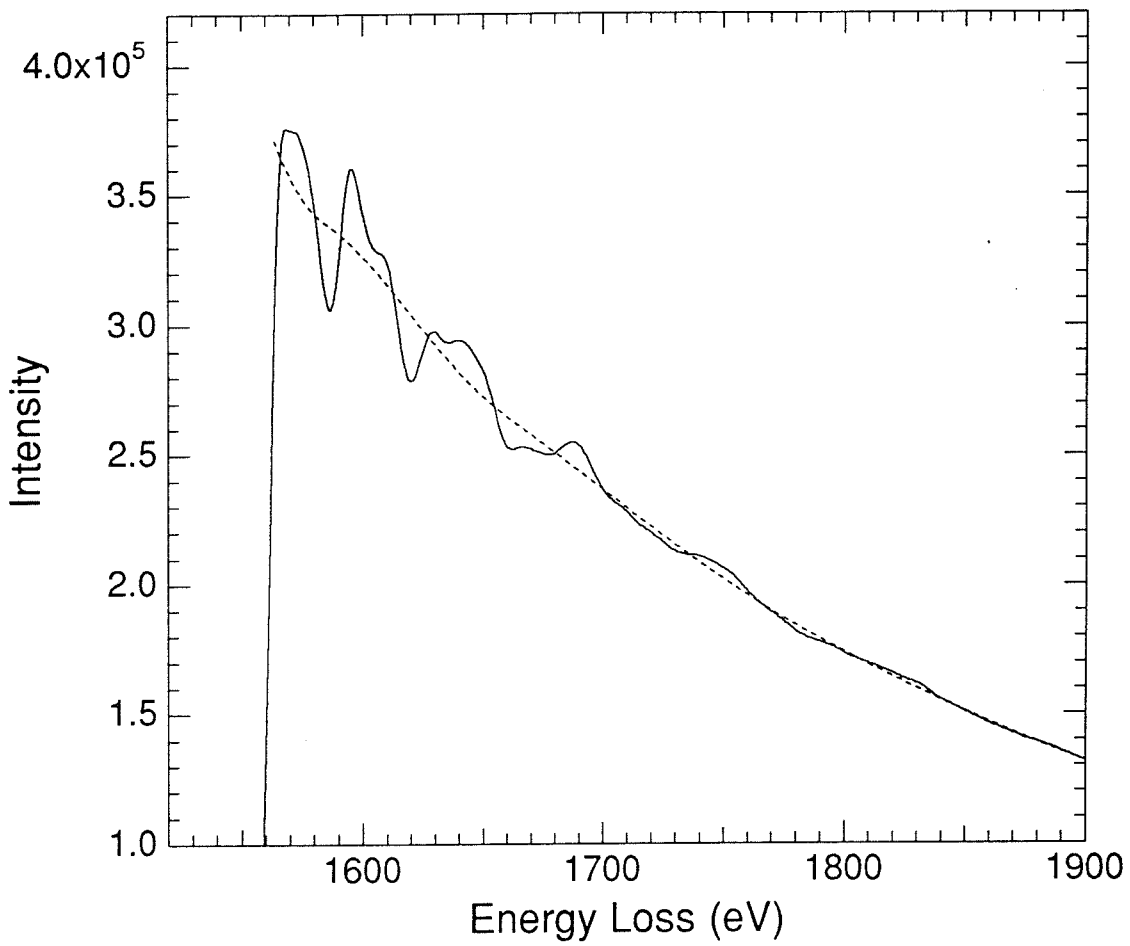

Figure 4.3. Cubic spline fit (broken line) for Al K edge of Al metal.

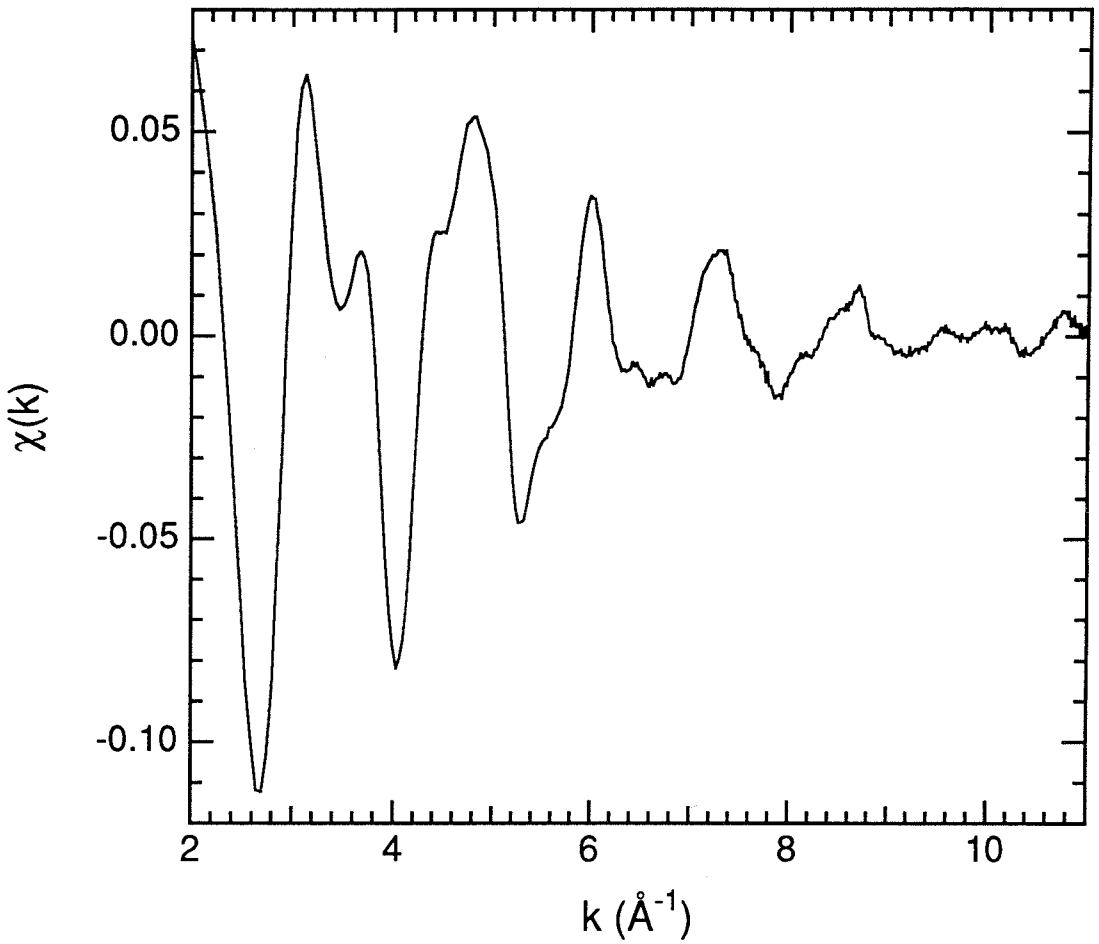

Figure 4.4. Al K-edge EXELFS from Al metal. Data taken at 97 K.

The symbols in Equation (2.23) have already been defined in §2.2.2.

The use of Equation (2.23) is justified only if the l_0 to (l_0 + 1) transition dominates over all others. Figure 4.5, as calculated by the method in §A.1, shows this holds true for the Al K edge. Given realistic experimental parameters, the partial energy-differential cross section for transitions to final states with p symmetry is seen to be at least 100 times larger than that for all other transitions combined. This result is interesting because it is well-known that non-dipole transitions are not strictly forbidden in EELS.

To compensate for its attenuation at high-k values, $\chi(k)$ is usually multiplied by k^n, where n = 1, 2, or 3. This prevents the low-k data from dominating the high-k data in the determination of interatomic distances which depend only on the frequency, and not the amplitude, of the oscillations (Teo, 1986). In general, when the neighboring atoms are light elements, n=3 should work well. Heavier neighbors require smaller n values (Teo and Lee, 1979). In practice, the value of n which best compensates for the attenuation is chosen.

Fourier band-pass filtering of the EXELFS data is the most common method used to isolate the structural information from individual atomic shells. Fourier transformation (FT) is performed on $k^n\chi(k)$ using Equation (4.3).

$$\begin{aligned} FT\,(k^n\chi) &= \int_{k_{min}}^{k_{max}} W(k)k^n\chi(k)\cos(2kr)dk + i\int_{k_{min}}^{k_{max}} W(k)k^n\chi(k)\sin(2kr)dk \\ &= Re[FT(k^n\chi)] + i\,Im[FT(k^n\chi)] \end{aligned} \qquad (4.3)$$

where W(k) is a window function whose edges are smoothed by Gaussian lineshapes to reduce ringing effects. The magnitude of the FT is given by Equation (4.4):

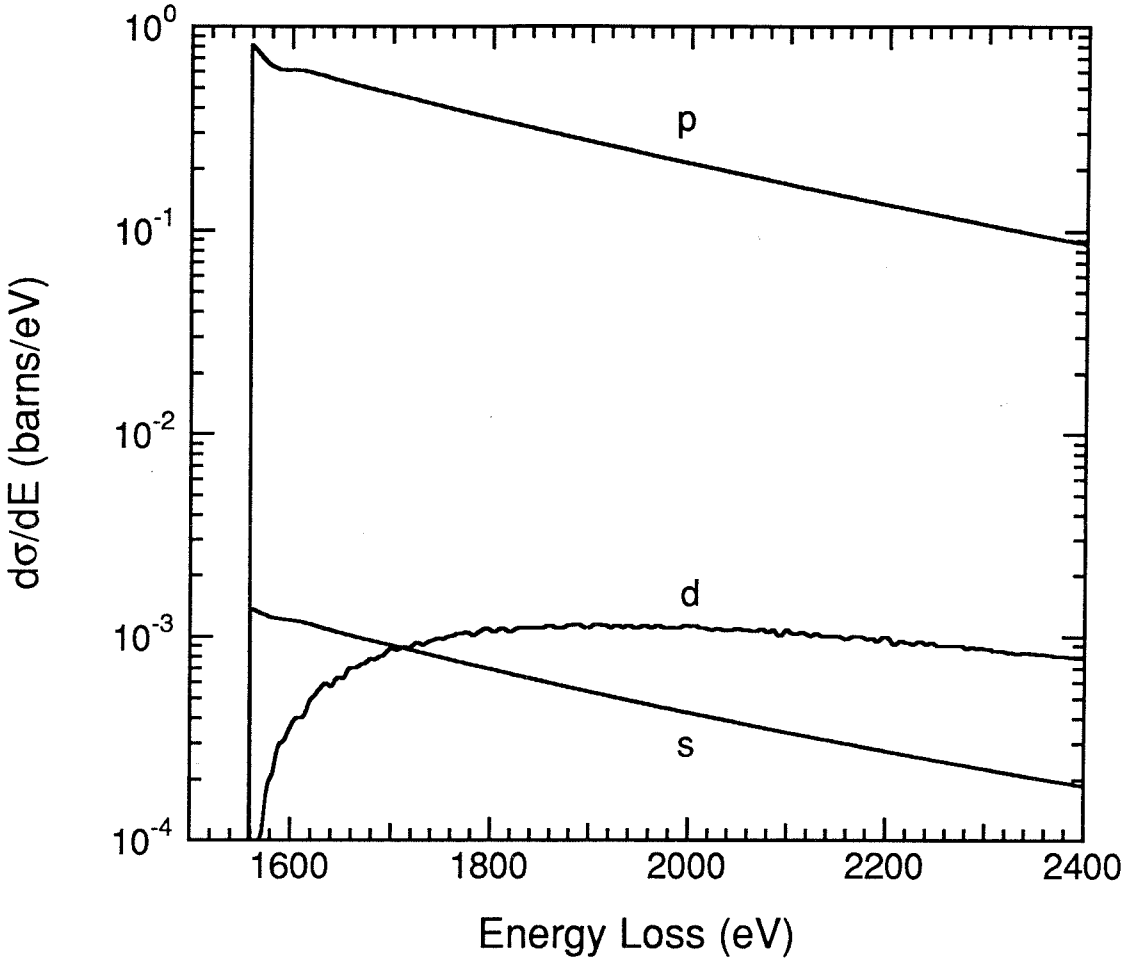

Figure 4.5. Partial energy-differential cross sections of Al K edge. Letters indicate angular momentum of final state. Energy of incident beam = 200 keV. Collection semiangle = 10 mrad.

$$\left|FT(k^n\chi)\right| = \{Re^2[FT(k^n\chi)] + Im^2[FT(k^n\chi)]\}^{1/2} \qquad (4.4)$$

Peaks in $\left|FT(k^n\chi)\right|$ correspond to shells of nearest-neighbor atoms, although their positions are shifted slightly from the actual radial distances because of the k-dependence of the scattering phase shifts $\eta_j(\pi,k)$ and $2\delta_{l_0+1}(k)$ in Equation (2.23). The reverse transform of the data within a selected window in r-space isolates the EXELFS oscillation due to a particular atomic shell. The reverse transform of the data is given by Equation (4.5):

$$FT^{-1}\,[FT(k^n\chi)] = \frac{1}{\pi}\int_{r_{min}}^{r_{max}} w(r)\left\{Re\left[FT(k^n\chi)\right]\cos(2kr) - Im\left[FT(k^n\chi)\right]\sin(2kr)\right\}dr \qquad (4.5)$$

where w(r) is a window function whose edges are smoothed by Gaussian lineshapes, like the window for the forward transform.

Figures 4.6 through 4.8 present the Fourier filtering for the Al K edge of Al metal. Figure 4.6 displays the EXELFS data weighted by k^2 and the window in k-space for the forward transform. Figure 4.7 shows the magnitude of the FT and the window in r-space for the reverse transform. Finally, Figure 4.8 presents the oscillation, due to the 1nn shell, which was isolated with this Fourier filtering process.

In Figure 4.7, the 1nn peak is located at r = 2.34 Å. The actual distance to the 1nn shell in Al metal is 2.86 Å. As mentioned previously, this shift in the peak position is due to the dependence of the scattering phase shifts on k. The peak near r = 1.6 Å can be identified with Al-O bonds in surface oxide. Note that some of the 1nn peak was removed by the window in r-space. Therefore, theoretical calculations of the 1nn shell oscillation must also be put through the

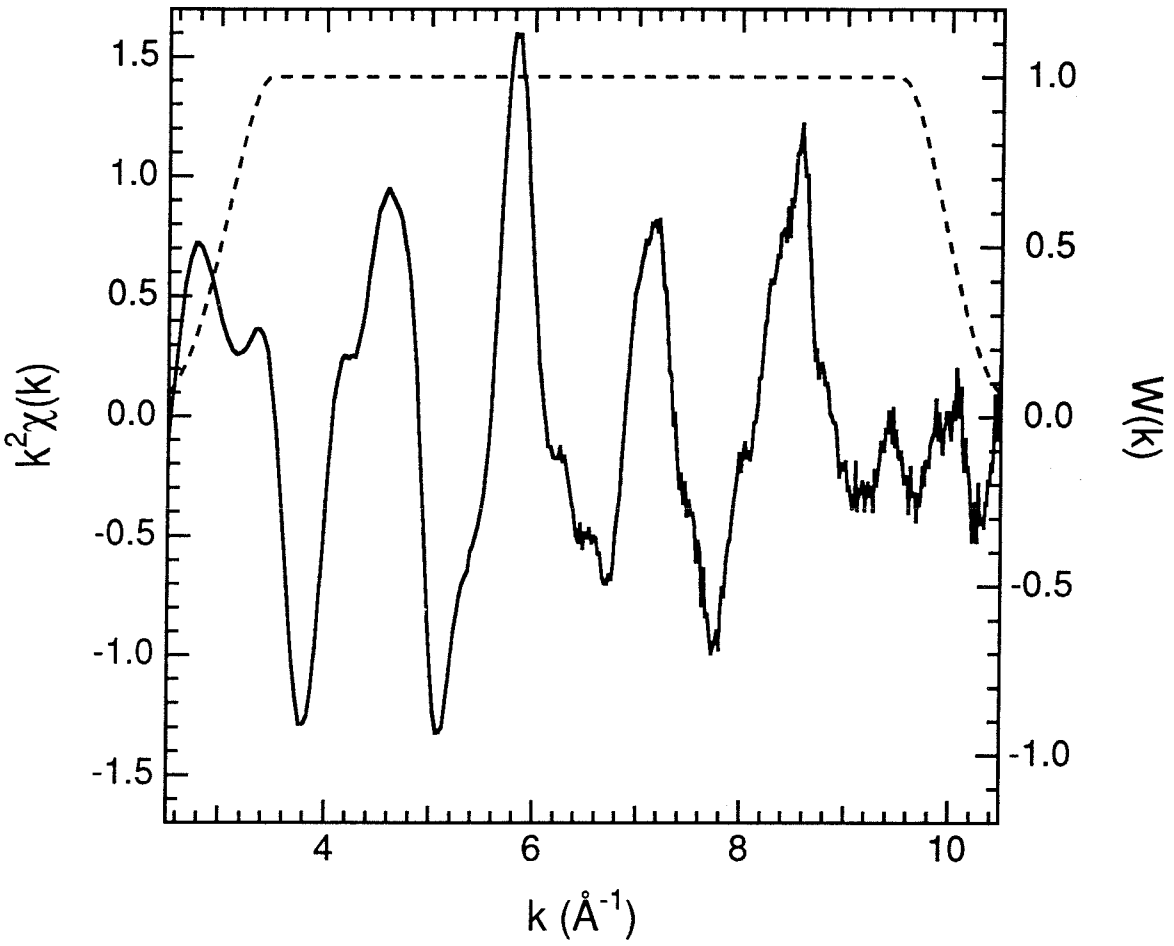

Figure 4.6. Al K-edge EXELFS from Al metal weighted by k^2 (solid line). Also shown is window in k-space for Fourier transform (dashed line). Data taken at 97 K.

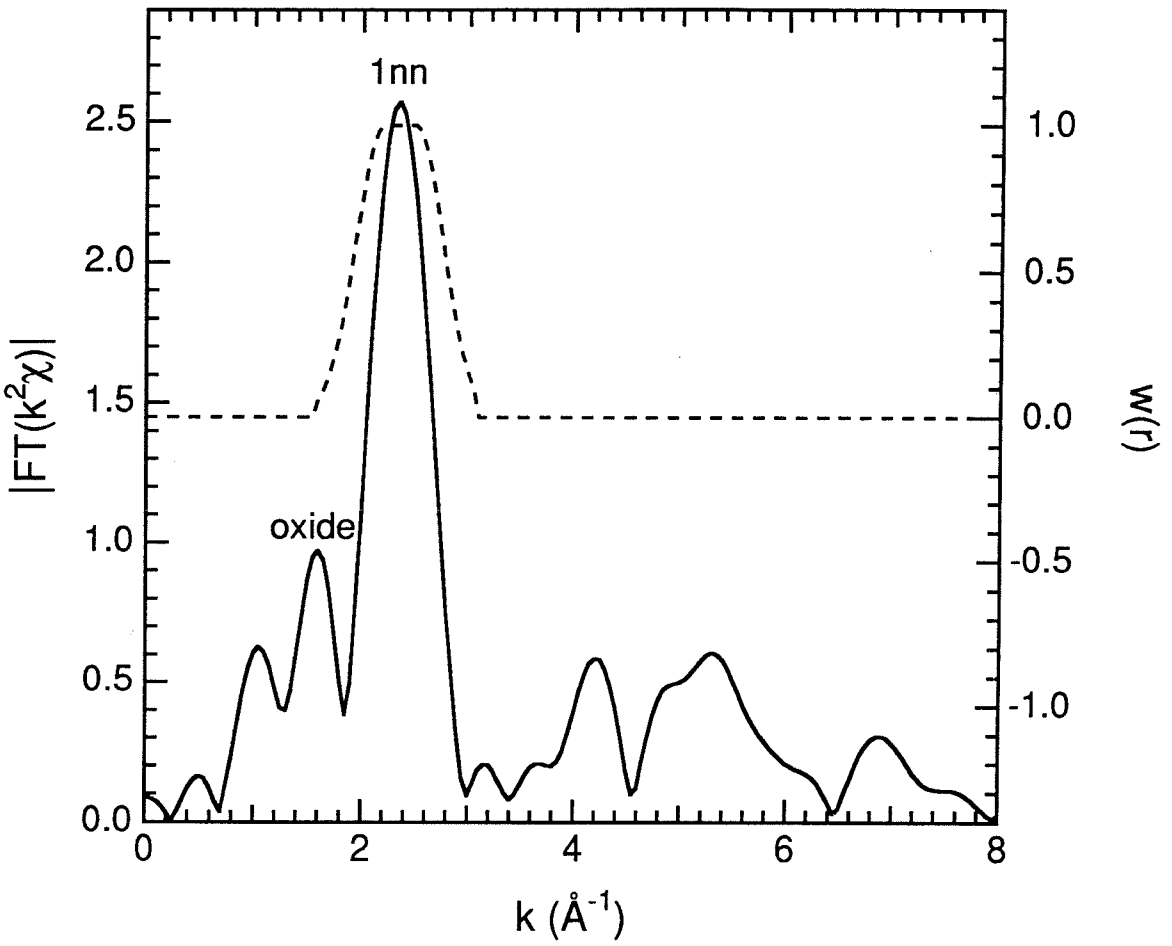

Figure 4.7. Magnitude of Fourier transform of Al K-edge EXELFS from Al metal (solid line). Also shown is window in r-space to select 1nn shell data for inverse Fourier transform (dashed line). Data taken at 97 K.

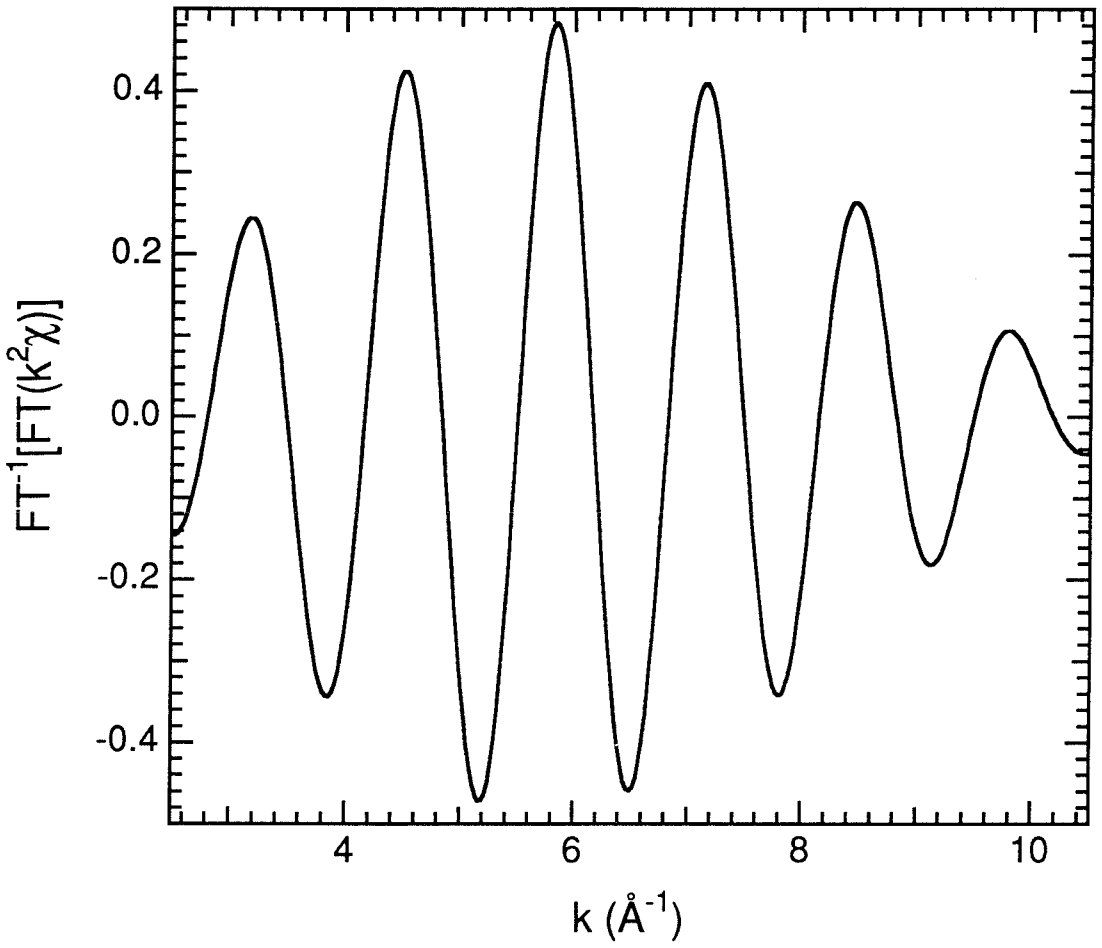

Figure 4.8. Al K-edge EXELFS from Al metal after Fourier filtering to isolate 1nn shell data. Note filtered oscillation is still weighted by k^2. Data taken at 97 K.

same Fourier filtering process before they can be compared to the experimental oscillation in Figure 4.8.

The first principles calculation of phase shifts and scattering amplitudes in the plane-wave approximation is discussed and presented in §A.2. These calculated phase shifts and scattering amplitudes can be used to determine theoretical EXELFS oscillations using Equation (2.23). Figure 4.9 displays the theoretical oscillation on the Al K edge due to the 1nn shell in Al metal and compares it with the measured EXELFS from Figure 4.4. The calculation of the theoretical oscillation used phase and amplitude functions from Teo and Lee (1979) and furthermore assumed: $S(k) = 0.7$; $\lambda(k)$ followed Equation (2.51) with $C = 1$, $D = 3$, and $n = 1.2$; and $\sigma^2 = 0.006$ Å^2. Given the experimental temperature of 97 K, the results of §5.3 were used to choose the value for σ^2.

Figures 4.10 through 4.12 display the result of applying the Fourier filtering process on the theoretical 1nn oscillation. Figure 4.10 shows the theoretical oscillation weighted by k^2, along with the measured EXELFS weighted by k^2 from Figure 4.6, and the window for the forward transform. Figure 4.11 presents the magnitude of the FT of the theoretical oscillation, along with the measured data from Figure 4.7, and the window for the reverse transform. The theoretical data shows a shift in the 1nn peak position of -0.43 Å which compares reasonably well with the measured shift of -0.52 Å. The discrepancy between the two values is less than 0.1 Å and is probably due to my arbitrary choice of edge onset energy, E_0. Lee and Beni (1977) suggest choosing E_0 using the requirement that the imaginary part and the absolute value of the Fourier transform should peak at the same distance. I simply chose E_0 to be at the location of the maximum edge height. Lastly, Figure 4.12 gives the theoretical oscillation after Fourier filtering, along with the measured

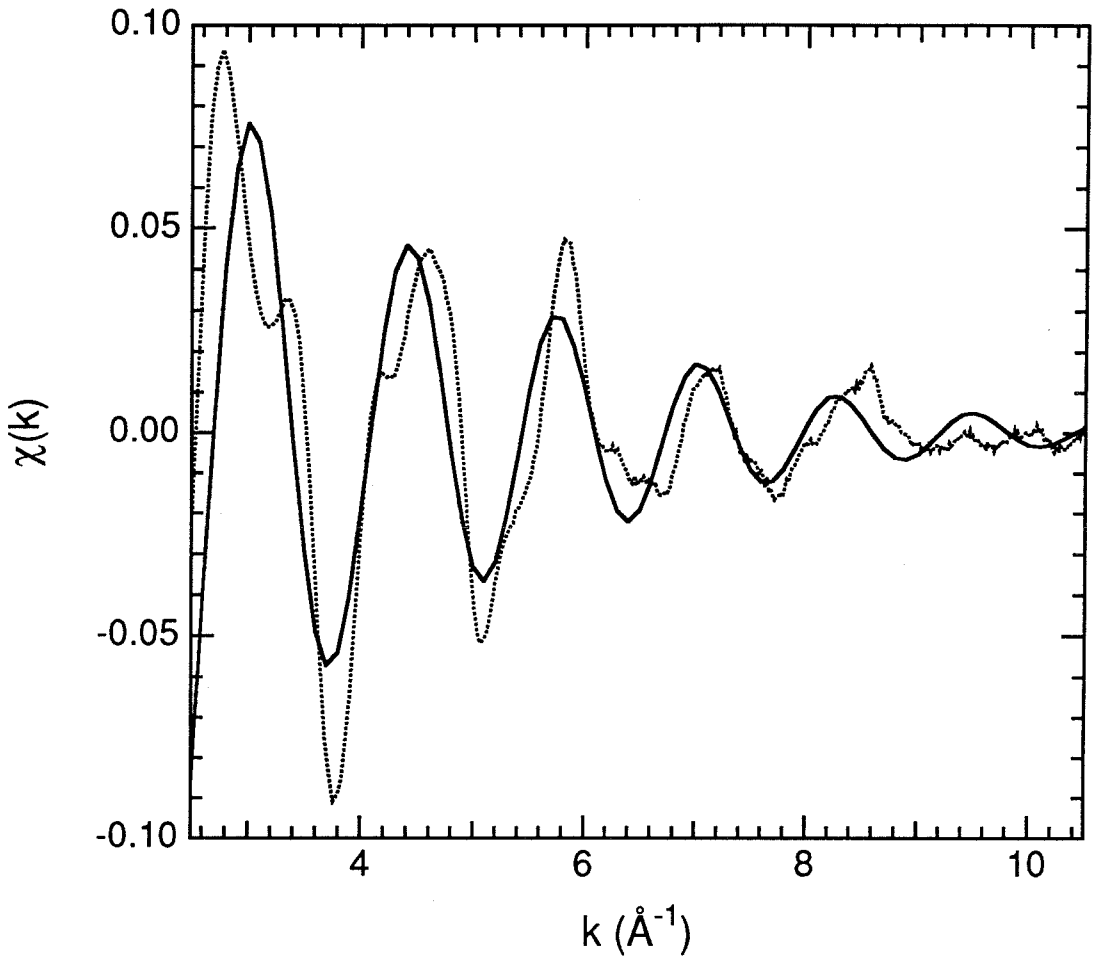

Figure 4.9. Theoretical (solid line) and experimental (dotted line) Al K-edge EXELFS due to 1nn shell in Al metal.

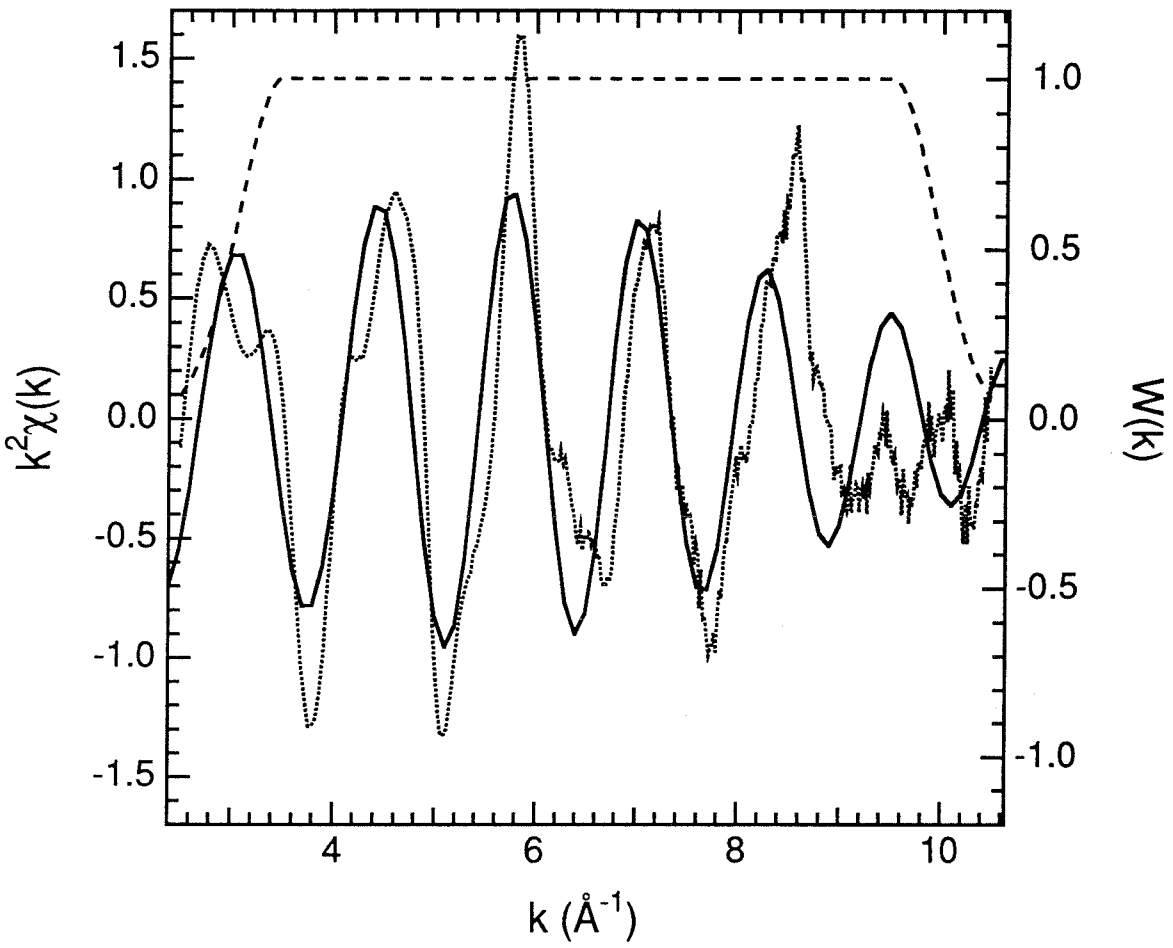

Figure 4.10. Theoretical (solid line) and experimental (dotted line) EXELFS on Al K-edge due to 1nn shell in Al metal after weighting by k^2. Also shown is window for FT (dashed line).

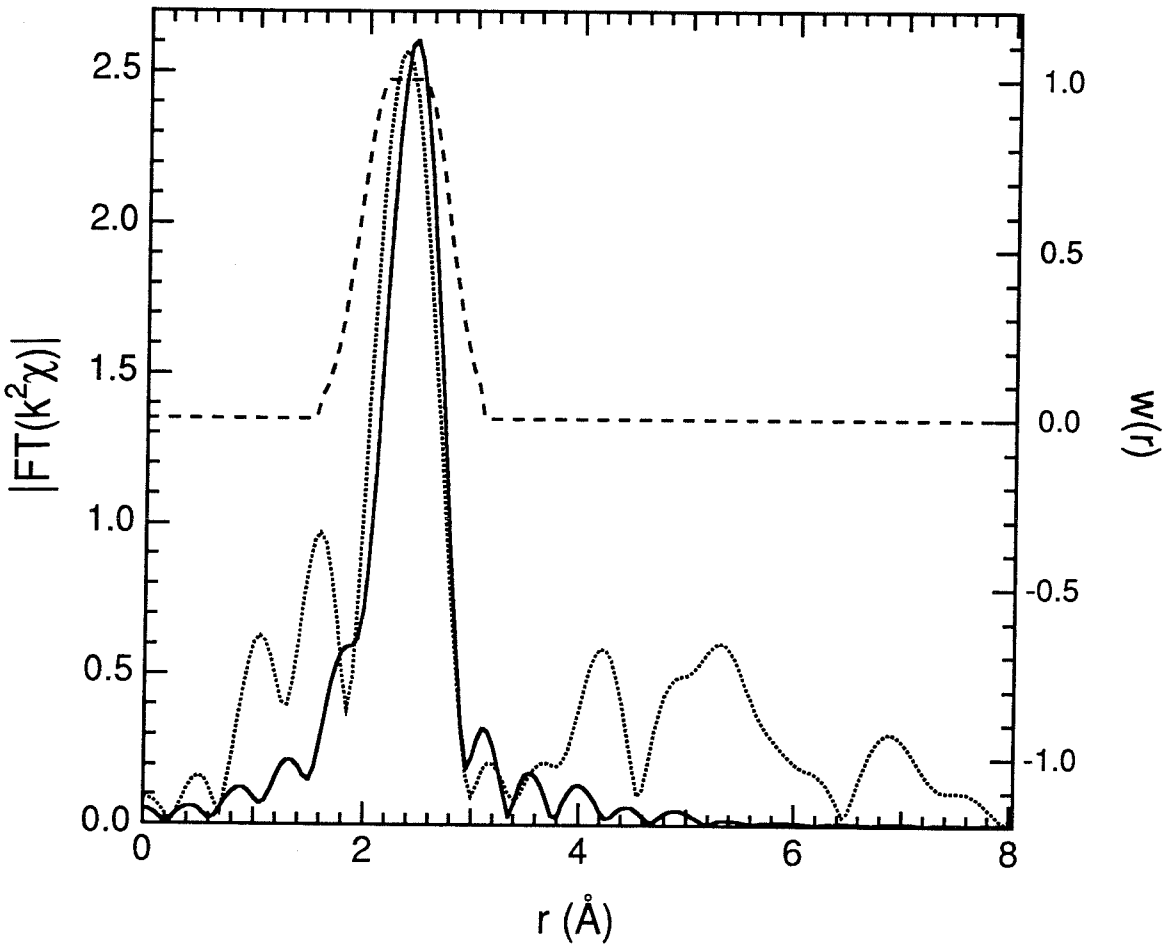

Figure 4.11. Magnitude of FT of theoretical (solid line) and experimental (dotted line) Al K-edge EXELFS due to 1nn shell in Al metal. Also shown is window for inverse FT (dashed line).

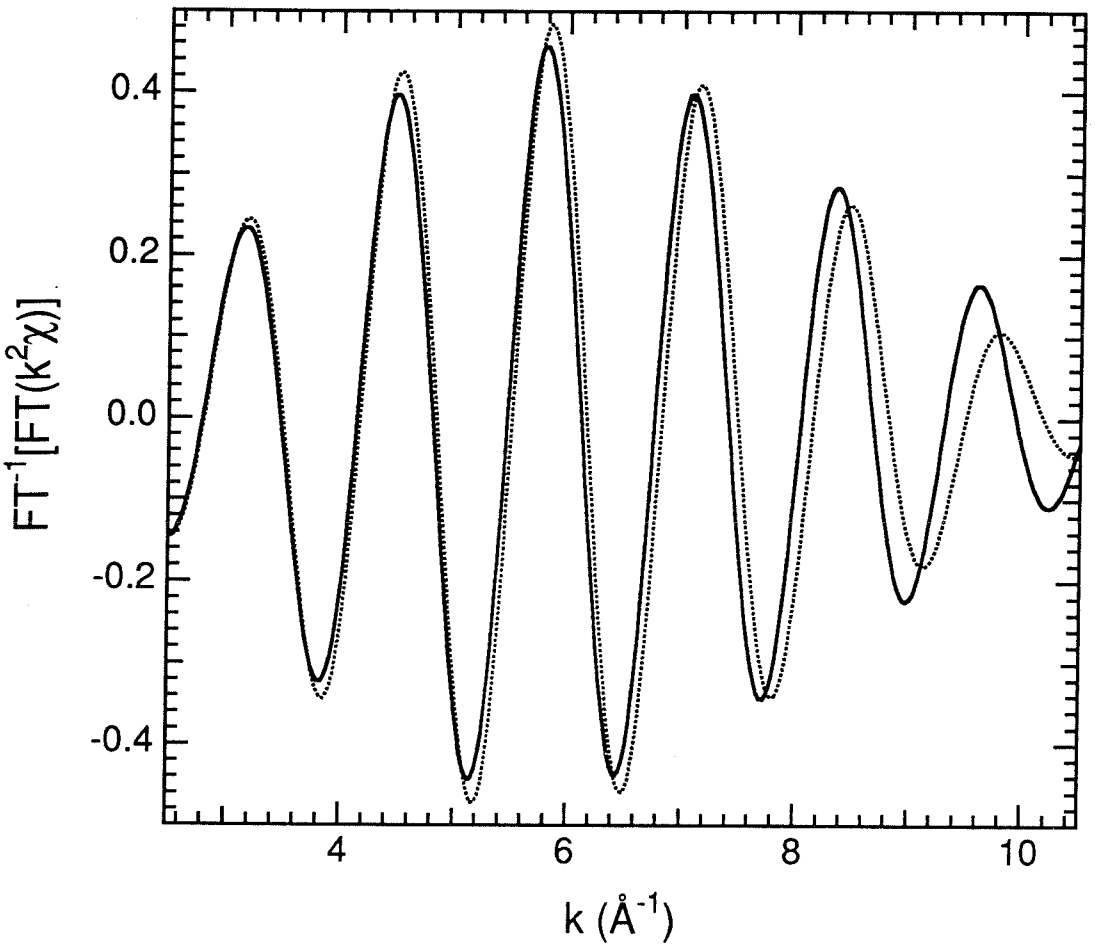

Figure 4.12. Theoretical (solid line) and experimental (dotted line) Al K-edge EXELFS due to 1nn shell in Al metal after Fourier filtering.

oscillation after Fourier filtering from Figure 4.8. Comparing the amplitudes of the two oscillations and neglecting the presence of Al oxide gives an experimental coordination number of 11.9 ± 1.4 for the 1nn shell in Al metal. Given the relatively crude and somewhat arbitrary nature of the approximations made, this is in coincidentally good agreement with the known value of 12 for the fcc structure.

4.2 Extension to L_{23} and M_{45} Edges

EXELFS occurs above all the ionization edges in a condensed matter sample, but the analysis of EXELFS is usually performed only for K-edge data. K edges are simple to analyze because they correspond to transitions from 1s core states to only those unbound final states with p symmetry (assuming the dipole selection rule holds, as is typical in these cases). L and M edges, on the other hand, are complicated by the variety of possible initial and final angular momentum states. L edges, for instance, have both 2s and 2p initial states, and transitions from the 2p initial states can result in final states with either s or d symmetry. L edges have been previously used for EXELFS by Leapman et al. (1982), but I believe the present work is the first time that M edges have been used. In particular, I show that nearest-neighbor distances can be obtained by comparing first principles calculations with the experimental Fe L_{23} and Pd M_{45} EXELFS data.

4.2.1 Fe L_{23}

Figure 4.13 displays the experimentally measured EELS spectrum of the Fe L_{23} edge from Fe metal. Figure 4.14 presents the extracted Fe L_{23} EXELFS signal. As with my Al K-edge EXELFS data, E_0 was chosen to be at the location

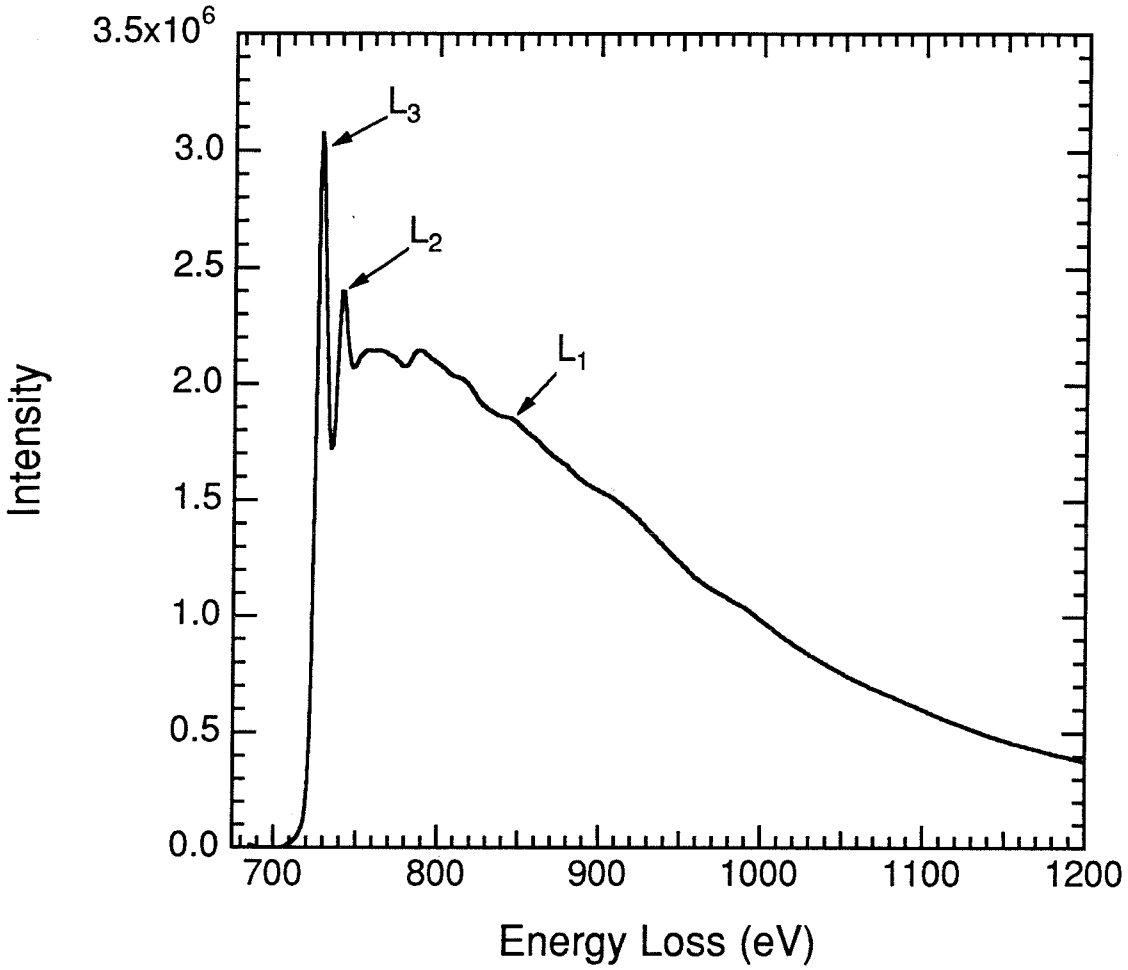

Figure 4.13. Background subtracted Fe L edge from foil of pure Fe metal. Spectrum was not deconvoluted, so it contains multiple inelastic scattering. Sample thickness roughly 1/2 times mean free path for inelastic scattering.

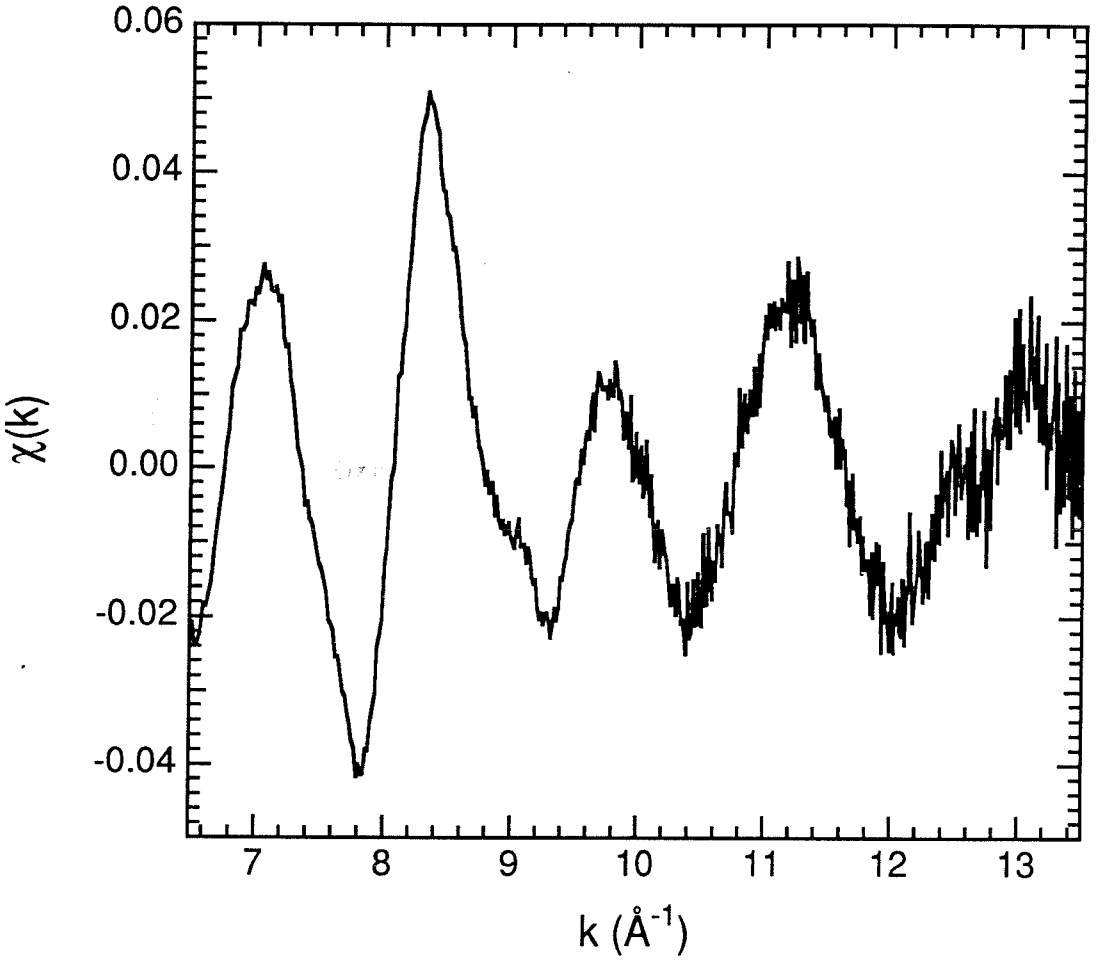

Figure 4.14. Fe L_{23}-edge EXELFS from Fe metal. Data taken at 97 K.

of the maximum edge height. Fourier transformation of the EXELFS signal is illustrated in Figures 4.15 and 4.16. Figure 4.15 displays the signal weighted by k and the window in k-space. Figure 4.16 shows the magnitude of the FT. Note that the main peak contains data from both 1nn and 2nn shells because the distance to the 2nn shell (2.86 Å) in bcc Fe is relatively close to that of the 1nn shell (2.48 Å).

Consider the analysis of the Fe L_{23}-edge EXELFS. First, I show that the Fe L_{23} edge is dominated by the 2p to d channel. Figure 4.17 contains calculated partial energy-differential cross sections for the excitation of 2p electrons in Fe into final states of s, p, d, or f character. It is seen that, in the EXELFS region, the 2p to d channel dominates over the sum of all others by a factor of about 25. This domination by the 2p to d channel makes possible the interpretation of the Fe L_{23} EXELFS using Equation (2.23) with $l_0 = 1$.

Having shown that transitions to final states of d character dominate over all others for the Fe L_{23} edge, now consider the complications arising from the presence of different initial states in the Fe L edge. The spin-orbit splitting between the L_3 and L_2 edges of about 13 eV is not a major problem because it is small compared with the spacing between EXELFS maxima far above the ionization threshold energy, so EXELFS oscillations from L_3 and L_2 edges will be nearly in phase in this energy range. The presence of the Fe L_1 edge can complicate the analysis of the Fe L_{23} EXELFS for two reasons. First, the L_1 edge, which occurs as a relatively sharp jump near E = 846 eV (corresponding to k = 6.0 $Å^{-1}$ for the L_{23} edge), interrupts the L_{23} EXELFS signal. This problem can be eliminated by using only L_{23} EXELFS data sufficiently past the L_1 edge jump. Second, the L_1 EXELFS signal overlaps with the L_{23} EXELFS. However, as shown in Figure 4.18, the differential cross section of the Fe L_1 edge in the

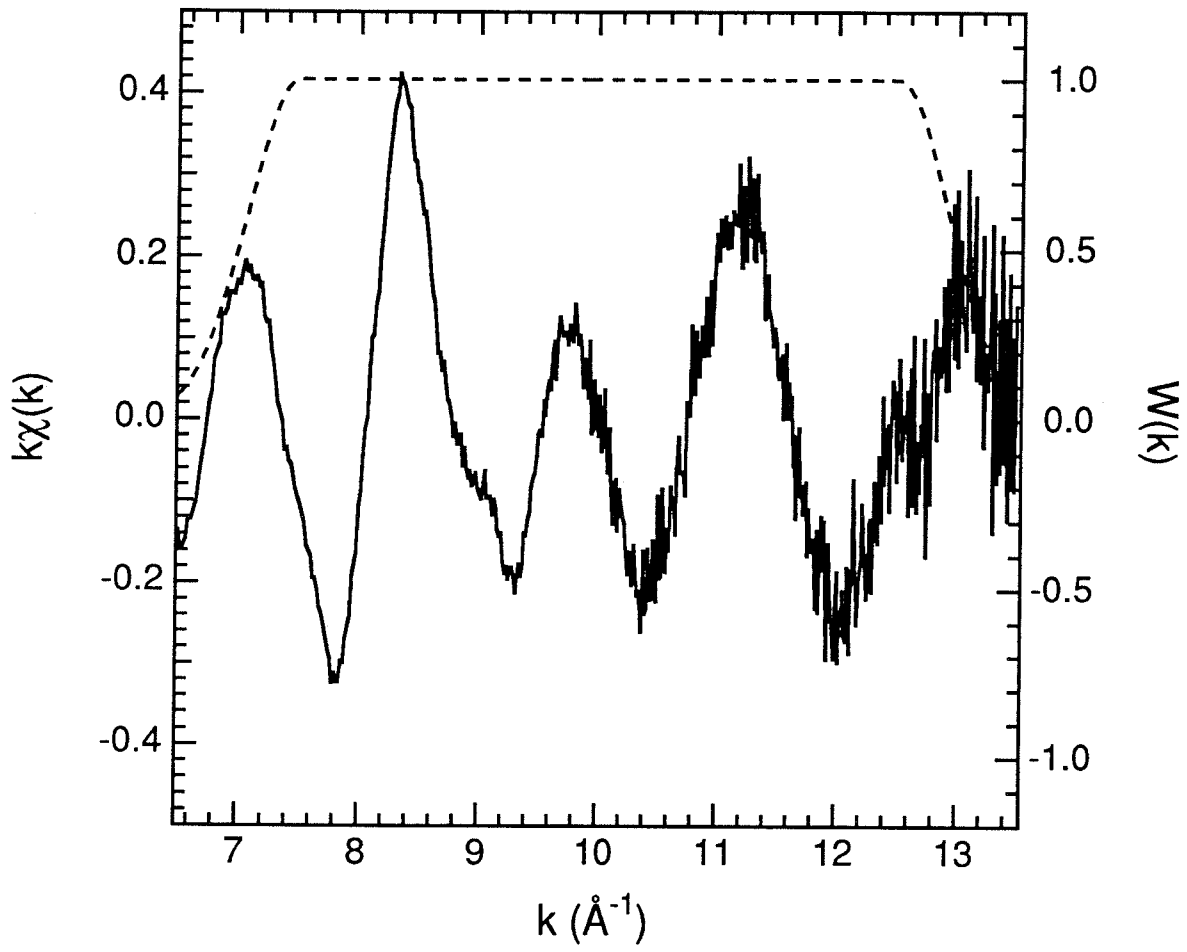

Figure 4.15. Fe L_{23}-edge EXELFS from Fe metal weighted by k (solid line). Also shown is window for FT (dashed line). Data taken at 97 K.

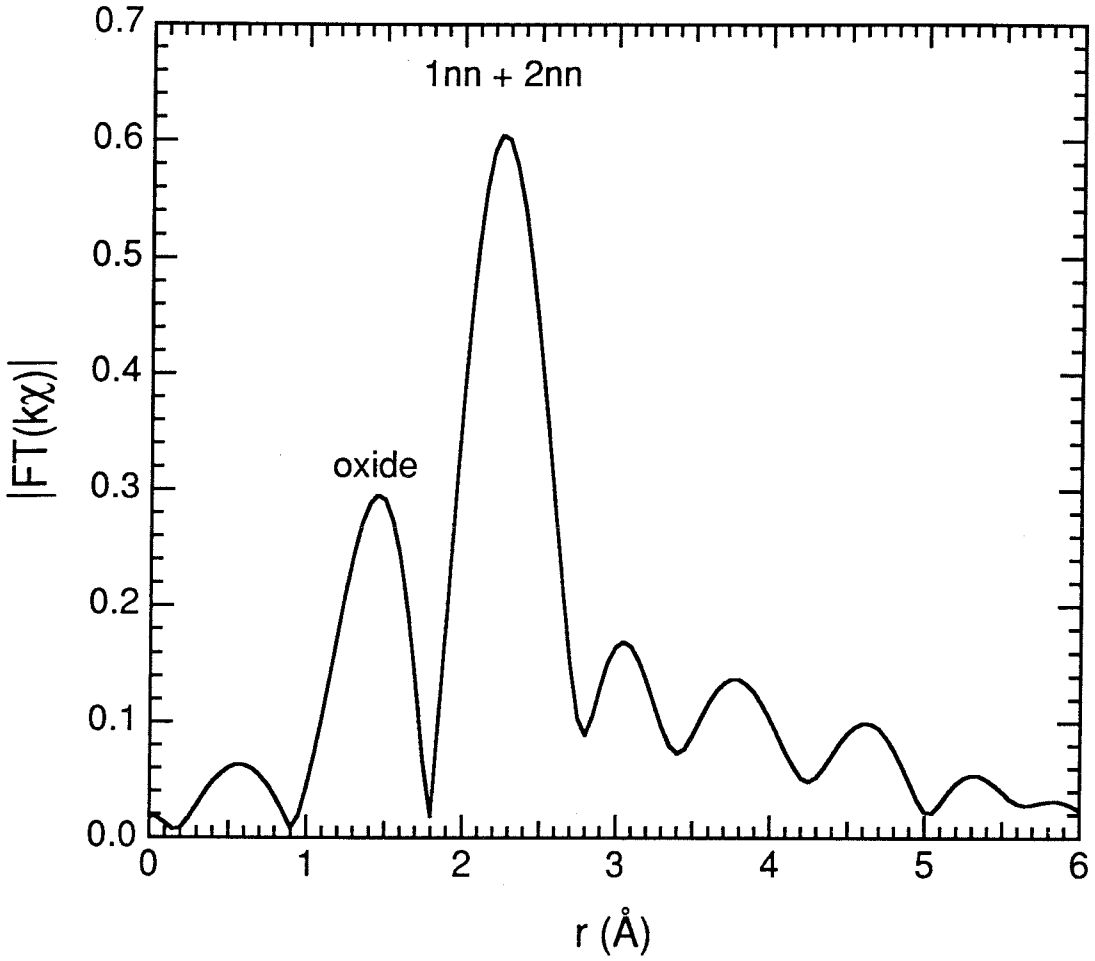

Figure 4.16. Magnitude of Fourier transform of Fe L_{23}-edge EXELFS from Fe metal. Data taken at 97 K.

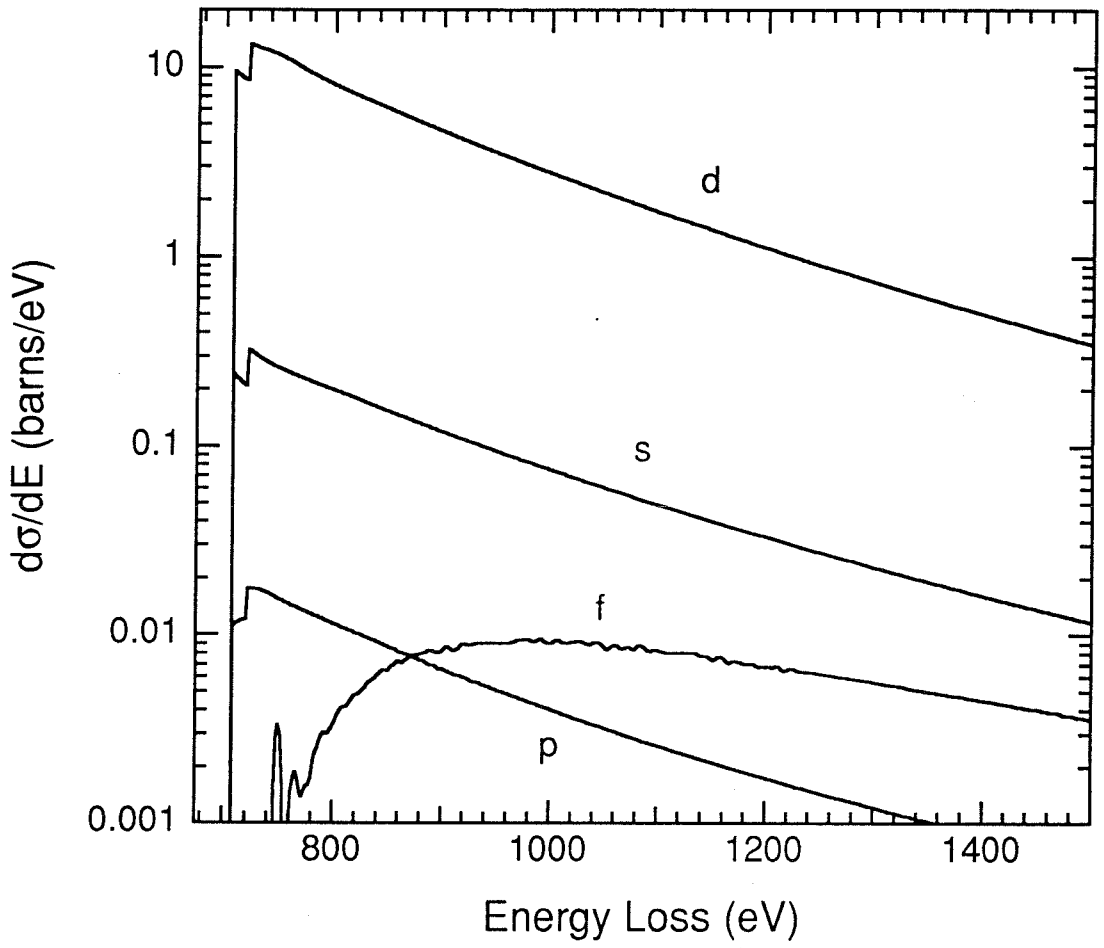

Figure 4.17. Partial energy-differential cross sections of Fe L_{23} edge. Letters indicate angular momentum of final state. Energy of incident beam = 200 keV. Collection semiangle = 5 mrad.

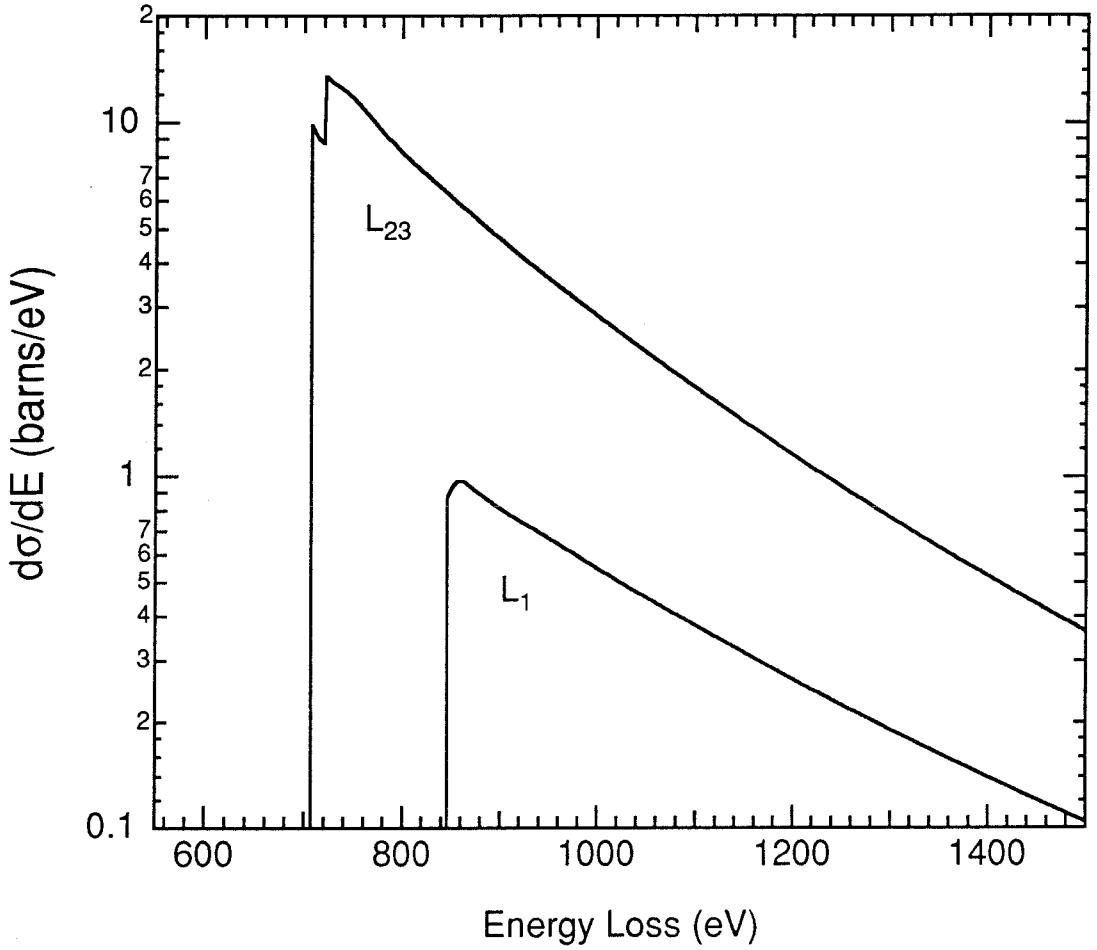

Figure 4.18. Energy-differential cross sections of Fe L_{23} and L_1 edges. Energy of incident beam = 200 keV. Collection semiangle = 5 mrad.

region of interest is about four times smaller than that of the Fe L_{23} edge. Moreover, transforming the data from the L_1 edge to the k-space corresponding to the L_3 edge effectively raises the frequencies of the L_1 EXELFS oscillations and makes them somewhat incoherent.

Figure 4.19 displays, in energy-loss space, the theoretical L_3, L_2, and L_1 EXELFS signals from the combined 1nn and 2nn shells in Fe metal. The theoretical EXELFS were generated using phase and amplitude functions from Teo and Lee (1979) and additionally assumed S(k) = 0.7; $\lambda(k)$ followed Equation (2.51) with C=1, D=3, and n=1.2; and $\sigma^2_{1nn} = \sigma^2_{2nn} = 0.003$ Å^2. The results of §5.3 were used to choose the value for σ^2.

Figure 4.20 presents the sum of the three theoretical EXELFS signals and superimposes the measured EXELFS for comparison. The general shape of the theoretical and experimental oscillations compare well, especially in the range 8 Å^{-1}< k <12 Å^{-1}, where the experimental data are most reliable. The main discrepancy seems to be a phase shift between the two. This is probably due to my arbitrary choice of E_0 for the experimental data. Figure 4.21 compares the two oscillations after E_0 for the experimental data was shifted by -15 eV. After this adjustment of E_0, the two oscillations match very well.

Fourier filtering of the EXELFS is displayed in Figures 4.22 through 4.24. Figure 4.22 displays the EXELFS weighted by k and the window for the Fourier transform. Figure 4.23 shows the magnitude of the FT and the window for the inverse FT. The main peak in the theoretical spectrum is at r = 2.29 Å which compares well with the experimental peak position of r = 2.23 Å. The secondary peak near r = 3 Å can be attributed to the higher-frequency L_1 EXELFS signal. This peak does not greatly affect the combined 1nn and 2nn peak from the L_{23} EXELFS, but it does interfere with the weaker 3nn peak which, after accounting

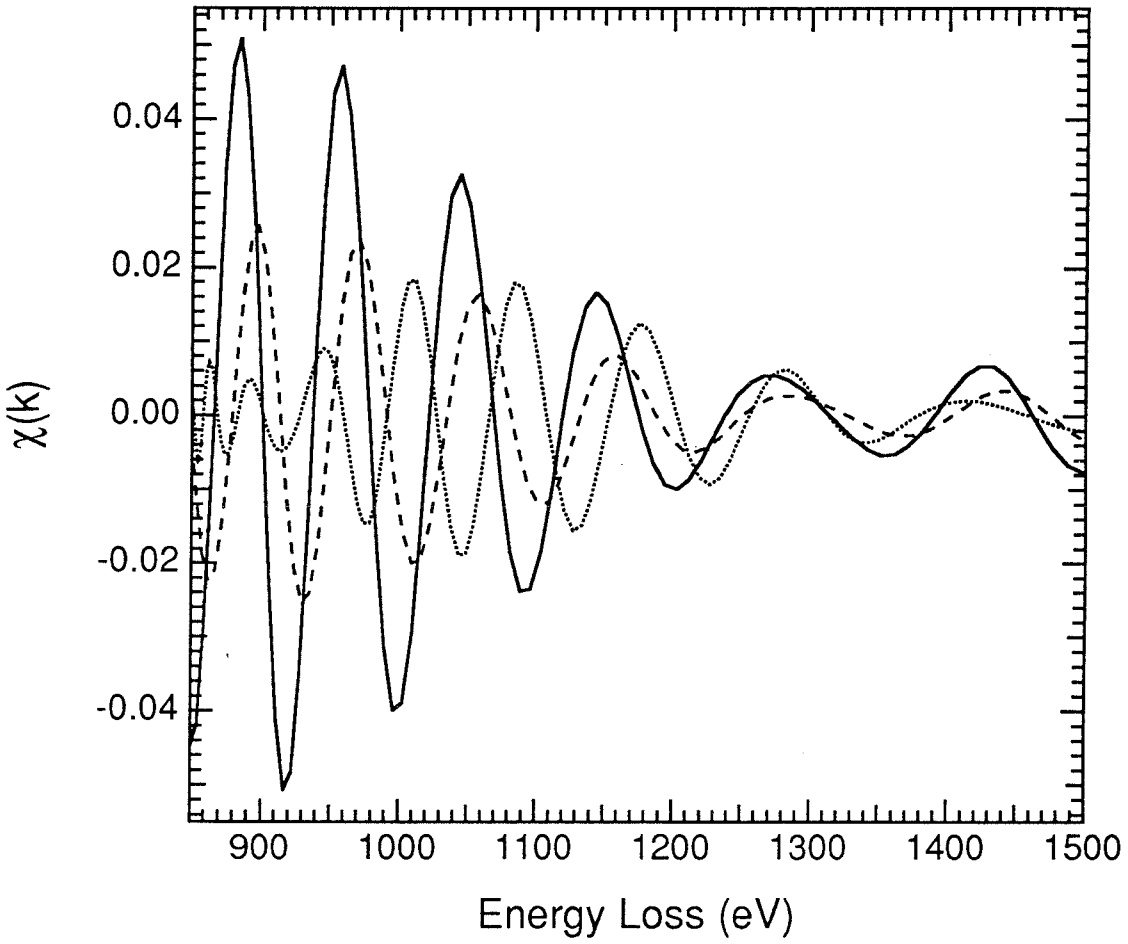

Figure 4.19. Theoretical Fe L_3 (solid line), L_2 (dashed line), and L_1 (dotted line) EXELFS due to combined 1nn and 2nn shells in Fe metal.

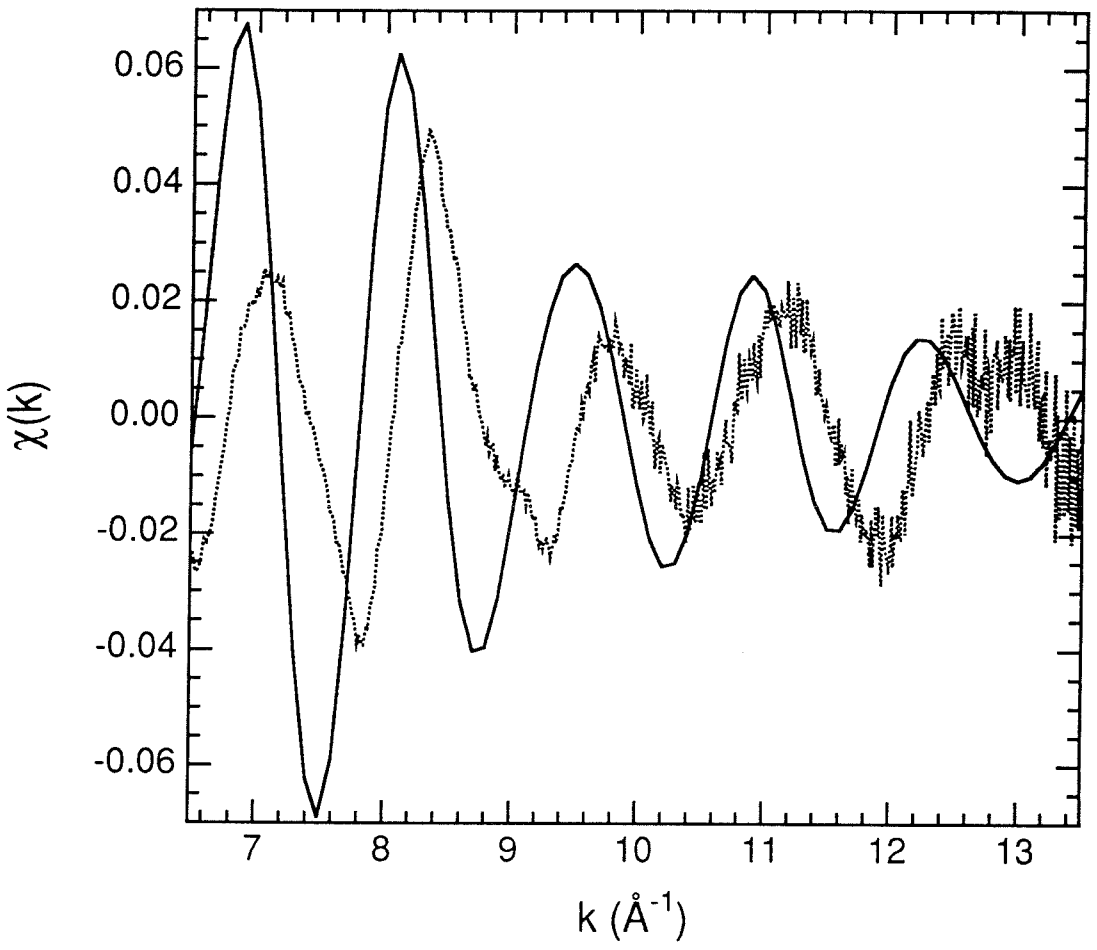

Figure 4.20. Sum of theoretical Fe L_3, L_2, and L_1 EXELFS due to combined 1nn and 2nn shells in Fe metal (solid line). Also shown is experimental EXELFS (dotted line).

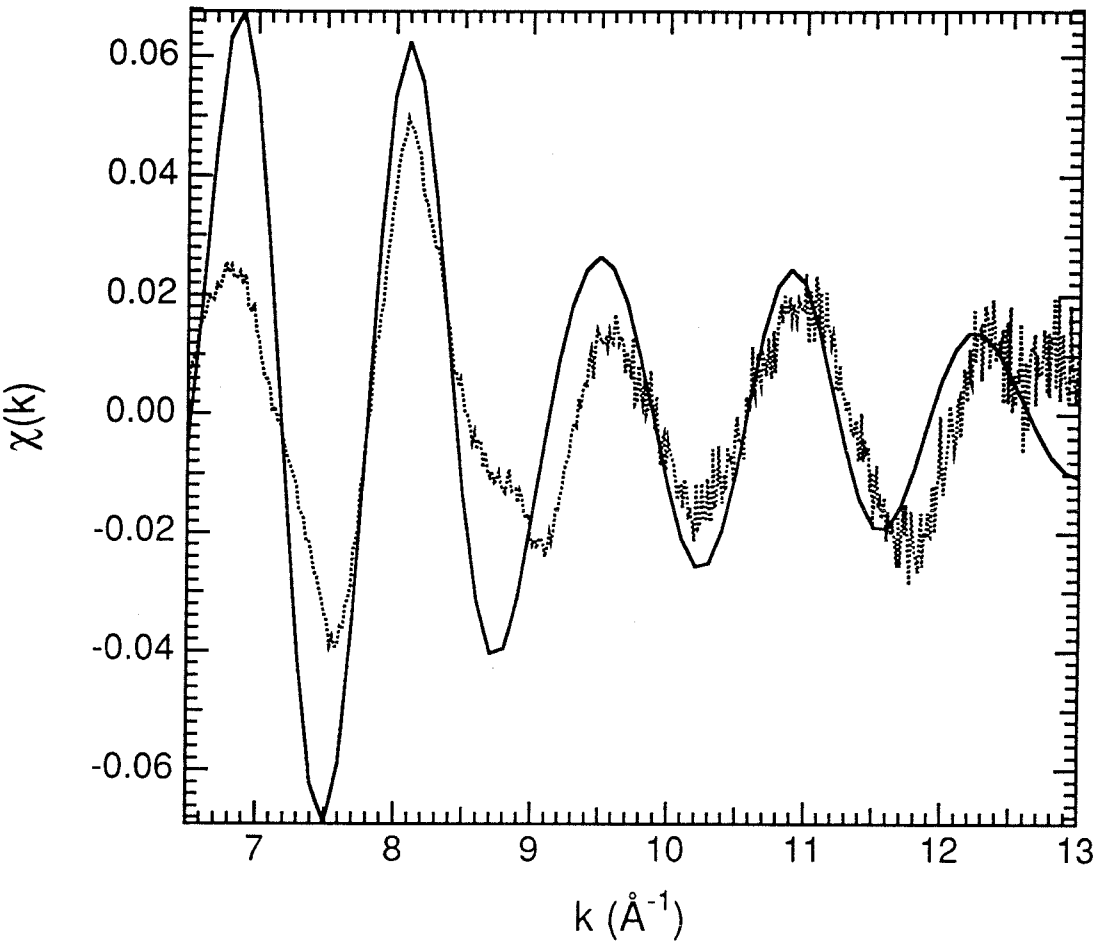

Figure 4.21. Theoretical (solid line) and experimental (dotted line) Fe L_{23}-edge EXELFS after E_0 for experimental data shifted by -15 eV.

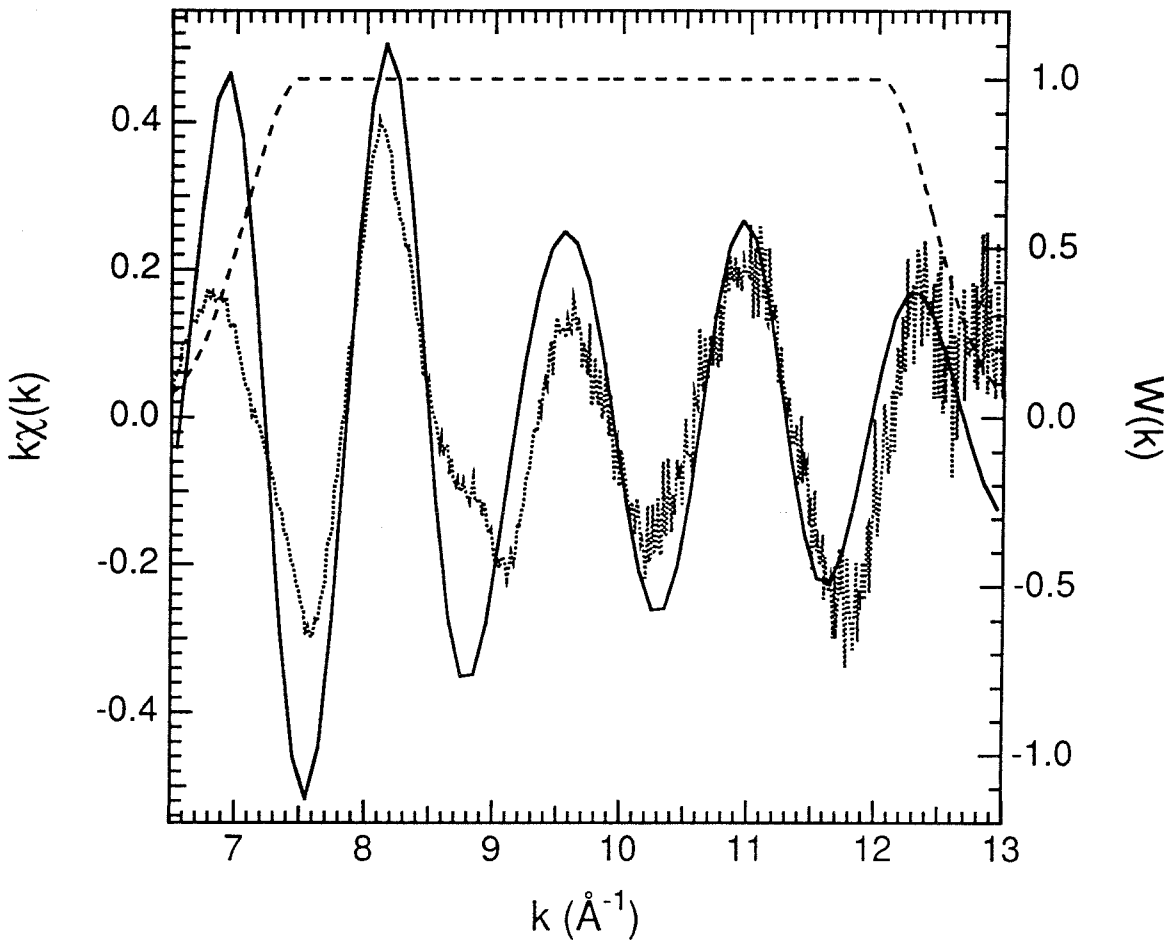

Figure 4.22. Theoretical (solid line) and experimental (dotted line) Fe L_{23}-edge EXELFS weighted by k. Also shown is window for FT (dashed line).

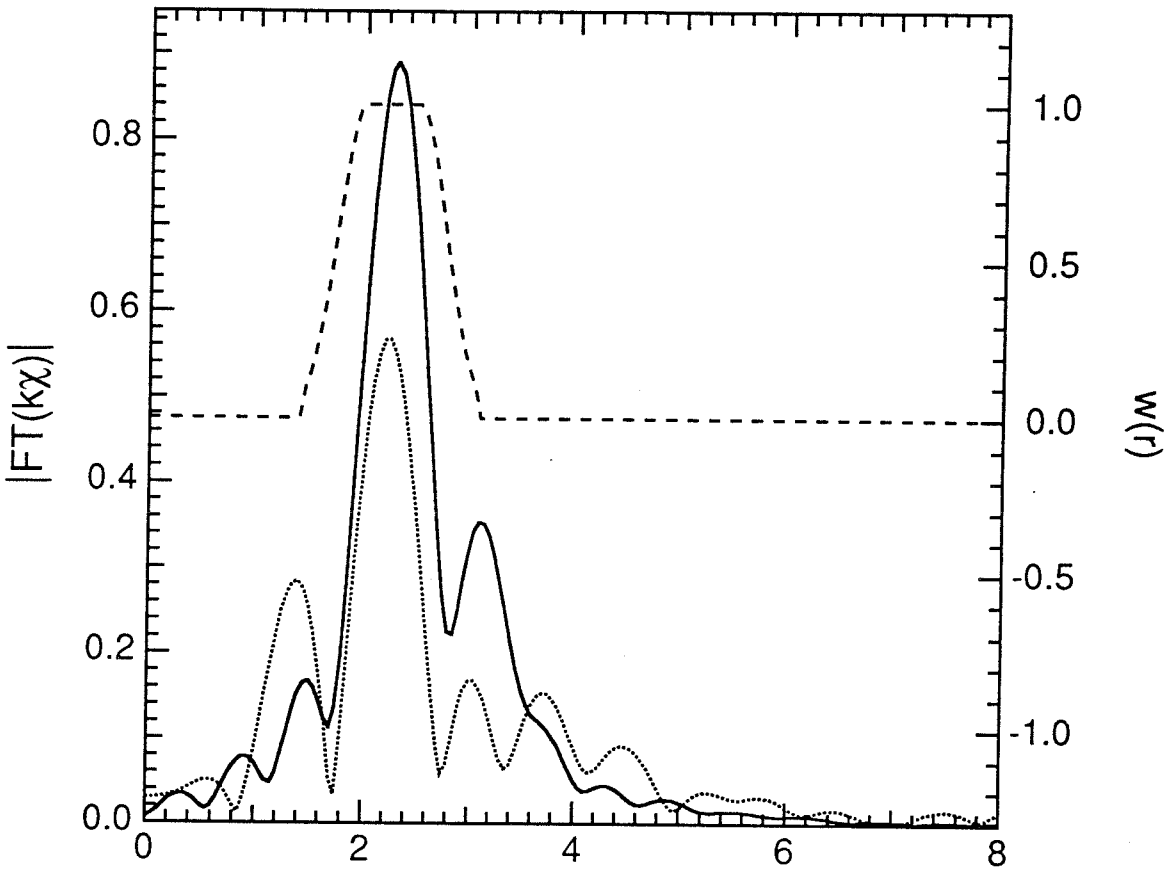

Figure 4.23. Magnitude of FT of theoretical (solid line) and experimental (dotted line) Fe L_{23}-edge EXELFS. Also shown is window to select 1nn and 2nn data for inverse FT (dashed line).

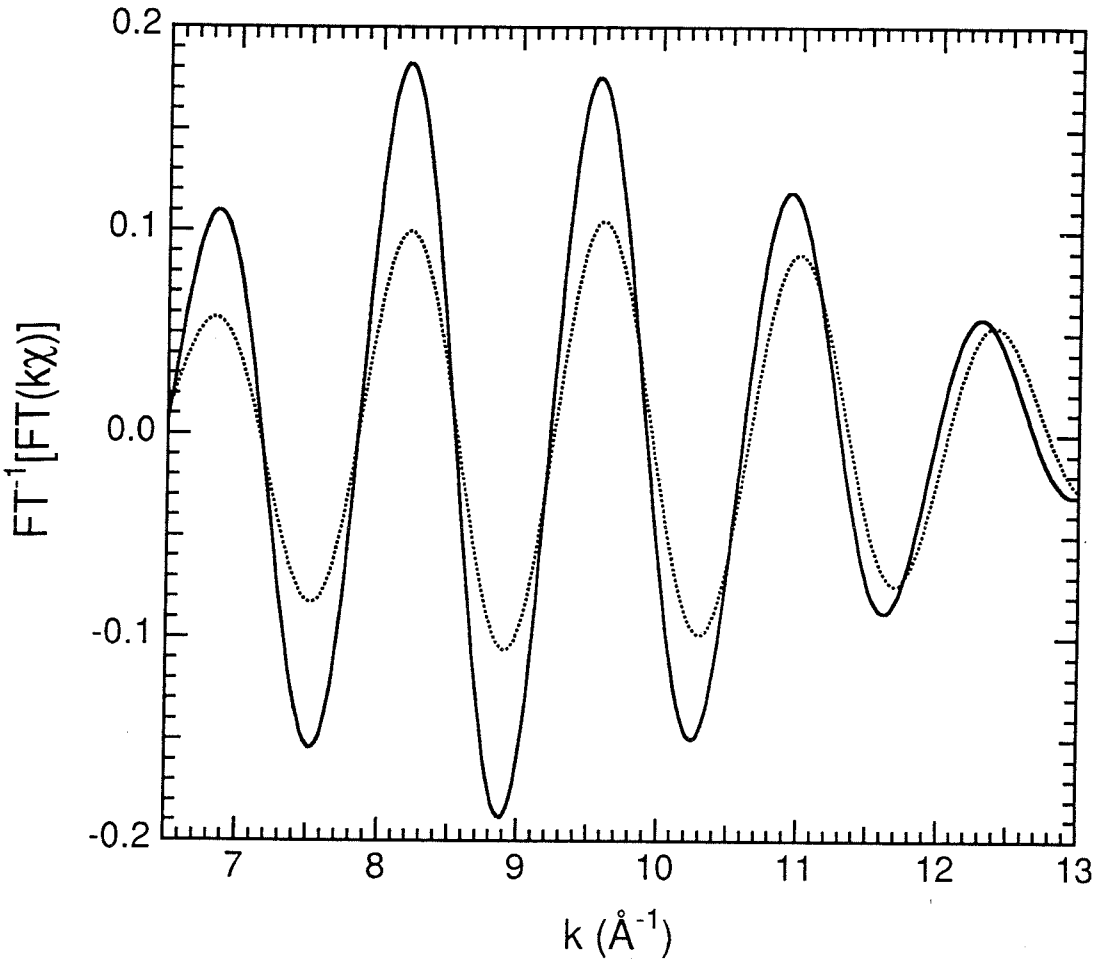

Figure 4.24. Fourier filtered theoretical (solid line) and experimental (dotted line) Fe L_{23}-edge EXELFS.

for phase shifts, should be located near r = 3.2 Å. Figure 4.24 displays the EXELFS oscillations after the inverse FT. Comparing the amplitudes of the two oscillations and neglecting the presence of Fe oxide gives an experimental coordination number of about 8.5 ± 0.8 for the combined 1nn and 2nn shells in bcc Fe metal. This is 40% less than the known value of 14, but this level of accuracy is reasonable considering the somewhat arbitrary normalizations of both the theoretical and experimental EXELFS signals. Also, accounting for the presence of Fe oxide would raise the experimentally determined coordination number. This is because Fe atoms in the oxide contribute significantly to the edge height, but only slightly to the peak corresponding to the 1nn and 2nn shells in Fe metal.

4.2.2 Pd M_{45}

Figure 4.25 displays the EELS measurement of the Pd M_{45} edge from Pd metal. Note the large number of counts in the spectrum. Figure 4.26 presents the extracted Pd M_{45} EXELFS signal and the window for the Fourier transformation. E_0 was chosen to be near the bottom at the very beginning of the Pd M_{45} edge. Figure 4.27 shows the magnitude of the FT.

The EXELFS analysis of the Pd M_{45} edge parallels that of the Fe L_{23} edge. First, I show that the Pd M_{45} edge is dominated by the 3d to f channel. Figure 4.28 contains the calculated partial energy-differential cross sections for the excitation of 3d electrons in Pd into final states of various angular momentum. The 3d to f channel is seen to dominate over the sum of all others by a factor of about 20. This domination by the 3d to f channel makes possible the interpretation of the Pd M_{45} EXELFS using Equation (2.23) with $l_0 = 2$.

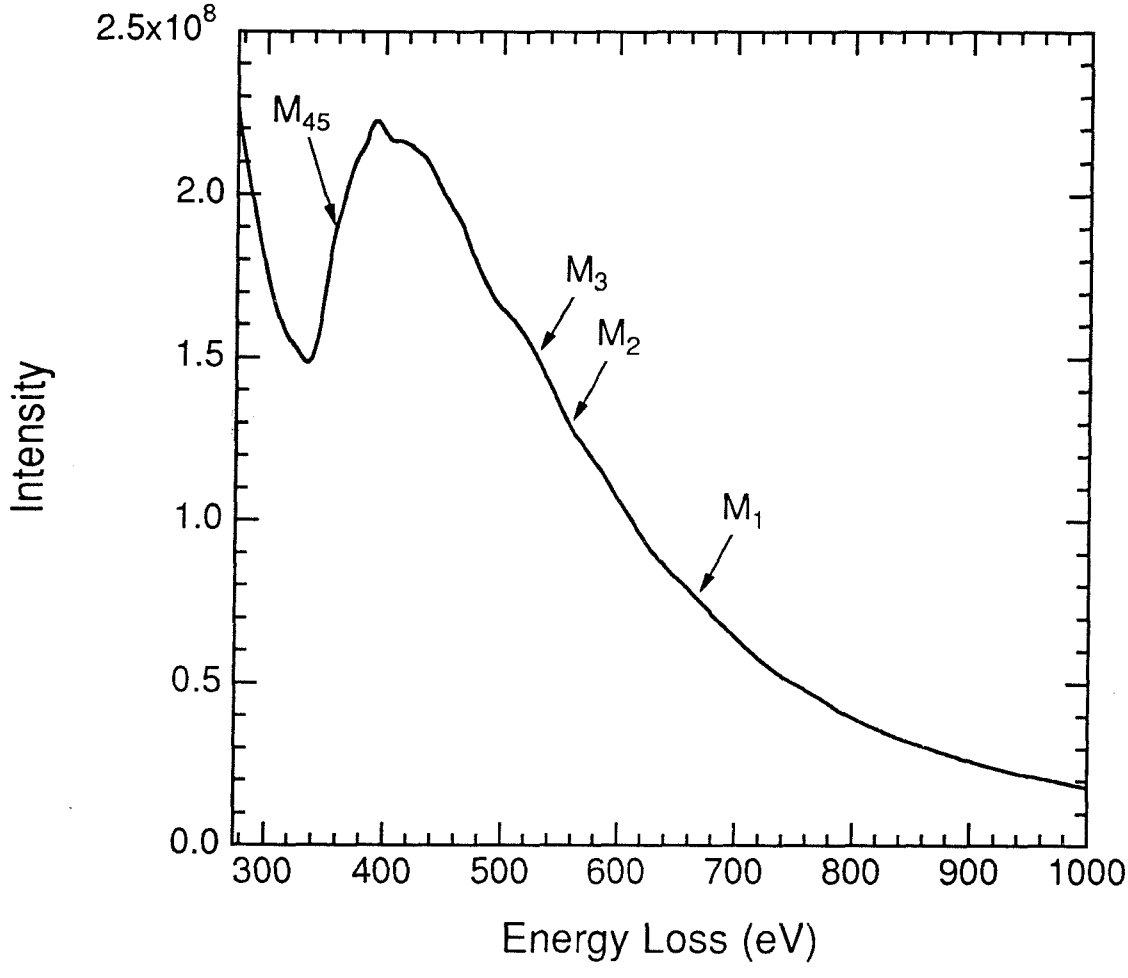

Figure 4.25. EELS measurement of Pd M edge from foil of pure Pd metal. Spectrum was not deconvoluted. Sample thickness roughly 0.6 times mean free path for inelastic scattering.

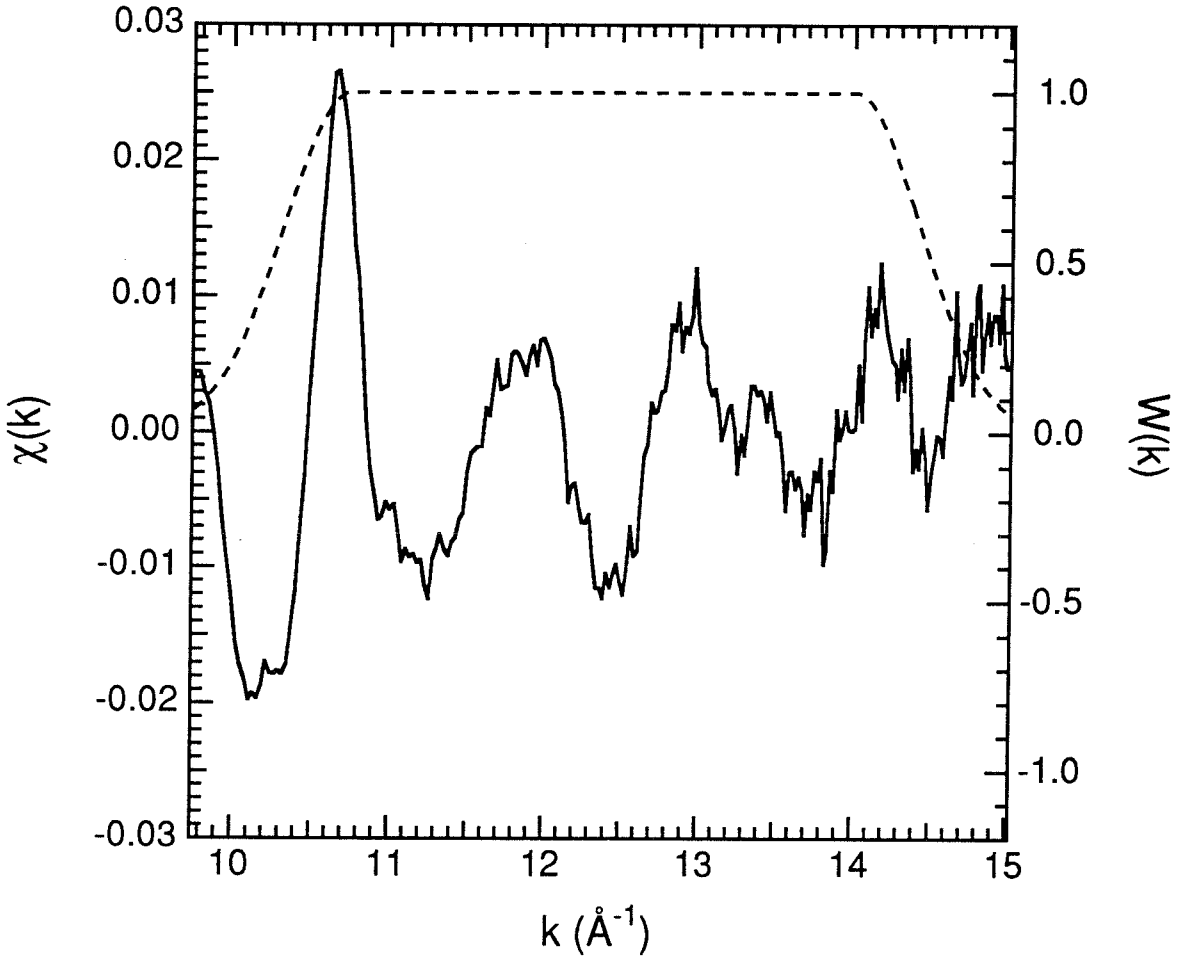

Figure 4.26. Pd M_{45}-edge EXELFS from Pd metal (solid line). Also shown is window for FT (dashed line). Data taken at 98 K.

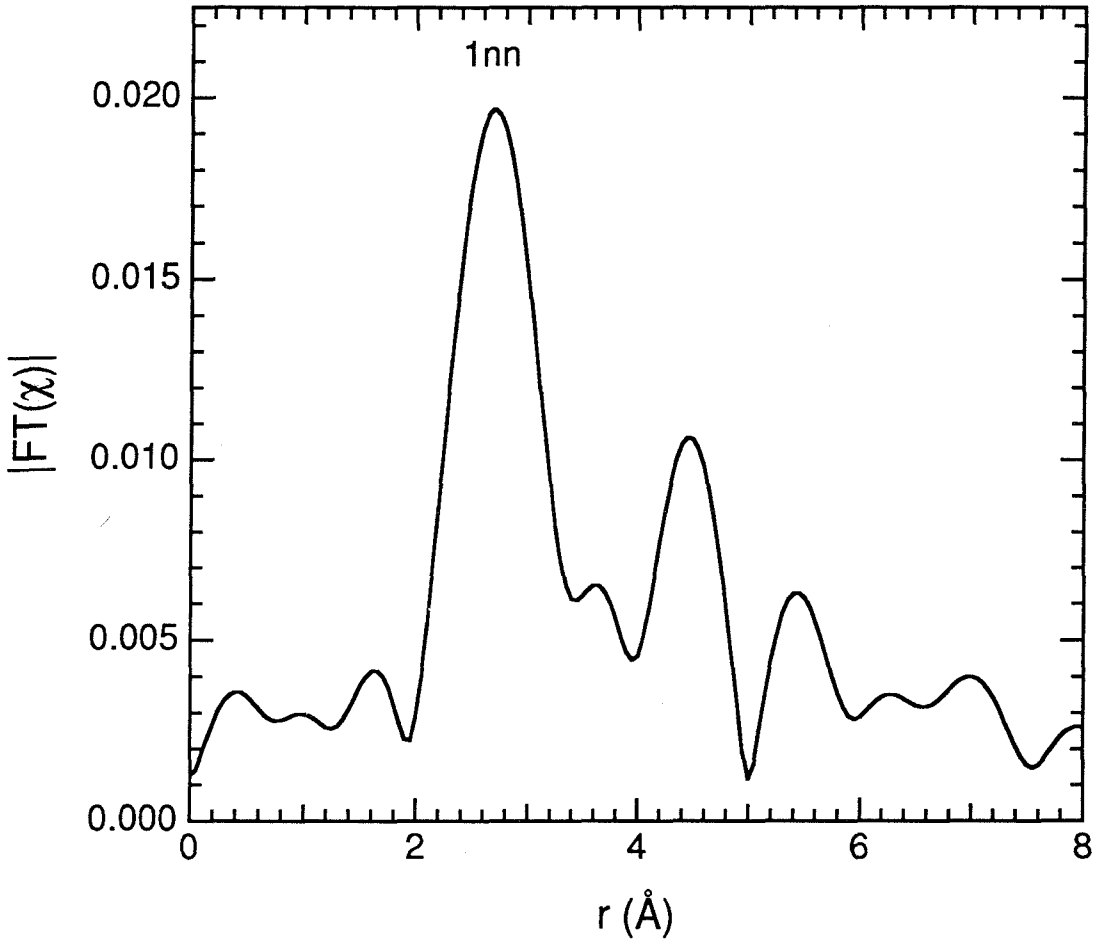

Figure 4.27. Magnitude of Fourier transform of Pd M_{45}-edge EXELFS from Pd metal. Data taken at 98 K.

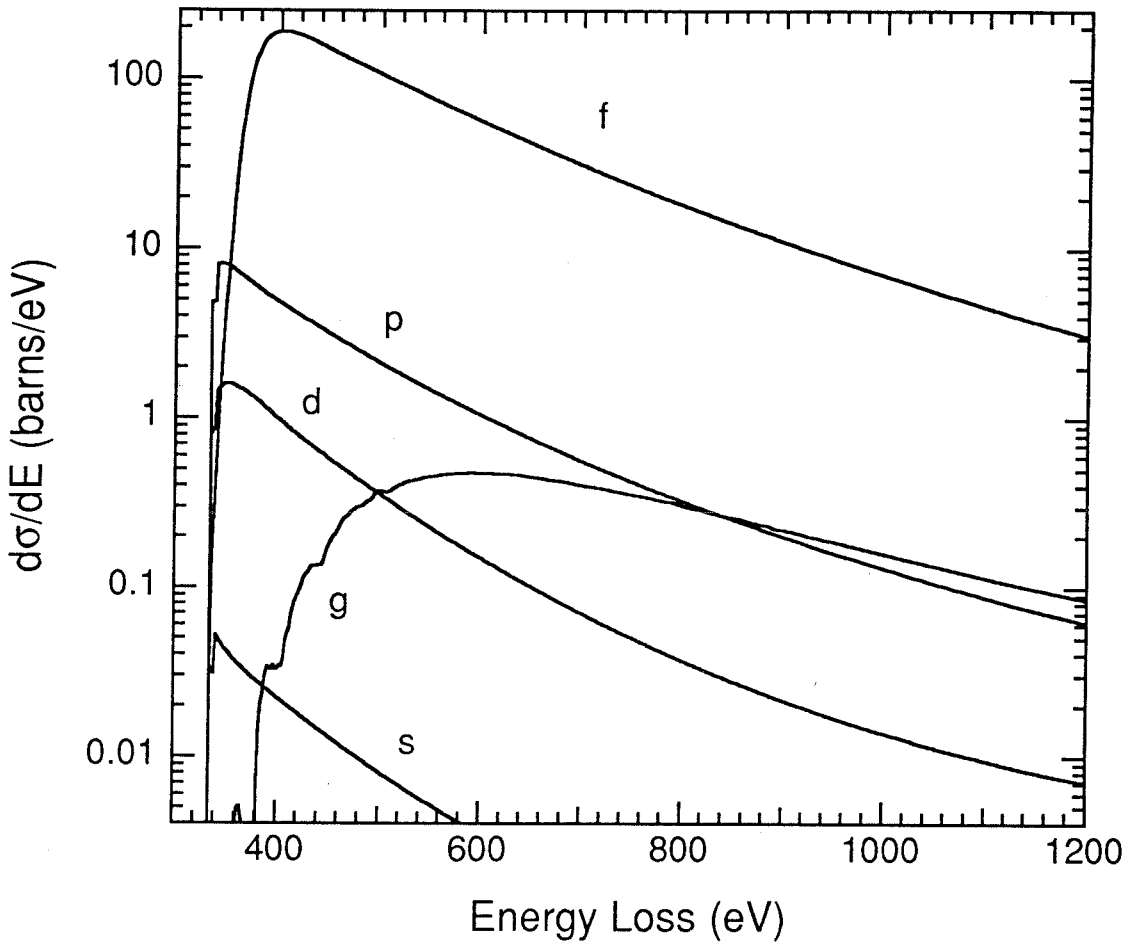

Figure 4.28. Partial energy-differential cross sections of Pd M_{45} edge. Letters indicate angular momentum of final state. Energy of incident beam = 200 keV. Collection semiangle = 5 mrad.

Having shown that transitions to final states of f character dominate over all others for the Pd M_{45} edge, now consider the complications arising from the presence of different initial states in the Pd M edge. The spin-orbit splitting between the M_5 and M_4 edges of about 5 eV has very little effect because it is much smaller than the spacing between the EXELFS maxima far above the ionization threshold energy. The M_{23} and M_1 edge jumps are removed from the M_{45} EXELFS signal by transforming only data sufficiently past the M_1 edge jump. Figure 4.29 compares the energy-differential cross sections of the Pd M_{45}, M_{23}, and M_1 edges. In the experimental EXELFS region, the Pd M_{45} edge is about three times larger than the M_3 edge, six times larger than the M_2 edge, and eight times larger than the M_1 edge.

Figure 4.30 displays the theoretical M_{45}, M_3, M_2, and M_1 EXELFS signals from the 1nn shell in Pd metal. The theoretical EXELFS were generated using $f(\pi,k)$ from Teo and Lee (1979), and $\delta_1(k)$, $\delta_2(k)$, and $\delta_3(k)$ from my Hartree-Slater calculations presented in §A.2. The following were also assumed: $S(k) = 0.7$; $\lambda(k)$ followed Equation (2.51) with C=1, D=3, and n=1.2; and $\sigma^2 = 0.002$ Å^2. The results of §5.3 were used to choose the value for σ^2.

Figure 4.31 presents the sum of the four theoretical EXELFS signals and superimposes the experimental EXELFS for comparison. The periodicity and phase of the theoretical and experimental oscillations compare reasonably well. Figure 4.32 displays the magnitude of the FT. The main peak in the theoretical spectrum is at r = 2.76 Å which is close to the experimental peak position of r = 2.68 Å. The theoretical spectrum also has a smaller peak near 3.9 Å which overlaps with the expected position of the 2nn peak. Figure 4.33 displays the EXELFS oscillations after the inverse FT. The amplitude of the theoretical oscillation is seen to be considerably greater than that of the experimental

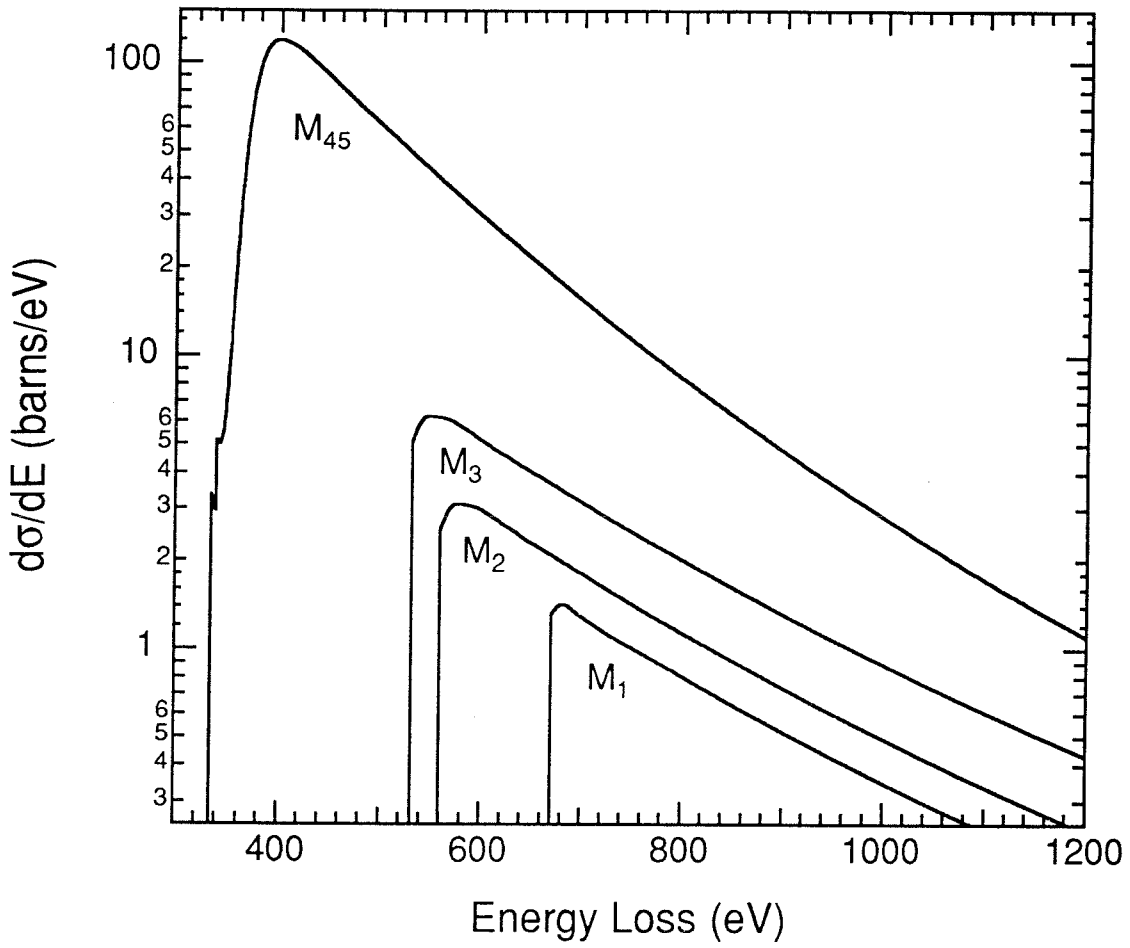

Figure 4.29. Energy-differential cross sections of Pd M_{45}, M_3, M_2, and M_1 edges. Energy of incident beam = 200 keV. Collection semiangle = 5 mrad.

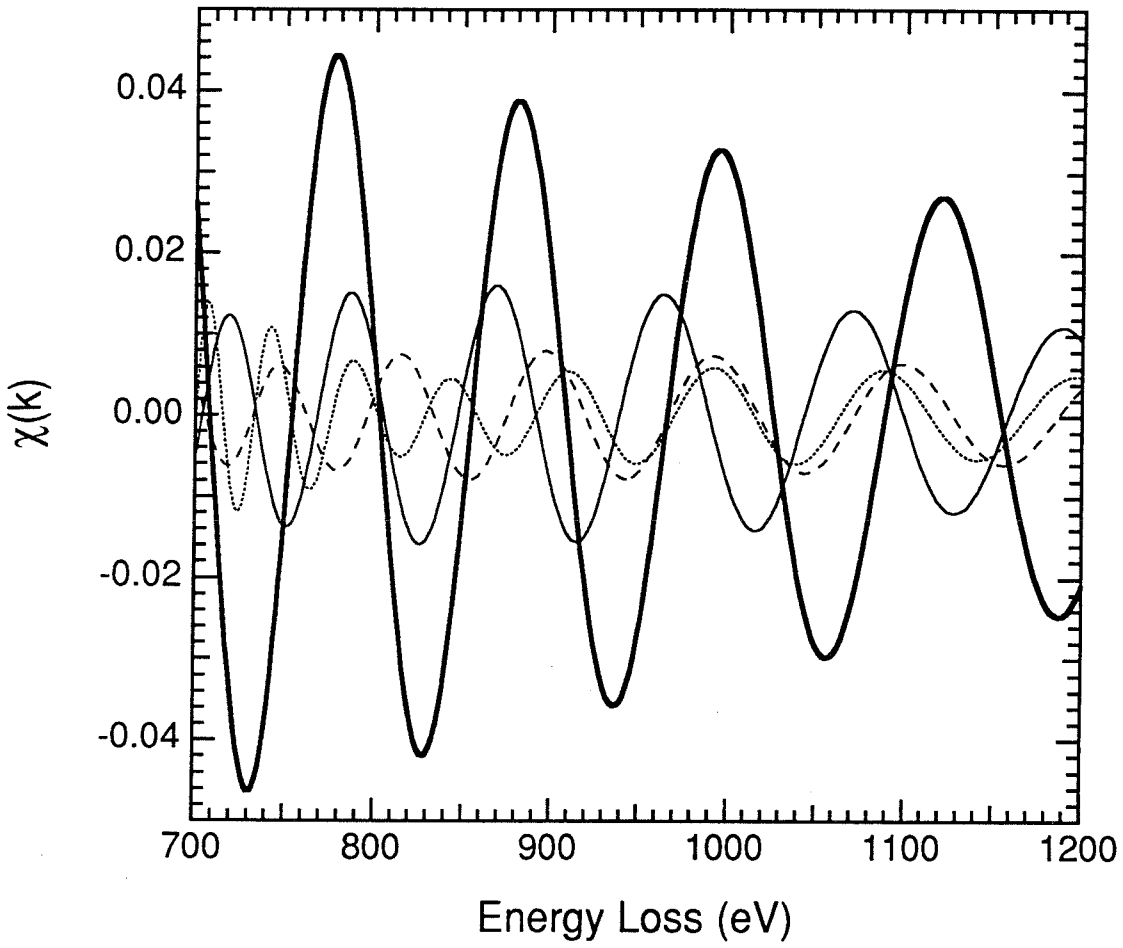

Figure 4.30. Theoretical Pd M_{45} (thick line), M_3 (thin line), M_2 (dashed line), and M_1 (dotted line) EXELFS due to 1nn shell in Pd metal.

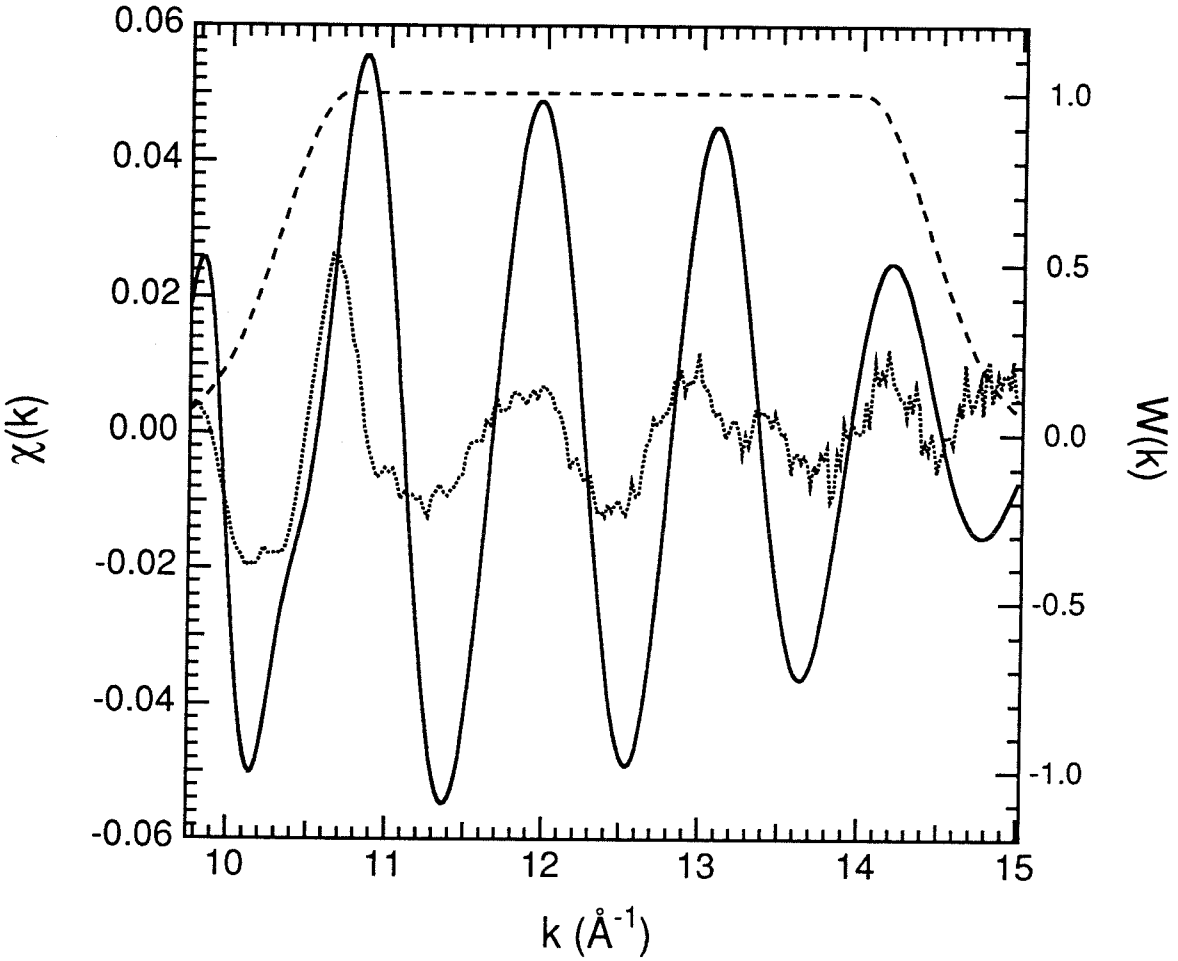

Figure 4.31. Theoretical (solid line) and experimental (dotted line) Pd M_{45}-edge EXELFS. Also shown is window for Fourier transform (dashed line).

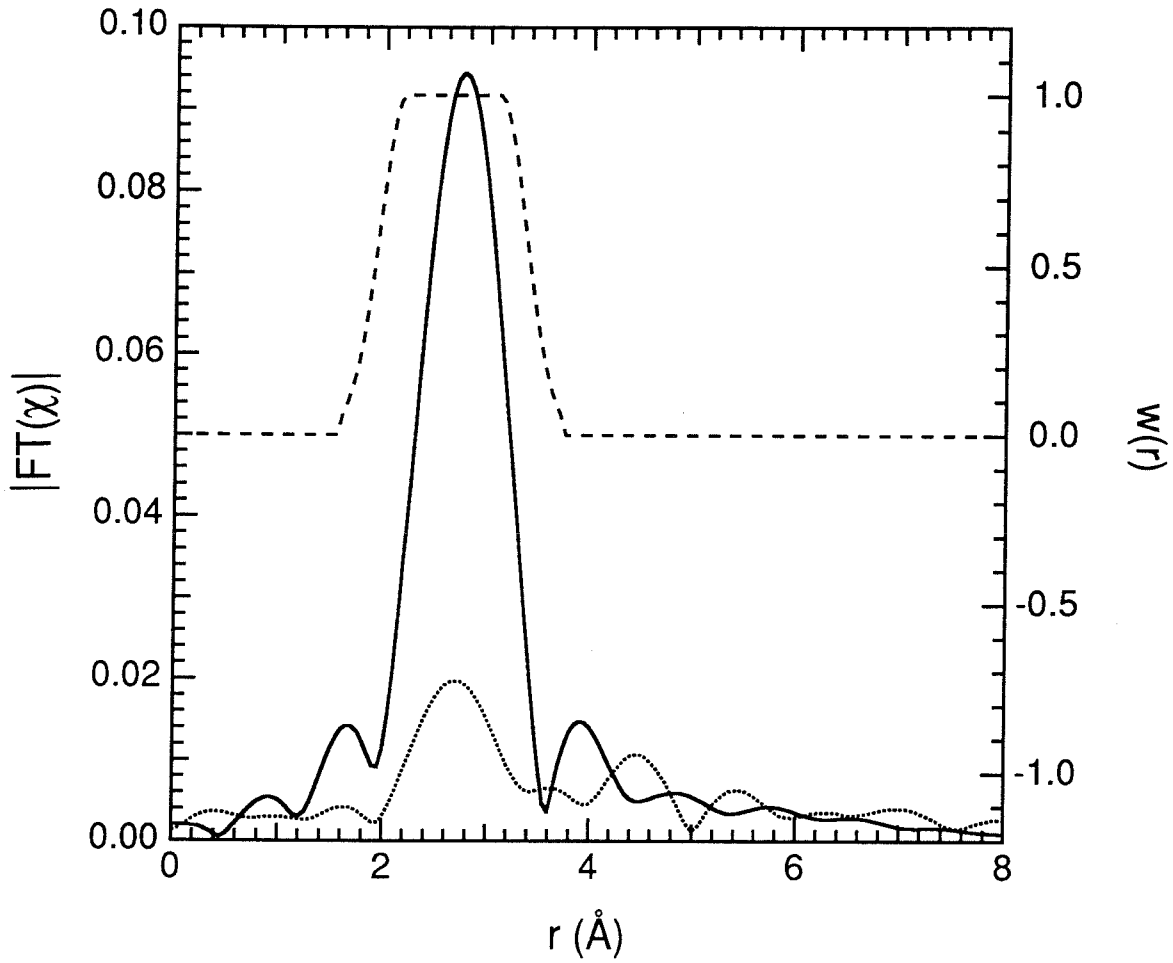

Figure 4.32. Magnitude of FT of theoretical (solid line) and experimental (dotted line) Pd M_{45}-edge EXELFS. Also shown is window for inverse FT (dashed line).

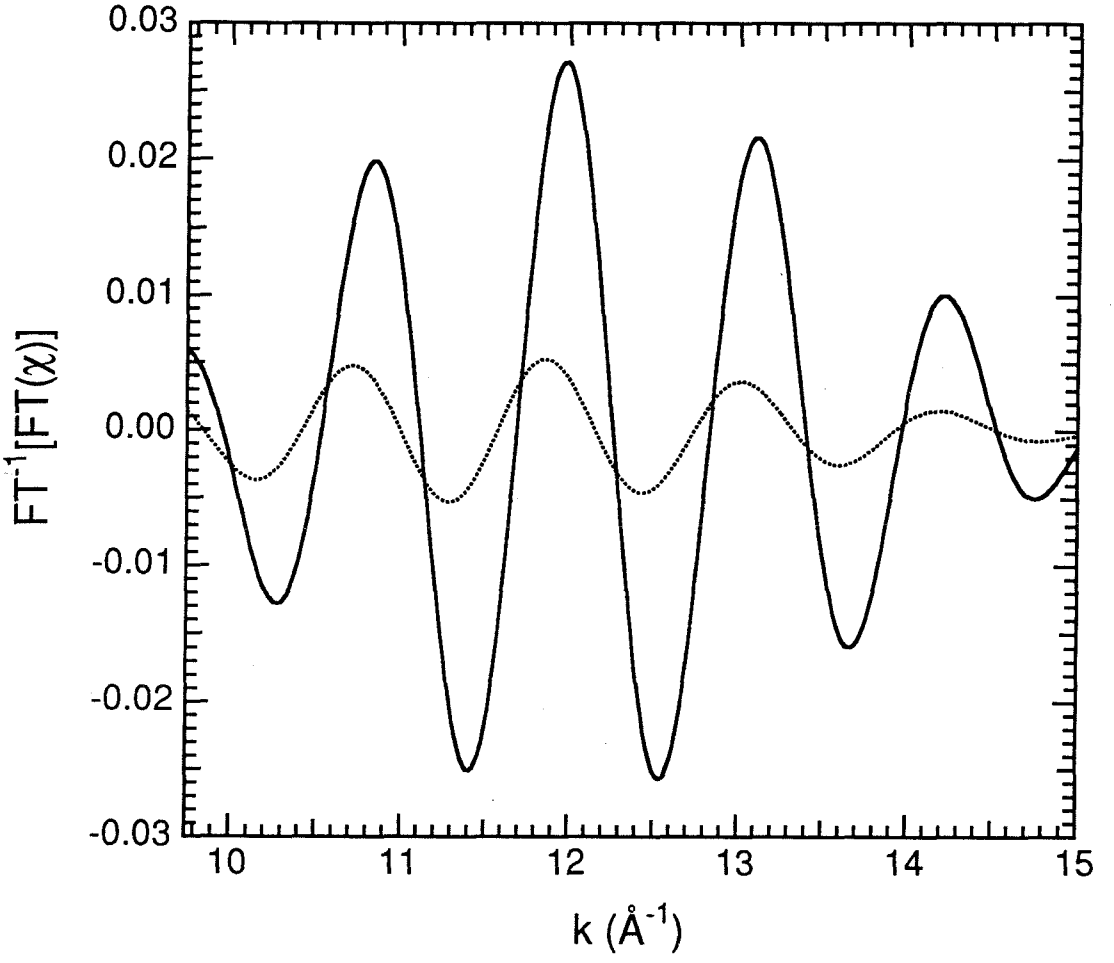

Figure 4.33. Fourier filtered theoretical (solid line) and experimental (dotted line) Pd M_{45}-edge EXELFS.

oscillation. This disparity is not surprising because of the somewhat arbitrary normalizations of both the theoretical and experimental EXELFS signals.

In conclusion, the cross-section for high energy electron scattering makes EELS possible only for core edges at energy losses below about 5 keV (Ahn and Krivanek, 1983). Only elements lighter than vanadium (Z = 23) have K edges below 5 keV. This does not, however, limit EXELFS experiments to only elements of low atomic number. As this section has shown, useful EXELFS information can be extracted from L_{23} and M_{45} edges as well. The use of L_{23} and M_{45} edges opens up most of the periodic table to possible EXELFS experiments.

Nearest-neighbor distances in Al, Fe, and Pd have been determined using EXELFS which agree with x-ray diffraction results (Ashcroft and Mermin, 1976) to within ± 0.1 Å. Distances to more distant neighbor shells, however, are probably not reliable. It should be pointed out that diffraction is, of course, far superior than EXELFS for determining distances in crystalline solids, which have long-range order. EXELFS is useful because it has the ability to measure short-range order.

4.3 Effect of Multiple Inelastic Scattering on EXELFS

§2.1.3 described the use of Fourier transform deconvolution methods to remove multiple inelastic scattering from energy-loss spectra. However, this section shows that unless the TEM sample is exceedingly thick, useful EXELFS information can be obtained without prior deconvolution of the energy-loss spectrum.

The simulation presented in Figures 4.34 through 4.37 demonstrates the effect of multiple inelastic scattering on a hypothetical inner-shell edge and its extended fine structure. To simplify the simulation, perfect instrumental

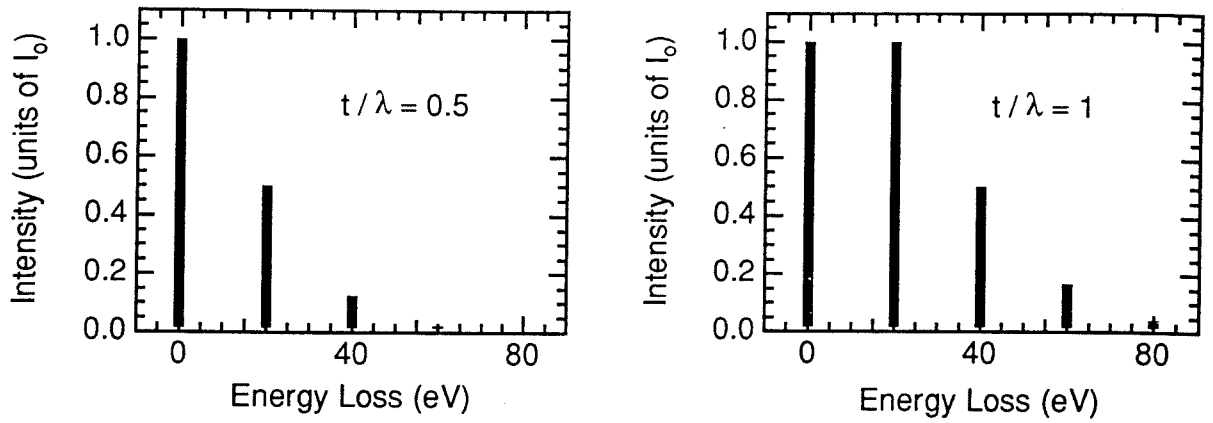

Figure 4.34. Idealized low-loss spectra used to simulate the effect of multiple inelastic scattering. Low-loss spectra for two different sample thicknesses are shown.

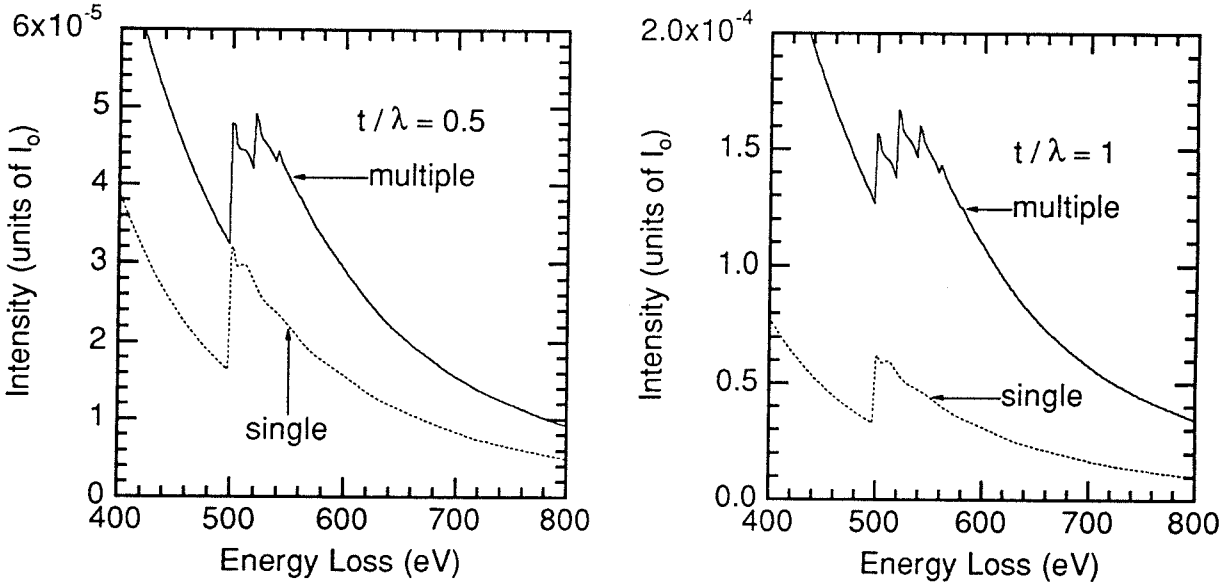

Figure 4.35. Simulated effect of multiple inelastic scattering on the general shape of a hypothetical inner-shell edge. Multiple-scattering (solid line) and single-scattering (dotted line) spectra are shown for two different sample thicknesses.

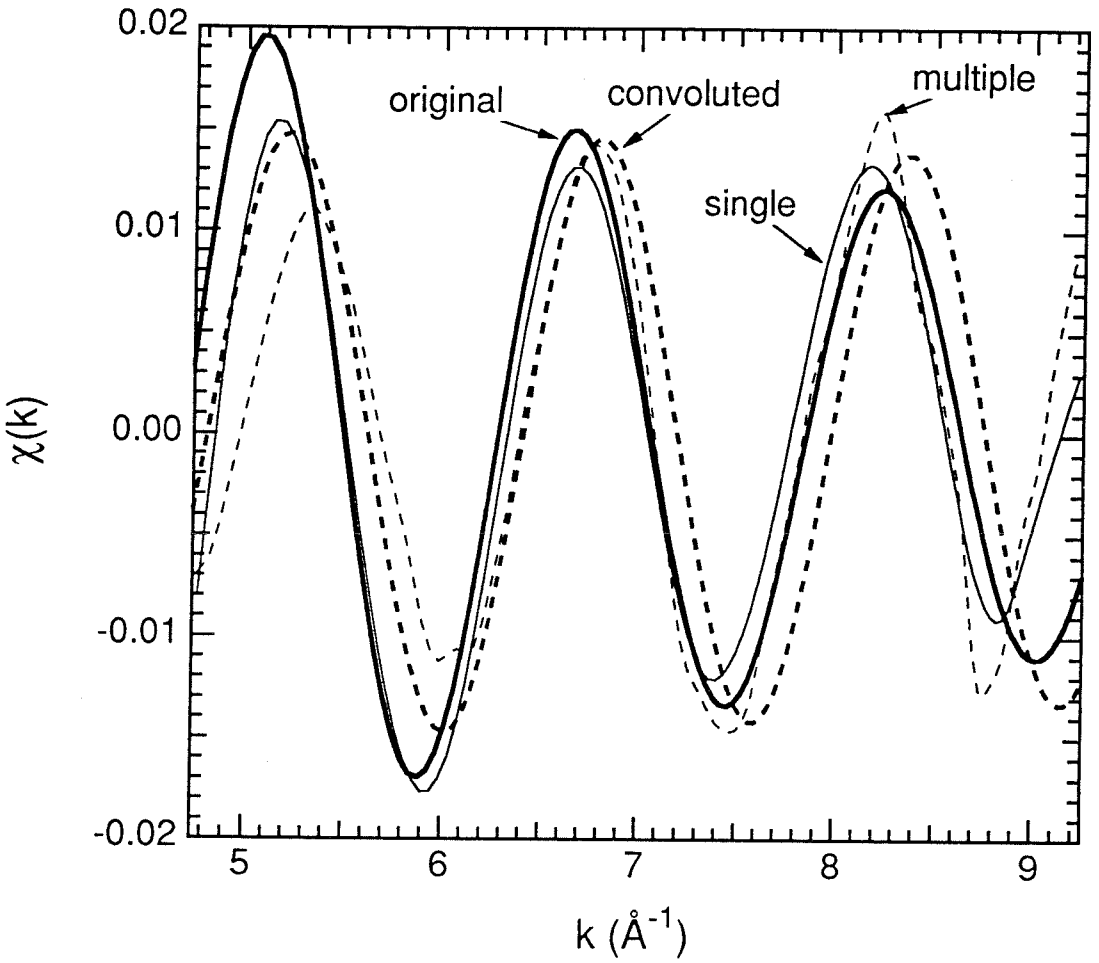

Figure 4.36. Simulated EXELFS extracted from single-scattering (thin solid) and multiple-scattering (thin dashed) spectra. Also shown is EXELFS originally superimposed on edge (thick solid) and original EXELFS convoluted with low-loss (thick dashed). $t / \lambda = 0.5$ assumed.

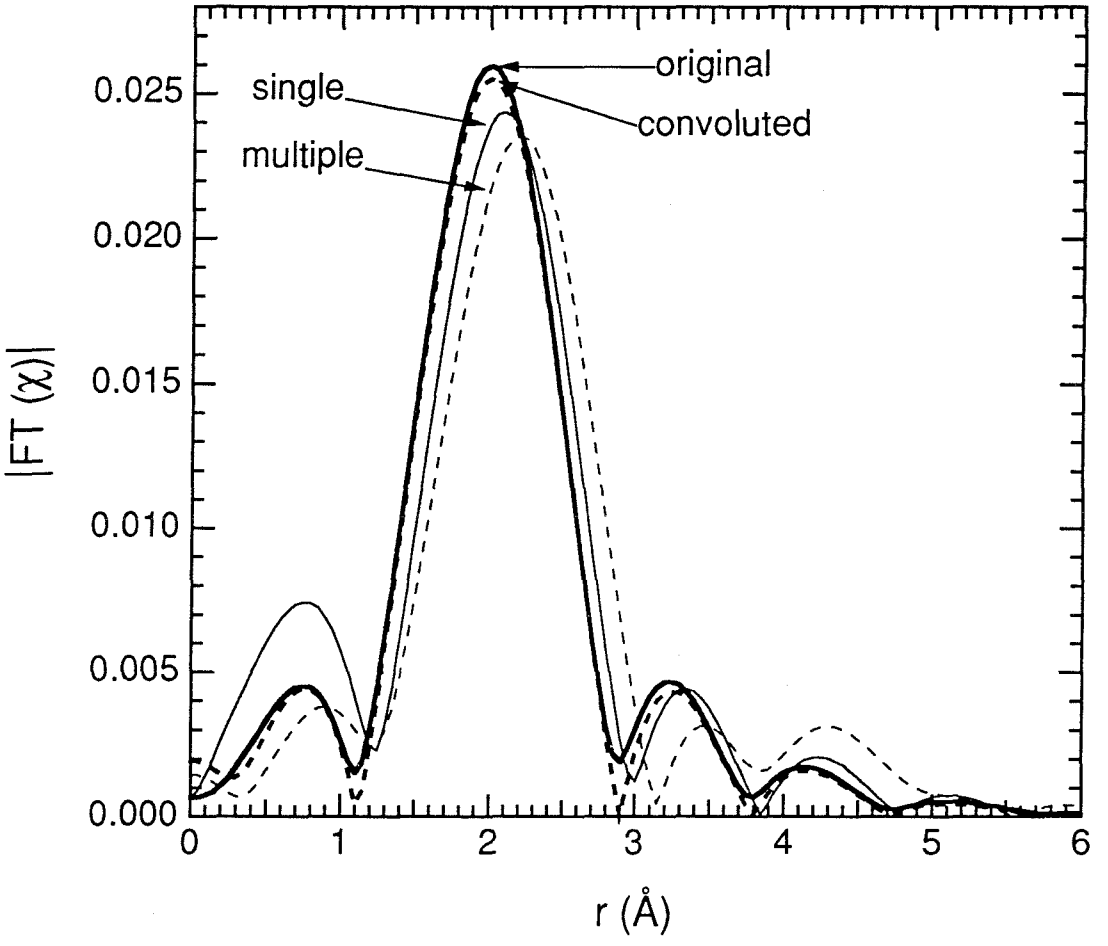

Figure 4.37. Magnitude of FT of simulated EXELFS extracted from single-scattering (thin solid) and multiple-scattering (thin dashed) spectra. Also shown is magnitude of FT of EXELFS originally superimposed on edge (thick solid) and original EXELFS convoluted with low-loss (thick dashed). Data in range from $5.25 < k < 8.75$ Å^{-1} were transformed.

resolution was assumed, i.e., $Z(E) = I_0\,\delta(E)$. A hypothetical single-scattering distribution, S(E), was constructed. The low-loss region was assumed to contain a single outer-shell scattering process with an energy of exactly 20 eV. The inner-shell edge and the background were calculated from the power law AE^{-4}, and the edge-to-background ratio in the single-scattering distribution was assumed to be unity. Extended fine structure from a single nearest-neighbor shell of atoms was superimposed upon the edge in the single-scattering distribution. The extended fine structure was calculated using the following simple equation:

$$\chi(k) = \frac{0.1}{k}\sin(2kR_{1nn}) \qquad (4.6)$$

where $\chi(k)$ is the EXELFS oscillation normalized to the non-oscillatory part of the edge intensity, $R_{1nn} = 2$ Å is a hypothetical 1nn peak position, and 0.1 is an arbitrarily chosen factor.

Figure 4.34 displays the idealized low-loss spectrum using two different sample thicknesses. The hypothetical inner-shell edge with and without multiple inelastic scattering is displayed in Figure 4.35. Figure 4.35 shows that the primary effect of multiple inelastic scattering on inner-shell edges is the presence of successively smaller "steps" in intensity above the edge. The first step above the edge (at 20 eV past the edge onset) is due to double inelastic scattering processes, the second step above the edge is due to triple inelastic scattering processes, and so on. Of course, for actual spectra these steps are rounded because the low-loss peaks are considerably broadened. Nevertheless, the simulation shows that while the multiple inelastic scattering steps affect strongly the near-edge structure, the steps are negligible in the

region more than 100 eV beyond the edge onset (corresponding to $k > 5$ Å^{-1}). It is possible, however, that the extended fine structure superimposed upon the steps may contribute incoherent higher-frequency oscillations to the EXELFS signal.

Using the procedure detailed in §4.1, EXELFS signals were extracted from the multiple-scattering spectrum with $t / \lambda = 0.5$ and from the single-scattering distribution. Figure 4.36 displays the two extracted EXELFS signals, along with the EXELFS that was originally superimposed upon the edge and the original EXELFS convoluted with the low-loss. The periodicity and phase of the four signals are seen to be very similar. From the figure, it can be deduced that the multiple-scattering signal is, in effect, the single-scattering signal convoluted with the low-loss. This results in a reduced signal at low k, where the multiple-scattering and single-scattering signals are out of phase, and an enhanced signal at higher k, as the signals become more in phase. Figure 4.37 shows the Fourier transforms of the four EXELFS signals. Each transform has a peak centered near 2 Å. The peak extracted from the single-scattering spectrum is shifted only by about +0.1 Å from the peak corresponding to the original oscillation. Since the EXELFS technique can generally determine radial distances to only within approximately ±0.1 Å, this small shift in peak position is within the expected error. The peak extracted from the multiple-scattering spectrum is shifted by about +0.1 Å from the peak extracted from the single-scattering spectrum.

The preceding simulation demonstrated that useful EXELFS data can, in principle, be extracted without prior deconvolution of the EELS spectrum. The following analysis of actual experimental data shows that this is true in practice as well. Experimentally, EELS spectra covering the range below about 2 keV in

energy loss were collected from a relatively thick sample of Fe_3Al. The sample thickness was approximately 1.1 times the mean free path for inelastic scattering, i.e., $t/\lambda = 1.1$. Channel-to-channel gain variations in the parallel detector were compensated using the procedure given in §3.4. Multiple inelastic scattering was removed using a Fourier-log deconvolution procedure. In the deconvolution procedure, high-frequency noise amplification was reduced by reconvolving the single-scattering distribution with a unit area Gaussian function whose full width at half maximum (FWHM) was 4 eV. The FWHM was chosen to be approximately equal to the instrumental resolution.

Figures 4.38 through 4.40 display the three relevant regions in the EELS data both before and after Fourier-log deconvolution. The low loss region is displayed in Figure 4.38, the Fe L_{23} edge in Figure 4.39, and the Al K edge in Figure 4.40. After deconvolution, one can more clearly see the Fe M_{23} edge at 54 eV in Figure 4.38 and the "white lines" on the Fe L_{23} edge in Figure 4.39. The small edge-to-background ratio makes it difficult to see any details on top of the Al K edges in Figure 4.40. To better resolve the structure of the Al K edges, Figure 4.41 displays the Al K edge data after background subtraction. Without the background intensity, the Al K edges are effectively magnified. As Figure 4.41 shows, although the overall shapes of the Al K edges before and after deconvolution are very different, the EXELFS oscillations superimposed on the edges are remarkably similar.

For a more quantitative analysis, EXELFS data were extracted from the multiple-scattering and single-scattering spectra using the procedure explained in §4.1. Figure 4.42 presents the Fe L_{23}-edge EXELFS data. Notice that the two sets of data follow the same general pattern, regardless of whether they were extracted from multiple-scattering or single-scattering spectra. Apparently,

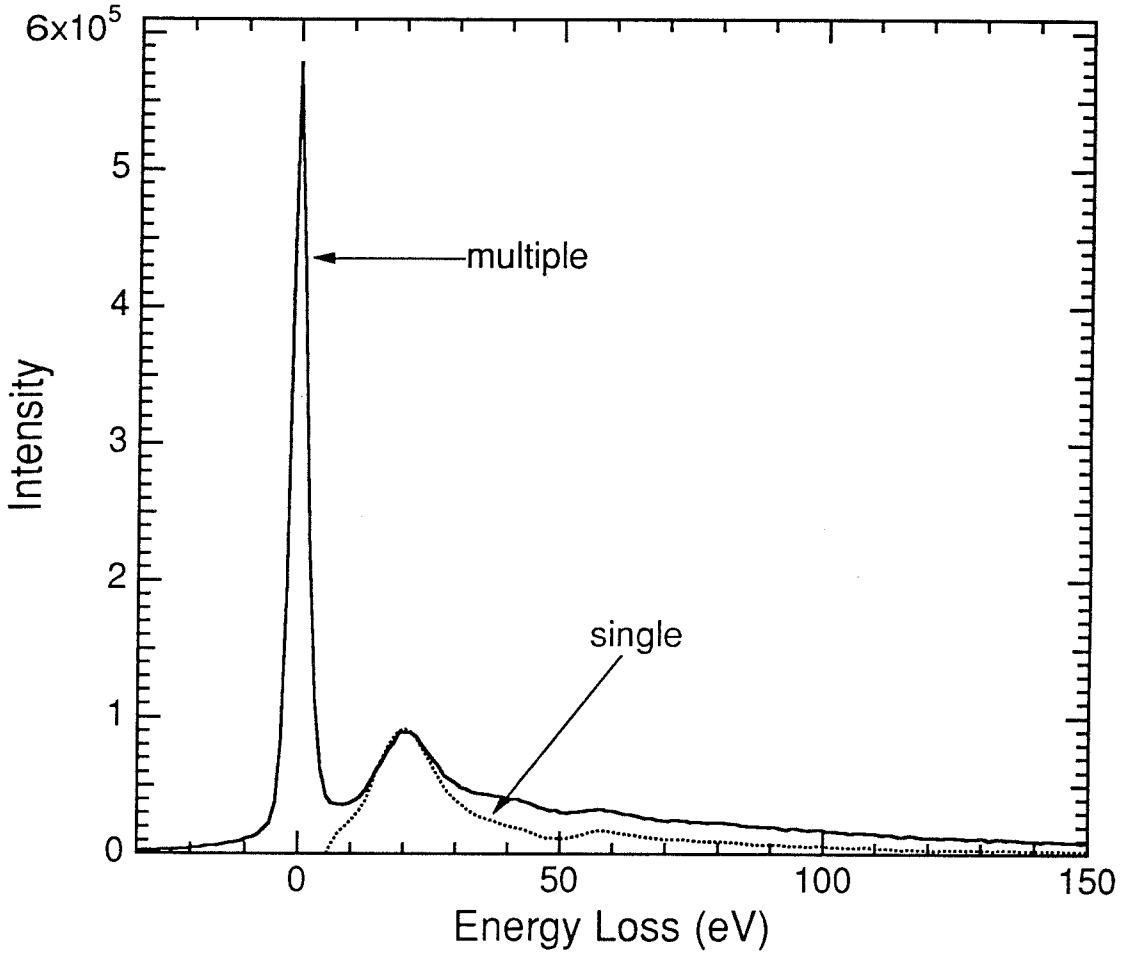

Figure 4.38. Low loss region from multiple-scattering (solid line) and single-scattering (dotted line) spectra of Fe_3Al.

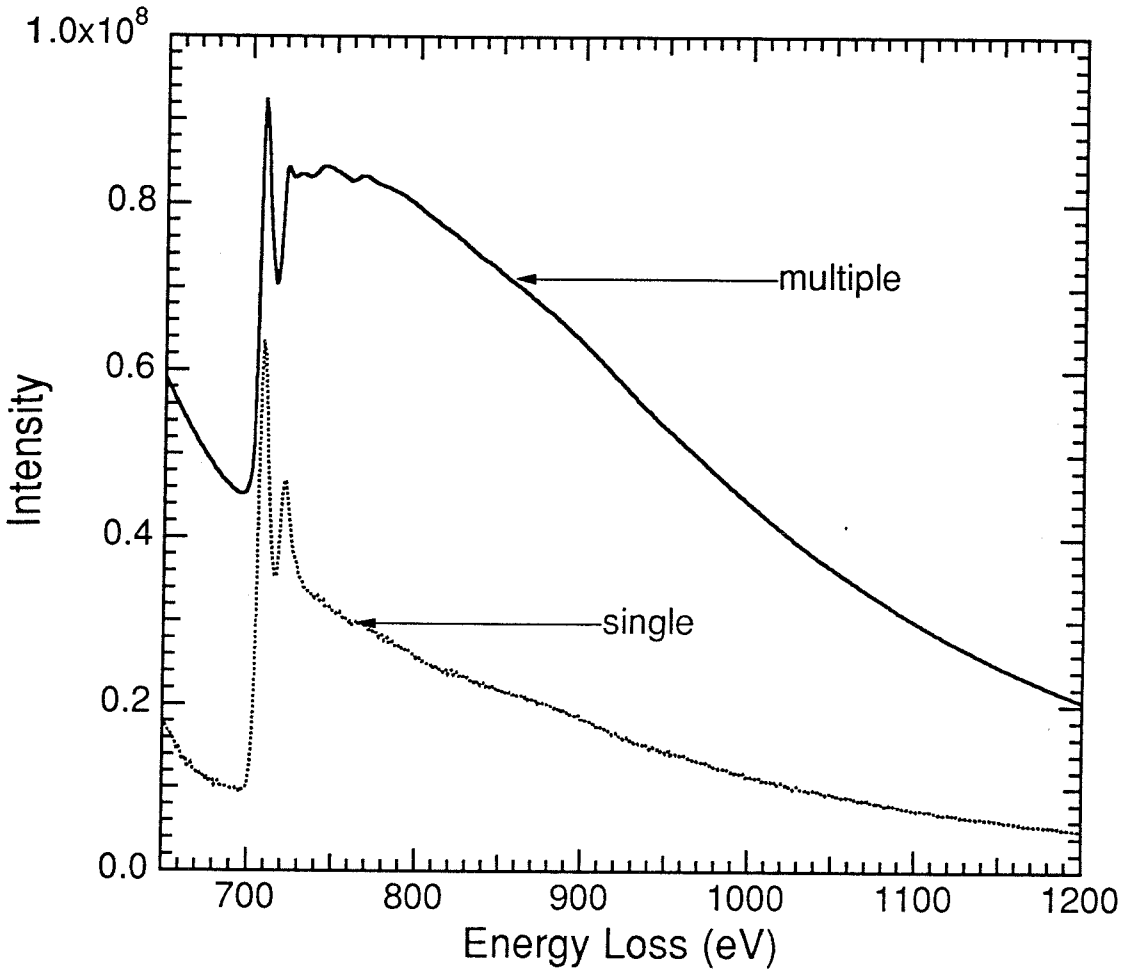

Figure 4.39. Fe L_{23} edge from multiple-scattering (solid line) and single-scattering (dotted line) spectra of Fe_3Al.

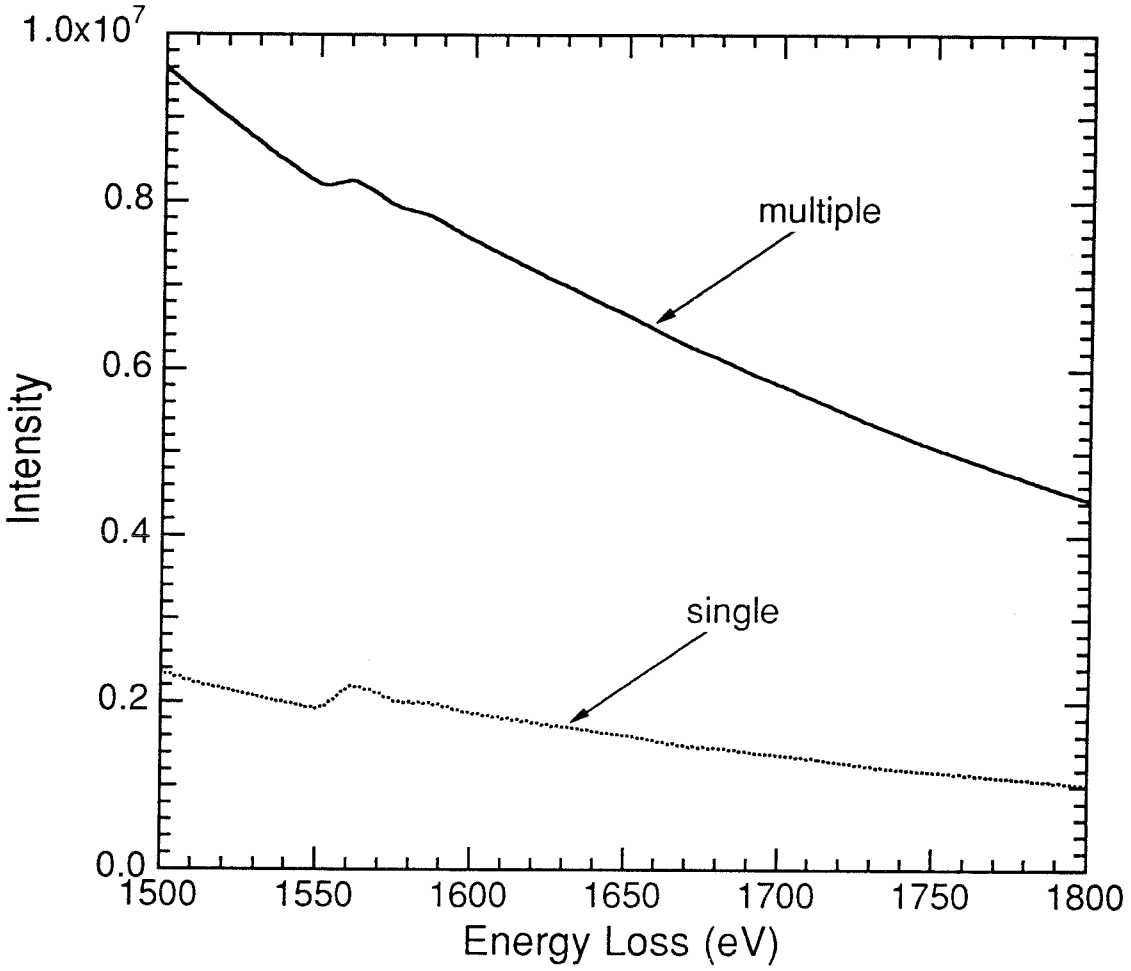

Figure 4.40. Al K edge from multiple-scattering (solid line) and single-scattering (dotted line) spectra of Fe_3Al.

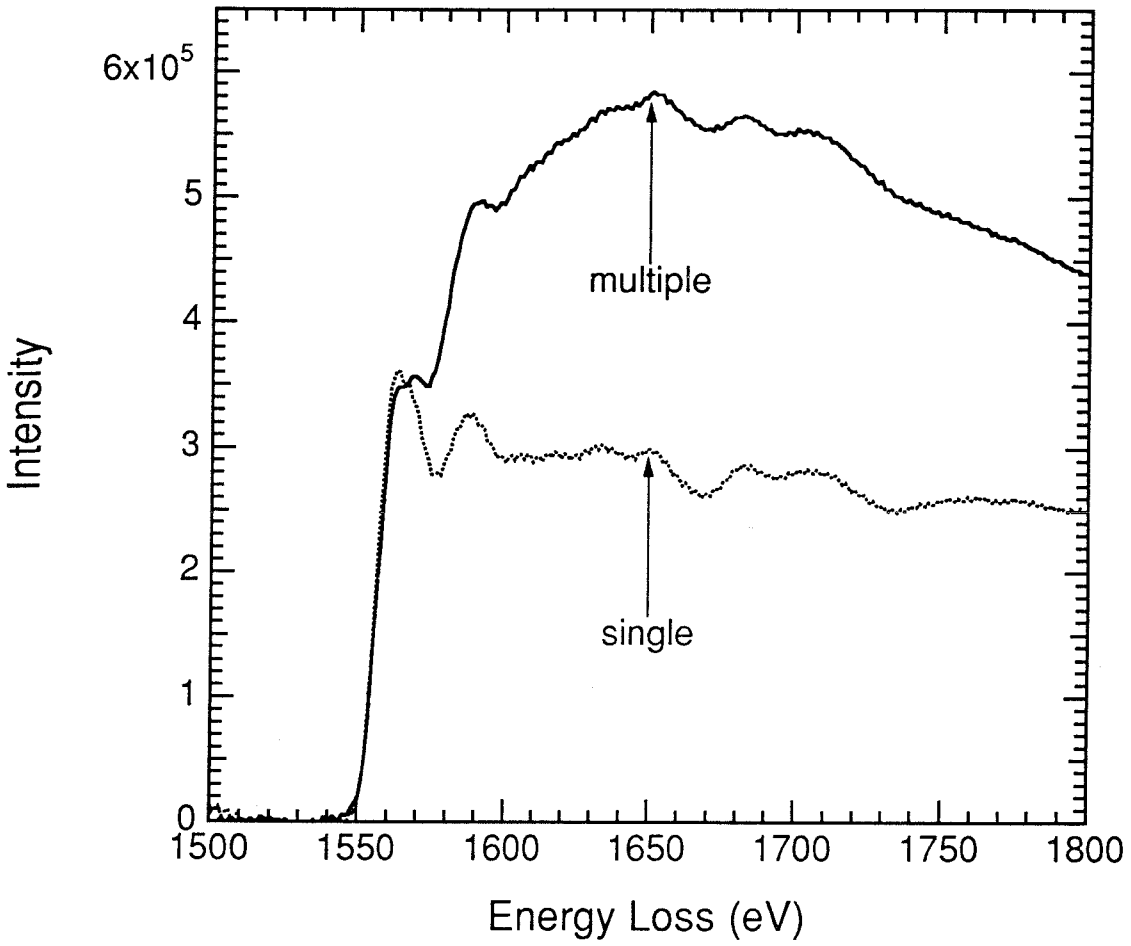

Figure 4.41. Background subtracted Al K edge from multiple-scattering (solid line) and single-scattering (dotted line) spectra of Fe_3Al.

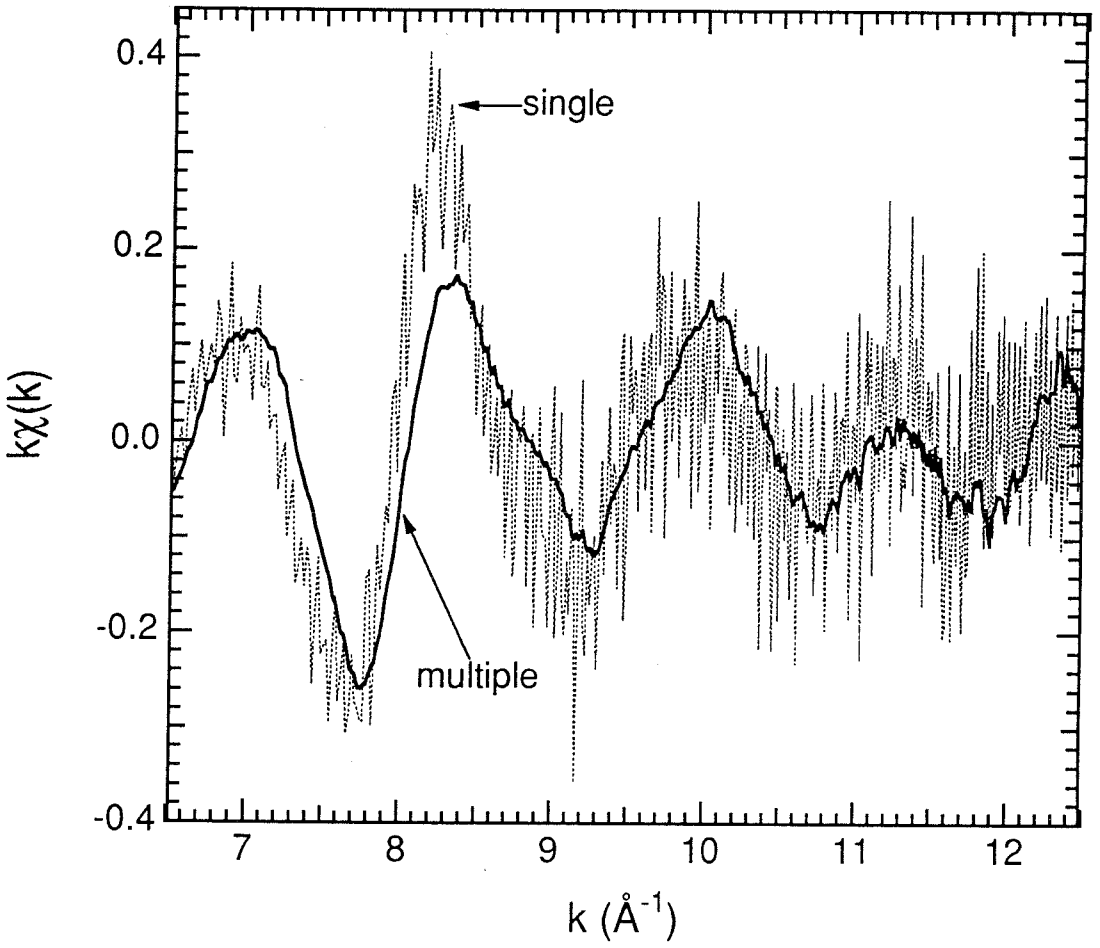

Figure 4.42. Fe L_{23}-edge EXELFS from multiple-scattering (solid line) and single-scattering (dotted line) spectra of Fe_3Al. Both signals have been "smoothed" to somewhat reduce noise.

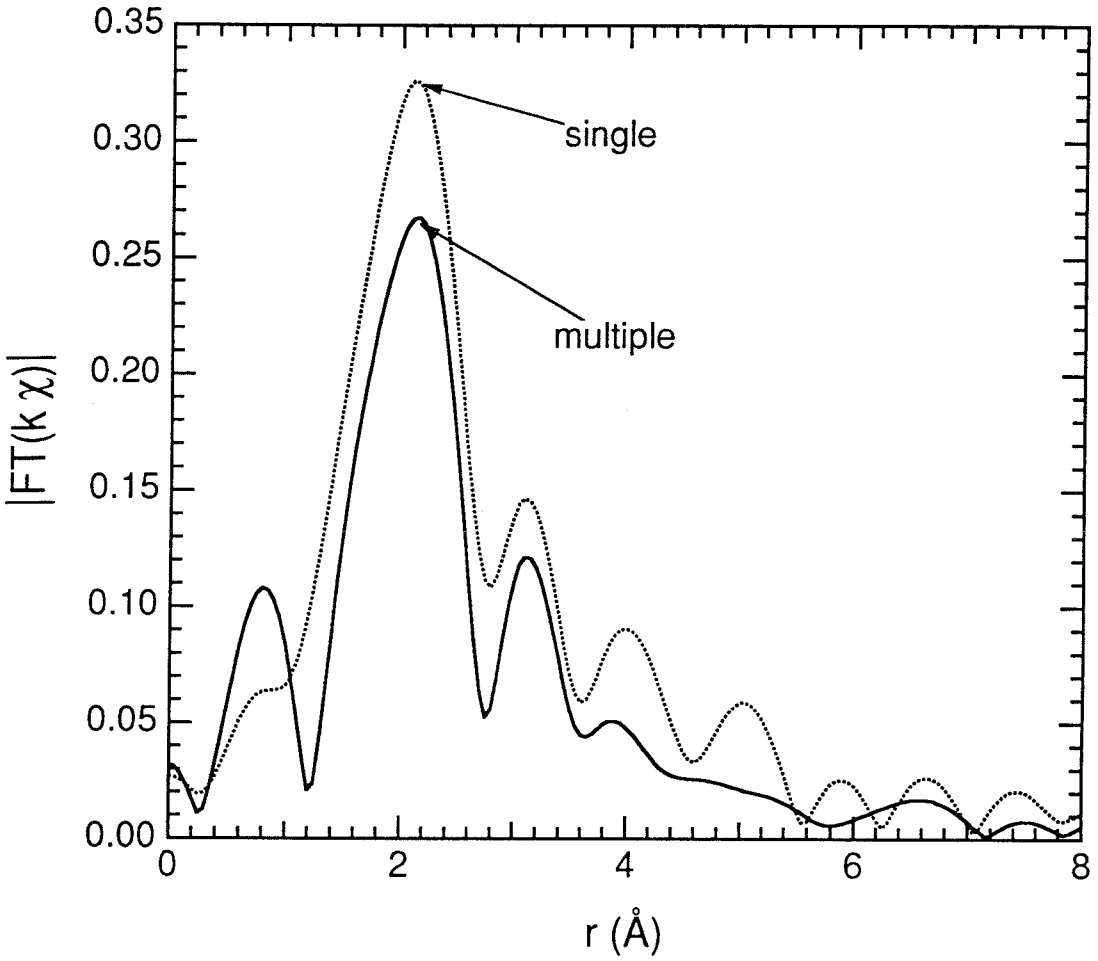

Figure 4.43. Fourier transforms of Fe L_{23}-edge EXELFS from multiple-scattering (solid line) and single-scattering (dotted line) spectra of Fe_3Al. Data in the range $7 < k < 12$ Å^{-1} were transformed.

the main difference between them is that the single-scattering data has a greater amount of high-frequency noise. As discussed in §2.1.3, a side-effect of the Fourier-log deconvolution procedure is the amplification of high frequency noise in the single-scattering spectrum.

Figure 4.43 displays the magnitude of the FT of the Fe L_{23}-edge EXELFS data. Notice the similarities between the transforms of both the multiple-scattering and single-scattering data. Each transform has a 1nn peak near 2.1 Å.

Figure 4.44 presents the Al K-edge EXELFS data. Both signals follow the same general pattern, although a greater amount of high-frequency noise is present in the single-scattering signal.

Figure 4.45 displays the magnitude of the FT of the Al K-edge EXELFS data. Both transforms contain a 1nn peak near 2.2 Å. In addition, the smaller peaks in the two transforms match well.

In conclusion, the analysis of both simulated and experimental data has shown that, unless the sample is exceedingly thick, useful EXELFS information can be obtained without first deconvolving the EELS spectrum. This is especially true for the experiments in this thesis which aim to measure only relative changes in the amplitude of the EXELFS oscillations as either the temperature or the state of SRO of the sample is varied, but the thickness is held constant.

On the other hand, deconvolution is important when comparing data from samples of different thicknesses. Deconvolution is also important when comparing EXELFS data with EXAFS data.

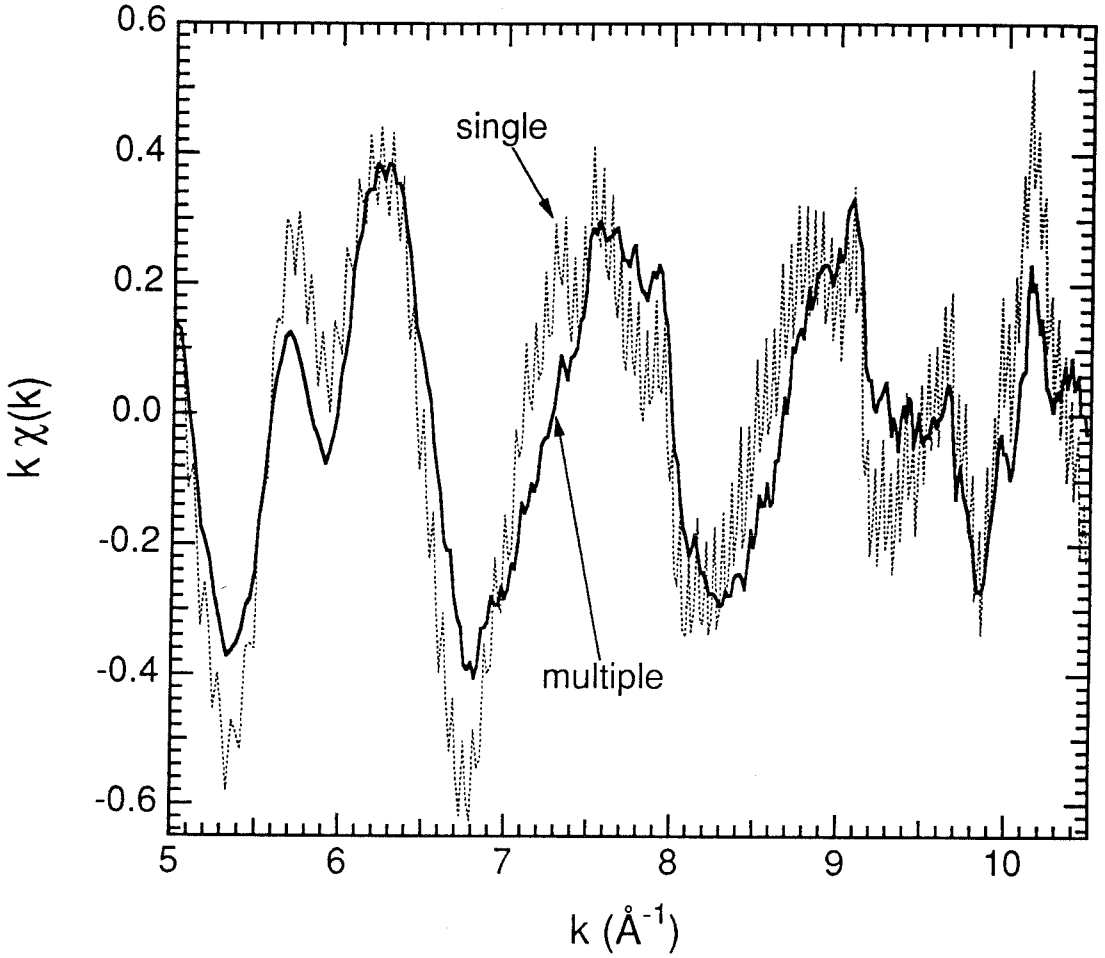

Figure 4.44. Al K-edge EXELFS from multiple-scattering (solid line) and single-scattering (dotted line) spectra of Fe_3Al. Both signals have been "smoothed" to somewhat reduce noise.

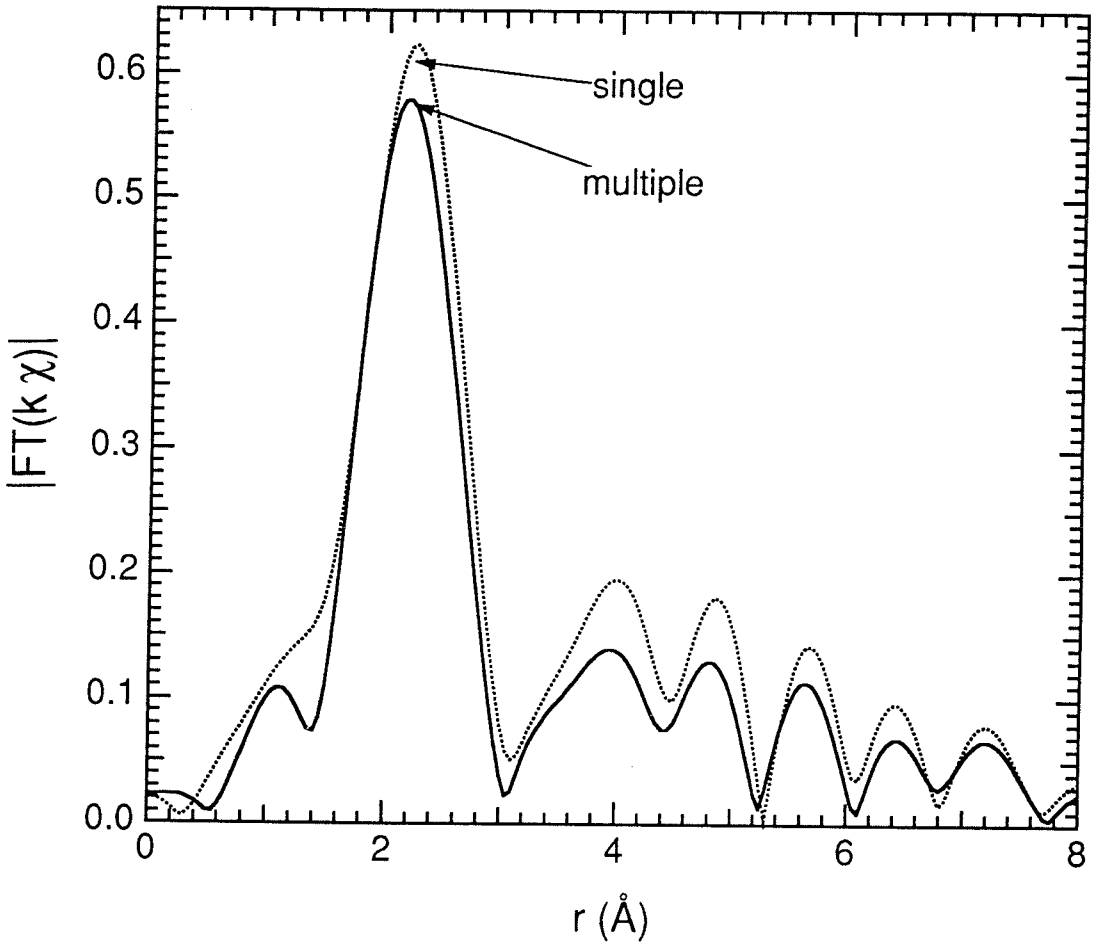

Figure 4.45. Magnitude of FT of Al K-edge EXELFS from multiple-scattering (solid line) and single-scattering (dotted line) spectra of Fe_3Al. Data in range $5.5 < k < 10$ Å^{-1} were transformed.

Chapter 5 Temperature-Dependent EXELFS of Elemental Metals

This chapter discusses the interpretation of my temperature-dependent EXELFS data from Al, Fe, and Pd metals. As temperature increases, vibrations between atoms in the sample increase. This causes a decrease in amplitude of the EXELFS oscillations which is accounted for in Equation (2.23) by the Debye-Waller type factor $\exp(-2\sigma_j^2 k^2)$, where σ_j^2 is the vibrational mean-square relative displacement (MSRD).

§5.1 contains a brief derivation of the Debye-Waller type factor. §5.2 then derives an expression for the vibrational MSRD as a function of the "projected" density of vibrational modes and contrasts the vibrational MSRD with the vibrational mean-square displacement (MSD). §5.3 discusses the force constant model of lattice dynamics. Finally, §5.4 presents my experimental data on elemental metals and analyzes them within the Einstein, Debye, and force constant models. Debye temperatures from my MSRD measurements are compared with published Debye temperatures from heat capacity measurements.

5.1 Debye-Waller Type Factor for EXELFS

This section briefly derives the Debye-Waller type factor for EXELFS. For simplicity consider "half" of the sine term in Equation (2.23):

$$\left\langle \exp\left(i2k\left|\mathbf{r}_j - \mathbf{r}_0\right|\right)\right\rangle \tag{5.1}$$

where $\mathbf{r}_0$ and $\mathbf{r}_j$ are the instantaneous position vectors of the central and neighboring atoms, respectively. The brackets $\langle\ \rangle$ represent averaging over an ensemble of systems. The amplitude-reducing terms of Equation (2.23) which

depend on the bond length $|\mathbf{r}_j - \mathbf{r}_0|$ can be neglected because they are less sensitive to small changes in the bond length. The sine term, on the other hand, is very sensitive to changes in the bond length because such changes affect the phase of the sinusoidal oscillation.

$|\mathbf{r}_j - \mathbf{r}_0|$ can be approximated to first-order by $\hat{\mathbf{R}}_j \cdot (\mathbf{r}_j - \mathbf{r}_0)$, where $\hat{\mathbf{R}}_j$ is the equilibrium direction between the central and neighboring atoms. Substituting this approximation into Equation (5.1) gives

$$\left\langle \exp\left(i2k\left|\mathbf{r}_j - \mathbf{r}_0\right|\right)\right\rangle \cong \left\langle \exp\left[i2k\hat{\mathbf{R}}_j \bullet \left(\mathbf{r}_j - \mathbf{r}_0\right)\right]\right\rangle \tag{5.2a}$$

$$= \left\langle \exp\left[i2k\hat{\mathbf{R}}_j \bullet \left(\mathbf{R}_j + \mathbf{u}_j - \mathbf{0} - \mathbf{u}_0\right)\right]\right\rangle \tag{5.2b}$$

$$= \exp(i2k\mathbf{R}_j)\left\langle \exp\left[i2k\hat{\mathbf{R}}_j \bullet \left(\mathbf{u}_j - \mathbf{u}_0\right)\right]\right\rangle \tag{5.2c}$$

where $\mathbf{u}_0$ and $\mathbf{u}_j$ are the instantaneous displacements of the central and neighboring atoms from their equilibrium positions at $\mathbf{0}$ and $\mathbf{R}_j$, respectively.

The second factor on the right-hand side of Equation (5.2c) can be expanded into a series:

$$\left\langle \exp\left[i2k\hat{\mathbf{R}}_j \bullet \left(\mathbf{u}_j - \mathbf{u}_0\right)\right]\right\rangle = 1 + i2k\left\langle \hat{\mathbf{R}}_j \bullet \left(\mathbf{u}_j - \mathbf{u}_0\right)\right\rangle - \frac{4k^2}{2!}\left\langle \hat{\mathbf{R}}_j \bullet \left(\mathbf{u}_j - \mathbf{u}_0\right)\right\rangle^2 + \ldots \tag{5.3}$$

The first-order term on the right-hand side of Equation (5.3) vanishes because the ensemble averages of the displacements are zero. Thus, the second-order term is the lowest-order correction:

$$\left\langle \exp\left[i2k\hat{\mathbf{R}}_j \bullet \left(\mathbf{u}_j - \mathbf{u}_0\right)\right]\right\rangle \cong 1 - 2k^2\left\langle \hat{\mathbf{R}}_j \bullet \left(\mathbf{u}_j - \mathbf{u}_0\right)\right\rangle^2 \tag{5.4}$$

The right-hand side of Equation (5.4) is approximately equal to

$$\exp(-2k^2\sigma_j^2) \tag{5.5}$$

where $\sigma_j^2 = \left\langle \hat{\mathbf{R}}_j \bullet \left(\mathbf{u}_j - \mathbf{u}_0\right)\right\rangle^2$.

5.2 Vibrational Mean-Square Relative Displacement (MSRD)

This section derives an expression for the vibrational MSRD, $\sigma_{\mathbf{R}}^2$, as a function of the "projected" density of vibrational modes, $g_{\mathbf{R}}(\omega)$. This is done using the quantum theory of lattice dynamics. For contrast, the vibrational MSD, σ^2, is also discussed.

Consider a monatomic Bravais lattice. Let $\mathbf{u}_{\mathbf{R}}$ denote the displacement of the atom whose lattice site is associated with the Bravais lattice vector **R**. From the quantum theory of lattice dynamics, it is well known that $\mathbf{u}_{\mathbf{R}}$ can be expressed as a function of annihilation $a_{\mathbf{qs}}$ and creation $a^{\dagger}_{-\mathbf{qs}}$ operators:

$$\mathbf{u}_{\mathbf{R}} = \frac{1}{\sqrt{N}} \sum_{\mathbf{qs}} \sqrt{\frac{\hbar}{2M\omega_{\mathbf{qs}}}} \left(a_{\mathbf{qs}} + a^{\dagger}_{-\mathbf{qs}}\right) \hat{\mathbf{e}}_{\mathbf{qs}} \exp(i\mathbf{q}\bullet\mathbf{R}) \tag{5.6}$$

where $\omega_{\mathbf{qs}}$ is the frequency and $\hat{\mathbf{e}}_{\mathbf{qs}}$ is the polarization vector of the phonon with wavevector **q** and polarization s, N is the number of atoms in the crystal, and M is the atomic mass. The summation is over all allowed wavevectors **q** in the first Brillouin zone and over the three independent polarizations s (Ashcroft and Mermin, 1976).

As shown in §5.1, the vibrational MSRD between atoms at **0** and **R** is given in a first-order approximation by

$$\sigma_R^2 = \left\langle \left| (\mathbf{u}_R - \mathbf{u}_0) \bullet \hat{\mathbf{R}} \right|^2 \right\rangle \tag{5.7}$$

where the brackets $\langle\ \rangle$ indicate time (or thermal) averaging. From Equation (5.6), we find:

$$(\mathbf{u}_R - \mathbf{u}_0) \bullet \hat{\mathbf{R}} = \frac{1}{\sqrt{N}} \sum_{qs} \sqrt{\frac{\hbar}{2M\omega_{qs}}} (a_{qs} + a_{-qs}^{\dagger})\, \hat{\mathbf{e}}_{qs} \bullet \hat{\mathbf{R}}\, [\exp(i\mathbf{q} \bullet \mathbf{R}) - 1] \tag{5.8}$$

Squaring the magnitude of Equation (5.8):

$$\begin{aligned} \left| (\mathbf{u}_R - \mathbf{u}_0) \bullet \hat{\mathbf{R}} \right|^2 &= \frac{\hbar}{2NM} \sum_{qs} \frac{1}{\omega_{qs}} (\hat{\mathbf{e}}_{qs} \bullet \hat{\mathbf{R}})^2 \left| [\exp(i\mathbf{q} \bullet \mathbf{R}) - 1] \left(a_{qs} + a_{-qs}^{\dagger} \right) \right|^2 \\ &= \frac{\hbar}{NM} \sum_{qs} \frac{1 - \cos \mathbf{q} \bullet \mathbf{R}}{\omega_{qs}} (\hat{\mathbf{e}}_{qs} \bullet \hat{\mathbf{R}})^2 \left(a_{qs} a_{-qs} + a_{-qs}^{\dagger} a_{qs}^{\dagger} + a_{qs} a_{qs}^{\dagger} + a_{-qs}^{\dagger} a_{-qs} \right) \end{aligned} \tag{5.9}$$

where we have used the fact that operators on different modes (**q**,s) commute. In the Heisenberg picture, the time dependences of the annihilation and creation operator are determined to be

$$a_{qs}(t) = a_{qs} \exp(-i\omega t) \tag{5.10a}$$

$$a_{qs}^{\dagger}(t) = a_{qs}^{\dagger} \exp(i\omega t) \tag{5.10b}$$

Therefore, the $a_{qs}a_{-qs}$ and $a_{-qs}^{\dagger} a_{qs}^{\dagger}$ terms vanish when time averaged, leaving

$$\sigma_R^2 = \frac{\hbar}{NM} \sum_{qs} \frac{1 - \cos \mathbf{q} \bullet \mathbf{R}}{\omega_{qs}} (\hat{\mathbf{e}}_{qs} \bullet \hat{\mathbf{R}})^2 \left(2\langle n_{qs} \rangle + 1 \right) \tag{5.11}$$

where $\langle n_{qs} \rangle$ is the time-averaged phonon occupancy of the vibrational mode with wavevector **q** and polarization s. For phonons, the distribution function $\langle n_{qs} \rangle$ is well known to be

$$\langle n_{qs} \rangle = \frac{1}{\exp(\hbar\omega_{qs}/k_B T) - 1} \tag{5.12}$$

In this way, phonons are like bosons whose chemical potential is $\hbar\omega_{qs}/2$. Substituting Equation (5.12) into Equation (5.11) gives

$$\sigma_R^2 = \frac{\hbar}{NM} \sum_{qs} \frac{1-\cos \mathbf{q}\bullet\mathbf{R}}{\omega_{qs}} (\hat{\mathbf{e}}_{qs}\bullet\hat{\mathbf{R}})^2 \coth\left(\frac{\hbar\omega_{qs}}{2k_B T}\right) \tag{5.13}$$

or equivalently

$$\sigma_R^2 = \frac{\hbar}{M} \int d\omega\, g_R(\omega) \frac{\coth(\hbar\omega/2k_B T)}{\omega} \tag{5.14a}$$

where

$$g_R(\omega) = \frac{1}{N} \sum_{qs} (1-\cos \mathbf{q}\bullet\mathbf{R})(\hat{\mathbf{e}}_{qs}\bullet\hat{\mathbf{R}})^2\, \delta(\omega-\omega_{qs}) \tag{5.14b}$$

$g_R(\omega)$ is called the "projected" density of vibrational modes. $g_R(\omega)$ weights the contribution of each mode to the mean-square compression of the bond distance between the atoms at **0** and **R**.

For contrast, consider the vibrational mean-square displacement (MSD), represented by σ^2, which is used in the Debye-Waller factor for Bragg peaks in x-ray diffraction. In x-ray diffraction, the intensities of Bragg peaks are reduced by the factor $\exp(-\sigma^2 k^2)$, where k is the magnitude of the scattering vector.

Similarly, in Mössbauer spectrometry, the recoil-free fraction is also given by $\exp(-\sigma^2 k^2)$ (Gonser, 1975).

The vibrational MSD of an atom from its equilibrium lattice position is defined as

$$\sigma^2 = \left\langle \left| \mathbf{u} \bullet \hat{\mathbf{k}} \right|^2 \right\rangle \tag{5.15}$$

where $\mathbf{u}$ is the instantaneous displacement of the atom, $\hat{\mathbf{k}}$ is the direction of the scattering vector, and the brackets indicate time (or thermal) averaging. It turns out that

$$\sigma^2 = \frac{\hbar}{2M} \int d\omega \, g(\omega) \frac{\coth(\hbar\omega/2k_B T)}{\omega} \tag{5.16a}$$

where

$$g(\omega) = \frac{1}{N} \sum_{qs} (\hat{\mathbf{e}}_{qs} \bullet \hat{\mathbf{k}})^2 \, \delta(\omega - \omega_{qs}) \tag{5.16b}$$

$g(\omega)$ is equivalent to the normalized density of vibrational modes since $(\hat{\mathbf{e}}_{qs} \bullet \hat{\mathbf{k}})^2$ averages to 1/3 and there are a total of 3N vibrational modes. By normalized, I mean that

$$\int_0^\infty d\omega \, g(\omega) = 1 \tag{5.17}$$

Equation (5.16) should be contrasted with Equation (5.14). The most important difference is that the additional term $\cos \mathbf{q} \bullet \mathbf{R}$ in Equation (5.14b) insures that only the out-of-phase motion of the atoms in the direction of $\hat{\mathbf{R}}$ contributes to the MSRD (Beni and Platzman, 1976).

5.3 Force Constant Model of Lattice Dynamics

This section determines the vibrational modes of a lattice within the force constant model of lattice dynamics. This is done for a monatomic crystal using a classical description of the atomic vibrations which largely follows the one given in Ashcroft and Mermin (1976).

Assume that the equilibrium position of each atom in our monatomic crystal is a Bravais lattice vector **R**. Define **r**(**R**) to be the instantaneous position of the atom whose equilibrium position is **R**. The total potential energy or cohesive energy of the crystal can then be written as

$$U = \frac{1}{2}\sum_{\mathbf{R}}\sum_{\mathbf{R}'\neq\mathbf{R}} \phi[\mathbf{r}(\mathbf{R}) - \mathbf{r}(\mathbf{R}')] = \frac{1}{2}\sum_{\mathbf{R}}\sum_{\mathbf{R}'\neq\mathbf{R}} \phi[\mathbf{R} + \mathbf{u}(\mathbf{R}) - \mathbf{R}' - \mathbf{u}(\mathbf{R}')] \qquad (5.18)$$

where $\phi(\mathbf{r})$ is the interaction energy between atoms separated by **r**, and **u**(**R**) is the deviation of the atom from its equilibrium position **R**, i.e., **r**(**R**) = **u**(**R**) + **R**. From now on it will be implicitly assumed that the summations over **R'** exclude **R**.

Assume that the deviations **u**(**R**) are small compared with the interatomic spacing. The potential energy U can then be expanded about its equilibrium value, using Taylor's theorem in three dimensions:

$$\begin{aligned} U = {} & \frac{1}{2}\sum_{\mathbf{R}}\sum_{\mathbf{R}'} \phi(\mathbf{R}-\mathbf{R}') + \frac{1}{2}\sum_{\mathbf{R}}\sum_{\mathbf{R}'}[\mathbf{u}(\mathbf{R})-\mathbf{u}(\mathbf{R}')]\bullet\nabla\phi(\mathbf{R}-\mathbf{R}') \\ & + \frac{1}{4}\sum_{\mathbf{R}}\sum_{\mathbf{R}'}\{[\mathbf{u}(\mathbf{R})-\mathbf{u}(\mathbf{R}')]\bullet\nabla\}^2\phi(\mathbf{R}-\mathbf{R}') + \ldots \end{aligned} \qquad (5.19)$$

The zero-order term is simply the equilibrium potential energy. The coefficient of **u**(**R**) in the linear term is $\sum_{\mathbf{R}'}\nabla\phi(\mathbf{R}-\mathbf{R}')$, but this is simply the force exerted on

the atom at **R** by all the other atoms, when each is placed at its equilibrium position. Clearly, by definition of the equilibrium position, this coefficient and therefore the linear term must vanish.

Since the linear term vanishes, the quadratic term is the lowest order correction to the equilibrium potential energy. In the harmonic approximation only this term is retained:

$$U = U^{eq} + U^{harm} \tag{5.20}$$

where U^{eq} is the equilibrium potential energy, and U^{harm} is the harmonic approximation to the extra potential energy due to the deviations of the atoms from their equilibrium positions.

Changing notation and rearranging the expression for U^{harm}:

$$\begin{aligned} U^{harm} &= \frac{1}{4}\sum_{\mathbf{R}}\sum_{\mathbf{R}'}\{[\mathbf{u}(\mathbf{R})-\mathbf{u}(\mathbf{R}')]\bullet\nabla\}^2\phi(\mathbf{R}-\mathbf{R}') \\ &= \frac{1}{2}\sum_{\mathbf{R}}\sum_{\mathbf{R}'}\sum_{\mu}\sum_{\upsilon}\left[u_\mu(\mathbf{R})\phi_{\mu\upsilon}(\mathbf{R}-\mathbf{R}')u_\upsilon(\mathbf{R})-u_\mu(\mathbf{R})\phi_{\mu\upsilon}(\mathbf{R}-\mathbf{R}')u_\upsilon(\mathbf{R}')\right] \end{aligned} \tag{5.21}$$

where $\phi_{\mu\upsilon}(\mathbf{r}) \equiv \dfrac{\partial^2\phi(\mathbf{r})}{\partial r_\mu \partial r_\upsilon}$, and the summations over μ and υ are over x,y,z. The summations over the first term in Equation (5.21) can be manipulated to give

$$\begin{aligned} \sum_{\mathbf{R}}\sum_{\mathbf{R}'}\sum_{\mu}\sum_{\upsilon}u_\mu(\mathbf{R})\phi_{\mu\upsilon}(\mathbf{R}-\mathbf{R}')u_\upsilon(\mathbf{R}) &= \sum_{\mathbf{R}}\sum_{\mathbf{R}''}\sum_{\mu}\sum_{\upsilon}u_\mu(\mathbf{R})\phi_{\mu\upsilon}(\mathbf{R}-\mathbf{R}'')u_\upsilon(\mathbf{R}) \\ &= \sum_{\mathbf{R}}\sum_{\mathbf{R}'}\sum_{\mathbf{R}''}\sum_{\mu}\sum_{\upsilon}\delta_{\mathbf{R},\mathbf{R}'}u_\mu(\mathbf{R})\phi_{\mu\upsilon}(\mathbf{R}-\mathbf{R}'')u_\upsilon(\mathbf{R}') \\ &= \sum_{\mathbf{R}}\sum_{\mathbf{R}'}\sum_{\mu}\sum_{\upsilon}u_\mu(\mathbf{R})\left[\delta_{\mathbf{R},\mathbf{R}'}\sum_{\mathbf{R}''}\phi_{\mu\upsilon}(\mathbf{R}-\mathbf{R}'')\right]u_\upsilon(\mathbf{R}') \end{aligned} \tag{5.22}$$

Therefore, Equation (5.21) can be written simply as

$$U^{harm} = \frac{1}{2}\sum_{\mathbf{R}}\sum_{\mathbf{R'}}\sum_{\mu}\sum_{\upsilon} u_\mu(\mathbf{R})C_{\mu\upsilon}(\mathbf{R}-\mathbf{R'})u_\upsilon(\mathbf{R'}) \qquad (5.23)$$

where the force constant matrix $C_{\mu\upsilon}(\mathbf{R}\text{-}\mathbf{R'}) = \delta_{\mathbf{R},\mathbf{R'}}\sum_{\mathbf{R''}}\phi_{\mu\upsilon}(\mathbf{R}-\mathbf{R''}) - \phi_{\mu\upsilon}(\mathbf{R}-\mathbf{R'})$. Equation (5.23) is analogous to the familiar $U = \frac{1}{2}kx^2$ for a single spring.

Now consider the 3N equations of motion for the system. In analogy with the familiar $F = ma = -\frac{dU}{dx} = -kx$, the force on the atom at site **R** in the μ-direction is

$$M\ddot{u}_\mu(\mathbf{R}) = -\sum_{\mathbf{R'}}\sum_{\upsilon} C_{\mu\upsilon}(\mathbf{R}-\mathbf{R'})u_\upsilon(\mathbf{R'}) \qquad (5.24)$$

where M is the atomic mass, and double counting cancels the factor of 1/2 in Equation (5.23). Thus, $-C_{\mu\upsilon}(\mathbf{R}\text{-}\mathbf{R'})u_\upsilon(\mathbf{R'})$ is the force on the atom at site **R** in the μ-direction when the atom at site **R'** is displaced by $u_\upsilon(\mathbf{R'})$ in the υ-direction. Equation (5.24) can be rewritten in matrix notation as

$$M\ddot{\mathbf{u}}(\mathbf{R}) = -\sum_{\mathbf{R'}}\mathbf{C}(\mathbf{R}-\mathbf{R'})\mathbf{u}(\mathbf{R'}) \qquad (5.25)$$

Consider solutions to Equation (5.25) of the form $\mathbf{u}(\mathbf{R},t) = A\hat{\mathbf{e}}\exp[i(\mathbf{q}\cdot\mathbf{R} - \omega t)]$:

$$-M\omega^2 A\hat{\mathbf{e}}\exp(i\mathbf{q}\cdot\mathbf{R}) = -A\hat{\mathbf{e}}\left[\sum_{\mathbf{R'}}\mathbf{C}(\mathbf{R}-\mathbf{R'})\exp(i\mathbf{q}\cdot\mathbf{R'})\right]$$

$$= -A\hat{\mathbf{e}}\left\{\sum_{\mathbf{R''}=\mathbf{R}-\mathbf{R'}}\mathbf{C}(\mathbf{R''})\exp[i\mathbf{q}\cdot(\mathbf{R}-\mathbf{R''})]\right\} \qquad (5.26)$$

$$-M\omega^2\hat{\mathbf{e}} = \mathbf{D}(\mathbf{q})\ \hat{\mathbf{e}} \qquad (5.27)$$

where the dynamical matrix $\mathbf{D}(\mathbf{q}) = \sum_{\mathbf{R}} \mathbf{C}(\mathbf{R}) \exp(-i\mathbf{q}\cdot\mathbf{R})$. The dynamical matrix can be thought of as a Fourier transform of the force constant matrix. Using inherent symmetries of the force constant matrix $\mathbf{C}(\mathbf{R})$ (Ashcroft and Mermin, 1976), the dynamical matrix can be rewritten as

$$\mathbf{D}(\mathbf{q}) = -2\sum_{\mathbf{R}} \mathbf{C}(\mathbf{R}) \sin^2\left(\frac{\mathbf{q}\cdot\mathbf{R}}{2}\right) \tag{5.28}$$

Equation (5.28) shows that the dynamical matrix must be real and an even function of $\mathbf{q}$.

For each of the N allowed wavevectors $\mathbf{q}$ in the first Brillouin zone, solving Equation (5.27) gives three orthonormal eigenvectors $\hat{\mathbf{e}}_{\mathbf{q}s}$ and three corresponding eigenvalues $\omega_{\mathbf{q}s}$. Of course, the eigenvectors and eigenvalues correspond respectively to the polarization vectors and the frequencies of the normal modes of vibration. The normalized density of vibrational modes, $g(\omega)$, is simply the probability distribution of frequencies $\omega_{\mathbf{q}s}$. The projected density of vibrational modes, $g_{\mathbf{R}}(\omega)$, can be determined by applying Equation (5.14b).

5.4 Results from Al, Fe, and Pd

This section presents temperature-dependent EXELFS measurements from Al, Fe, and Pd foils and analyzes the results within the Einstein, Debye, and force constant models. Debye temperatures obtained from MSRD and heat capacity measurements are compared.

Figures 5.1 through 5.3 present the temperature dependence of the magnitude of the Fourier transform of the Al K-edge, Fe L_{23}-edge, and Pd M_{45}-edge EXELFS. In this section, for simplicity, it is reasonable to consider the

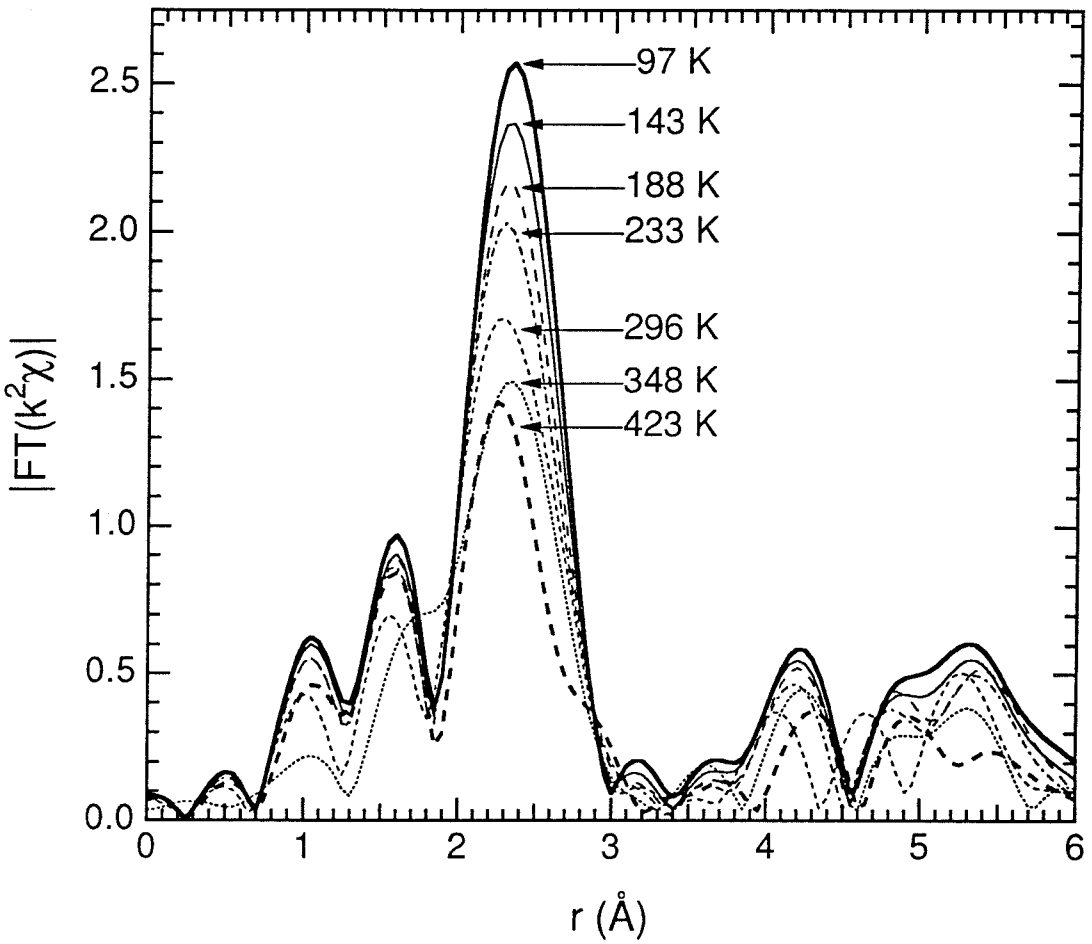

Figure 5.1. Temperature dependence of magnitude of FT of Al K-edge EXELFS ($3 < k < 10$ Å^{-1}) from Al metal.

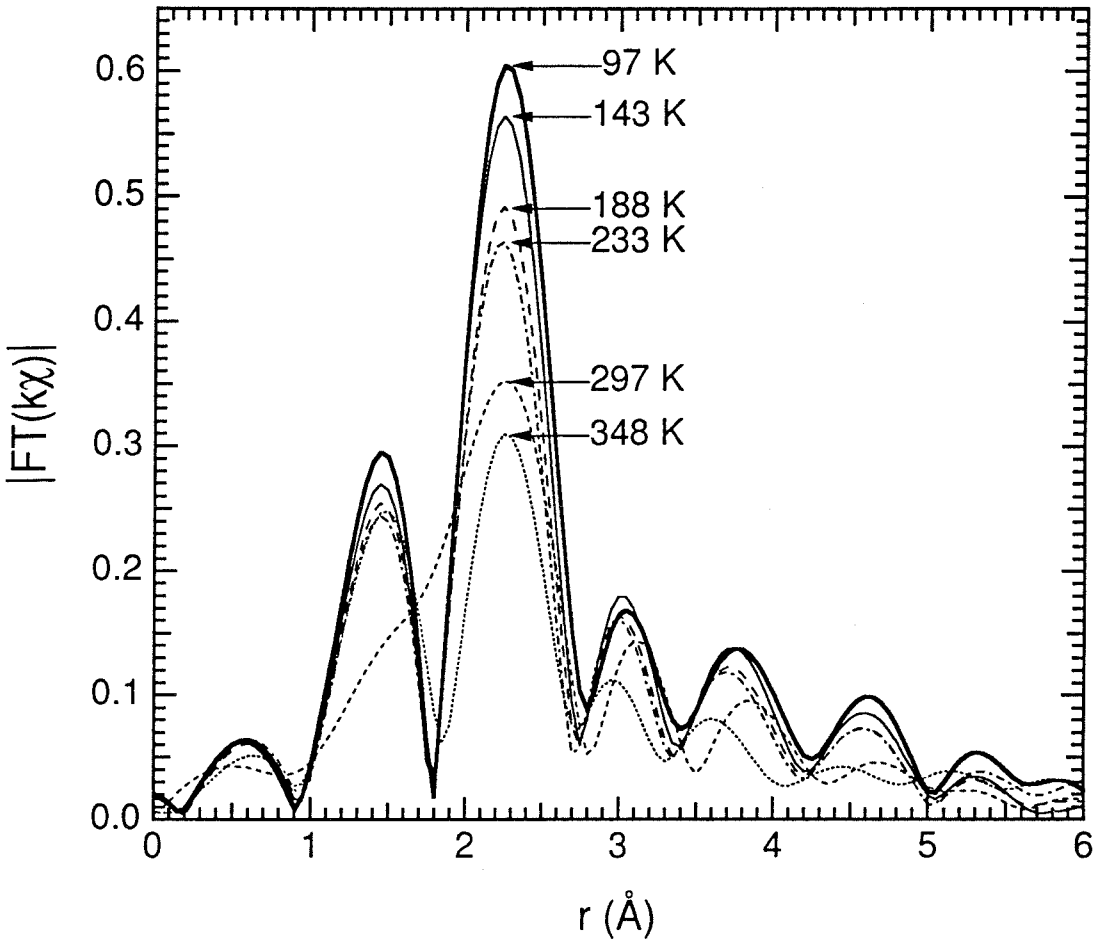

Figure 5.2. Temperature dependence of magnitude of FT of Fe L_{23}-edge EXELFS ($7 < k < 13$ Å^{-1}) from Fe metal.

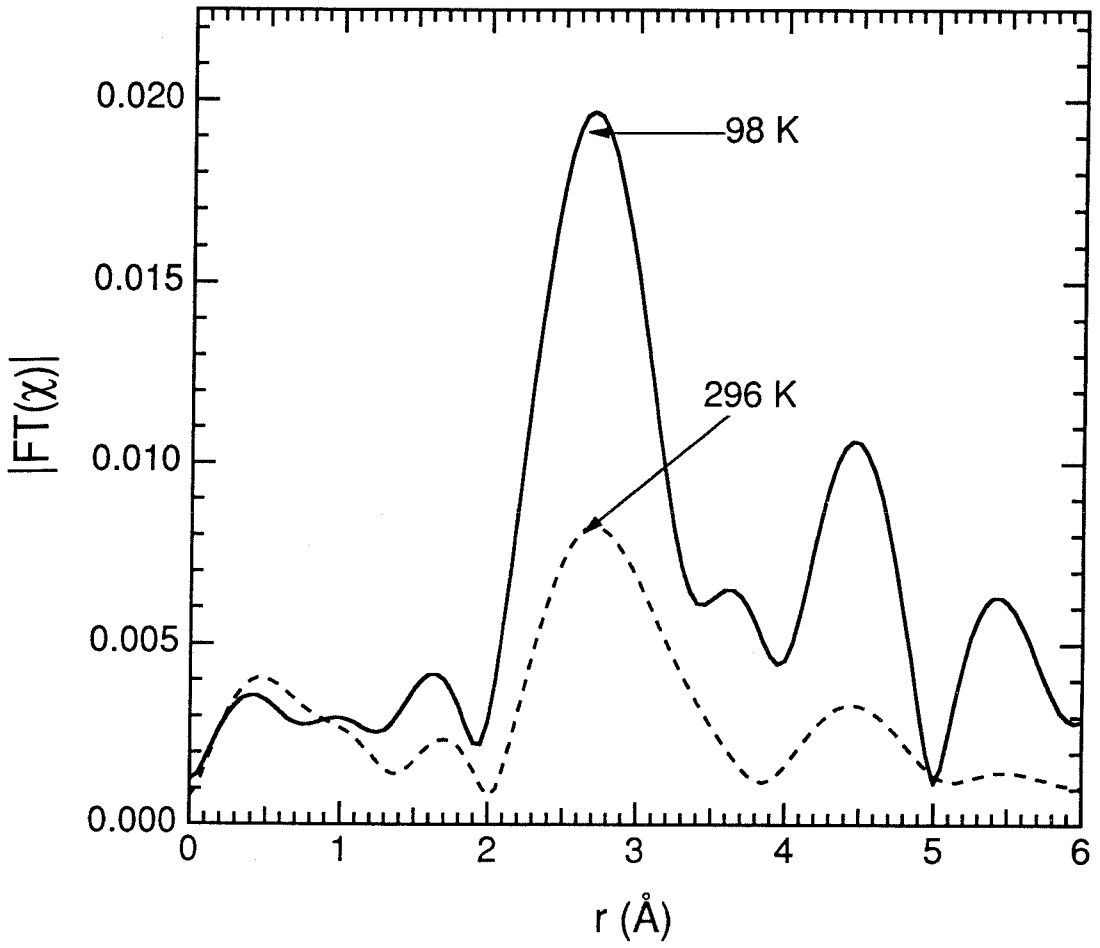

Figure 5.3. Temperature dependence of magnitude of FT of Pd M_{45}-edge EXELFS ($10.25 < k < 14.5$ Å^{-1}) from Pd metal.

major peak in the FT of the Fe L_{23}-edge EXELFS to be due solely to the 1nn shell although the 2nn shell also contributes to it.

In general, the 1nn peaks are seen to decrease in size with increasing temperature. This effect is usually represented by the Debye-Waller type factor $\exp(-2\sigma^2_{1nn}k^2)$, where σ^2_{1nn} is the mean-square relative displacement (MSRD) between the central atom and the 1nn shell.

Figure 5.4 compares the Fourier filtered 1nn shell EXELFS from Al at 97 K and 296 K. Using a simple least-squares routine given in §B.4, the difference in MSRD between the two oscillations is determined. This difference in MSRD is denoted by $\Delta\sigma^2_{1nn}$. To show the quality of the fit, Figure 5.2 also displays the 97 K data multiplied by $\exp(-2\Delta\sigma^2_{1nn}k^2)$, where $\Delta\sigma^2_{1nn} = 5.3 \times 10^{-3}$ Å^2.

Figure 5.5 through 5.7 display $\Delta\sigma^2_{1nn}$ for the EXELFS from Al, Fe, and Pd metals relative to the EXELFS at the lowest temperature. The error bars were obtained from values of $\Delta\sigma^2_{1nn}$ at which the variance of the least-squares fit increased by 20%. As expected, $\Delta\sigma^2_{1nn}$ is seen to increase with increasing temperature. The temperature dependence of $\Delta\sigma^2_{1nn}$ can be interpreted within the Einstein, Debye, and force constant models.

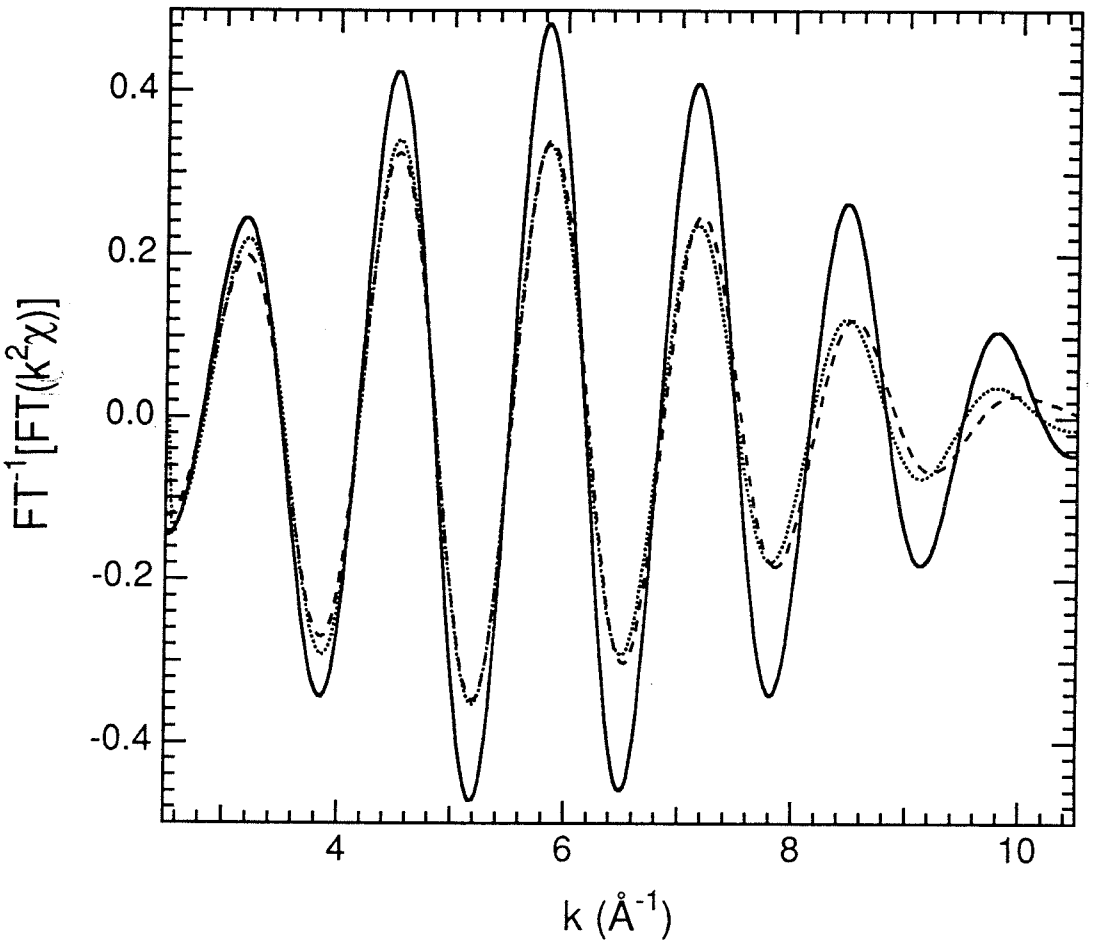

Figure 5.4. Fourier filtered 1nn shell EXELFS from Al metal at 97 K (solid line) and 296 K (dashed line). Also shown is 97 K data multiplied by exp[-2(5.3x10^{-3}Å^2) k^2] (dotted line).

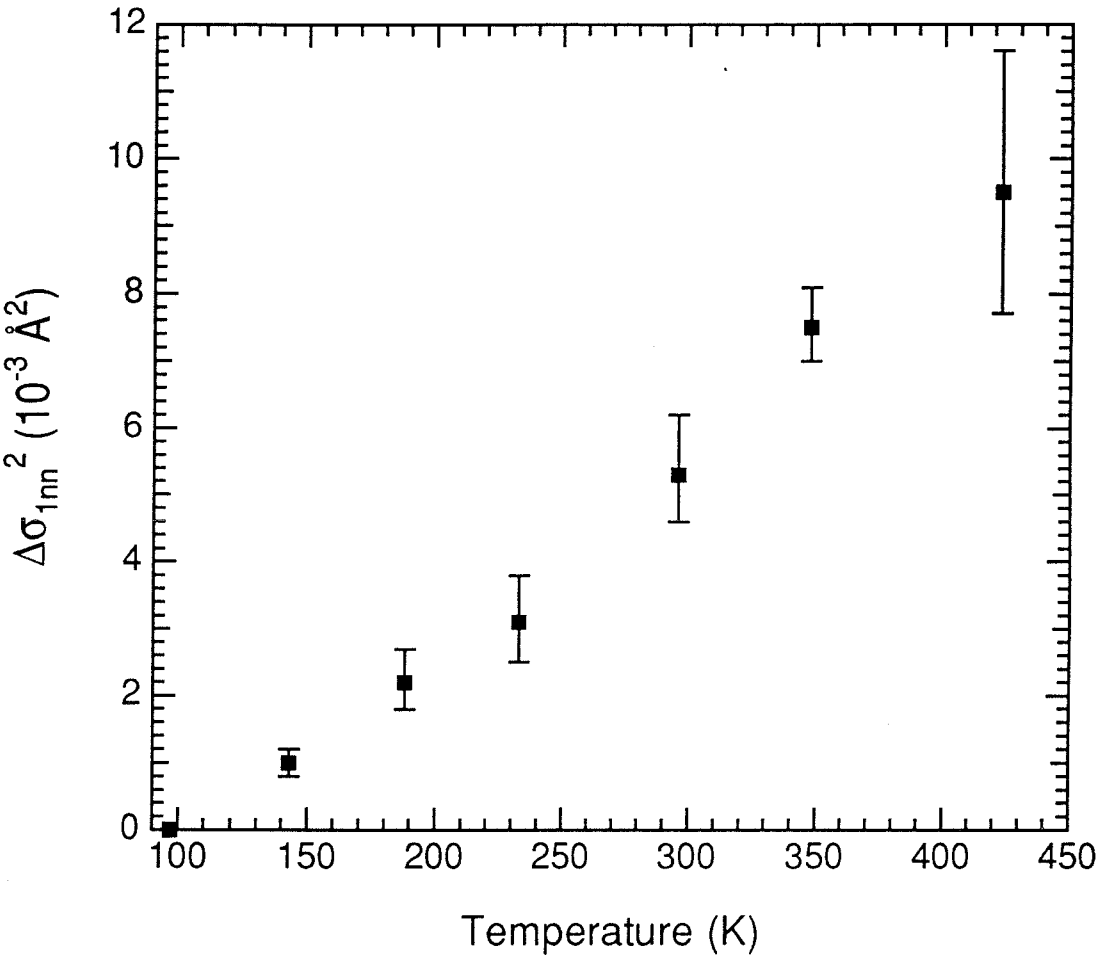

Figure 5.5. Change in 1nn MSRD for EXELFS from Al metal relative to EXELFS at 97 K. Error bars obtained from values of $\Delta\sigma_{1nn}^2$ at which variance of least-squares fit increased by 20%.

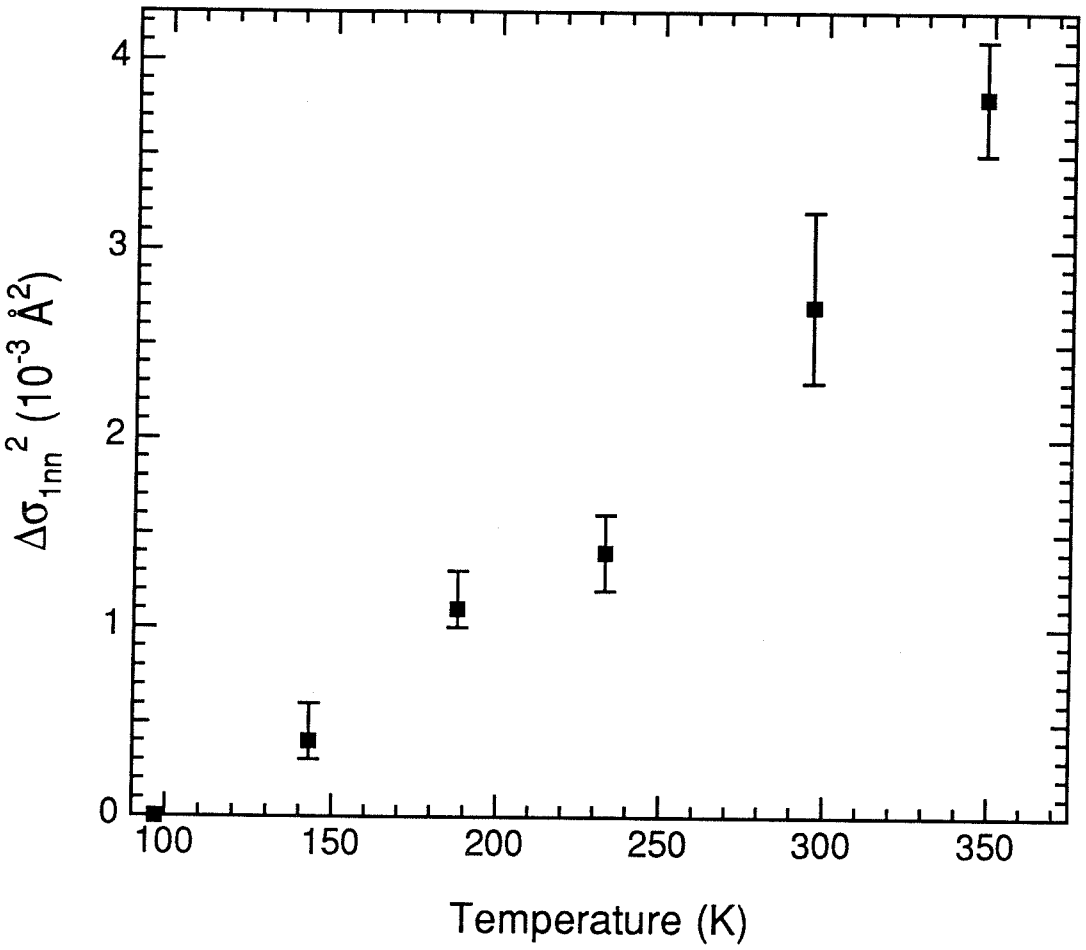

Figure 5.6. Change in 1nn MSRD for EXELFS from Fe metal relative to EXELFS at 97 K. Error bars obtained from values of $\Delta\sigma_{1nn}^2$ at which variance of least-squares fit increased by 20%.

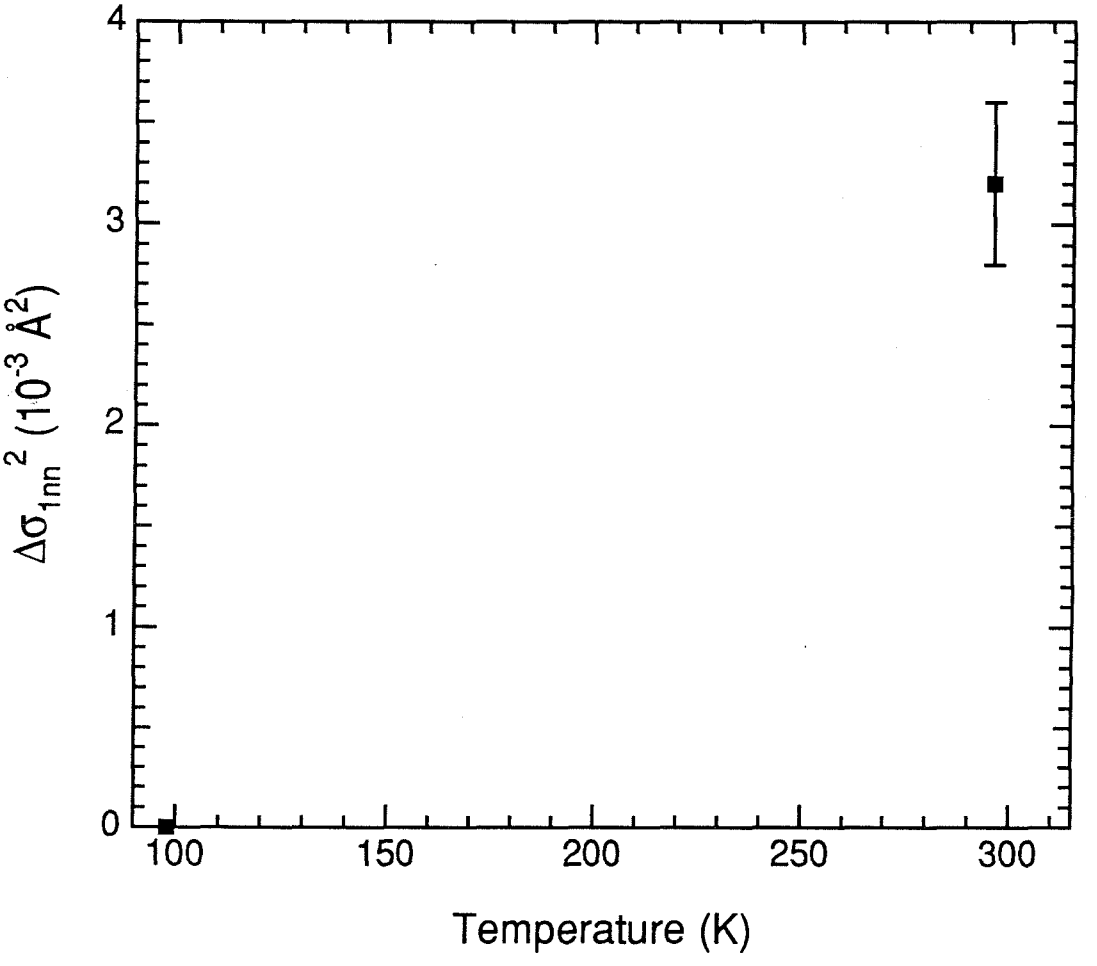

Figure 5.7. Change in 1nn MSRD for EXELFS from Pd metal relative to EXELFS at 98 K. Error bars obtained from values of $\Delta\sigma_{1nn}^2$ at which variance of least-squares fit increased by 20%.

5.4.1 Einstein Analysis

The Einstein model is the simplest. In solid-state theory, a solid of N atoms is considered to have 3N vibrational modes. The Einstein model assumes that all 3N modes have the same characteristic frequency ω_E. In other words, the Einstein model assumes that the density of vibrational modes is simply

$$g(\omega) = \delta(\omega - \omega_E) \tag{5.29}$$

The projected density of vibrational modes in the correlated Einstein model is also a delta function:

$$g_R(\omega) = \delta(\omega - \omega_E) \tag{5.30}$$

Substituting Equation (5.30) into Equation (5.14a) gives the following expression for the MSRD within the Einstein model:

$$\sigma_R^2 = \frac{\hbar}{M\omega_E} \coth\left(\hbar\omega_E / 2k_B T\right) \tag{5.31}$$

The Einstein frequency ω_E and Einstein temperature θ_E are related by the simple equation

$$\hbar\omega_E = k_B\theta_E \tag{5.32}$$

Using the computer program listed in §C.1, Einstein temperatures can be determined from $\Delta\sigma^2_{1nn}$ vs temperature data. Allowing the value of σ^2_{1nn} at the lowest temperature to float, the program fits the temperature-dependent data to Equation (5.31). Figures 5.8 through 5.10 display the Einstein model fits to the $\Delta\sigma^2_{1nn}$ data from Al, Fe, and Pd metals. The fits gave $\theta_E = 318 \pm 10$ K for Al, 306 $\pm$ 16 K for Fe, and 223 $\pm$ 30 K for Pd.

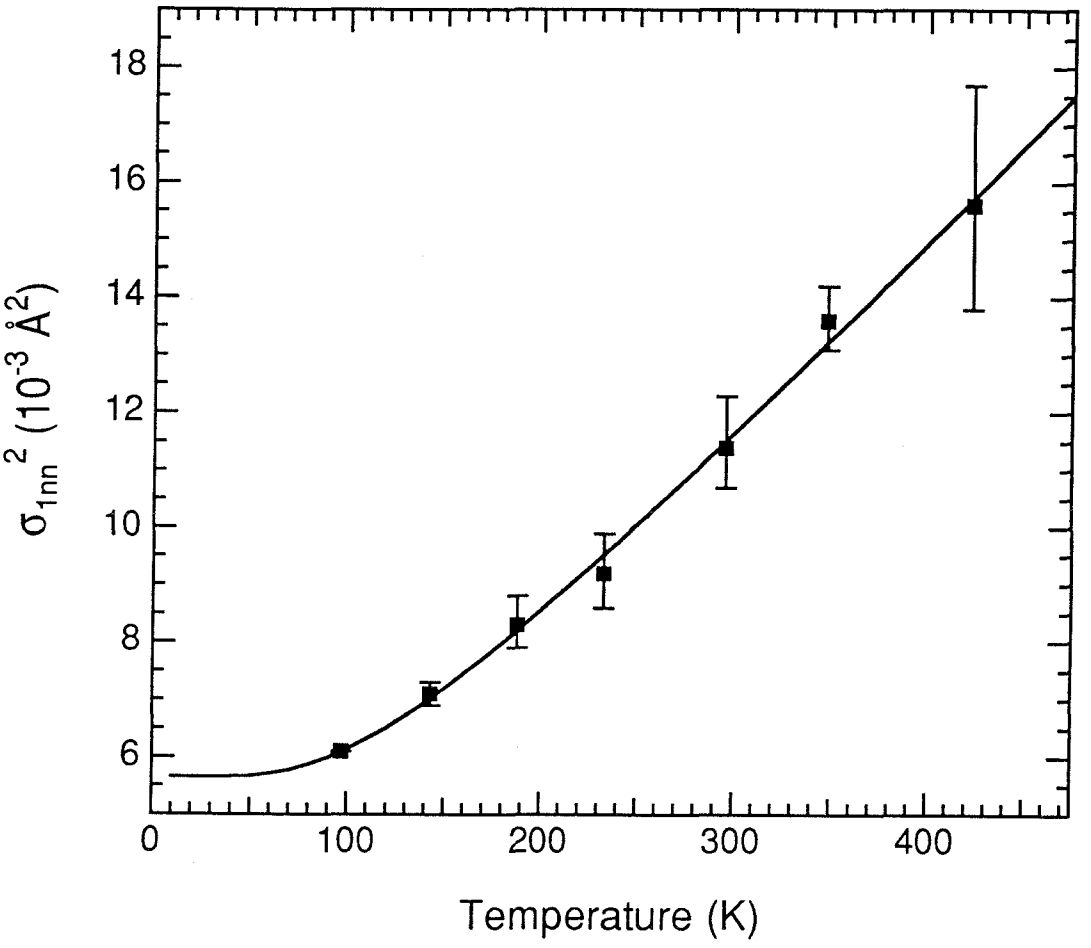

Figure 5.8. Einstein model fit to 1nn MSRD data from Al metal. Absolute offset of data was allowed to float. Fit gave $\theta_E = 318 \pm 10$ K.

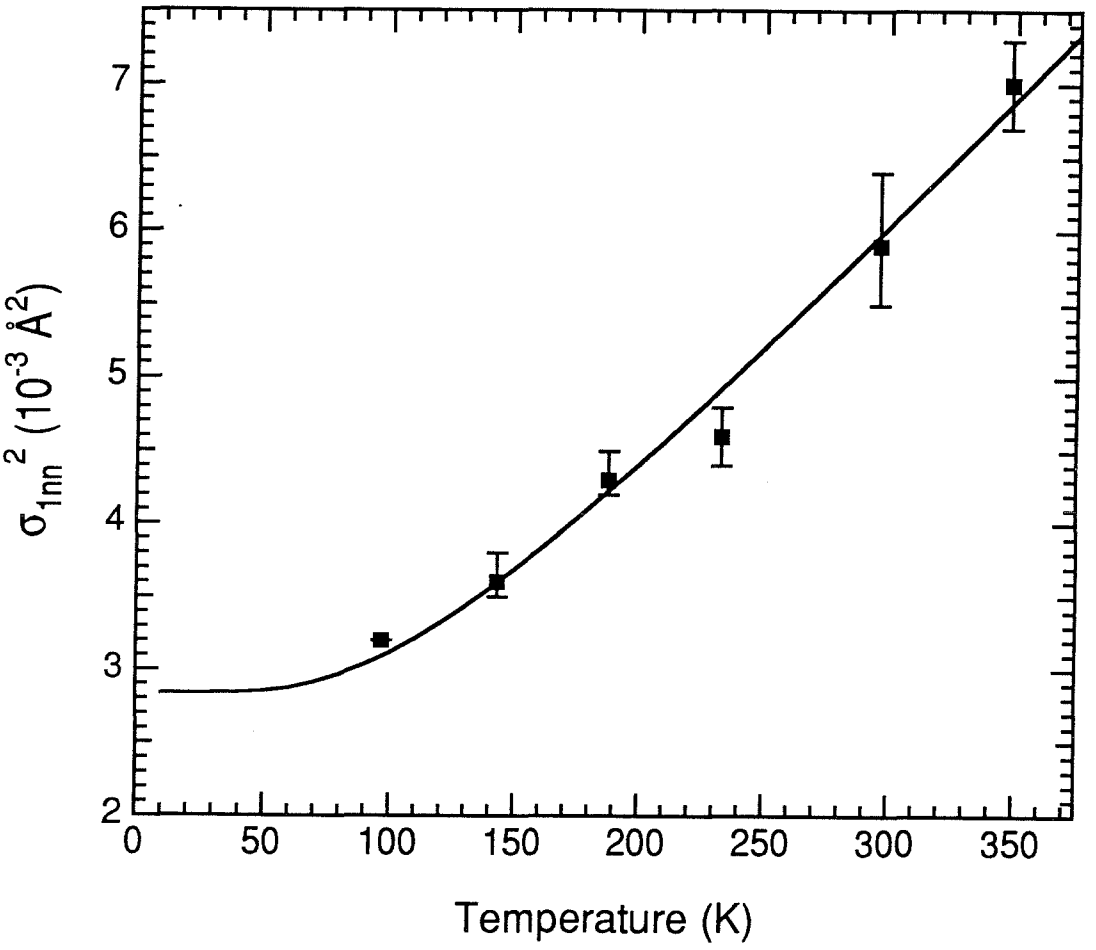

Figure 5.9. Einstein model fit to 1nn MSRD data from Fe metal. Absolute offset of data was allowed to float. Fit gave $\theta_E = 306 \pm 16$ K.

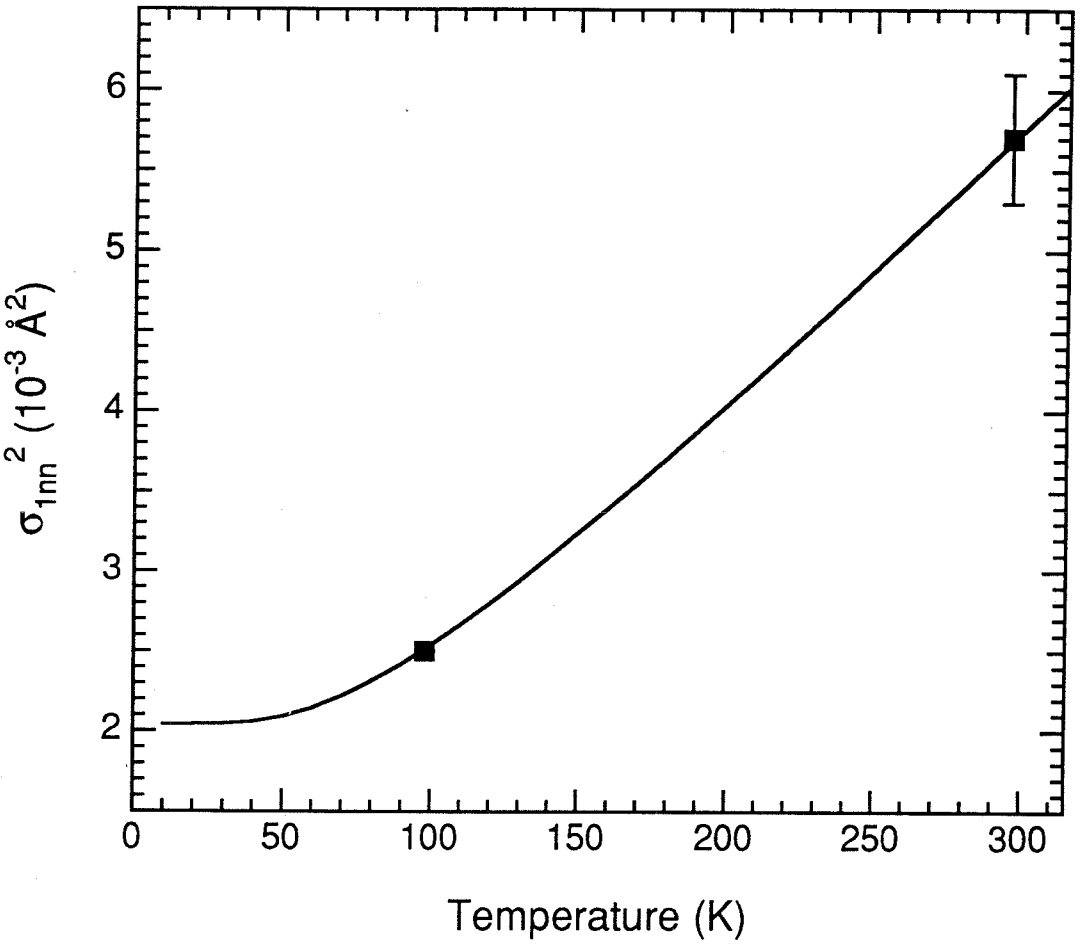

Figure 5.10. Einstein model fit to 1nn MSRD data from Pd metal. Absolute offset of data was allowed to float. Fit gave $\theta_E = 223 \pm 30$ K.

5.4.2. Debye Analysis

The Debye model is slightly more sophisticated than the Einstein model. The Debye model assumes a linear dispersion relation $\omega = cq$ and that the density of vibrational modes is given by

$$g(\omega) = \frac{V\omega^2}{2\pi^2 c^3} \quad , \quad \text{if } \omega < \omega_D = \frac{k_B\theta_D}{\hbar}$$
$$= 0 \quad , \quad \text{if } \omega > \omega_D \tag{5.33}$$

where V = atomic volume, $c = \frac{k_B\theta_D}{\hbar q_D}$, $q_D = (6\pi^2/V)^{1/3}$, θ_D = Debye temperature.

In the correlated Debye model, the summation in Equation (5.14b) over all allowed **q** in the first Brillouin zone is replaced by an integral in **q**-space over a sphere of radius q_D. Furthermore, since the polarization directions are orthonormal, $\sum_s (\hat{\mathbf{e}}_{\mathbf{q},s} \cdot \hat{\mathbf{R}})^2 = 1$. The projected density of vibrational modes becomes

$$g_R(\omega) = \frac{\int_0^{q_D} dq' 2\pi q'^2 \frac{\delta(q-q')}{c} \int_0^{\pi} d\theta [1-\cos(q'r\cos\theta)]\sin\theta}{\frac{4\pi}{3} q_D^3} \tag{5.34}$$

The integral over θ works out to

$$\int_0^{\pi} d\theta [1-\cos(q'r\cos\theta)]\sin\theta = 2\left(1 - \frac{\sin q'R}{q'R}\right) \tag{5.35}$$

Therefore, Equation (5.34) becomes

$$g_R(\omega) = \frac{3}{cq_D^3}\int_0^{q_D} dq'\ \delta(q-q')q'^2\left(1 - \frac{\sin q'R}{q'R}\right)$$

$$= \frac{3q^2}{cq_D^3}\left(1 - \frac{\sin qR}{qR}\right)$$

$$= \frac{3\omega^2}{\omega_D^3}\left(1 - \frac{\sin\frac{\omega R}{c}}{\frac{\omega R}{c}}\right) \qquad (5.36)$$

Substituting Equation (5.36) into Equation (5.14a) gives

$$\sigma_R^2 = \frac{3\hbar}{M\omega_D^3}\int_0^{\omega_D} d\omega\ \coth(\hbar\omega/2k_BT)\ \omega\left(1 - \frac{\sin\frac{\omega R}{c}}{\frac{\omega R}{c}}\right) \qquad (5.37)$$

(Sevillano et al., 1979).

The Debye frequency ω_D and the Debye temperature θ_D are related by

$$\hbar\omega_D = k_B\theta_D \qquad (5.38)$$

Using the computer program listed in §C.2, Debye temperatures can be determined from $\Delta\sigma_{1nn}^2$ vs temperature data. Figures 5.11 through 5.13 display the Debye model fits to the $\Delta\sigma_{1nn}^2$ data from Al, Fe, and Pd metals. The fits gave $\theta_D = 438 \pm 13$ K for Al, 417 ± 22 K for Fe, and 306 ± 40 K for Pd. These values for θ_D are approximately 0.73 times the corresponding values for θ_E. Disko et

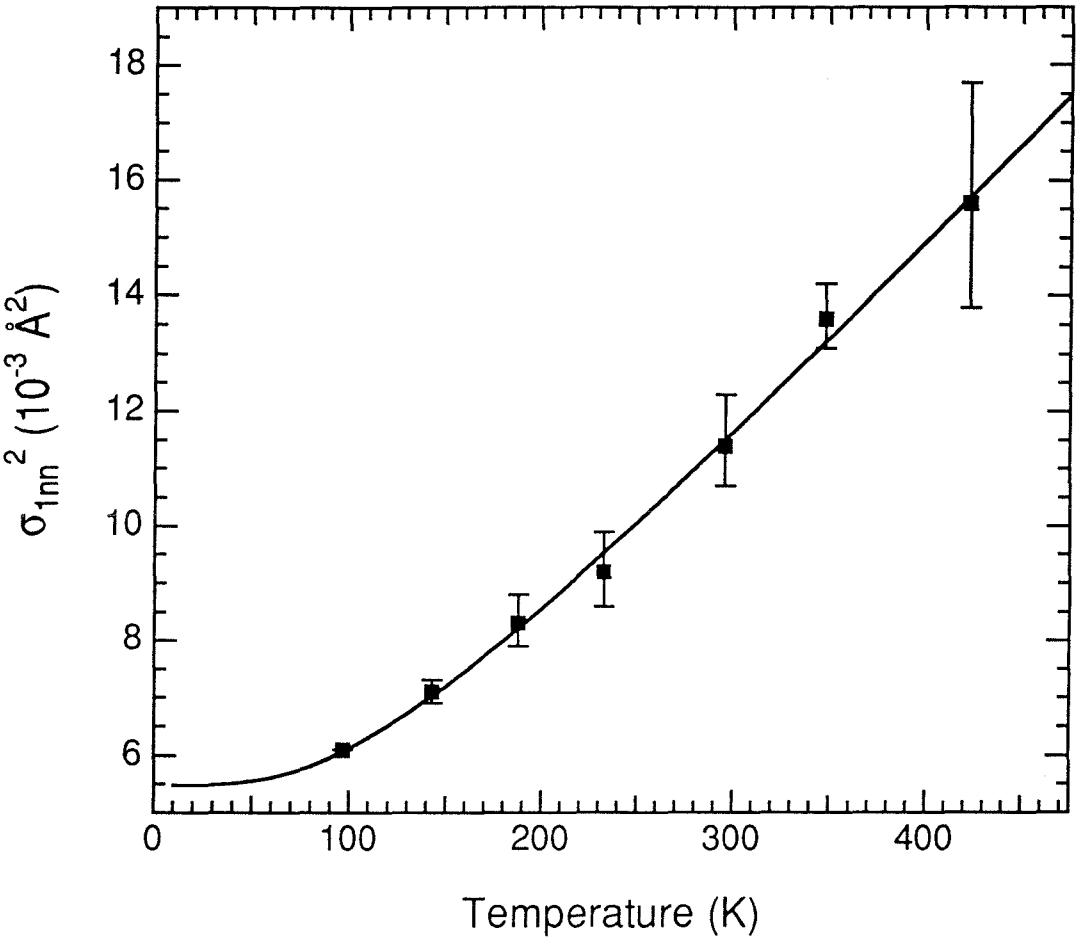

Figure 5.11. Debye model fit to 1nn MSRD data from Al metal. Absolute offset of data was allowed to float. Fit gave $\theta_D = 438 \pm 13$ K.

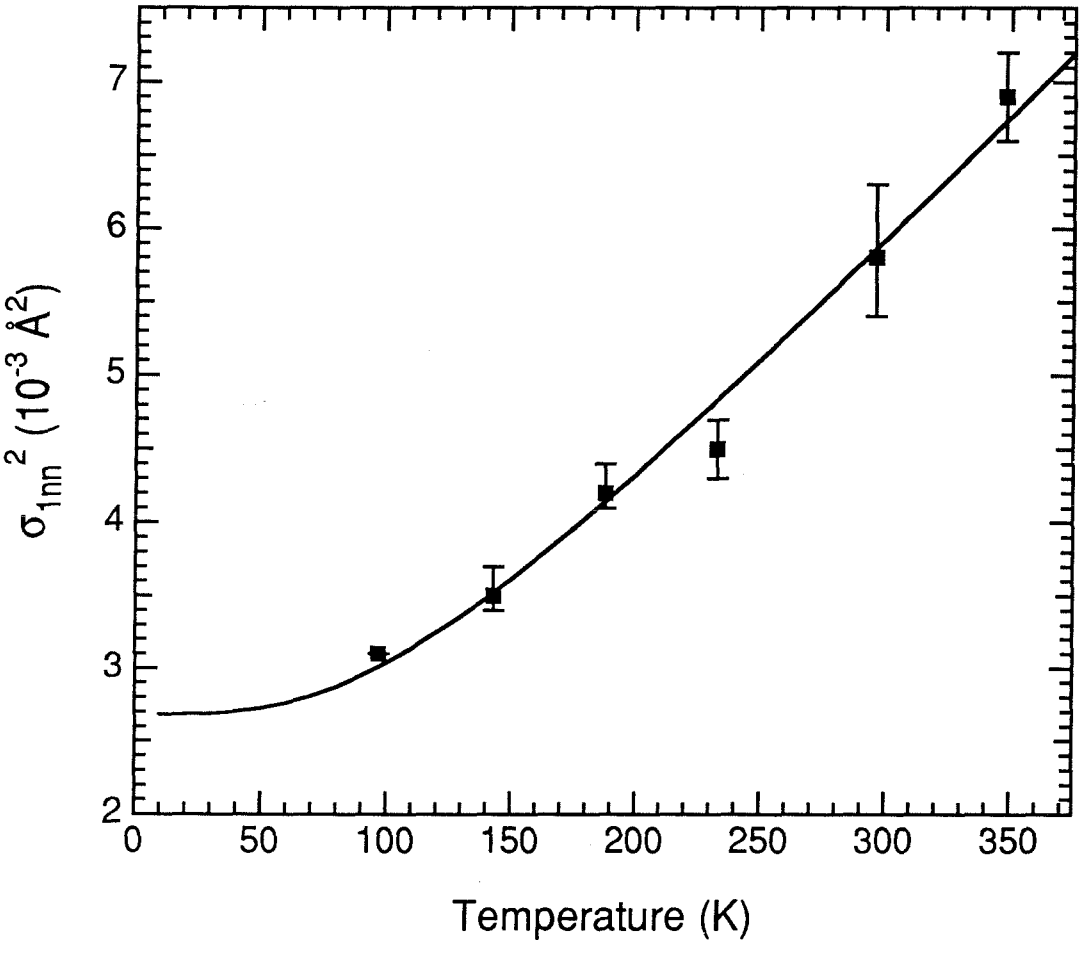

Figure 5.12. Debye model fit to 1nn MSRD data from Fe metal. Absolute offset of data was allowed to float. Fit gave $\theta_D = 417 \pm 22$ K.

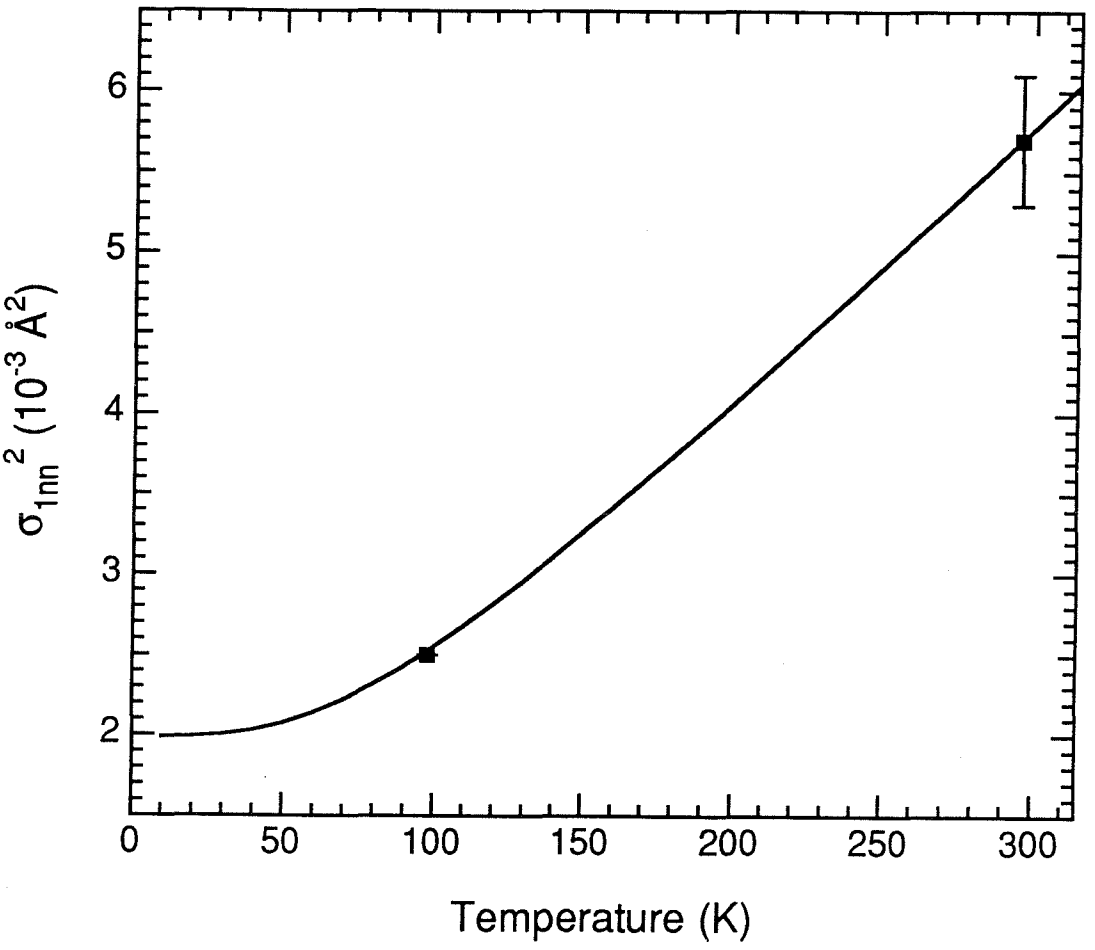

Figure 5.13. Debye model fit to 1nn MSRD data from Pd metal. Absolute offset of data was allowed to float. Fit gave $\theta_D = 306 \pm 40$ K.

al. (1989) obtained a value of $\theta_D = 415 \pm 30$ K from the temperature-dependent EXELFS of Al.

θ_D derived from MSRD measurements are expected to be different from θ_D derived from MSD or heat capacity measurements. Each measurement can be thought of as placing emphasis on different regions of the frequency distribution of vibrational modes. MSD data emphasizes the lower-frequency modes more than MSRD or heat capacity data. Moreover, θ_D are usually derived from heat capacity data by matching the data near the point where the heat capacity is about half the Dulong and Petit value. Obviously, θ_D must be determined from MSRD and MSD data using a completely different methodology. Despite these differences, the values for θ_D determined from these measurements should be roughly comparable. From heat capacity measurements, $\theta_D = 394$ K for Al, 420 K for Fe, and 275 K for Pd (Seitz and Turnbull, 1956); these values are roughly comparable to those from my MSRD measurements, which were 438, 417, and 306 K, respectively.

5.4.3. Force Constant Analysis

The force constant model discussed in §5.3 uses interatomic force constants from inelastic neutron scattering experiments to determine the frequencies and polarizations of the 3N vibrational modes in a crystal. Unlike the Einstein and Debye models, the force constant model does not have any "free" parameters because all the necessary parameters are determined from the neutron scattering data.

Table 5.1 contains interatomic force constants for Al, Fe, and Pd metals which were derived from neutron scattering data. The density of vibrational modes, $g(\omega)$, can be determined from these force constants using my program

fcc				bcc		
force const		Al	Pd	force const		Fe
110	XX	10.46	19.76	111	XX	16.88
	ZZ	-2.63	-2.51		XY	15.01
	XY	10.37	23.19	200	XX	14.63
200	XX	2.43	0.92		YY	0.55
	YY	-0.14	0.42	220	XX	0.92
211	XX	0.099	0.91		ZZ	-0.57
	YY	-0.24	0.13		XY	0.69
	YZ	-0.29	0.61	311	XX	-0.12
	XZ	-0.18	0.91		YY	0.03
220	XX	0.14	-1.04		YZ	0.52
	ZZ	0.19	-0.13		XZ	0.007
	XY	0.38	-1.86	222	XX	-0.29
310	XX	-0.30	0.09		XY	0.32
	YY	0.18	-0.23			
	ZZ	0.26	-0.27			
	XY	-0.32	0.12			
222	XX	-0.14	0.22			
	XY	0.20	0.15			

Table 5.1. Interatomic (Born-von Karman) force constants (in N/m) for the first several near-neighbor shells in Al (Cowley, 1974), Fe (Minkiewicz et al., 1967), and Pd (Miiller and Brockhouse, 1971).

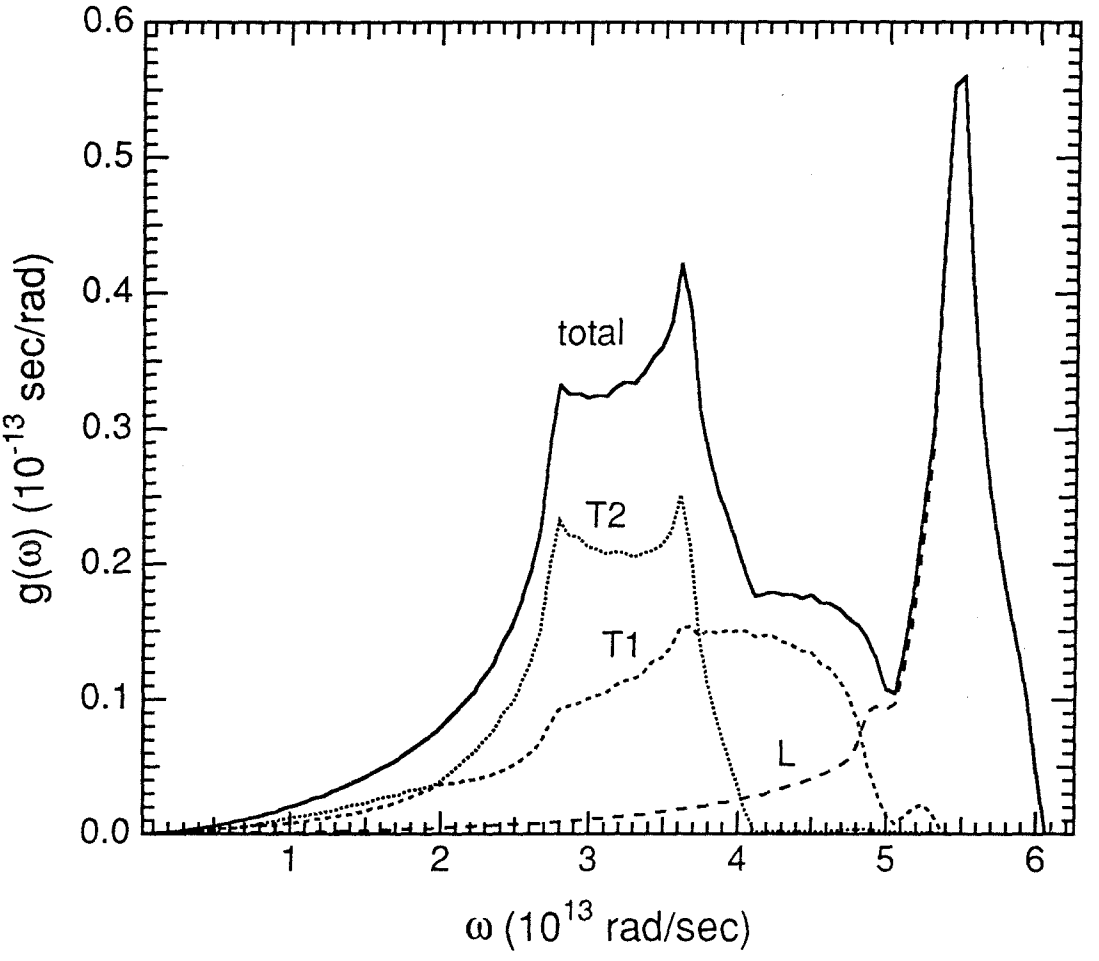

Figure 5.14. Density of vibrational modes for Al metal determined from interatomic force constants. Breakdown into longitudinal and two transverse branches is indicated.

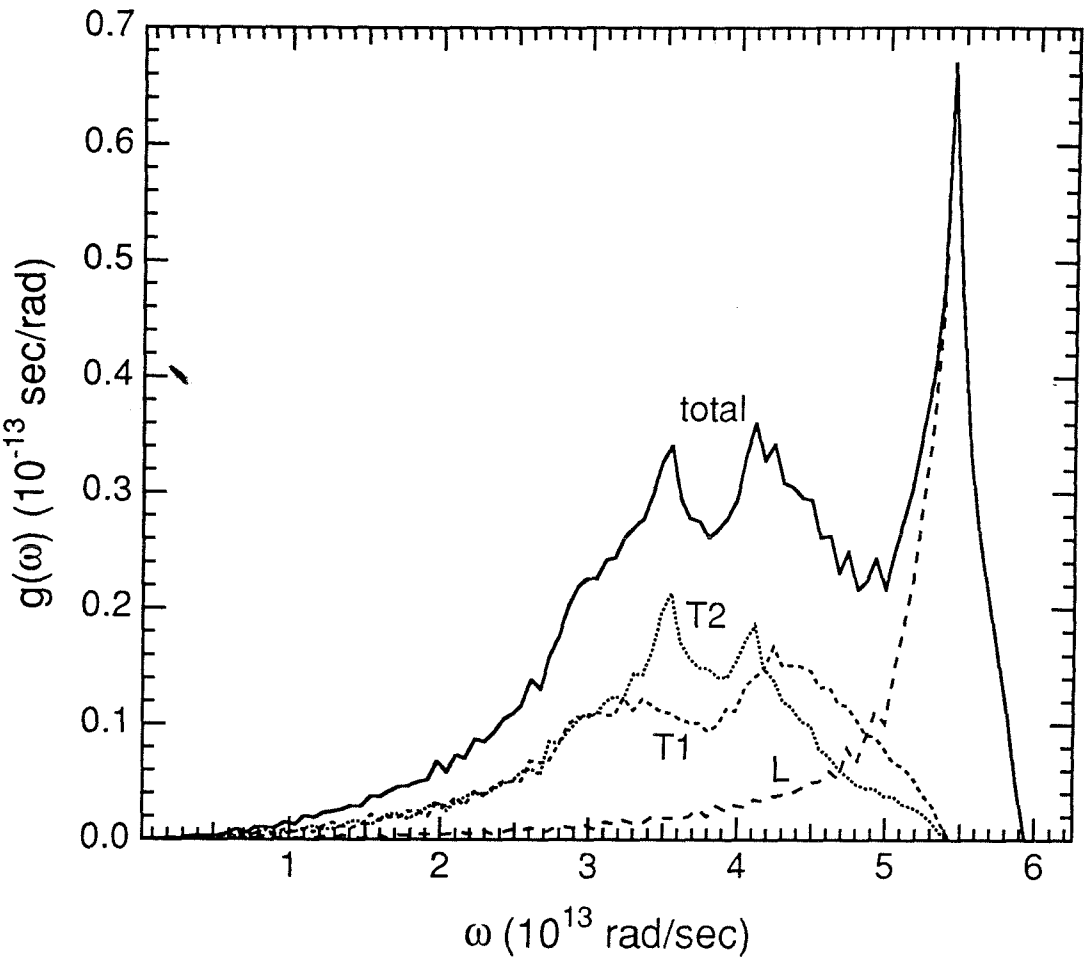

Figure 5.15. Density of vibrational modes for Fe metal determined from interatomic force constants. Breakdown into longitudinal and two transverse branches is indicated.

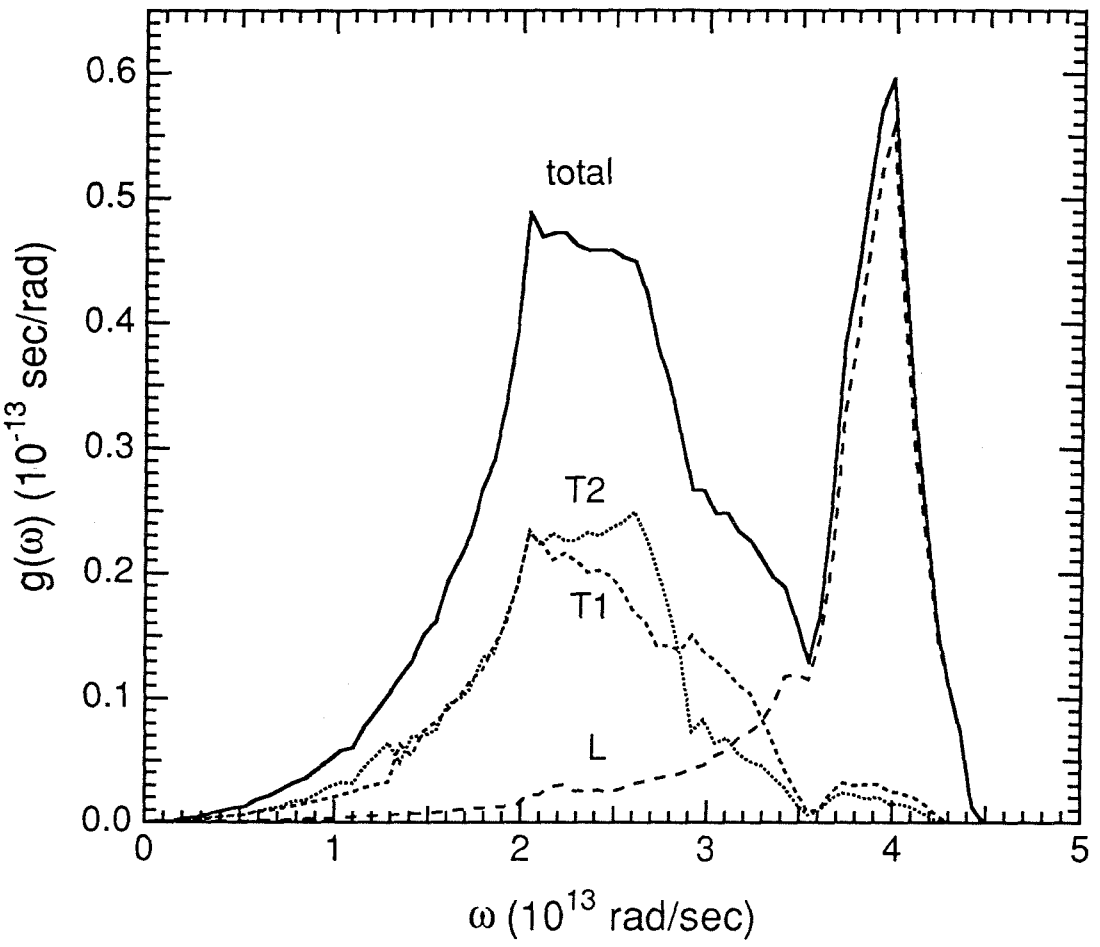

Figure 5.16. Density of vibrational modes for Pd metal determined from interatomic force constants. Breakdown into longitudinal and two transverse branches is indicated.

listed in §C.3. Figures 5.14 through 5.16 display $g(\omega)$ for Al, Fe, and Pd metals. In each case, the breakdown into the longitudinal and two transverse branches is indicated.

Figures 5.17 through 5.19 show the projected density of vibrational modes, $g_{1nn}(\omega)$, for the 1nn shell in Al, Fe, and Pd metals. In comparison to the density of modes, the projected density of modes weights more heavily the higher frequency modes. In particular, the high frequency (or equivalently the short wavelength) longitudinal modes are most heavily weighted. This is as expected because the short wavelength longitudinal modes contribute most heavily to the MSRD between 1nn atoms.

Applying Equation (5.14a), these $g_{1nn}(\omega)$ can be used to determine the vibrational MSRD σ_{1nn}^2 as a function of temperature. Figures 5.20 through 5.22 shows σ_{1nn}^2 calculated from the force constant models for Al, Fe, and Pd. My experimental data are superimposed for comparison, and they match well with the predictions of the force constant models.

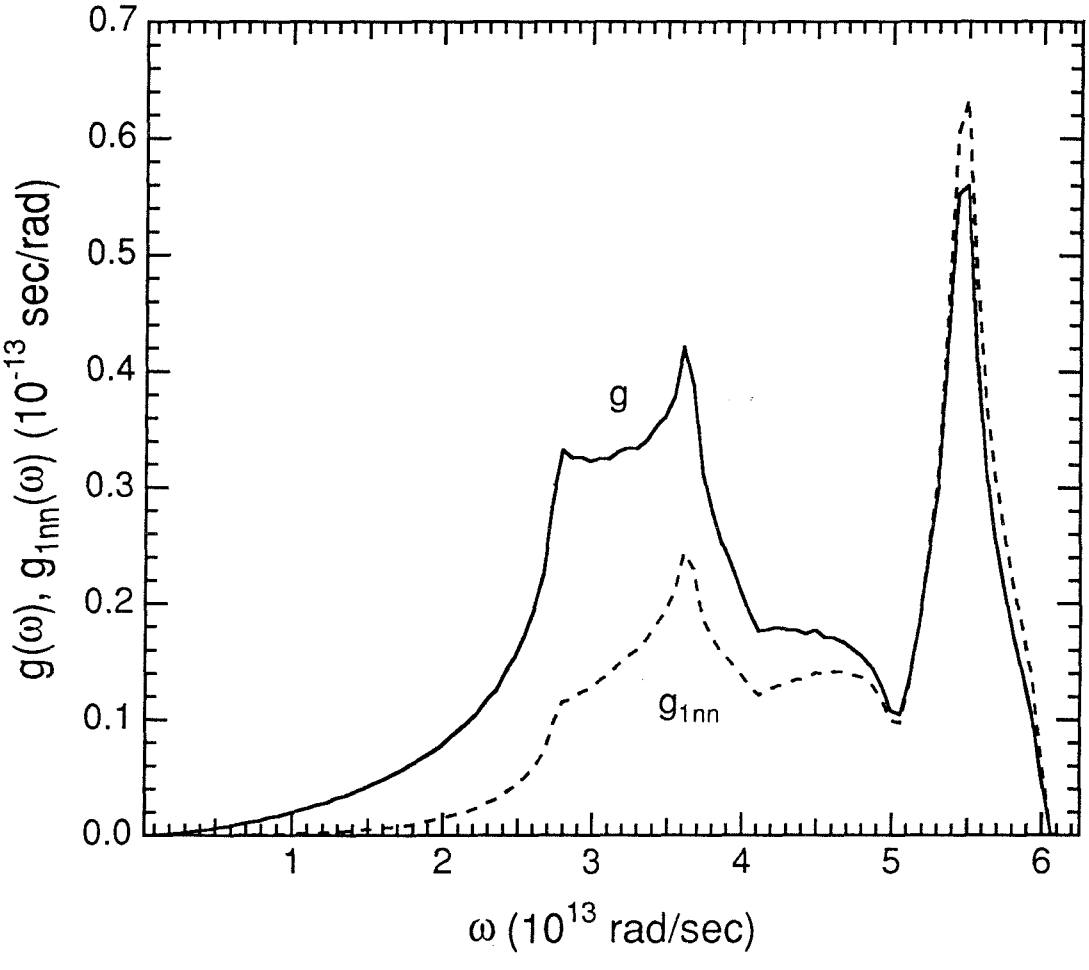

Figure 5.17. Projected density of vibrational modes for 1nn shell (dashed line) compared with density of vibrational modes (solid line) for Al metal.

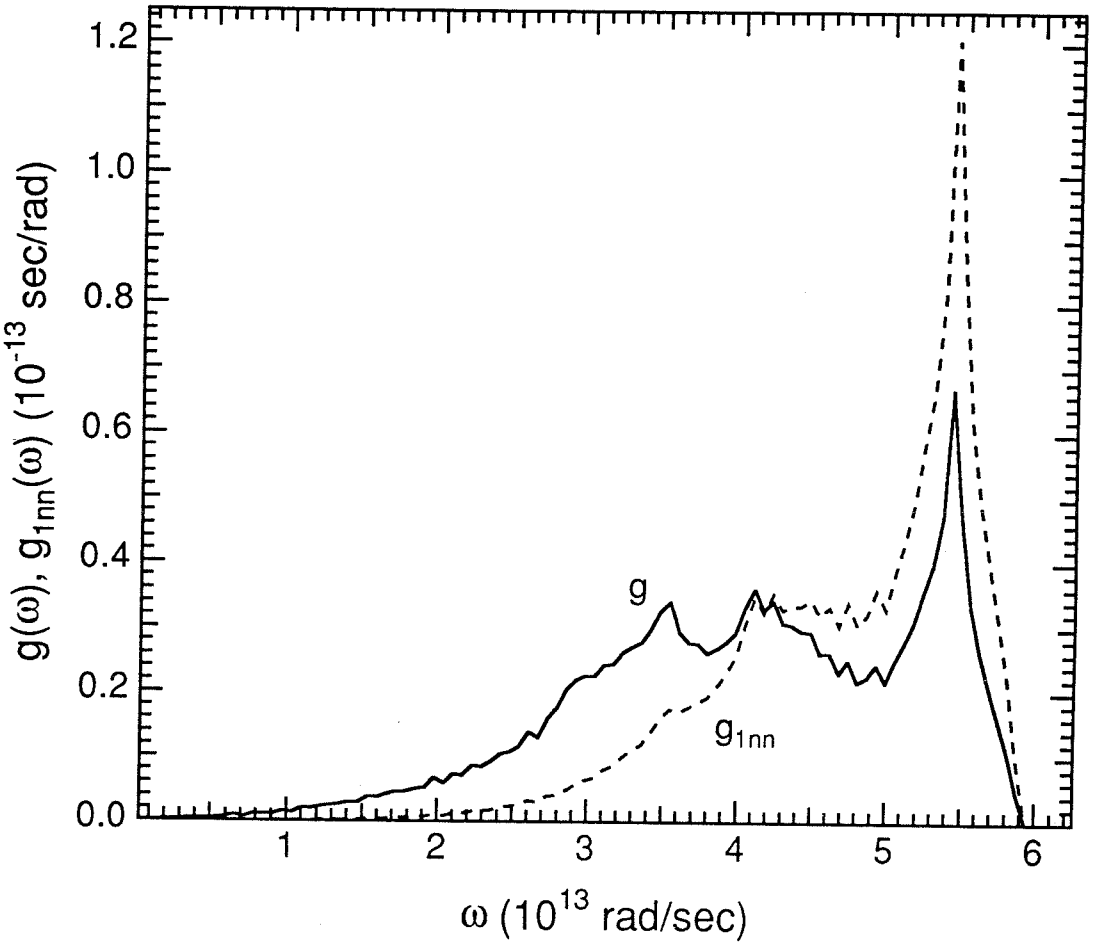

Figure 5.18. Projected density of vibrational modes for 1nn shell (dashed line) compared with density of vibrational modes (solid line) for Fe metal.

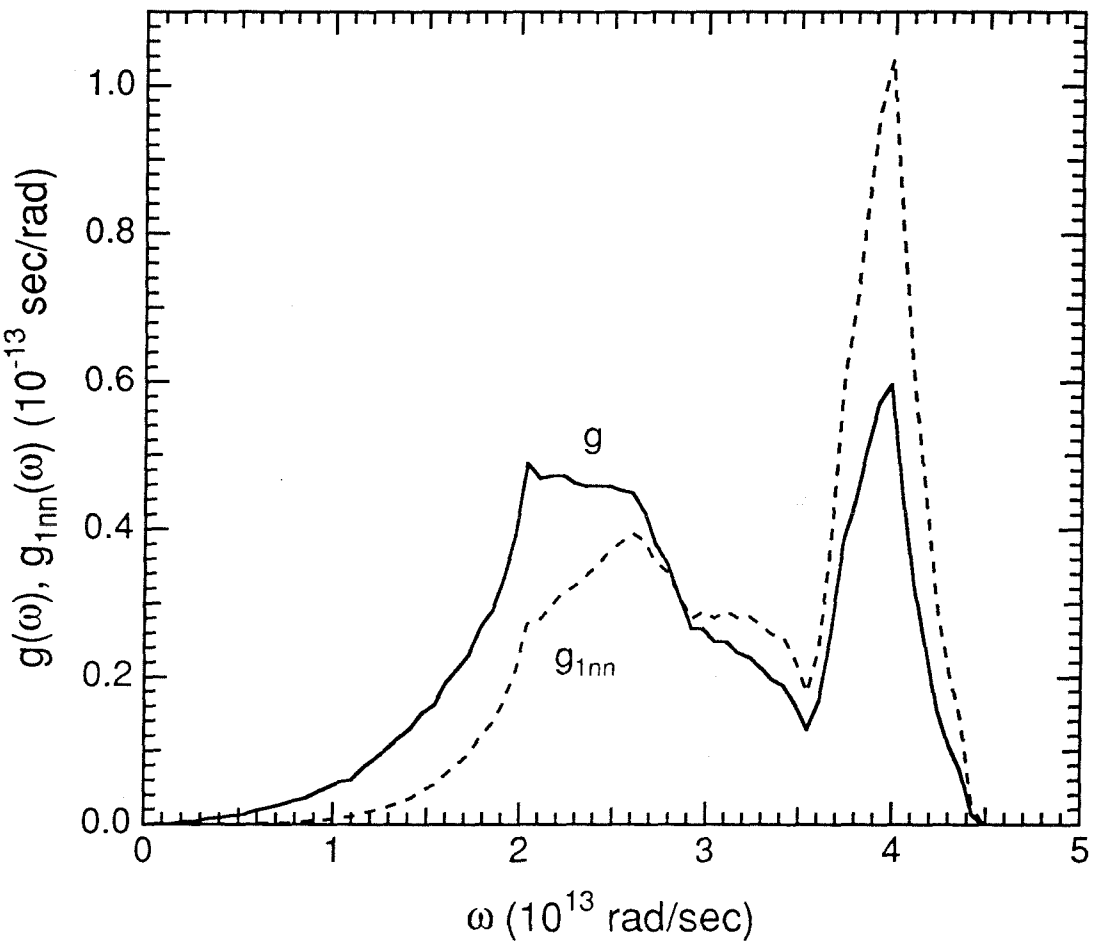

Figure 5.19. Projected density of vibrational modes for 1nn shell (dashed line) compared with density of vibrational modes (solid line) for Pd metal.

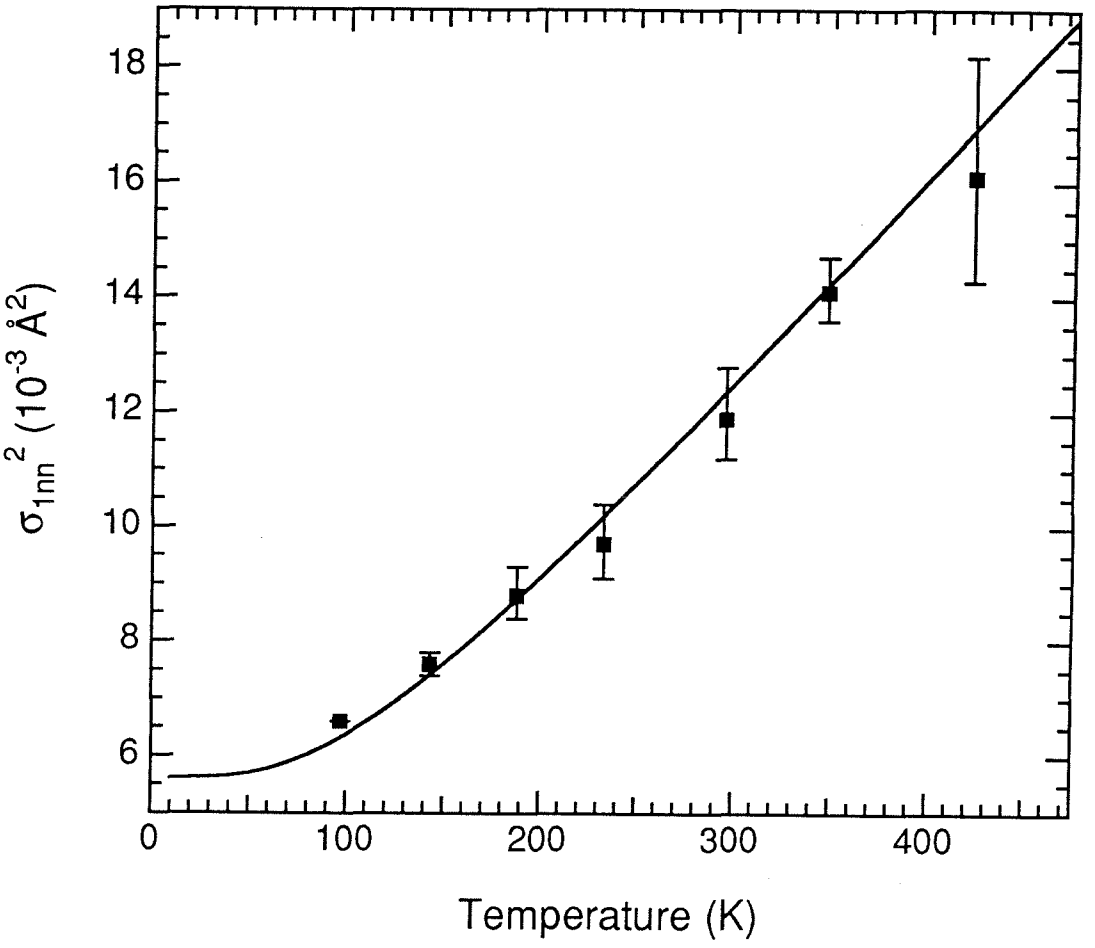

Figure 5.20. Force constant model prediction of 1nn MSRD in Al metal. Experimental data superimposed for comparison, after adjusting absolute offset.

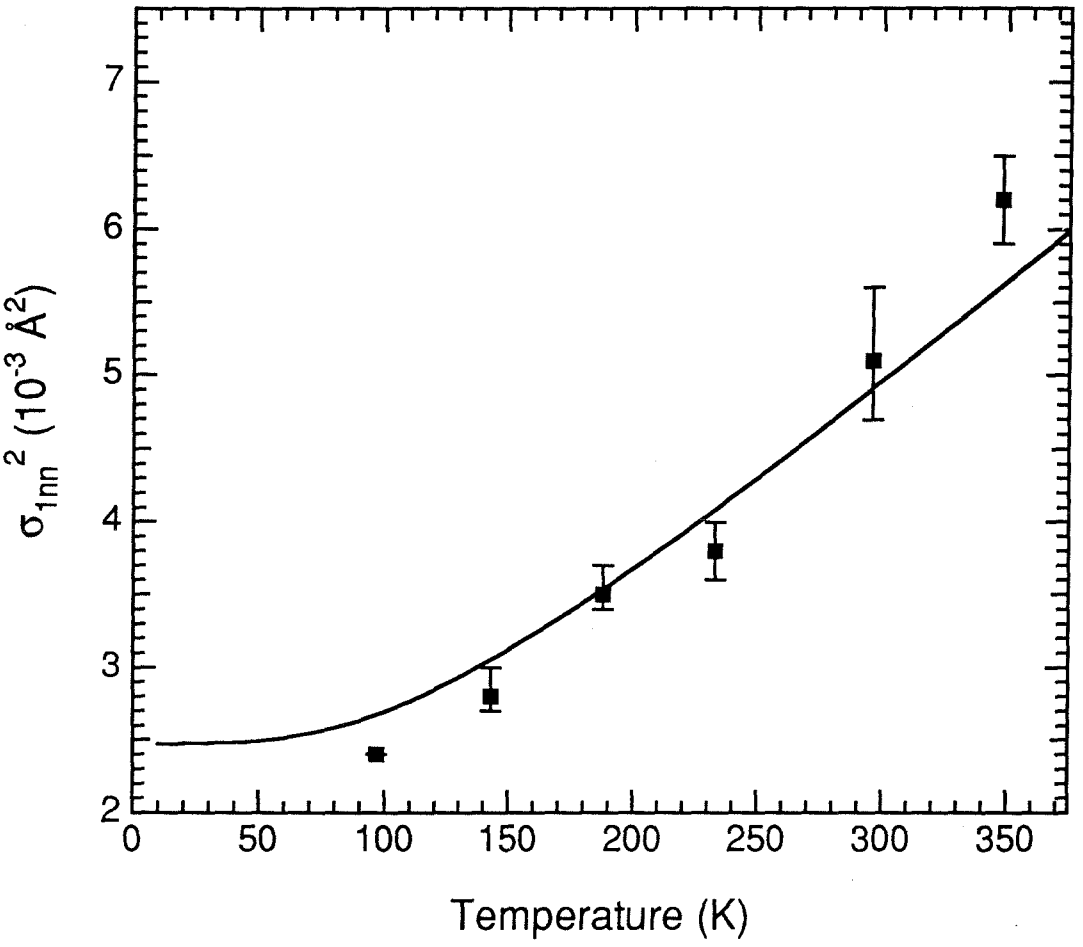

Figure 5.21. Force constant model prediction of 1nn MSRD in Fe metal. Experimental data superimposed for comparison, after adjusting absolute offset.

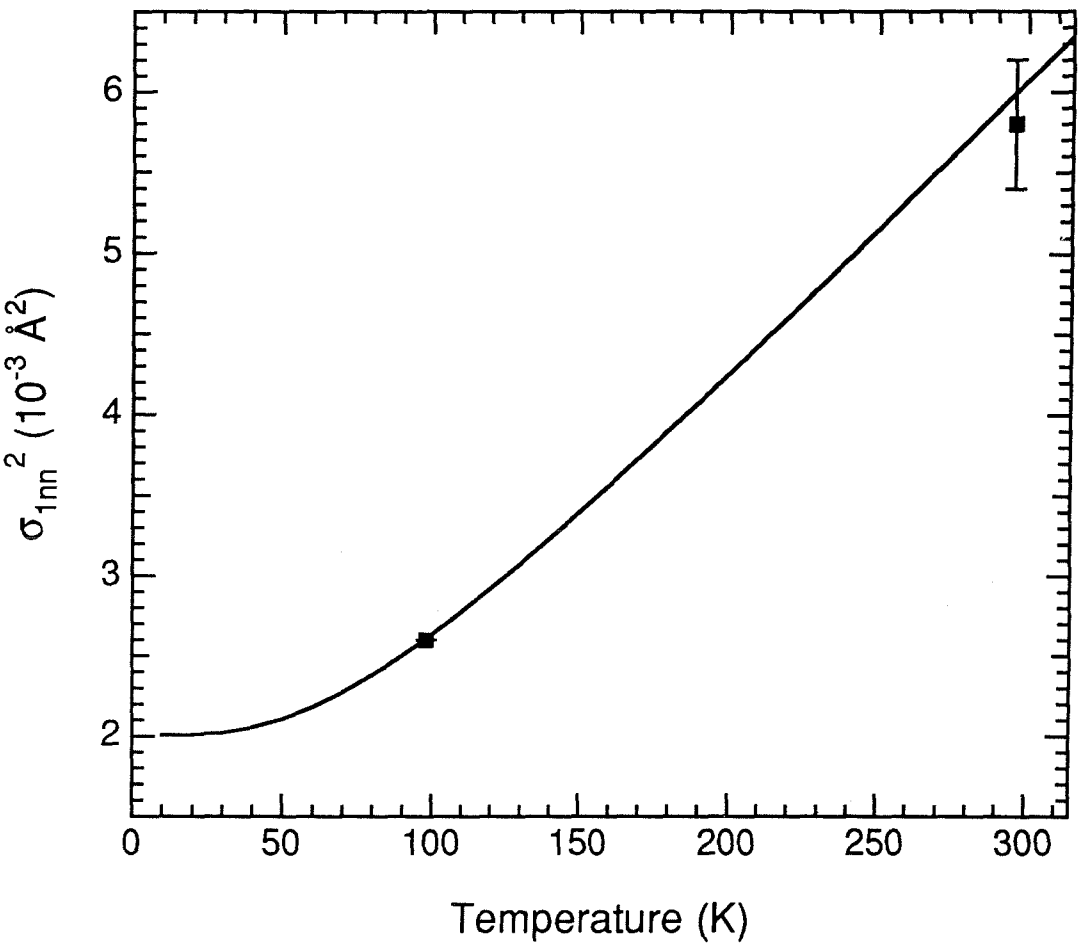

Figure 5.22. Force constant model prediction of 1nn MSRD in Pd metal. Experimental data superimposed for comparison, after adjusting absolute offset.

Chapter 6 Applications to Intermetallic Alloys and Nanocrystalline Materials

EXELFS can be applied to problems in materials science which utilize its sensitivity to local atomic environments. §6.1 presents measurements of chemical short-range order (SRO) and vibrational MSRD in Fe_3Al and Ni_3Al using EXELFS. Differences in vibrational entropy between the ordered and disordered alloys are discussed. §6.2 presents measurements of structural disorder and vibrational MSRD in samples of nanocrystalline Pd and TiO_2.

6.1 Chemical Short-Range Order (SRO) and Vibrational MSRD in Fe_3Al and Ni_3Al

This section presents EXELFS measurements from Fe_3Al and Ni_3Al alloys which were chemically disordered by piston-anvil quenching and high-vacuum evaporation, respectively. Chemical SRO was observed to increase as the as-quenched samples were annealed. Temperature-dependent measurements indicated that the local environments of the annealed samples were "stiffer" than those of the as-quenched samples.

6.1.1 Fe_3Al

Figures 6.1 displays the phase diagram for Fe-Al. The phase diagram shows that near the Fe-25at%Al composition, the equilibrium phase for the alloy below about 500 C is the intermetallic compound Fe_3Al. Intermetallic Fe_3Al has the DO_3 ordered structure which is displayed in Figure 6.2. The DO_3 structure can be thought of as consisting of four interpenetrating fcc sublattices, one of which is occupied by Al atoms. Basically, the Al atoms tend to repel each other as either first or second nearest neighbors.

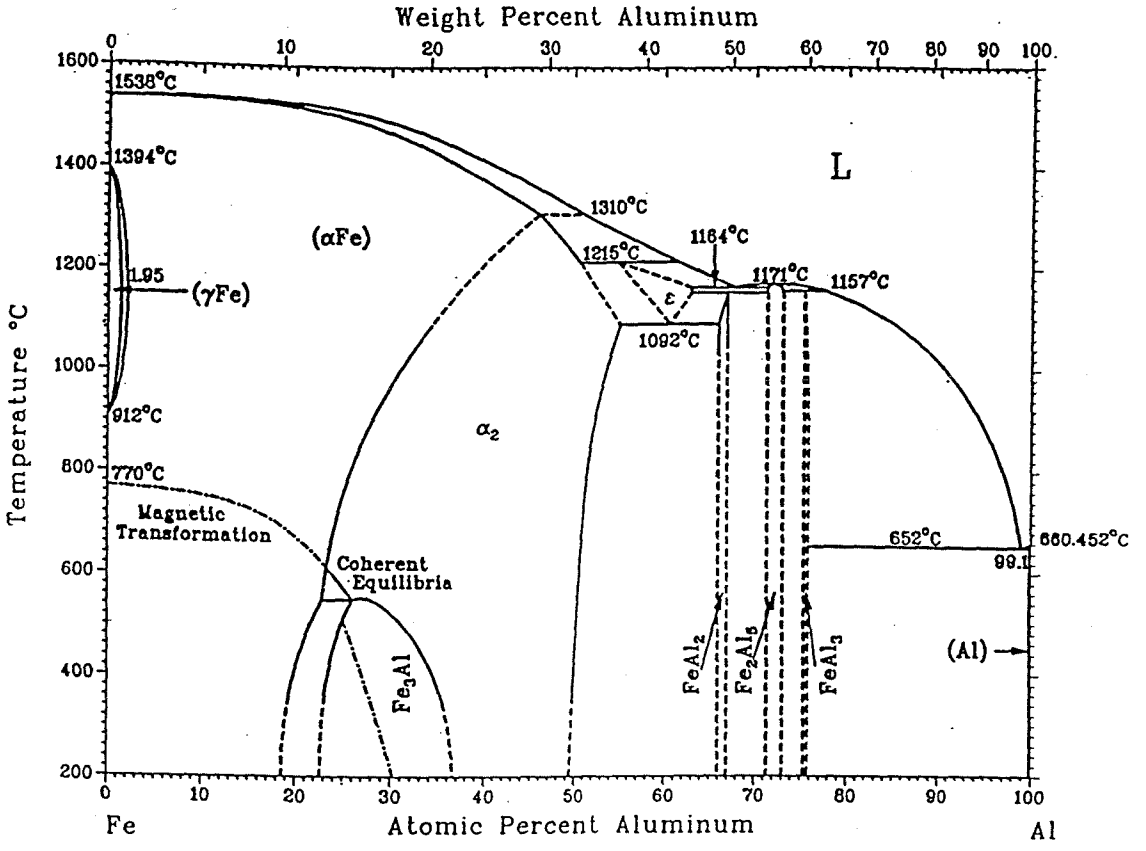

Figure 6.1. Phase diagram for Fe-Al (Massalski, 1986).

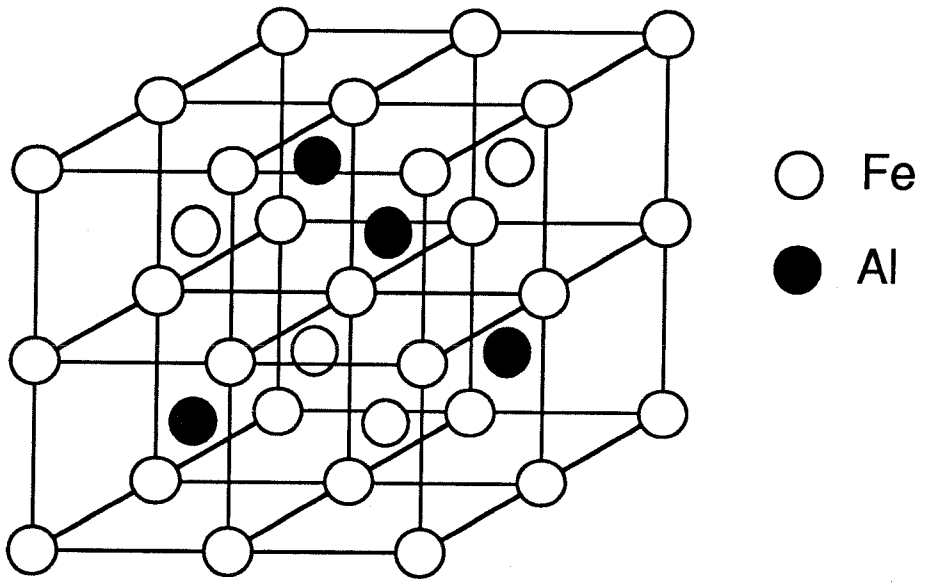

Figure 6.2. DO_3 ordered structure of Fe_3Al.

Piston-anvil quenching, described in §3.1, cools metals at rates on the order of 10^6 K per second. This cooling rate is rapid enough to preserve a significant amount of chemical disorder in the as-quenched bcc Fe_3Al samples. As shown in §3.2, the lack of superlattice peaks in x-ray diffraction spectra indicate a lack of long-range order in the as-quenched samples, while Mössbauer spectrometry shows a lack of short-range order. Both short-range and long-range order evolved when the as-quenched samples were annealed at 300 C.

Since EXELFS is sensitive to the chemical composition of the near-neighbor environment surrounding the central atom, Table 6.1 lists the average number of 1nn and 2nn Fe atoms surrounding either Al or Fe central atoms in disordered and ordered Fe_3Al. The number of neighboring Fe atoms is important because the backscattering in Fe_3Al is dominated by the heavier Fe atoms. It is interesting to note that for both 1nn and 2nn shells, when going from disordered to ordered Fe_3Al, the average number of Fe neighbors surrounding Al central atoms increases by one third, and the average number surrounding Fe central atoms decreases by one ninth.

To show the sensitivity of EXELFS to chemical SRO, the theoretical contribution to the EXELFS from the 1nn shell was calculated for completely disordered and perfectly ordered Fe_3Al. The calculations were made simply by substituting phase shifts and scattering amplitudes from Teo and Lee (1979) into Equation (2.50). For purposes of illustration, Figure 6.3 displays the theoretical Al K EXELFS signal from completely disordered Fe_3Al which has an average of 6 Fe and 2 Al 1nn atoms. It is seen that the 2 Al component of the signal destructively interferes with the dominant 6 Fe component. Fourier transforms of the theoretical EXELFS were taken over ranges in k-space which

	Average number of 1nn Fe atoms	
	Al central atom	Fe central atom
disordered Fe_3Al	6	6
ordered Fe_3Al	8	5.333

	Average number of 2nn Fe atoms	
	Al central atom	Fe central atom
disordered Fe_3Al	4.5	4.5
ordered Fe_3Al	6	4

Table 6.1. Average number of 1nn and 2nn Fe atoms surrounding Al and Fe atoms in completely disordered and perfectly ordered Fe_3Al.

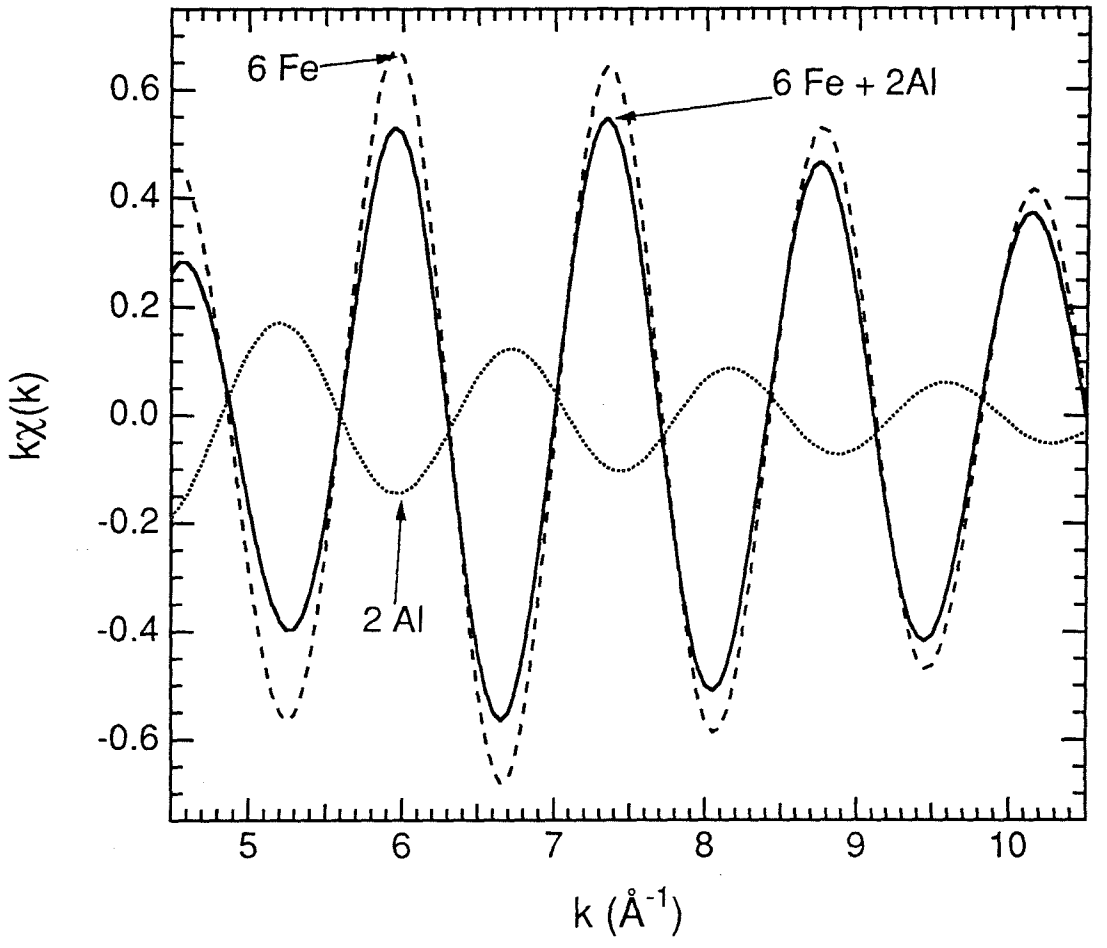

Figure 6.3. Theoretical Al K EXELFS signal from disordered Fe_3Al. The 1nn shell consists of an average of 6 Fe and 2 Al atoms. Signal is broken down into its two components.

are similar to the corresponding ranges in the experimental data. Figure 6.4 presents the magnitude of the FT of the theoretical Al K and Fe L_{23} EXELFS signals. In going from disorder to order, the height of the 1nn peak increases for the Al K EXELFS (which correspond to Al central atoms) and decreases by a smaller amount for the Fe L_{23} EXELFS (which correspond to Fe central atoms). This result makes sense intuitively when one considers the 1nn shell occupancies given in Table 6.1.

Figure 6.5 displays EELS measurements of the Al K and Fe L edges from an electropolished sample of piston-anvil quenched Fe_3Al. Figures 6.6 shows the Al K and Fe L_{23} EXELFS from a sample of the as-quenched Fe_3Al at 296 K. Figure 6.7 compares the magnitude of the FT of the EXELFS from the sample as-quenched and after it was annealed *in situ* at 300 C for 10 and 30 minutes. The positions of the experimental nearest-neighbor peaks are in good agreement with the theoretically calculated positions for the 1nn peaks shown in Figure 6.4. Moreover, after annealing, the increases in the height of the 1nn peak of the Al K EXELFS is accompanied by smaller decreases in the height of the 1nn peak of the Fe L_{23} EXELFS. Figure 6.8 displays the change in the EXELFS amplitudes as a function of annealing time. The quantitative determination of order parameters from these results is complicated by the changing vibrational characteristics of the local environment as the alloy orders. If the local environment stiffens as the alloy orders, then the size of the nearest-neighbor peaks for the annealed samples would increase. Taking this effect into account, my results are consistent with the results from the Mössbauer spectrometry experiments discussed in §3.2. My EXELFS results indicate that the piston-anvil quenched Fe_3Al develops partial short-range order after annealing at 300 C for 10 and 30 minutes.

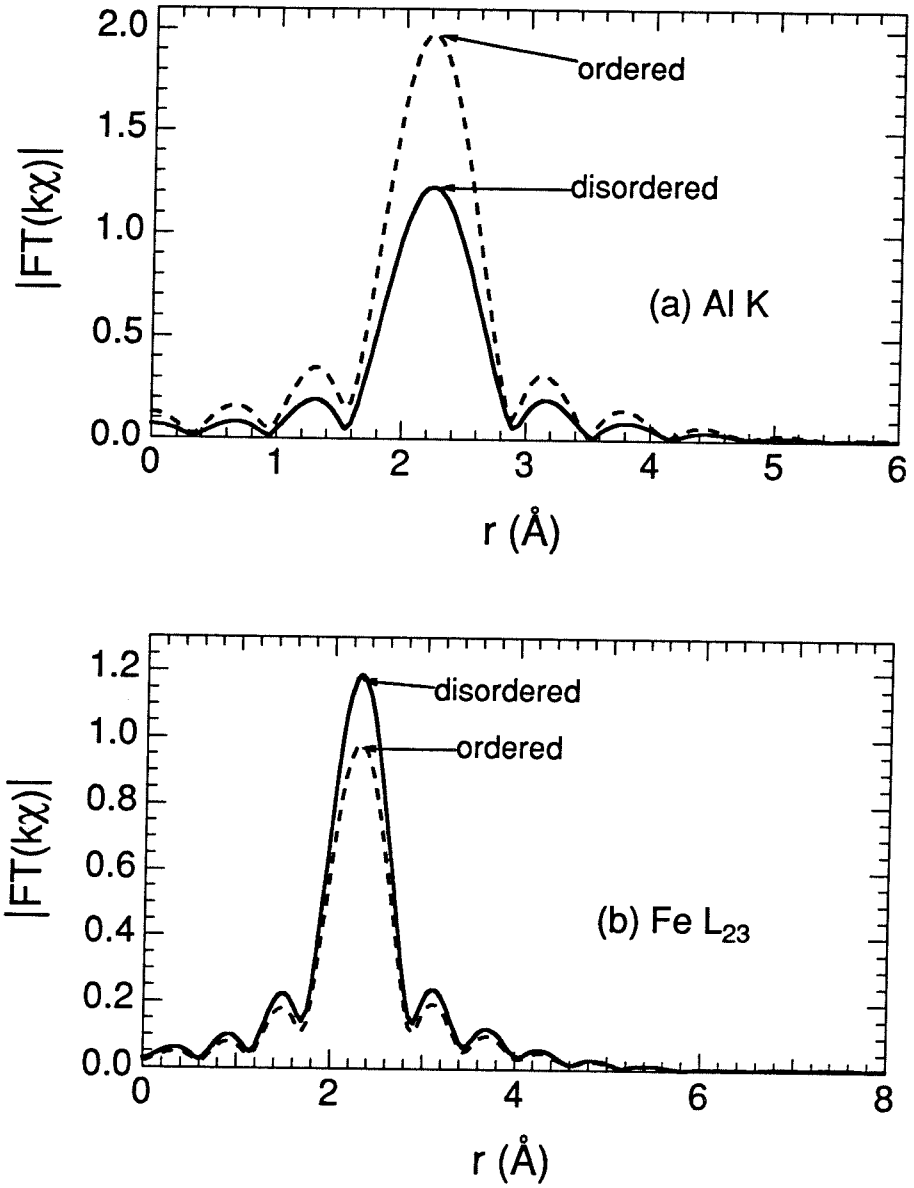

Figure 6.4. Magnitude of FT of theoretical (a) Al K and (b) Fe L_{23} EXELFS from 1nn shell of completely disordered and perfectly ordered Fe_3Al. Transformation range $5 < k < 10$ Å^{-1} for Al K data and $6.5 < k < 12$ Å^{-1} for Fe L_{23} data.

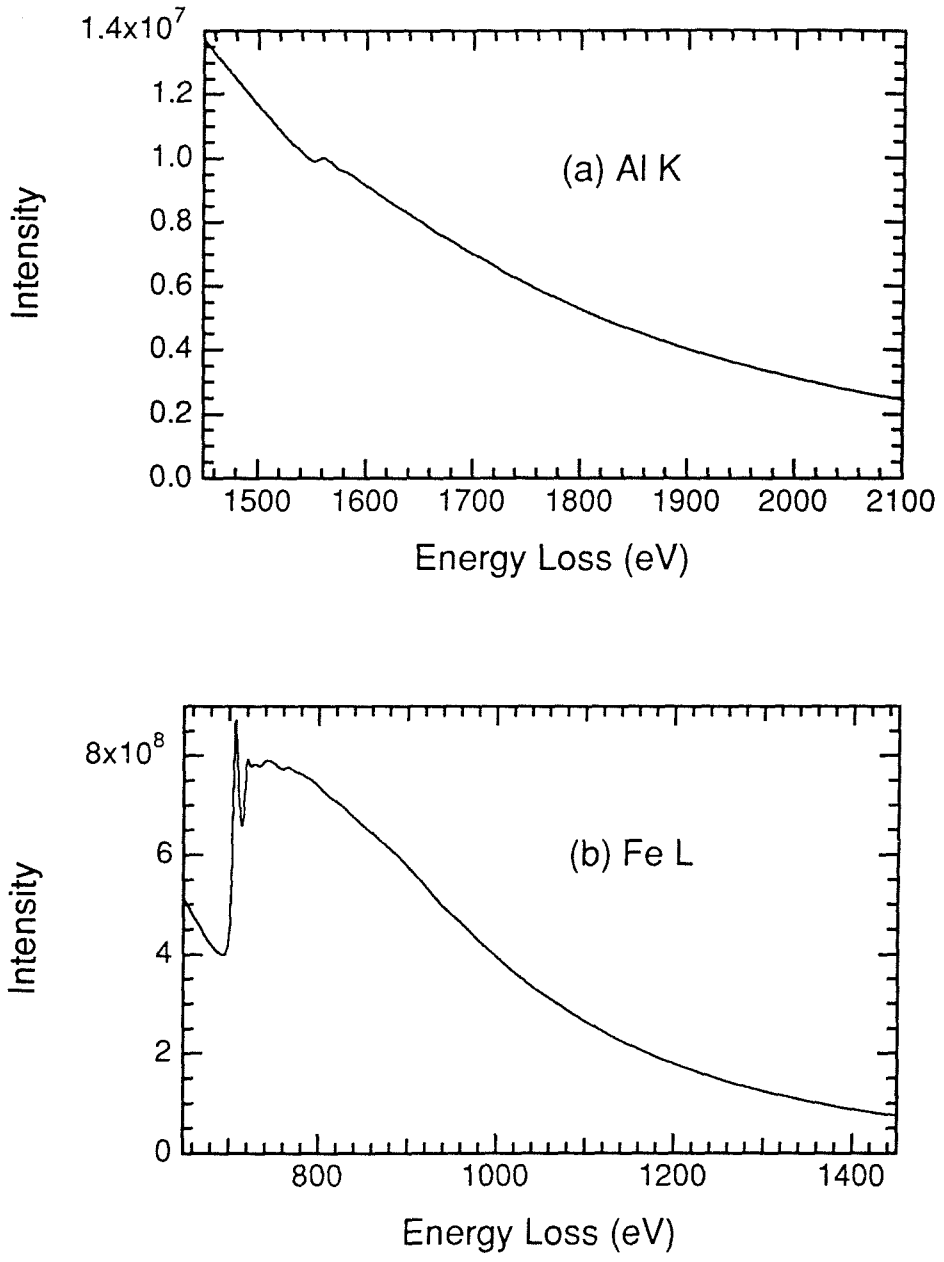

Figure 6.5. EELS measurements of (a) Al K and (b) Fe L edges from Fe_3Al. Spectra were not deconvoluted.

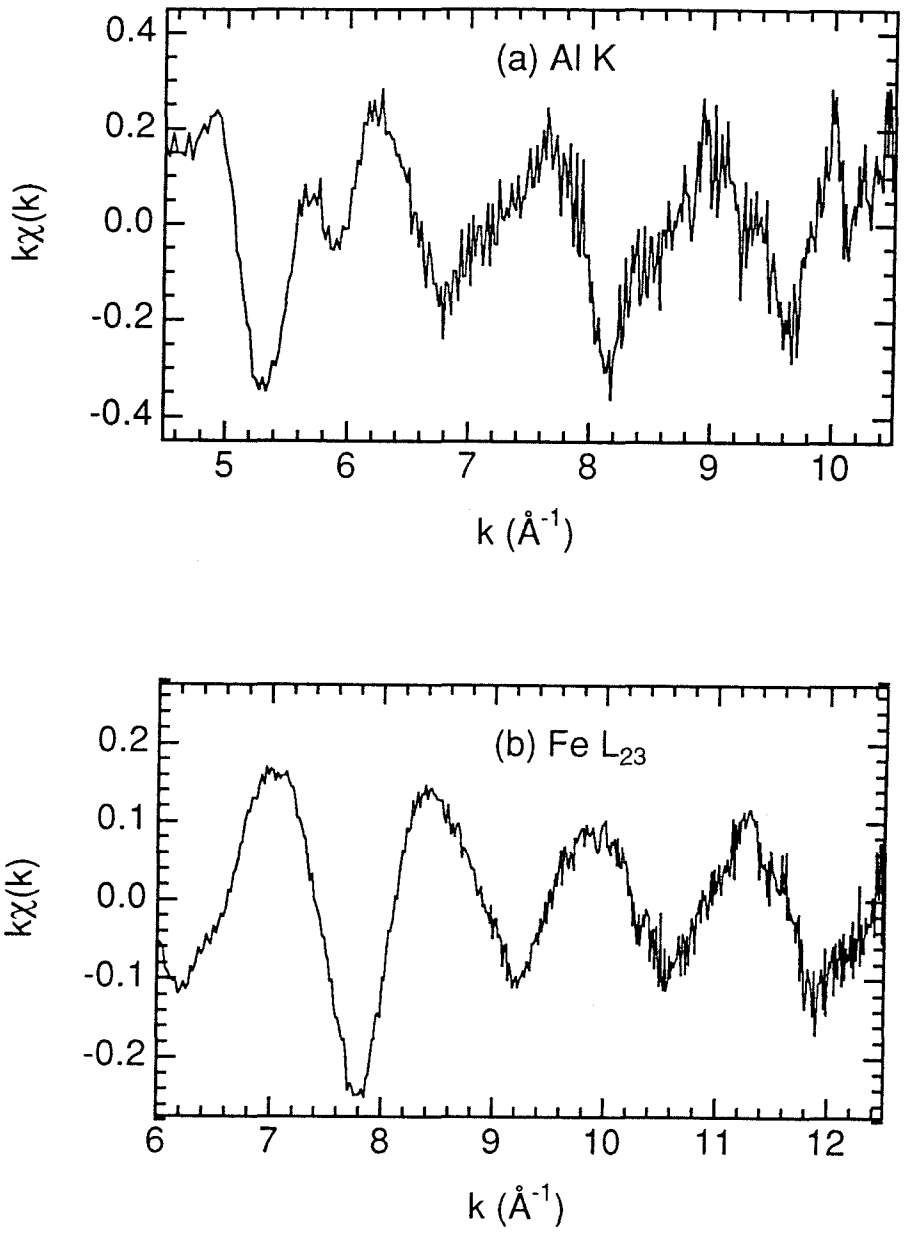

Figure 6.6. (a) Al K and (b) Fe L_{23} EXELFS from as-quenched Fe_3Al at 296 K.

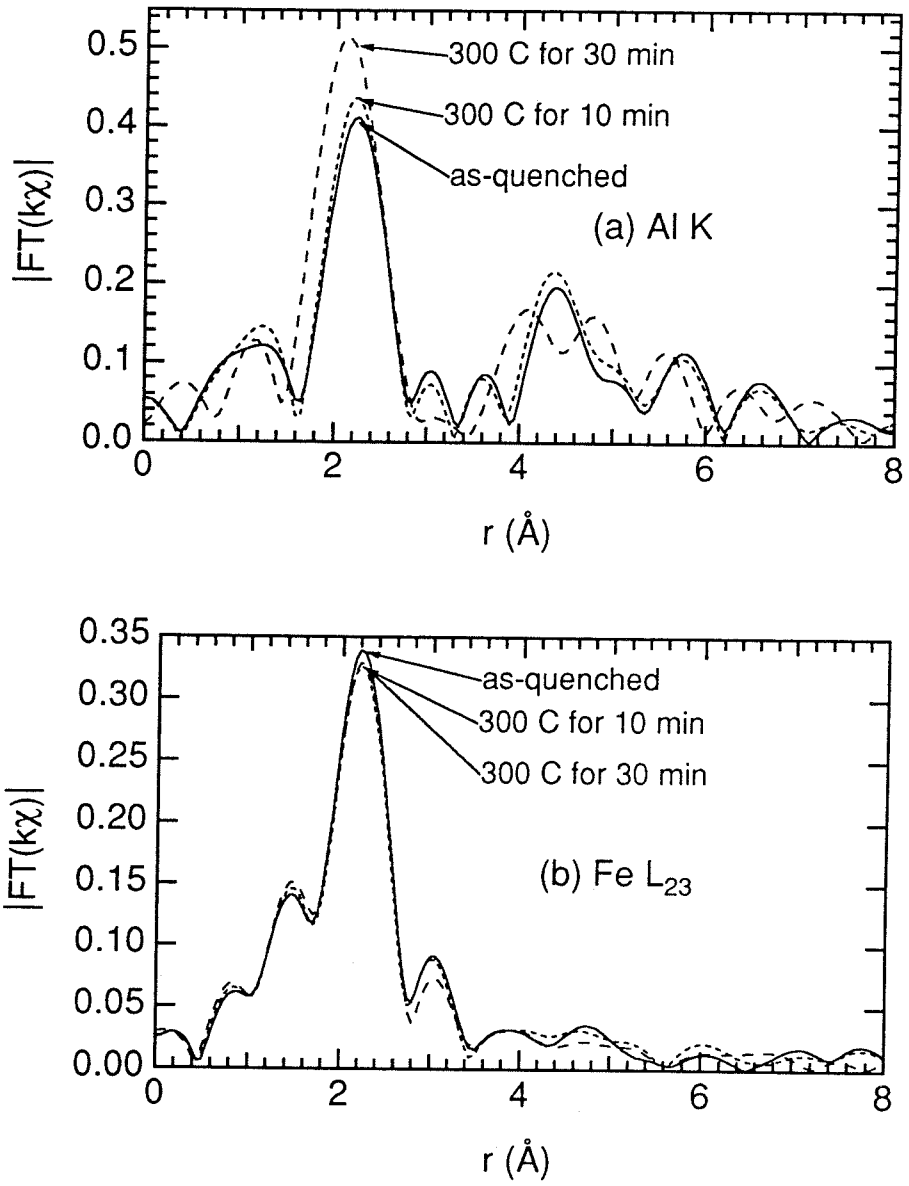

Figure 6.7. Magnitude of FT of experimental (a) Al K ($5 < k < 10$ Å^{-1}) and (b) Fe L_{23} ($6.5 < k < 12$ Å^{-1}) EXELFS from as-quenched Fe_3Al and after annealing *in situ* at 300 C for 10 minutes and 30 minutes. Data taken at 296 K.

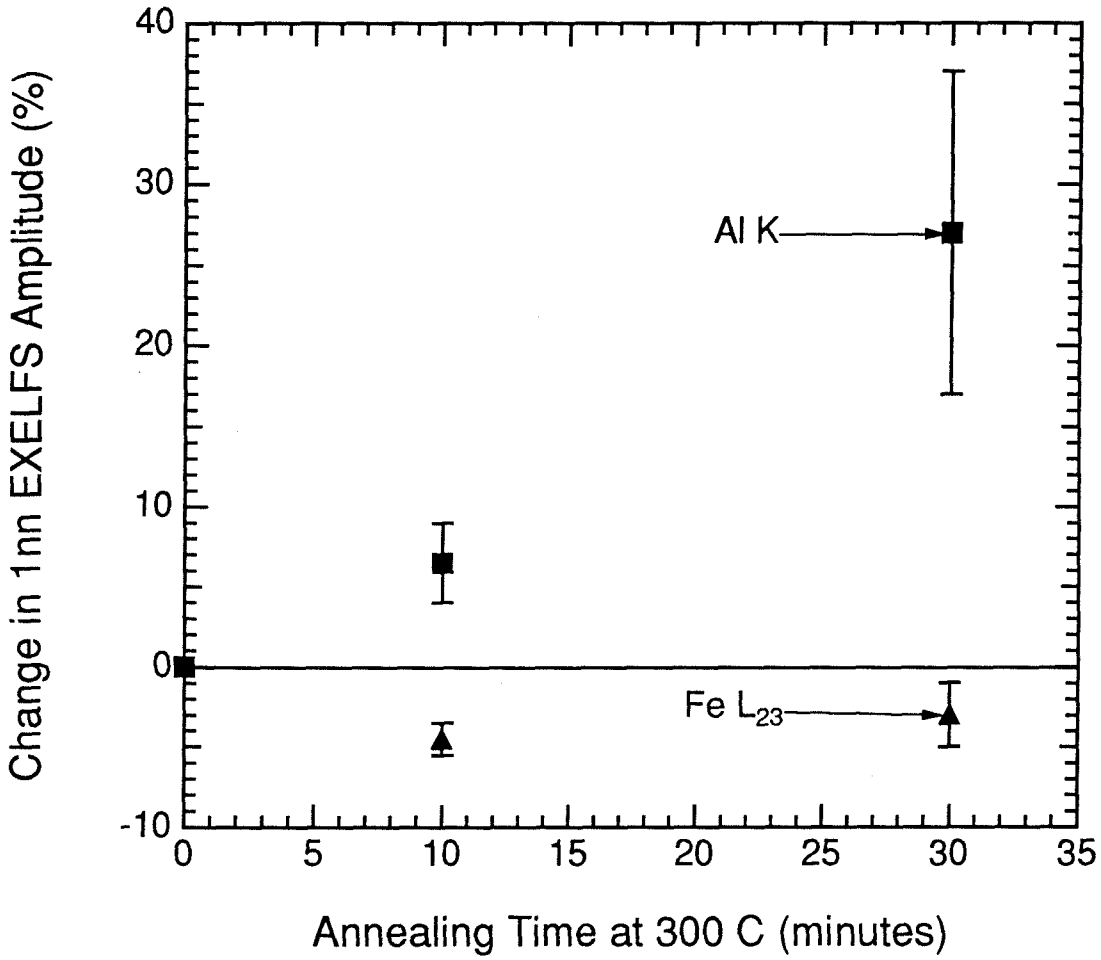

Figure 6.8. Change in 1nn EXELFS amplitudes as function of annealing time at 300 C for piston-anvil quenched Fe_3Al sample. Error bars obtained from values at which variance of least-squares fit increased by 20%.

Temperature-dependent EXELFS measurements can be used to probe vibrational characteristics of local atomic environments. Measurements of local vibrational characteristics can be used to estimate the vibrational entropy of a material.

Consider comparing a state, α, of a material having 3N vibrational modes (ω_1^α, ω_2^α, ..., ω_{3N}^α) to another state, β. In the classical (high temperature) limit, the difference in vibrational entropy between the two states is:

$$\Delta S_{vibr} = S_{vibr}^{\beta} - S_{vibr}^{\alpha} = k_B \ln\left(\frac{\prod_{i=1}^{3N}\omega_i^\alpha}{\prod_{j=1}^{3N}\omega_j^\beta}\right) = k_B \ln\left(\frac{\prod_{i=1}^{3N}\theta_i^\alpha}{\prod_{j=1}^{3N}\theta_j^\beta}\right) \qquad (6.1)$$

where the correspondence between characteristic frequencies ω and characteristic temperatures θ is made using $\hbar\omega = k_B\theta$.

From my temperature-dependent EXELFS experiments on Fe_3Al and Ni_3Al, I obtain local Einstein temperatures of the each atomic species in the two states (disordered and ordered) of the material. In the Einstein model of a solid, each atom behaves like three independent harmonic oscillators and so contributes three of the total 3N vibrational modes of a solid. Therefore, within the Einstein model, Equation (6.1) applied to Fe_3Al or Ni_3Al becomes

$$\Delta S_{vibr} = S_{vibr}^{dis} - S_{vibr}^{ord} = 3Nk_B\left(\frac{3}{4}\ln\left(\frac{\theta_{Fe/Ni}^{ord}}{\theta_{Fe/Ni}^{dis}}\right) + \frac{1}{4}\ln\left(\frac{\theta_{Al}^{ord}}{\theta_{Al}^{dis}}\right)\right) \qquad (6.2)$$

Since the correspondence between local Einstein frequencies and the frequencies of the normal modes is very rough at best, Equation (6.2) is expected to be only qualitatively useful.

The above approach is a mean-field approximation. Another approach would be to interpret my EXELFS results within a pair approximation. Instead of considering individual atoms, a pair approximation considers the interatomic bonds between each pair of 1nn atoms.

For a binary A-B alloy, there are three different types of bonds: A-A, B-B, and A-B bonds. For an alloy that develops chemical order, we expect the A-B bonds to be stiffer than the A-A and B-B bonds (i.e. $\omega_{AB}^2 > \omega_{AA}\omega_{BB}$).

Table 6.2 gives the fraction of each type of 1nn bond in completely disordered and perfectly ordered Fe_3Al (or Ni_3Al).

	Fraction of 1nn bond type		
	Al-Fe (or Al-Ni)	Fe-Fe (or Ni-Ni)	Al-Al
disordered Fe_3Al (or Ni_3Al)	3/8	9/16	1/16
ordered Fe_3Al (or Ni_3Al)	1/2	1/2	0

Table 6.2. Fraction of each type of 1nn bond in completely disordered and perfectly disordered Fe_3Al (or Ni_3Al).

Allowing the frequencies ω_{AlFe}, ω_{FeFe}, and ω_{AlAl} to be dependent on the state of order in the alloy, then the change in vibrational entropy between perfectly disordered and ordered Fe_3Al becomes in the classical limit

$$\Delta S_{vibr} = 3Nk_B \ln \left(\frac{\left(\theta^{ord}_{AlFe}\right)^{1/2}\left(\theta^{ord}_{FeFe}\right)^{1/2}}{\left(\theta^{dis}_{AlFe}\right)^{3/8}\left(\theta^{dis}_{FeFe}\right)^{9/16}\left(\theta^{dis}_{AlAl}\right)^{1/16}} \right) \qquad (6.3)$$

EXELFS is more sensitive to the heavier Fe neighbors than lighter Al neighbors. In fact, a first-order approximation would be to ignore the backscattering from the Al neighbors. In that case, the temperature-dependent Al K EXELFS measures values for θ_{AlFe}, and the temperature-dependent Fe L_{23} EXELFS measures values for θ_{FeFe}. Only values for θ_{AlAl} are not measured by EXELFS and must therefore be estimated.

Figures 6.9 and 6.10 presents the magnitude of the FT of the Al K and Fe L_{23} EXELFS from as-quenched and annealed samples of Fe_3Al at temperatures from 97 K to 348 K. Figures 6.11 and 6.12 display Einstein temperature fits to the Al K and Fe L_{23} 1nn MSRD data from as-quenched and annealed samples. The MSRD data indicate that the local environments of both Al and Fe atoms in Fe_3Al become "stiffer" as the alloy orders.

Using the mean-field approach, I substitute $\theta^{ord}_{Al} = 460 \pm 50$ K, $\theta^{dis}_{Al} = 391 \pm 45$ K, $\theta^{ord}_{Fe} = 430 \pm 30$ K, and $\theta^{dis}_{Fe} = 369 \pm 20$ K into Equation (6.2) to obtain

$$\begin{aligned} \Delta S_{vibr} &= [0.12 \pm 0.12\ (Al)] + [0.34 \pm 0.20\ (Fe)]\ k_B/atom \\ &= +0.46 \pm 0.23\ k_B/atom \end{aligned} \qquad (6.4)$$

Using the pair approach, I substitute $\theta^{ord}_{AlFe} = 460 \pm 50$ K, $\theta^{dis}_{AlAl} = \theta^{dis}_{AlFe} = 391 \pm 45$ K, $\theta^{ord}_{FeFe} = 430 \pm 30$ K, and $\theta^{dis}_{FeFe} = 369 \pm 20$ K into Equation (6.3) to obtain

$$\Delta S_{vibr} = +0.48 \pm 0.25\ k_B/atom \qquad (6.5)$$

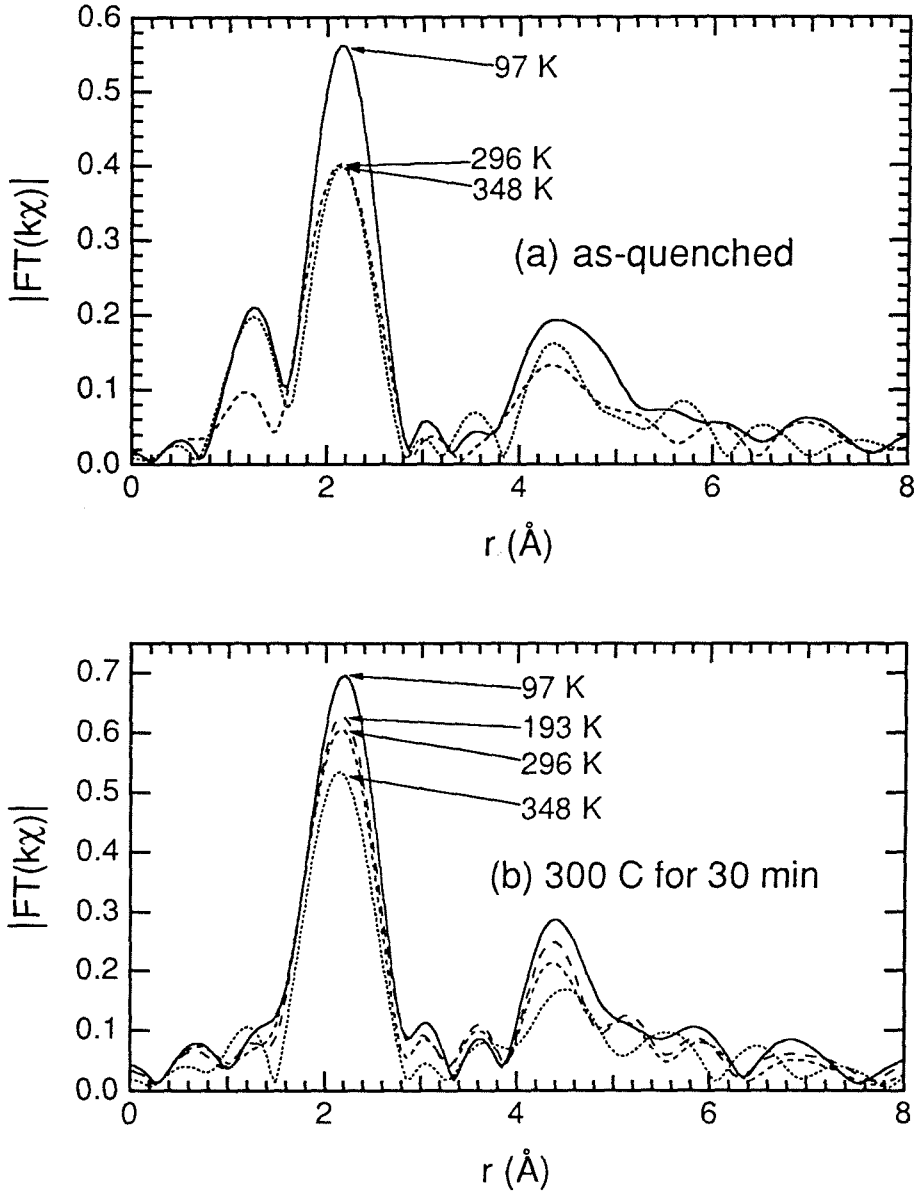

Figure 6.9. Temperature dependence of magnitude of FT of Al K EXELFS ($5 < k < 10$ Å^{-1}) from (a) as-quenched Fe_3Al and (b) after annealing at 300 C for 30 minutes.

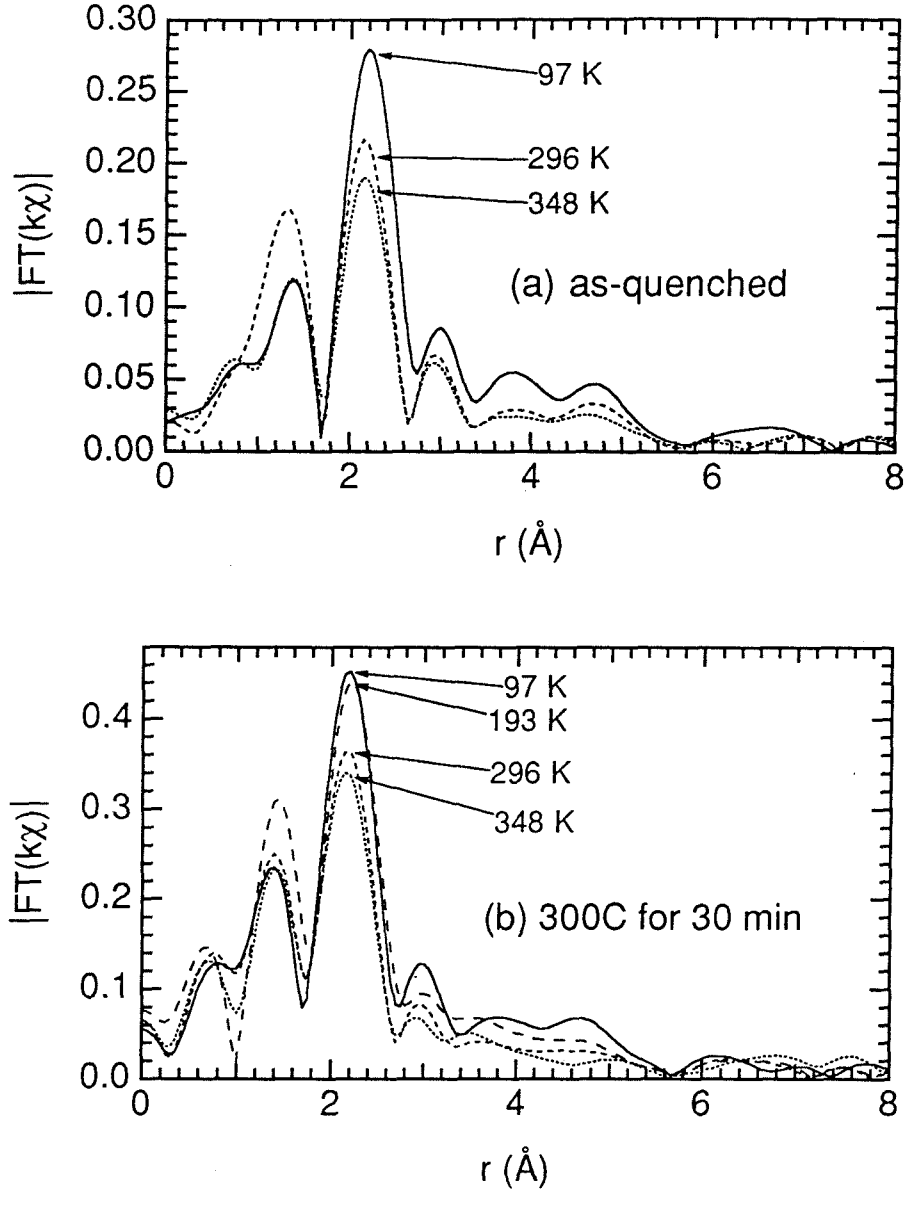

Figure 6.10. Temperature dependence of magnitude of FT of Fe L_{23} EXELFS ($6.5 < k < 12$ Å^{-1}) from (a) as-quenched Fe_3Al and (b) after annealing at 300 C for 30 minutes.

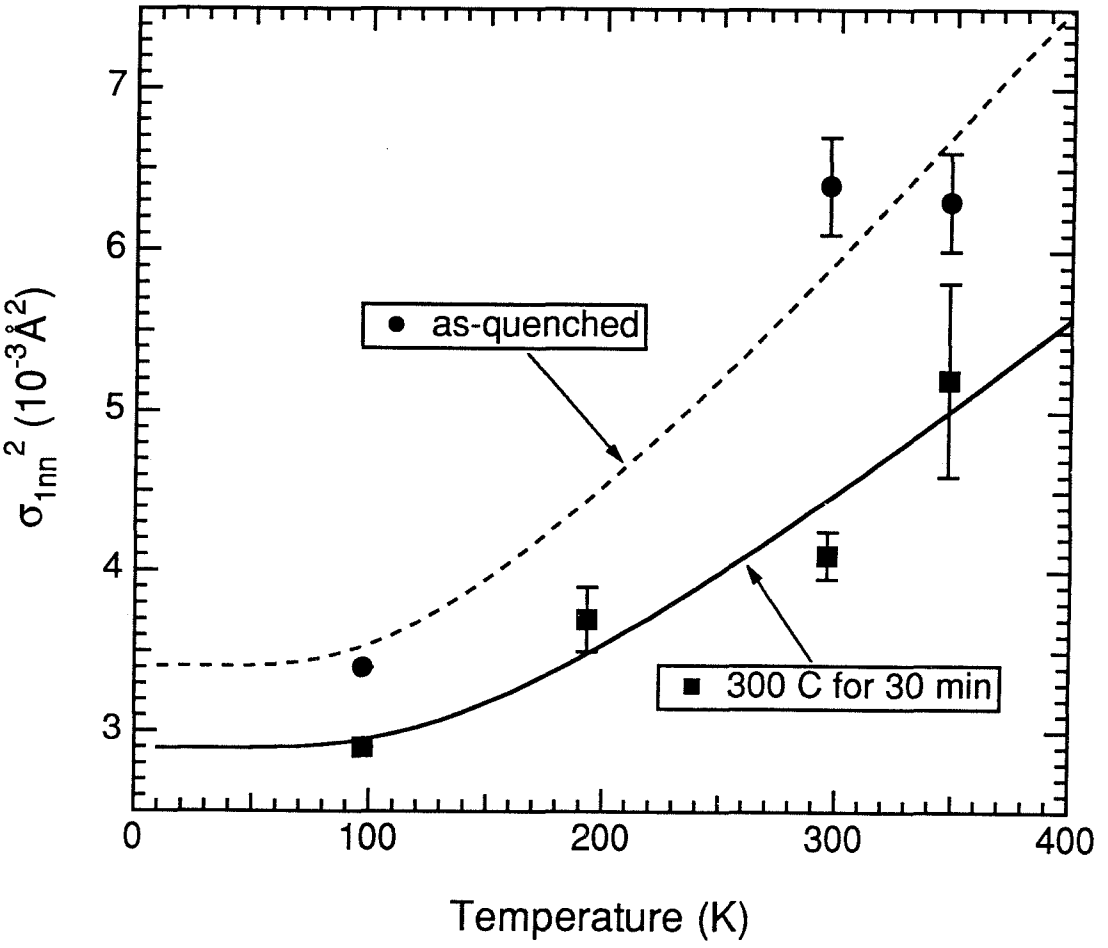

Figure 6.11. Einstein model fits to Al K EXELFS 1nn MSRD data from as-quenched Fe_3Al and after annealing at 300 C for 30 minutes. Absolute offsets of data were allowed to float. Fits gave θ_E = 391 ± 45 K for as-quenched Fe_3Al and θ_E = 460 ± 50 K after annealing.

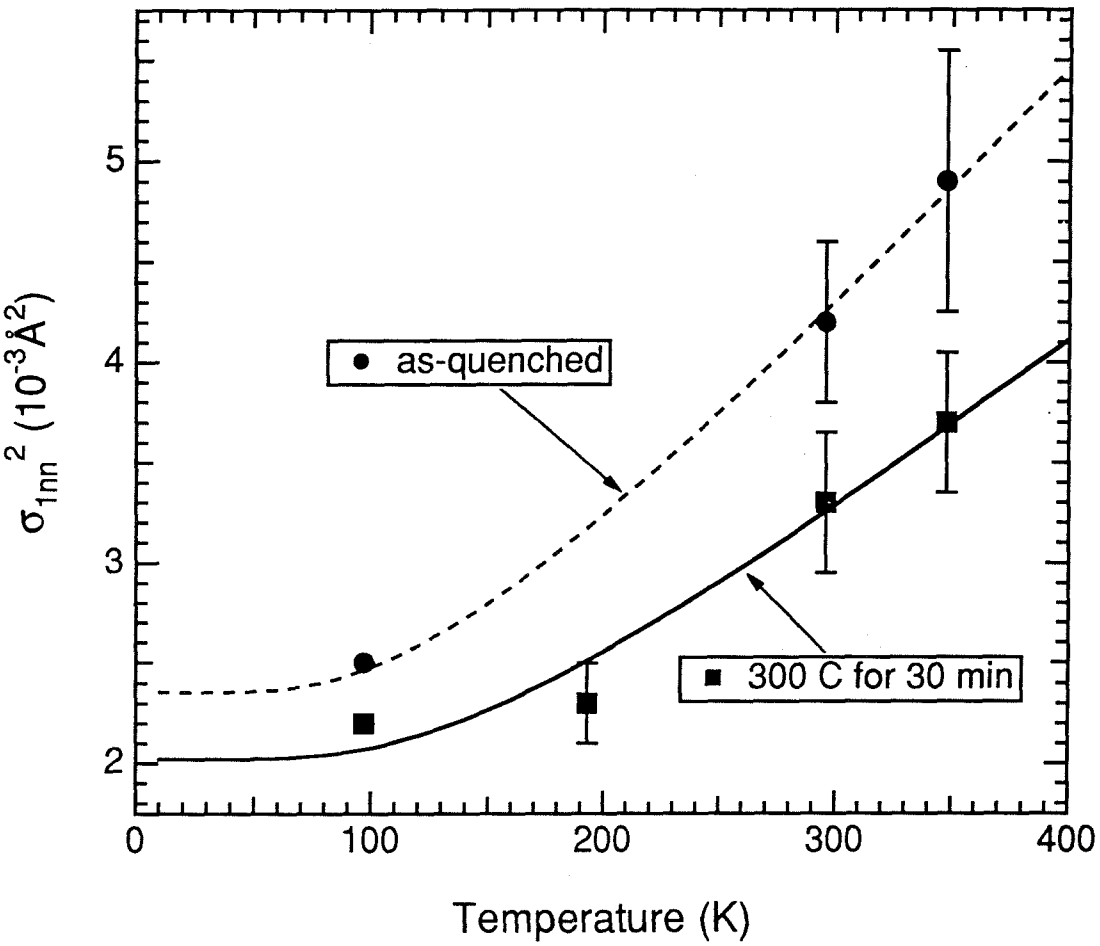

Figure 6.12. Einstein model fits to Fe L_{23} EXELFS 1nn MSRD data from as-quenched Fe_3Al and after annealing at 300 C for 30 minutes. Absolute offsets of data were allowed to float. Fits gave θ_E = 369 ± 20 K for as-quenched Fe_3Al and θ_E = 430 ± 30 K after annealing.

Note that in the above calculation, θ_{AlAl}^{dis} was estimated to be the same as θ_{AlFe}^{dis}.

Both the mean-field and pair approaches give approximately the same value for the difference in vibrational entropy between disordered and ordered Fe_3Al. While these values ΔS_{vibr} are slightly less than the configurational entropy of mixing for the A_3B alloys (+0.56 k_B/atom), they are large enough to affect the relative thermodynamic stabilities of the disordered and ordered states of Fe_3Al.

The sign of ΔS_{vibr} indicates that the vibrational entropy of the disordered state is greater than the ordered state. This would suppress the critical temperature for ordering in theoretical calculations of phase diagrams because the reduced entropy of the ordered phase would make it less stable at higher temperatures.

6.1.2 Ni_3Al

Now consider my EXELFS measurements from Ni_3Al. Figure 6.13 displays the phase diagram for Ni-Al. The phase diagram shows the intermetallic compound Ni_3Al near the Ni-25at%Al composition. Intermetallic Ni_3Al has the $L1_2$ ordered structure which is displayed in Figure 6.14. The $L1_2$ structure is an fcc lattice where the Ni atoms occupy the face sites and the Al atoms occupy the corner sites. This maximizes the number of unlike 1nn atoms. Table 6.3 lists the average number of 1nn Ni atoms surrounding either Al or Ni central atoms in chemically disordered and ordered Ni_3Al.

The critical temperature for the $L1_2$ ordering of Ni_3Al has been estimated to be near its melting temperature of 1385 C (Corey and Lisowsky, 1967; Cahn et al., 1987a; Bremer et al., 1988). This high critical temperature prevents the

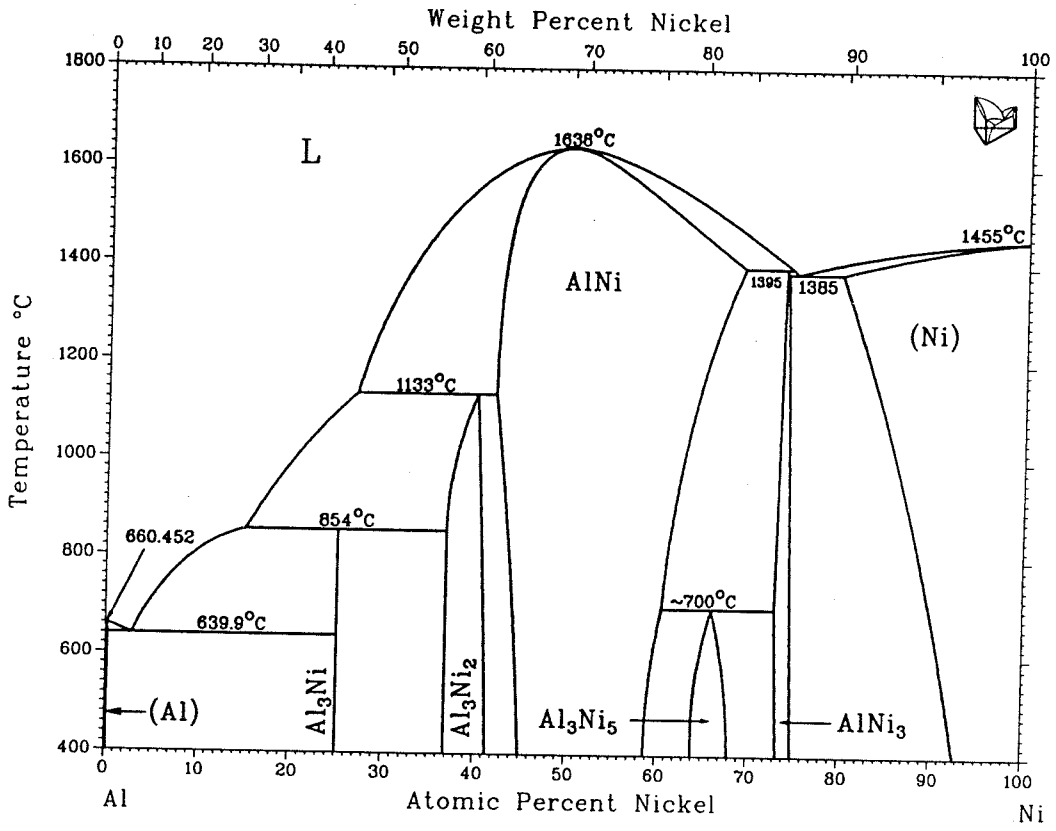

Figure 6.13. Phase diagram for Ni-Al (Massalski, 1986).

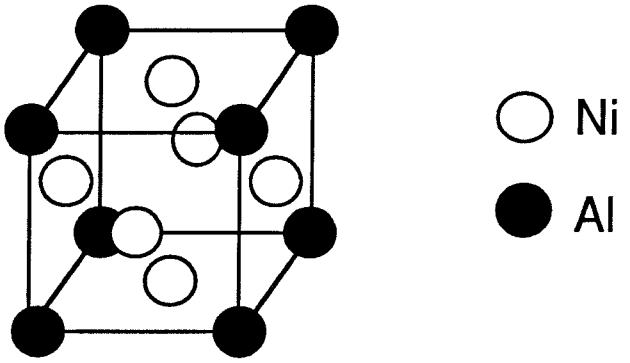

Figure 6.14. $L1_2$ ordered structure of Ni_3Al.

	Average number of 1nn Ni atoms	
	Al central atom	Ni central atom
disordered Ni_3Al	9	9
ordered Ni_3Al	12	8

Table 6.3. Average number of 1nn Ni atoms surrounding Al and Ni atoms in completely disordered and perfectly ordered Ni_3Al.

preparation of disordered fcc Ni_3Al by piston-anvil quenching from the melt (Inoue et al., 1983; Horton and Liu, 1985; Cahn et al., 1987b). High-vacuum evaporation, described in §3.1, cools metals at extremely high effective quenching rates. As discussed in §3.2, high-vacuum evaporation can successfully prepare disordered samples of fcc Ni_3Al.

Figure 6.15 presents the magnitude of the FT of theoretical Al K and Ni L_{23} EXELFS from completely disordered and perfectly ordered Ni_3Al. In going from disorder to order, the height of the 1nn peak increases for the Al K EXELFS and decreases by a smaller amount for the Ni L_{23} EXELFS. This result makes sense intuitively given Table 6.3 and is similar to the calculation for Fe_3Al shown in Figure 6.4.

Figure 6.16 displays EELS measurements of the Al K and Ni L edges from a sample of evaporated Ni_3Al. Figure 6.17 shows the Al K and Ni L_{23} EXELFS from the sample of as-evaporated Ni_3Al at 296 K. Figure 6.18 compares the magnitude of the FT of the EXELFS from the sample as-evaporated and after it was annealed *in-situ* at 150 C for 70 minutes. The increase in the height of the 1nn peak of the Al K EXELFS is accompanied by a smaller decrease in the height of the 1nn peak of the Ni L_{23} EXELFS. Figure 6.19 displays the change in EXELFS amplitudes as a function of annealing time. My EXELFS results indicate that the evaporated Ni_3Al undergoes short-range ordering at the relatively low temperature of 150 C. This evidence supports the hypothesis that the relaxation observed near 150 C in Figure 3.7 is associated with the onset of short-range ordering.

Figures 6.20 and 6.21 present the magnitude of the FT of the Al K and Ni L_{23} EXELFS from as-evaporated and annealed samples of Ni_3Al at temperatures from 105 K to 295 K. Figures 6.22 and 6.23 display Einstein

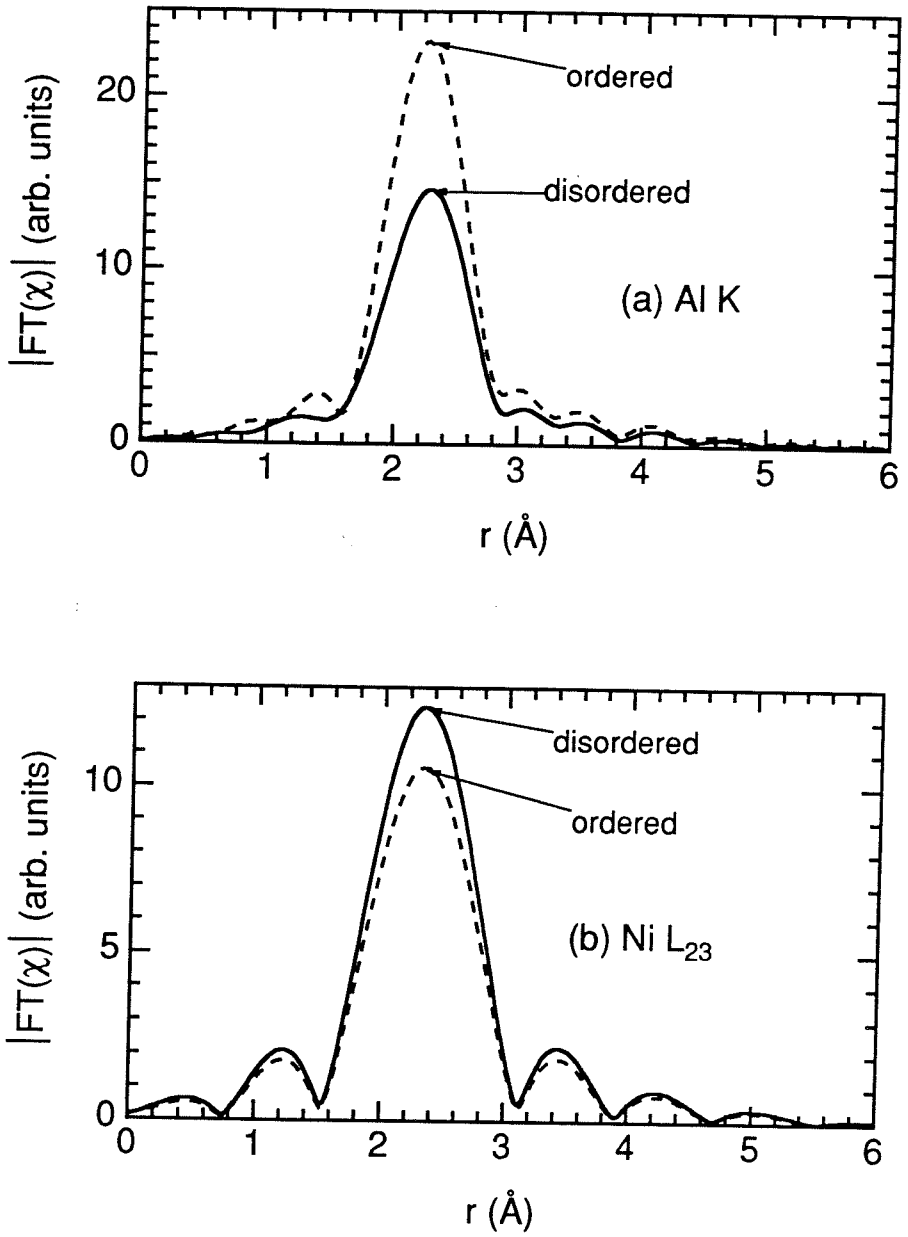

Figure 6.15. Magnitude of FT of theoretical (a) Al K and (b) Ni L_{23} EXELFS from 1nn shell of completely disordered and perfectly ordered Ni_3Al. Transformation range $4 < k < 10$ Å^{-1} for Al K data and $8.5 < k < 12.5$ Å^{-1} for Ni L_{23} data.

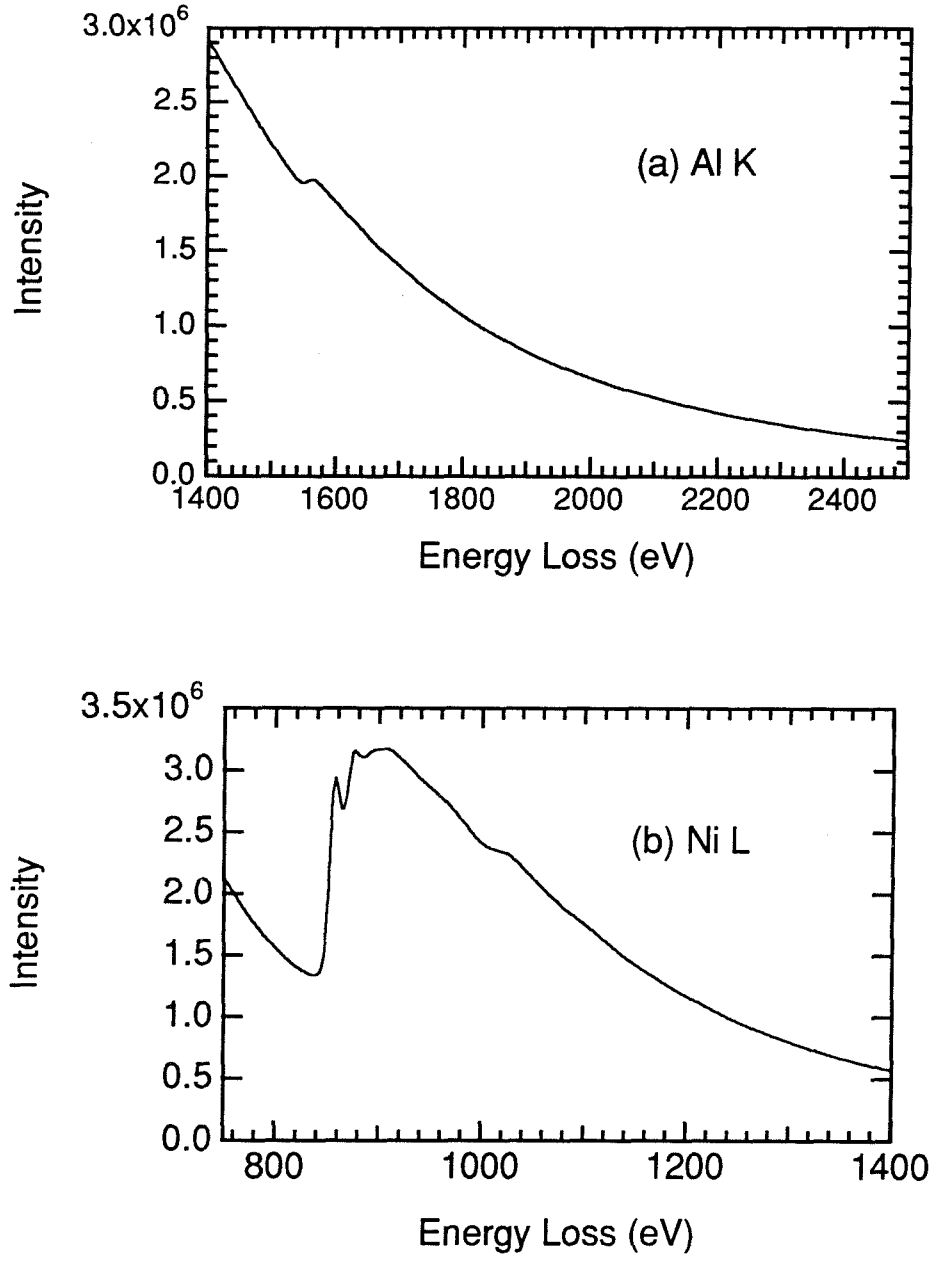

Figure 6.16. EELS measurements of (a) Al K and (b) Ni L edges from Ni_3Al. Spectra were not deconvoluted.

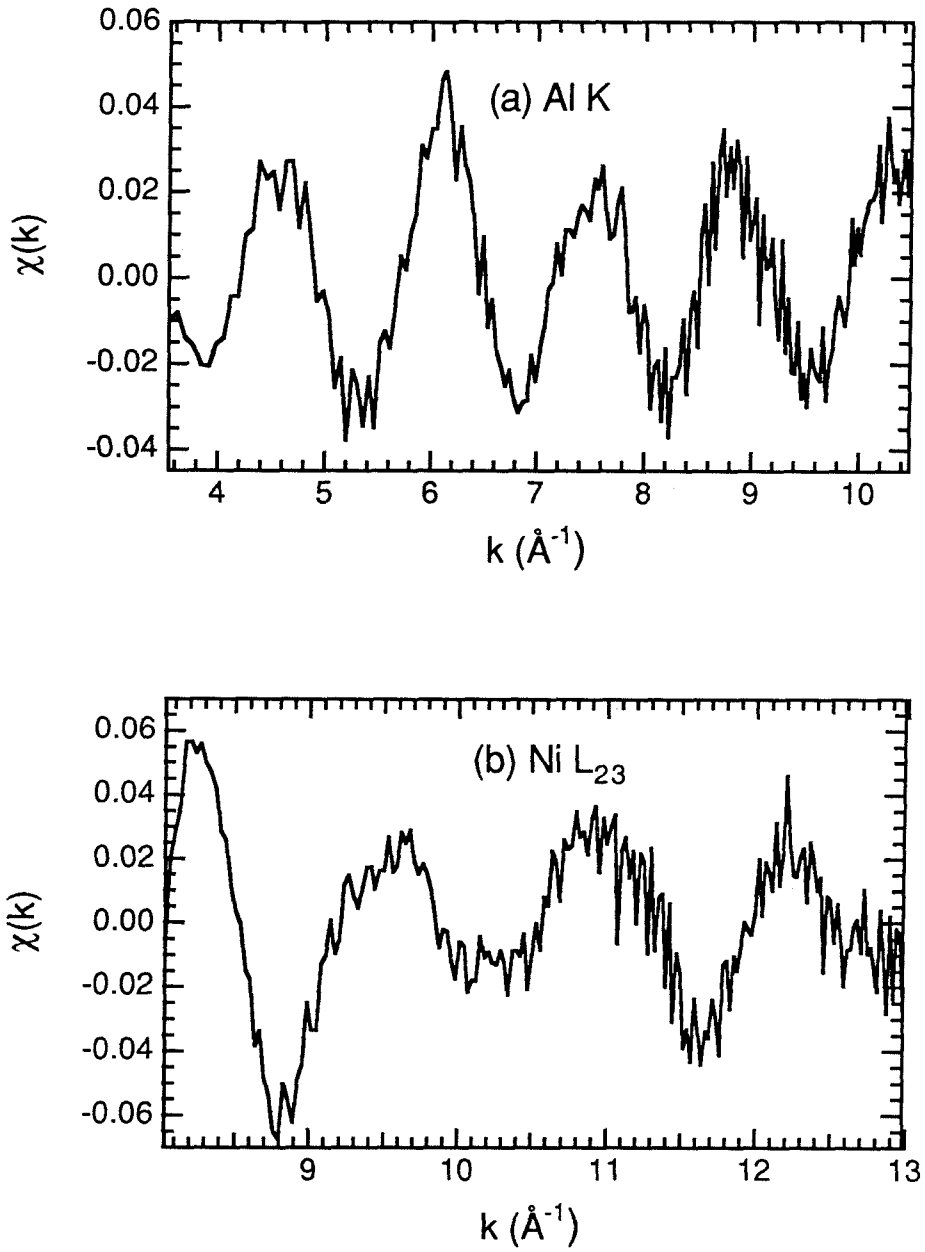

Figure 6.17. (a) Al K and (b) Ni L_{23} EXELFS from as-evaporated Ni_3Al at 105 K.

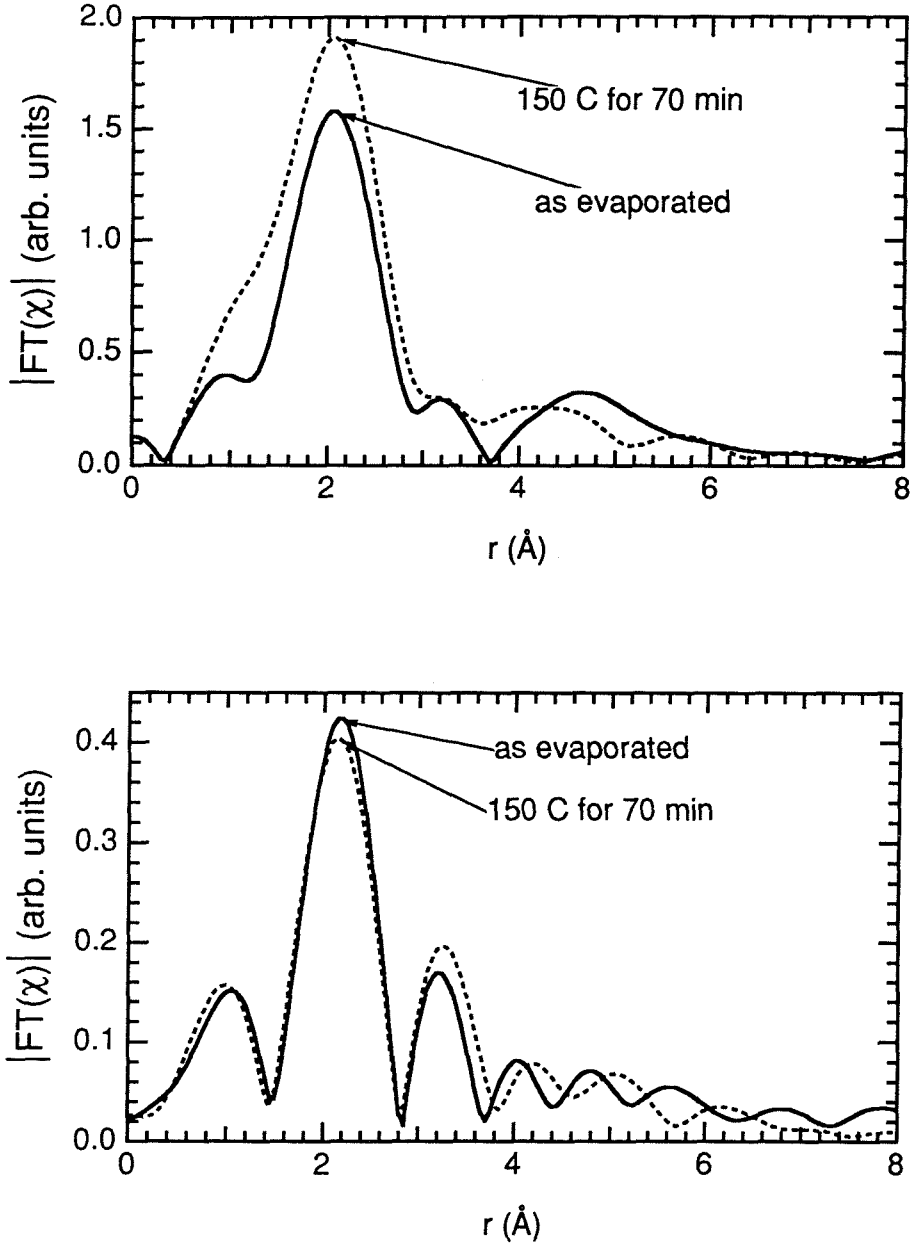

Figure 6.18. Magnitude of FT of experimental (a) Al K ($4 < k < 10$ Å^{-1}) and (b) Ni L_{23} ($8.5 < k < 12.5$ Å^{-1}) EXELFS from as-evaporated Ni_3Al and after annealing *in situ* at 150 C for 70 minutes. Data taken at 97 K.

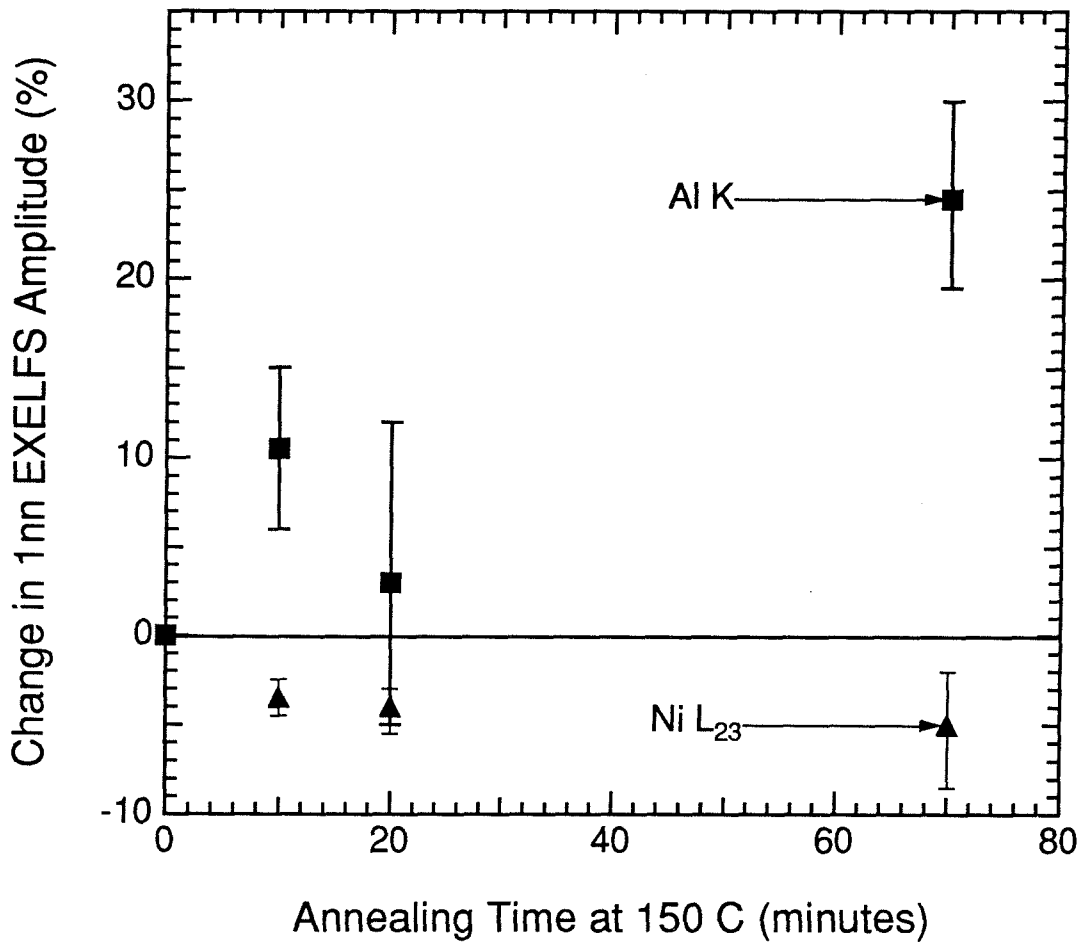

Figure 6.19. Change in 1nn EXELFS amplitudes as function of annealing time at 150 C for as-evaporated Ni_3Al sample. Error bars obtained from values at which variance of least-squares fit increased by 20%.

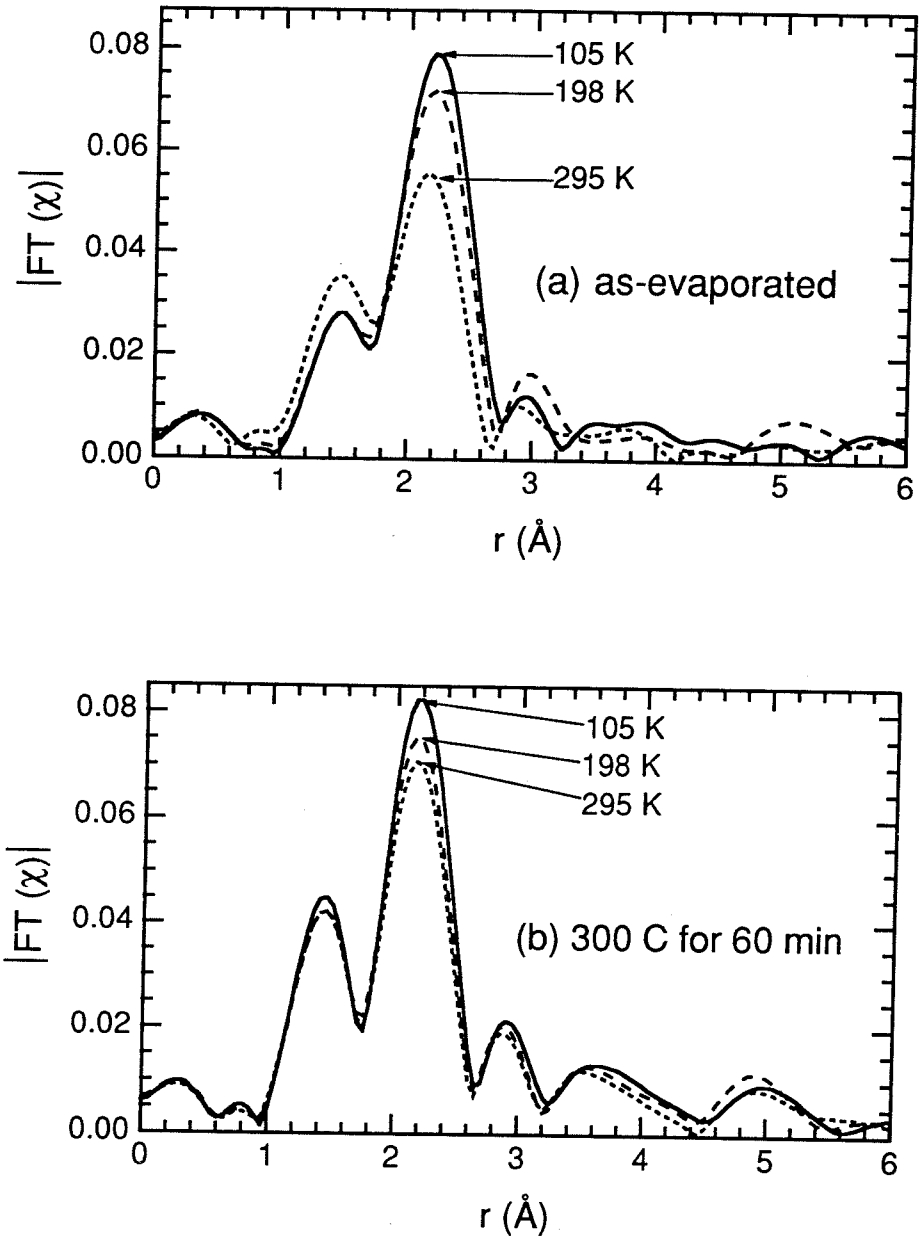

Figure 6.20. Temperature dependence of magnitude of FT of Al K EXELFS ($4 < k < 10$ Å^{-1}) from (a) as-evaporated Ni_3Al and (b) after annealing at 300 C for 60 minutes.

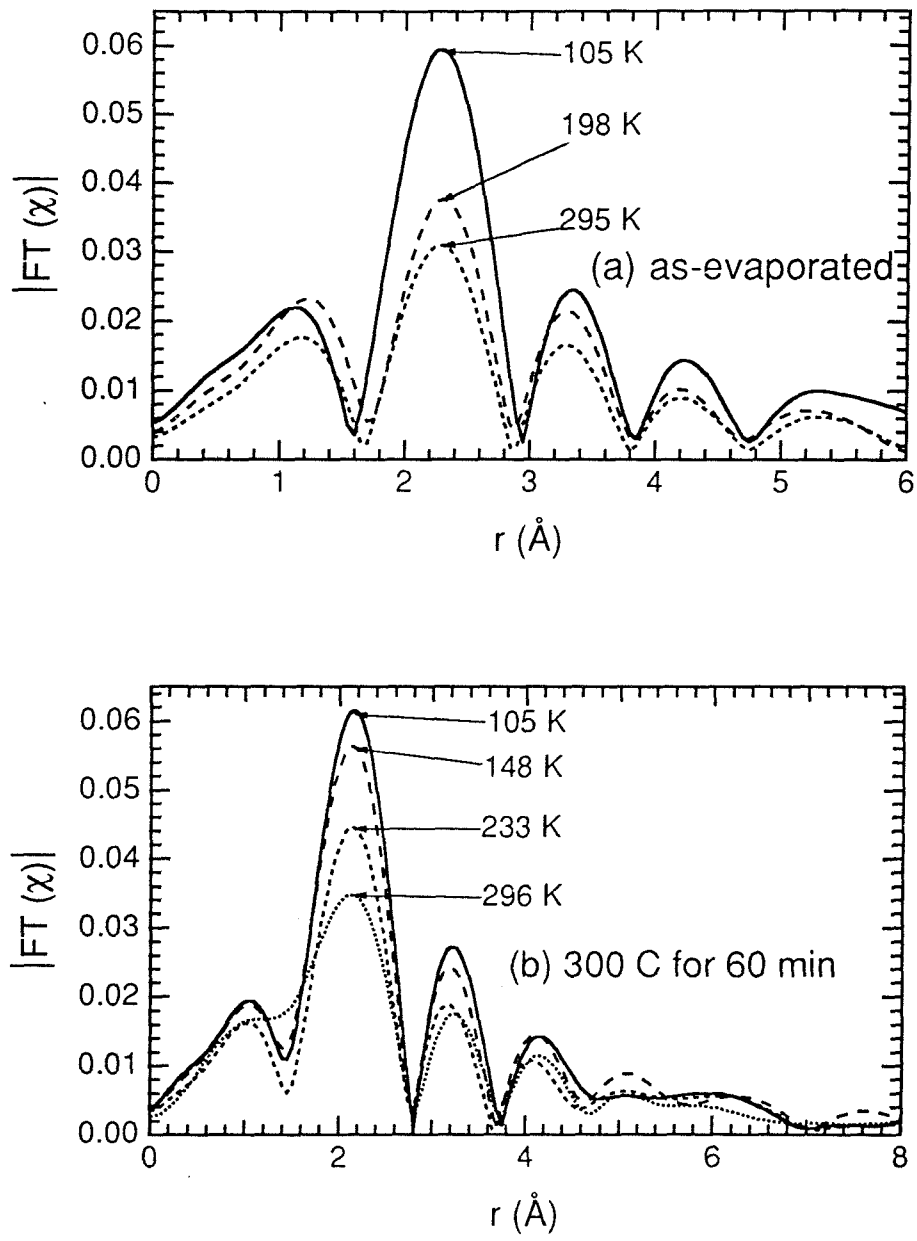

Figure 6.21. Temperature dependence of magnitude of FT of Ni L_{23} EXELFS ($8.5 < k < 12.5$ Å^{-1}) from (a) as-evaporated Ni_3Al and (b) after annealing at 300 C for 60 minutes.

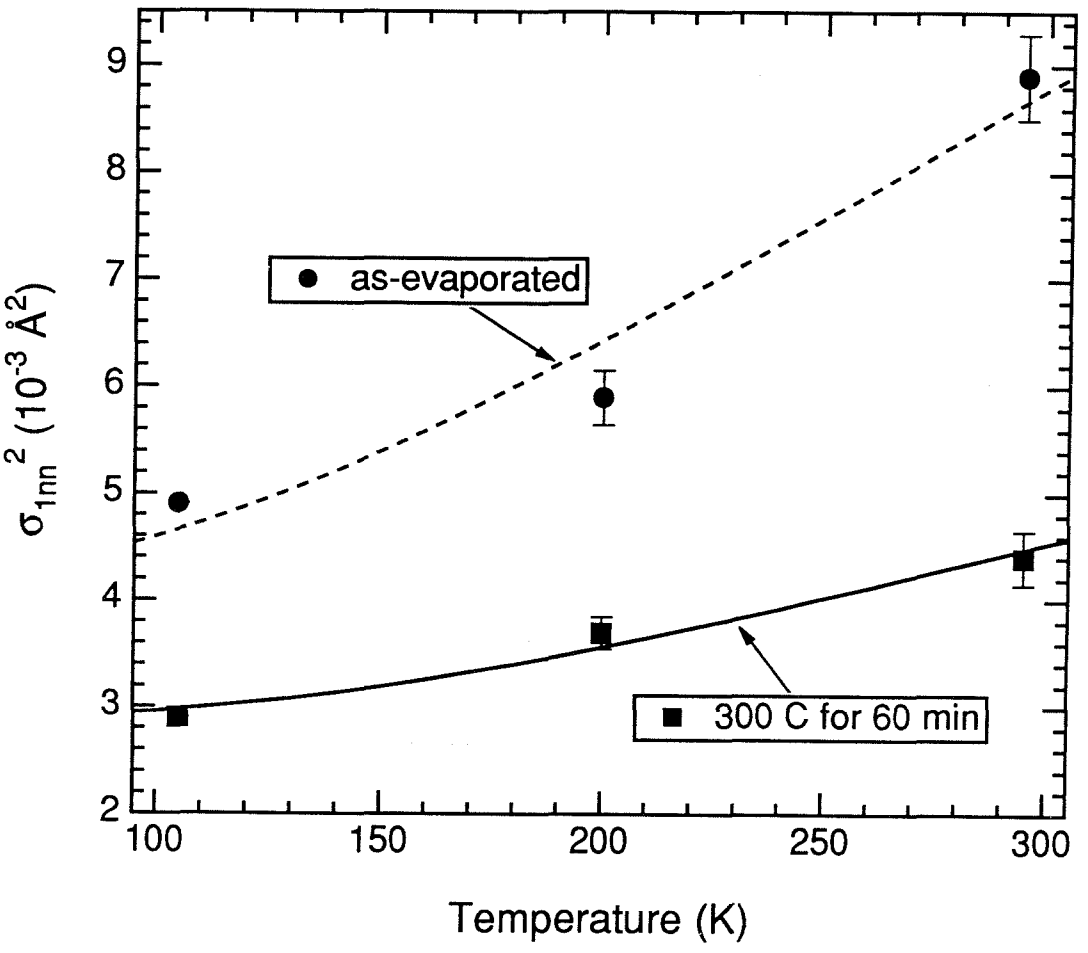

Figure 6.22. Einstein model fits to Al K EXELFS 1nn MSRD data from as-evaporated Ni_3Al and after annealing at 300 C for 60 minutes. Absolute offsets of data were allowed to float. Fits gave θ_E = 312 ± 35 K for as-evaporated Ni_3Al and θ_E = 453 ± 30 K after annealing.

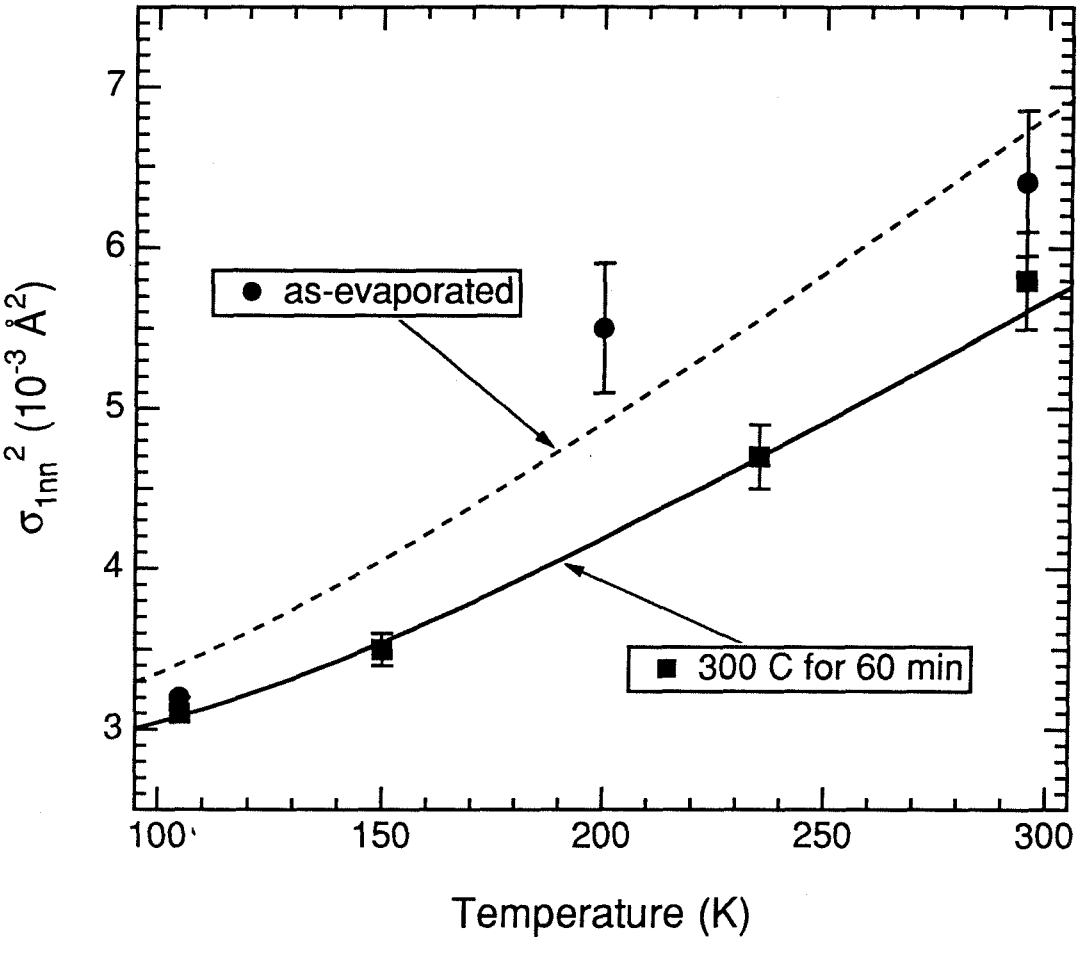

Figure 6.23. Einstein model fits to Ni L_{23} EXELFS 1nn MSRD data from as-evaporated Ni_3Al and after annealing at 300 C for 60 minutes. Absolute offsets of data were allowed to float. Fits gave θ_E = 279 ± 45 K for as-evaporated Ni_3Al and θ_E = 304 ± 20 K after annealing.

temperature fits to the Al K and Ni L_{23} 1nn MSRD data from as-evaporated and annealed samples. The MSRD data indicate that the local environments of both Al and Ni atoms in Ni_3Al become "stiffer" as the alloy orders. The "stiffening" of local environments is similar to that which I observed in Fe_3Al.

First, using the mean-field approach, I substitute $\theta_{Al}^{ord} = 453 \pm 30$ K, $\theta_{Al}^{dis} = 312 \pm 35$ K, $\theta_{Ni}^{ord} = 304 \pm 20$ K, and $\theta_{Ni}^{dis} = 279 \pm 45$ K into Equation (6.2) to obtain

$$\Delta S_{vibr} = [0.28 \pm 0.10\ (Al)] + [0.19 \pm 0.39\ (Ni)]\ k_B/atom$$
$$= +0.47 \pm 0.40\ k_B/atom \qquad (6.6)$$

Second, using the pair approach, I substitute $\theta_{AlNi}^{ord} = 453 \pm 30$ K, $\theta_{AlAl}^{dis} = \theta_{AlNi}^{dis} = 312 \pm 35$ K, $\theta_{NiNi}^{ord} = 304 \pm 20$ K, and $\theta_{NiNi}^{dis} = 279 \pm 45$ K into the appropriate form of Equation (6.3) to obtain

$$\Delta S_{vibr} = +0.71 \pm 0.38\ k_B/atom \qquad (6.7)$$

Like the analogous calculation for Fe_3Al, the above calculation for Ni_3Al assumes that θ_{AlAl}^{dis} can be estimated by θ_{AlNi}^{dis}.

The pair approach gives a larger value for the difference in vibrational entropy between disordered and ordered Ni_3Al than the mean-field approach. This is because the pair approach puts greater emphasis on the contribution from the Al K EXELFS data. While the mean-field approach puts three times more weight on the Ni L_{23} EXELFS than on the Al K EXELFS, the pair approach weights the Al K and Ni L_{23} EXELFS almost equally. I believe that the pair approach is more correct.

Anthony et al. (1993) measured ΔS_{vibr} for disordered and ordered Ni_3Al using low temperature calorimetry and temperature-dependent x-ray diffractometry. The calorimetry measurement gave $\Delta S_{vibr} = 0.3\ k_B$/atom and the x-ray measurement gave $\Delta S_{vibr} = 0.7\ k_B$/atom. The accuracy of the x-ray measurement was questionable, however.

It may be expected that ΔS_{vibr} would increase with the enthalpy of ordering for an alloy. Using this criterion, one would expect ΔS_{vibr} to be larger for Ni_3Al than for Fe_3Al. While this was the observed trend, the uncertainties of my measurements are too large to discern definitely such a correlation.

6.2 Structural Disorder and Vibrational MSRD in Nanocrystalline Pd and TiO_2

Nanocrystalline materials, both metals and ceramics, have recently become a topic of great interest (Gleiter, 1989). Nanocrystalline materials are defined as materials whose grains are on the order of several (typically 5 - 15) nanometers in length. EXAFS measurements have been used to support the claim that grain boundaries in some nanocrystalline materials are highly disordered (Haubold et al., 1989). This section compares EXELFS measurements from nanocrystalline Pd and TiO_2 with those from the larger grained materials. Low temperature measurements indicated that the nanocrystalline materials contained a significant amount of structural disorder. Temperature-dependent measurements did not show any strong differences between bulk and nanophase materials.

6.2.1 Nanocrystalline Pd

Currently, inert gas condensation is the most popular technique used to synthesize nanocrystals. Such nanocrystals, however, must be consolidated in order to form a bulk nanocrystalline material.

Inert gas condensation and compaction have been used previously to synthesize nanocrystalline Pd (Birringer et al., 1984). As discussed in Chapter 3, I found that dense nanocrystalline Pd can also be synthesized by high-vacuum evaporation. The evaporated Pd formed a thin film whose average grain size was approximately 6 nm, as determined by x-ray diffraction and TEM. To grow the grains, some of the evaporated Pd samples were annealed *in-situ* in the heating holder of the TEM at approximately 550 C. The annealed Pd had an average grain size of approximately 30 nm.

Figure 6.24 compares EELS measurements from the nanocrystalline Pd and from electropolished bulk Pd. The spectra were deconvolved to remove the effects of sample thickness. In comparison with the spectrum from the bulk Pd, the spectrum from the nanocrystalline Pd has a significant edge near an energy loss of 284 eV which is the location of the C K edge. Although elemental analysis with EELS is only approximate, the relative size of the edge nevertheless indicates that the nanocrystalline Pd contains on the order of 10% C atoms. Furthermore, notice the edge near 532 eV which is a combination of Pd M_3 and O K edges. This edge is slightly larger for the evaporated Pd than for the bulk Pd. Analyzing this change in edge size indicates that the nanocrystalline Pd may also contain on the order of 10% O atoms.

Figure 6.25 displays the Pd-C phase diagram. The phase diagram shows that the atomic solubility limit of C in Pd at room temperature is

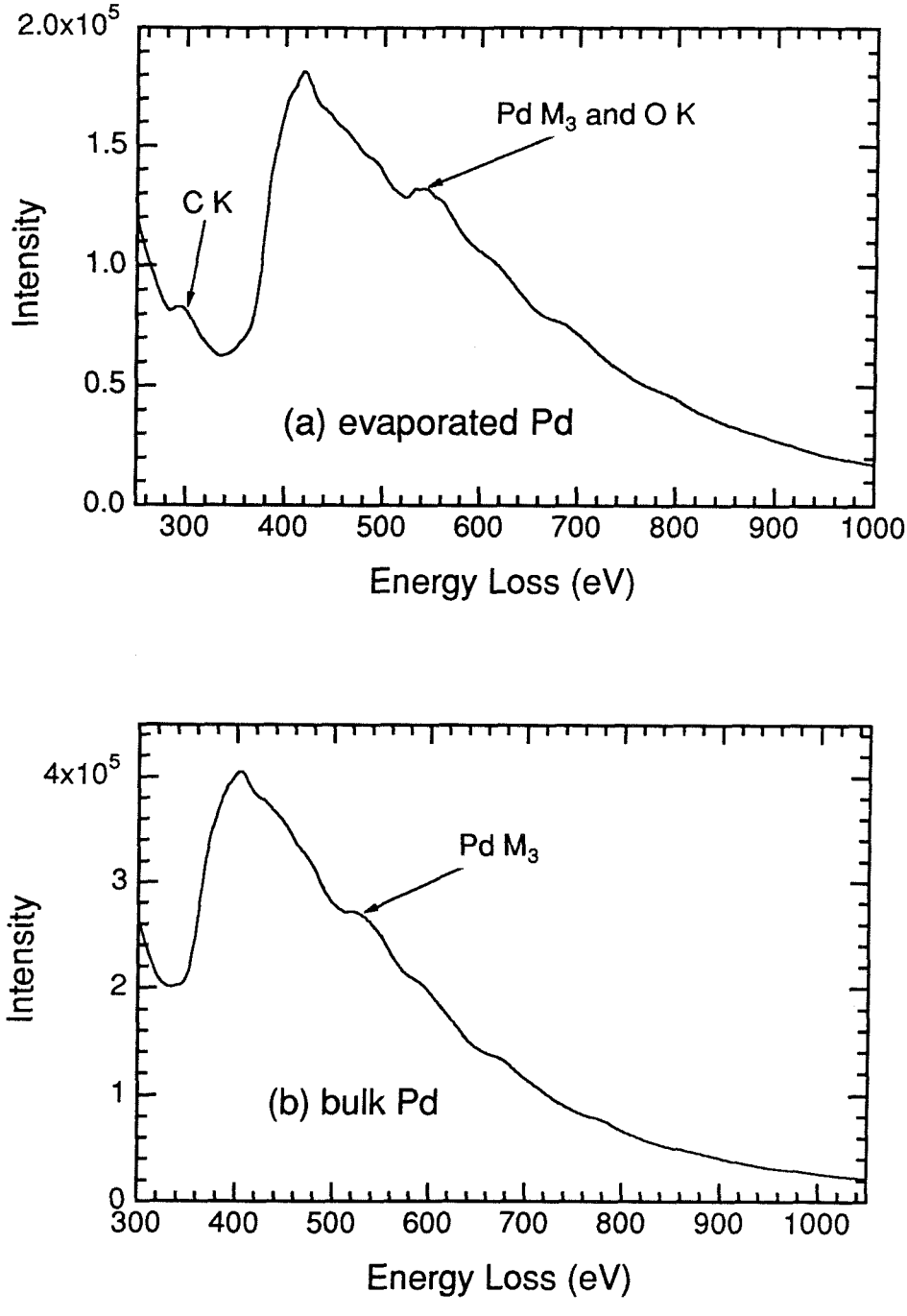

Figure 6.24. EELS measurements from (a) evaporated nanocrystalline Pd at 105 K and (b) electropolished bulk Pd at 98 K. Spectra were deconvolved to remove thickness effects.

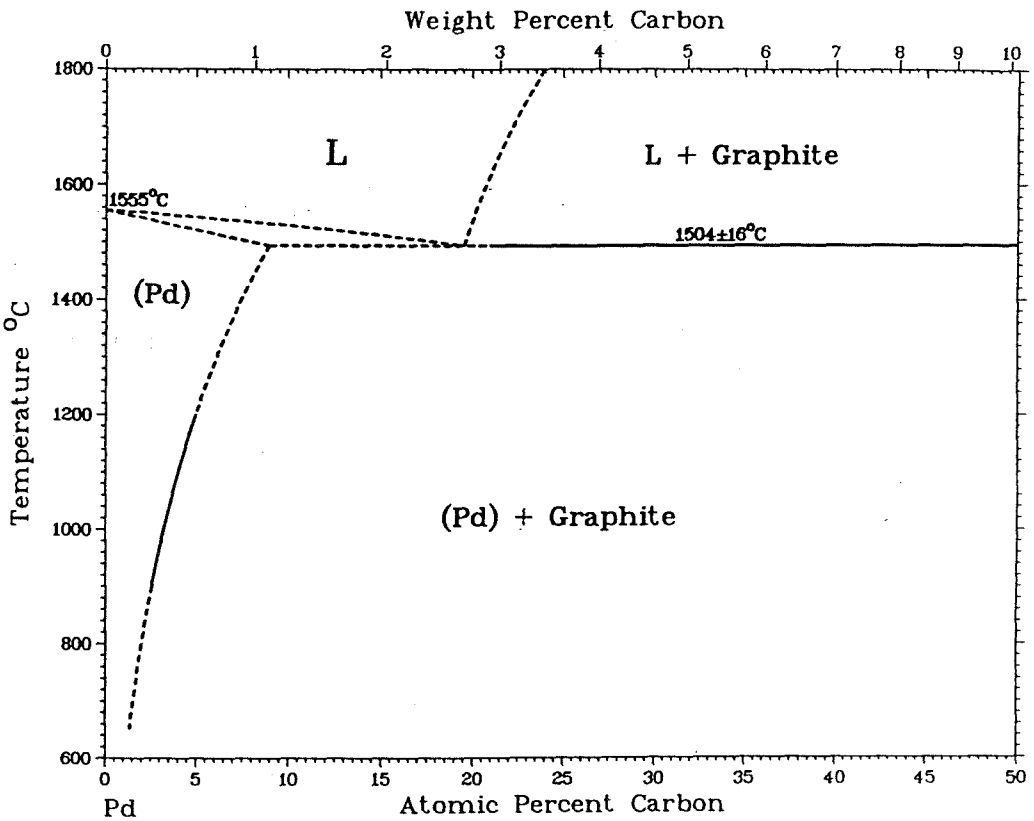

Figure 6.25. Phase diagram for Pd-C (Massalski, 1986).

approximately 1%. This means that only one atomic percent of C is soluble in the fcc matrix of bulk Pd. Nevertheless, more than one atomic percent of C may be soluble in my thin film of nanocrystalline Pd, especially in grain boundaries.

Figure 6.26 presents the magnitude of the FT of the Pd M_{45} EXELFS from nanocrystalline and annealed samples of Pd at temperatures from 105 K to 295 K. Note that because C and O are much lighter than Pd, these EXELFS signals must be dominated by Pd neighbors. Figure 6.27 displays the 1nn MSRD data from nanocrystalline and annealed samples. Debye model fits yielded $\theta_D = 357 \pm 60$ K for the nanocrystalline Pd and $\theta_D = 273 \pm 35$ K for the annealed Pd. The behavior of the annealed Pd matches well that of the bulk Pd given in Chapter 5. Surprisingly, the nanocrystalline material seems slightly "stiffer" in comparison. The scatter in the MSRD data, however, makes this conclusion unreliable.

Figure 6.28 compares the magnitude of the FT of the EXELFS from the nanocrystalline and annealed Pd at 105 K. The amplitude of the 1nn peak from the nanocrystalline material is significantly suppressed. Interpreting my measurements in terms of a Debye-Waller type factor indicate that the MSRD between Pd atoms in the nanocrystalline Pd is greater than that in the annealed Pd by 1.8 ± 0.3 Å^2. This increase in MSRD would give the structural MSRD of the nanocrystalline Pd if the vibrational MSRD of the two materials were equal at 105 K. However, my temperature-dependent measurements indicate that the structural MSRD of the nanocrystalline Pd may be even greater because some of it is masked by the greater vibrational MSRD in the annealed Pd.

I also used a partially compacted powder of Pd nanocrystals, synthesized by inert gas condensation, to make EXELFS measurements. Figure 6.29

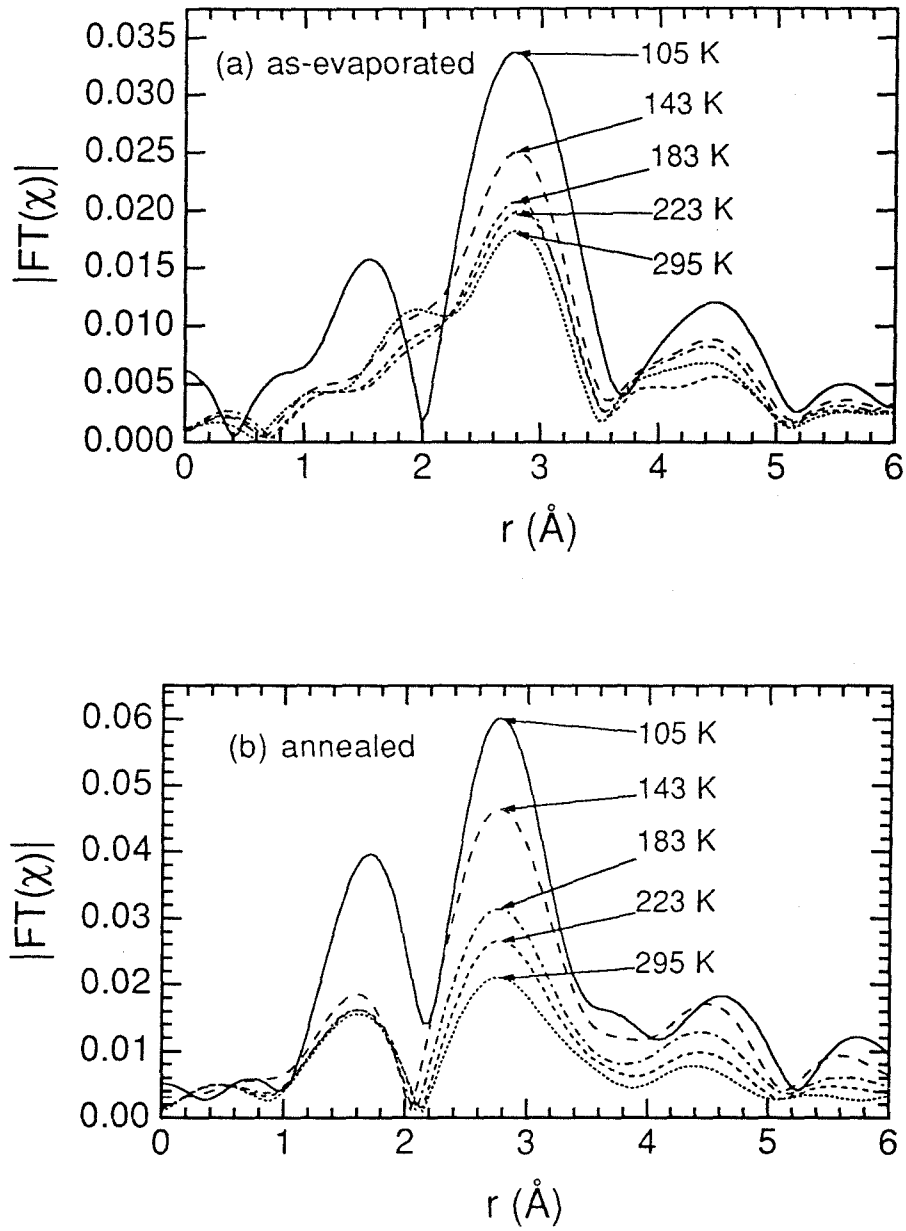

Figure 6.26. Temperature dependence of magnitude of FT of Pd M_{45} EXELFS ($10.25 < k < 14.5$ Å^{-1}) from (a) as-evaporated nanocrystalline Pd and after annealing *in-situ* at 550 C to grow grains.

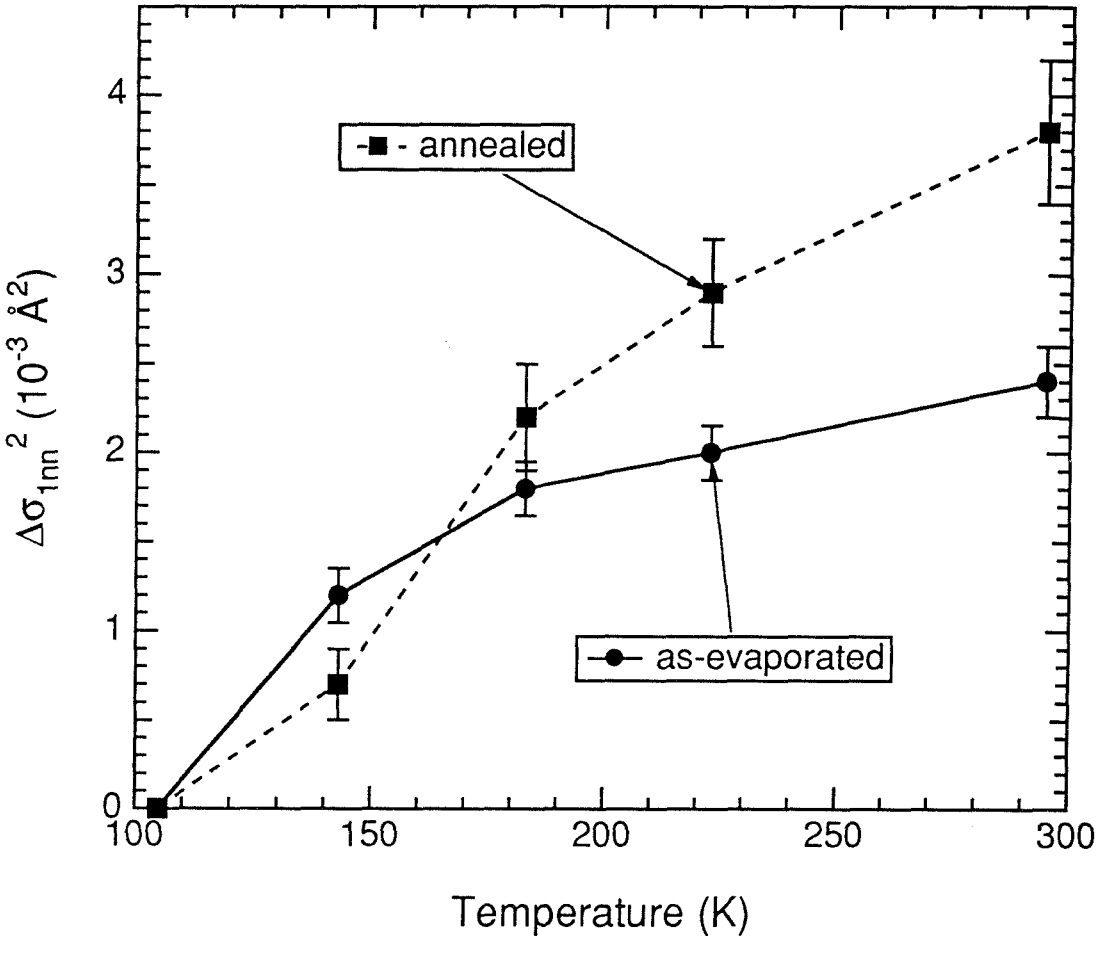

Figure 6.27. Change in 1nn MSRD for EXELFS relative to EXELFS at 105 K from as-evaporated nanocrystalline Pd and after annealing *in-situ* at 550 C to grow grains.

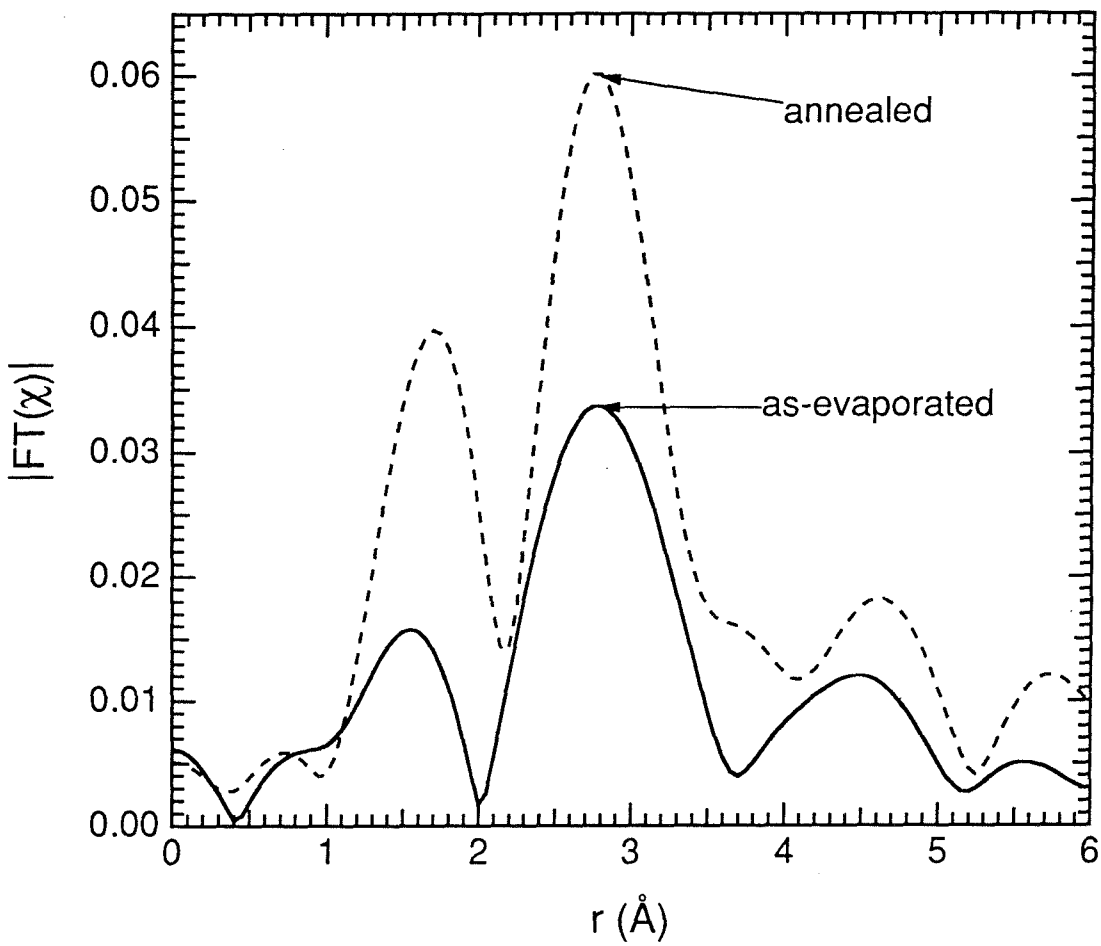

Figure 6.28. Magnitude of FT of Pd M_{45} EXELFS ($10.25 < k < 14.5$ Å^{-1}) from as-evaporated nanocrystalline Pd and after annealing *in-situ* at 550 C to grow grains. Data taken at 105 K.

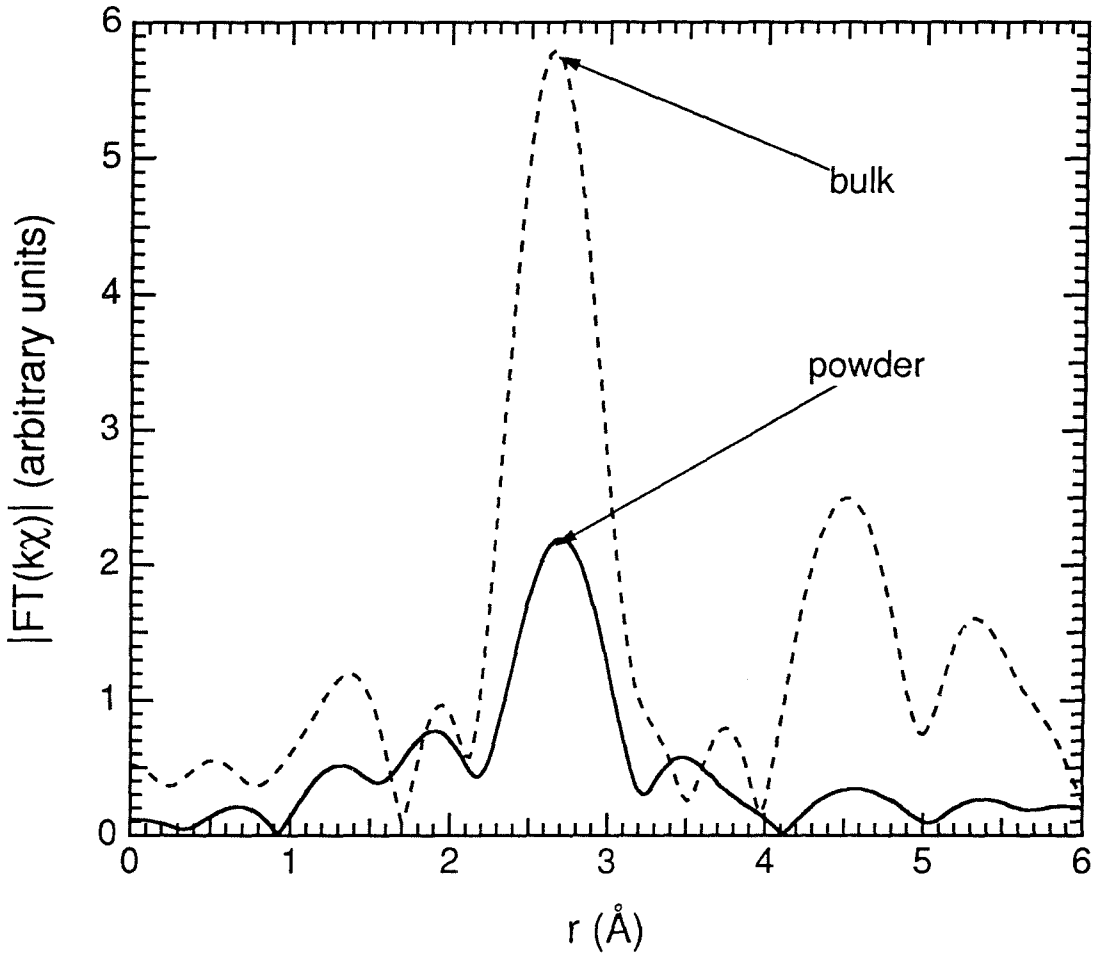

Figure 6.29. Magnitude of FT of Pd M_{45} EXELFS from partially compacted powder of Pd nanocrystals and bulk Pd foil. Data taken at 96 K.

compares the magnitude of the FT of the EXELFS from the powder with that of bulk Pd. The EXELFS amplitude for the powder is greatly suppressed, even more so than for the nanocrystalline thin film. This result, however, may be complicated by problems due to the low thermal conductivity of the powder.

The measurements shown in Figures 6.28 and 6.29 are consistent with previous EXAFS measurements of Haubold et al. (1989) and Eastman et al. (1992). Both Haubold et al. and Eastman et al. observed large reductions in EXAFS amplitudes from compacted Pd nanocrystals in comparison to bulk Pd. Moreover, as shown in Figure 6.30, Eastman and co-workers also observed a slightly larger reduction in EXAFS amplitude from the uncompacted powder of Pd nanocrystals.

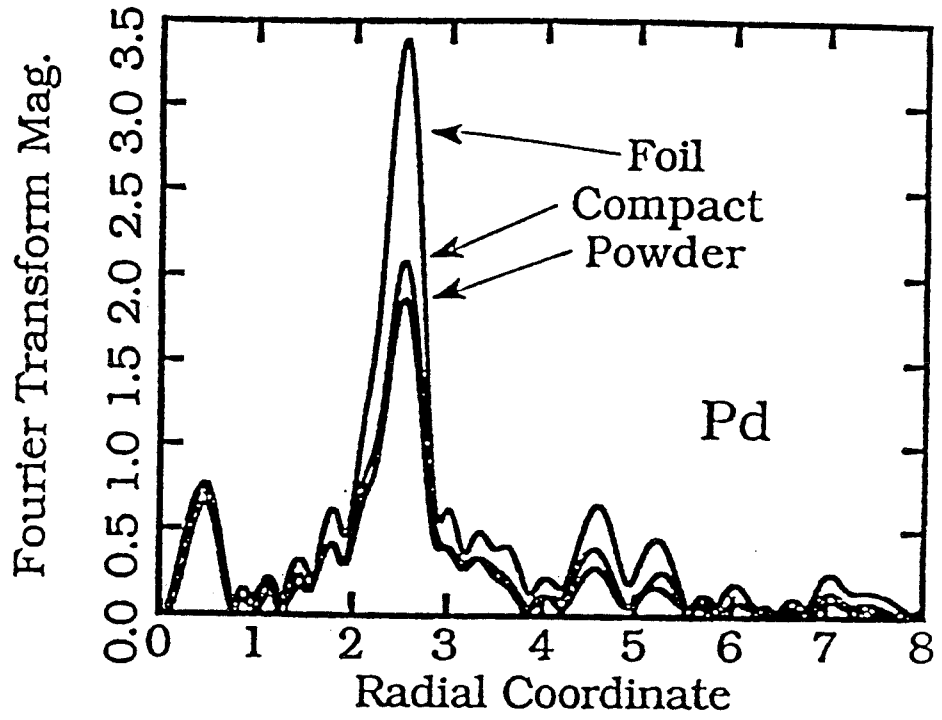

Figure 6.30. Magnitude of FT of k^2 weighted EXAFS above Pd edge for coarse-grained Pd foil, compacted nanocrystalline Pd, and powder of uncompacted Pd nanocrystals (Eastman et al., 1992).

6.2.2 Nanocrystalline TiO_2

Nanocrystalline TiO_2 is one of the most studied nanocrystalline materials. Previous studies have synthesized nanocrystalline TiO_2 *via* various methods (Gleiter, 1989). One popular method involved inert gas condensation of Ti powder, followed by oxidation, then compaction (Siegel et al., 1988). Nanocrystalline TiO_2 has shown interesting mechanical properties, including a potential for significant ductility for a ceramic material (Mayo et al., 1990).

As described in Chapter 3, I synthesized nanocrystalline TiO_2 by evaporating a thin film of Ti metal on a substrate of rock salt, then oxidizing the Ti metal by heating the substrates in air in a furnace at 500 C. The as-prepared TiO_2 had an average grain size of roughly 7 nm and was dominated by the rutile phase, but also contained some of the anatase phase. After annealing in vacuum at 900 C for 11 hours, the grains grew to approximately 20 nm and consisted of only the rutile phase.

Both rutile and anatase have tetragonal symmetry. The unit cell of rutile contains two Ti atoms and four O atoms. The larger unit cell of anatase has four Ti atoms and eight O atoms. In both structures, the 1nn shell surrounding Ti atoms consists of six O atoms, two of them being slightly closer (1.95 ± 0.01 Å) than the other four (1.97 ± 0.01 Å). Rutile is known to be harder than anatase (Kepert, 1972).

Figure 6.31 displays the EELS measurements of the Ti L, O K and Ti K edges from the as-prepared TiO_2. The overlap between Ti L and O K edges precludes the straightforward EXELFS analysis of these edges. Therefore, I analyzed only the EXELFS on the Ti K edge.

Figure 6.32 displays the theoretical Ti K EXELFS signal from the 1nn shell in TiO_2. This calculation was made by substituting the relevant phase and

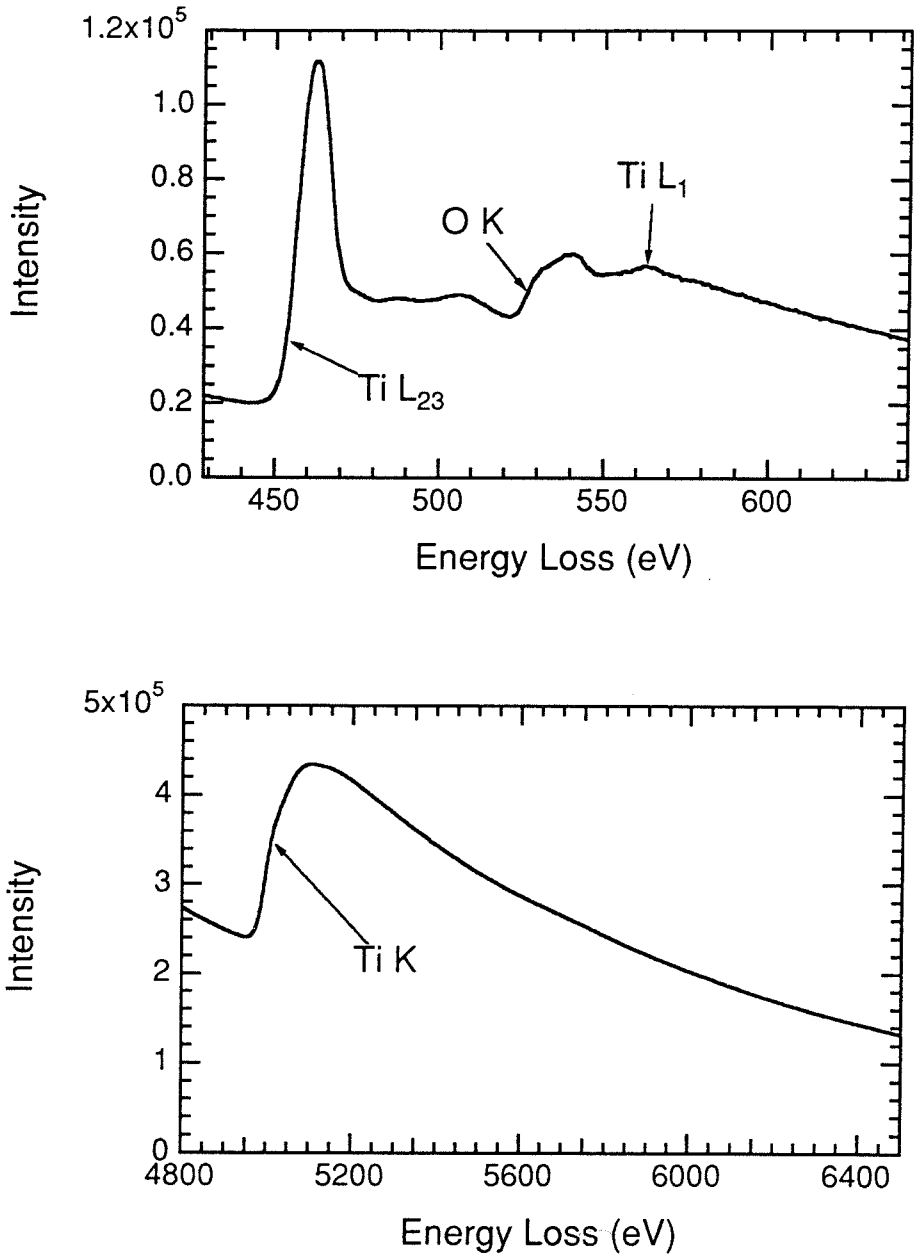

Figure 6.31. EELS measurements of Ti L, O K, and Ti K edges from as-prepared nanocrystalline TiO_2. Spectra were not deconvoluted.

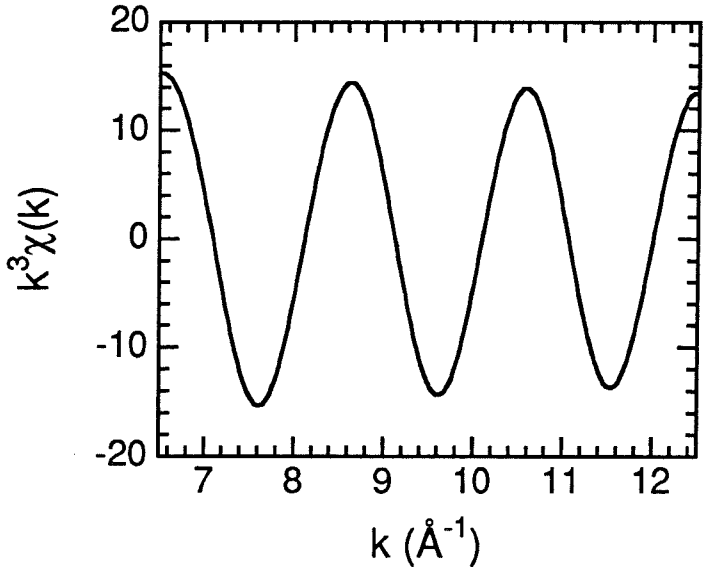

Figure 6.32. Theoretical Ti K EXELFS from 1nn shell of TiO_2.

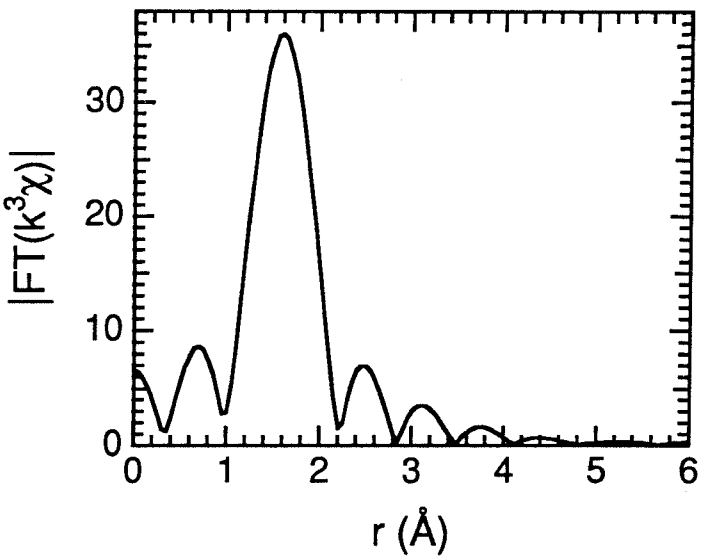

Figure 6.33. Magnitude of FT of theoretical Ti K EXELFS from 1nn shell of TiO_2. Transformation range $7 < k < 12$ Å^{-1}.

amplitude functions from Teo and Lee (1979) into Equation (2.50). The magnitude of the FT of the theoretical signal is shown in Figure 6.33. Theory predicts the 1nn peak to be near r = 1.6 Å.

Figure 6.34 compares the EXELFS from as-prepared and annealed TiO_2. A relatively high range in k-space was chosen to avoid any distortions due to multiple-inelastic scattering in the low-k region. The period and phase of my measured EXELFS match well with those of the theoretical EXELFS given in Figure 6.32. Figure 6.35 presents the magnitude of the FT of the EXELFS from as-prepared and annealed TiO_2. The 1nn peaks are near r = 1.45 Å, which is within 0.02 Å from the theoretical calculation. The difference may be due to the choice of edge onset energy, E_0. The signal of the as-prepared sample is seen to be smaller than that of the annealed sample. Interpreting the damping in terms of MSRD, the 1nn MSRD is $1.8 \pm 0.4 \times 10^{-3}$ Å^2 greater in the as-prepared sample.

Although single-crystal rutile has a Young's modulus of about 490 GPa, Mayo et al. (1990) found moduli as low as 50 GPa for nanocrystalline TiO_2 using nanoindenter (Doerner and Nix, 1986) measurements. This suggests that the Debye temperature of their nanocrystalline TiO_2 is much lower than that of their large-grained TiO_2.

My temperature-dependent Ti K EXELFS measurements, however, were not able to determine local Debye temperatures because the amplitude of the EXELFS did not damp appreciably for either sample. Figure 6.36 displays the temperature-dependent 1nn MSRD data. Relative to the uncertainty in my measurements, the changes in MSRD between 105 K and 295 K are near zero. This result is not particularly surprising because the ionic Ti-O bonds are expected to be very strong.

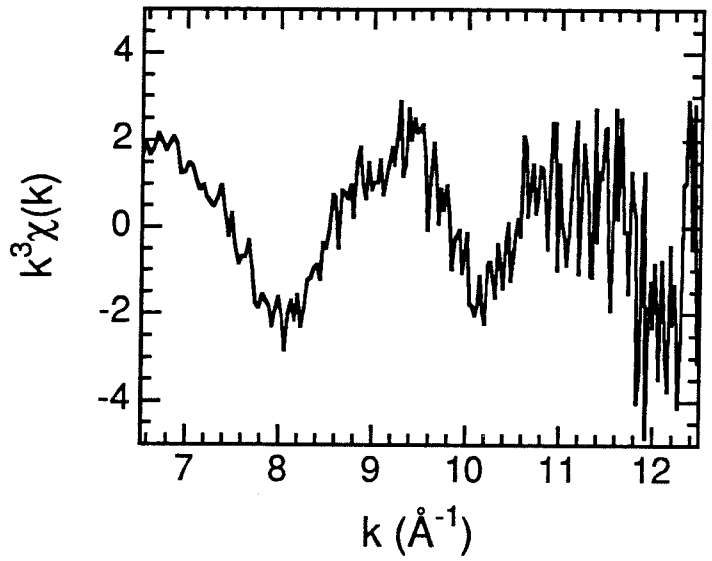

Figure 6.34. Ti K EXELFS from as-prepared nanocrystalline TiO_2 at 105 K.

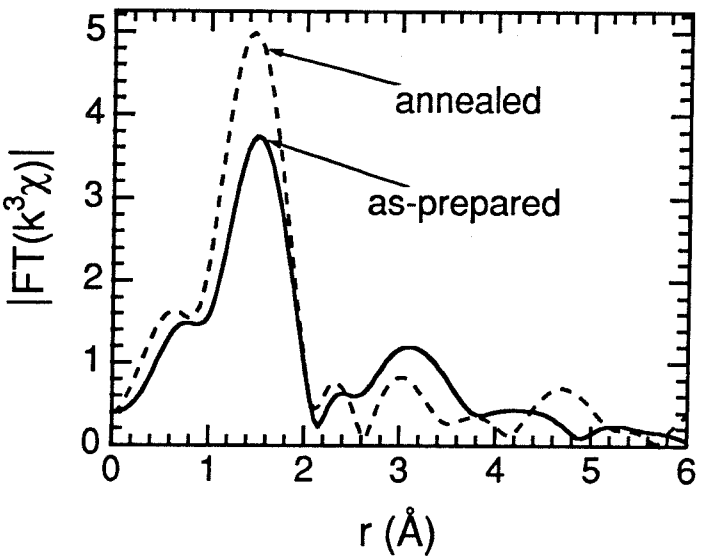

Figure 6.35. Magnitude of FT of experimental Ti K EXELFS ($7 < k < 12$ Å^{-1}) from as-prepared nanocrystalline TiO_2 and after annealing at 900 C for 11 hours to grow grains. Data taken at 105 K.

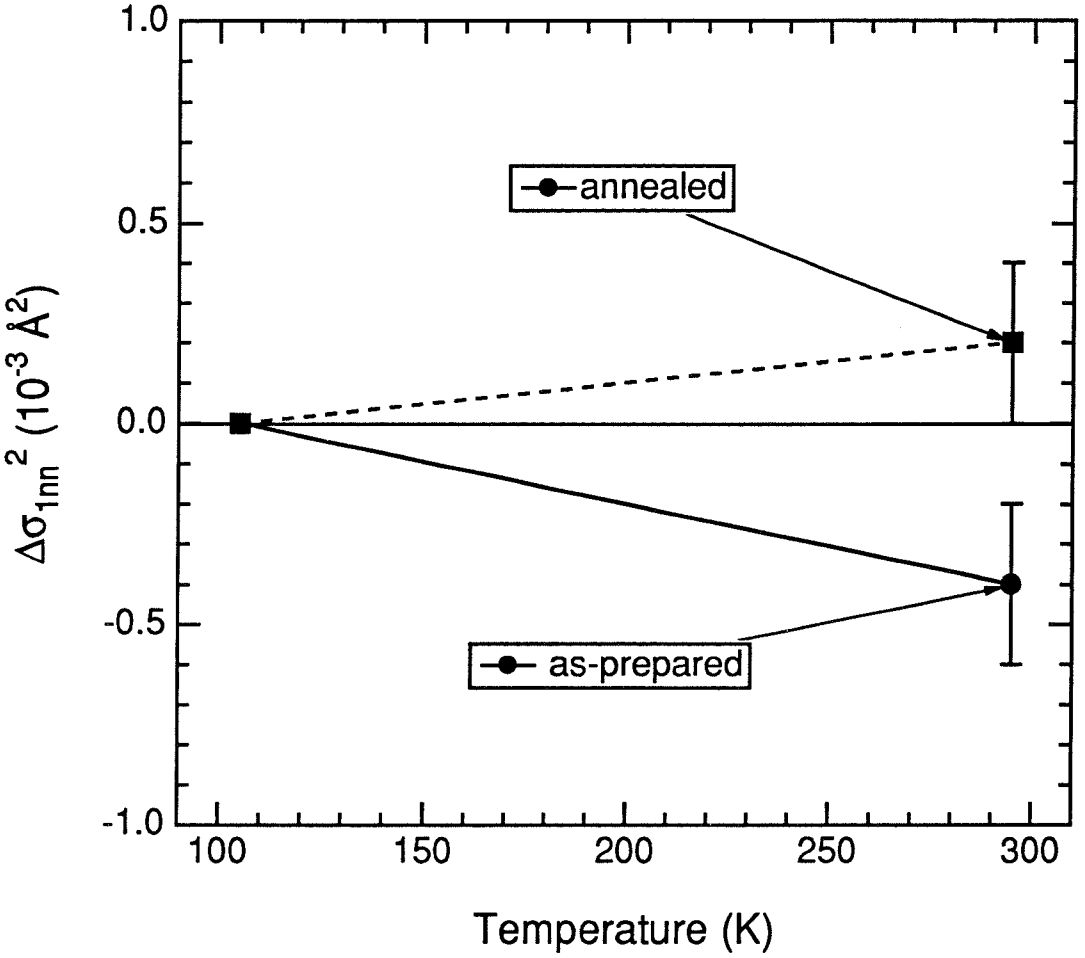

Figure 6.36. Change in 1nn MSRD for Ti K EXELFS relative to EXELFS at 105 K from as-prepared nanocrystalline TiO_2 and after annealing at 900 C for 11 hours to grow grains. Error bars obtained from values at which variance of least-squares fit increased by 20%.

6.3 Conclusions and Perspective

With a parallel detector, EXELFS is a viable structural probe with certain advantages over EXAFS. EXELFS can generally measure core edge fine structure in lower atomic number elements than EXAFS. Very small electron probes can be used, allowing inhomogeneous samples to be studied. The instrumentation is more accessible and less expensive than synchrotron sources. Finally, EXELFS can be combined with electron diffraction and imaging in the TEM.

I have shown that EXELFS can measure characteristics of local atomic environments using not only K edges, but L_{23} and M_{45} edges as well. Central atom phase shifts for outgoing f-waves were calculated which are needed to analyze M_{45}-edge EXELFS. This opens up most of the periodic table to EXELFS experiments.

An important feature of the technique is its ability to probe independently the environments of different atomic species. I have presented EXELFS measurements of chemical short-range order and local atomic vibrations in intermetallic alloys. Chemical short-range order was observed to evolve as samples of chemically disordered Fe_3Al and Ni_3Al were annealed in-situ in the electron microscope. Temperature-dependent measurements indicated that the local atomic vibrations in the disordered alloys were significantly greater than those in the ordered alloys. These results suggested that including vibrational entropy in theoretical treatments of phase transformations would lower significantly the critical temperature of ordering for these alloys.

I have also presented EXELFS measurements of local structural disorder and atomic vibrations in nanocrystalline Pd and TiO_2. The nanocrystalline materials were observed to have significantly greater amounts of local structural

disorder than the large-grained materials. Temperature-dependent measurements were inconclusive in measuring differences in local atomic vibrations between the nanocrystalline and large-grained materials.

While EXELFS can give results which are comparable to those of EXAFS, previous investigations of EXELFS have been mostly meager and exploratory. This dissertation was an in-depth discussion of EXELFS and was the first to apply the technique to contemporary problems in materials science. There are many other important problems in materials science to which EXELFS can be applied.

Appendix A Electron-Atom Scattering Calculations

The electron-atom scattering theory discussed in Chapter 2 can be used to make first principles calculations of important quantities in the EXELFS technique. This appendix discusses the computer software which implements these calculations and presents the results.

Energy-differential cross sections for ionization were discussed theoretically in §2.1.2 within the framework of the Born approximation. §A.1 briefly discusses the computer software used to implement this theory. Energy-differential cross sections are displayed for the elements relevant to the experiments in this thesis.

Phase shifts and scattering amplitudes were discussed in §2.2.1. §A.2 presents the calculation of central atom phase shifts and backscattering amplitudes for EXELFS. Phase shifts and scattering amplitudes relevant to the experiments in this thesis are presented, along with many additional phase shifts which should be useful for future EXELFS experiments. The computer program which I wrote to make the calculations is listed.

A.1 Energy-Differential Cross Sections for Ionization

This section briefly outlines the computer programs which I used to calculate energy-differential cross sections for ionization. Calculations relevant to the experiments in this thesis are presented.

First, Hartree-Slater atomic potentials and wavefunctions are calculated using a program that was originally written by Herman and Skillman (1963). These calculations assume a spherically symmetric atomic potential V(r) which is the sum of the nuclear Coulomb potential, the total electronic Coulomb potential, and the exchange potential. The exchange potential $V_{exch}(r)$ is approximated by 0.7 times the free-electron exchange potential, which is proportional to the cube root of the total charge density of the atomic electrons:

$$V_{exch}(r) = -(0.7)6\left[\frac{3}{8\pi}|\rho(r)|\right]^{1/3} \qquad (A.1)$$

where energies are expressed in Rydberg units and distances in Bohr units. The factor of 0.7 is attributed to Kohn and Sham (1965).

The electronic wavefunctions are expressed as products of radial wavefunctions $R_{nl}(r)$ and spherical harmonics $Y_{lm}(\theta,\phi)$. Applying the method of separation of variables, the three-dimensional Schrödinger equation is reduced to the one-dimensional radial wave equation:

$$\left[-\frac{d^2}{dr^2} + \frac{l(l+1)}{r^2} + V(r)\right]R(r) = ER(r) \qquad (A.1)$$

Figures A.1 through A.6 display the calculated atomic potentials and radial wavefunctions relevant to O K, Al K, Ti K, Fe L, Ni L, and Pd M edges.

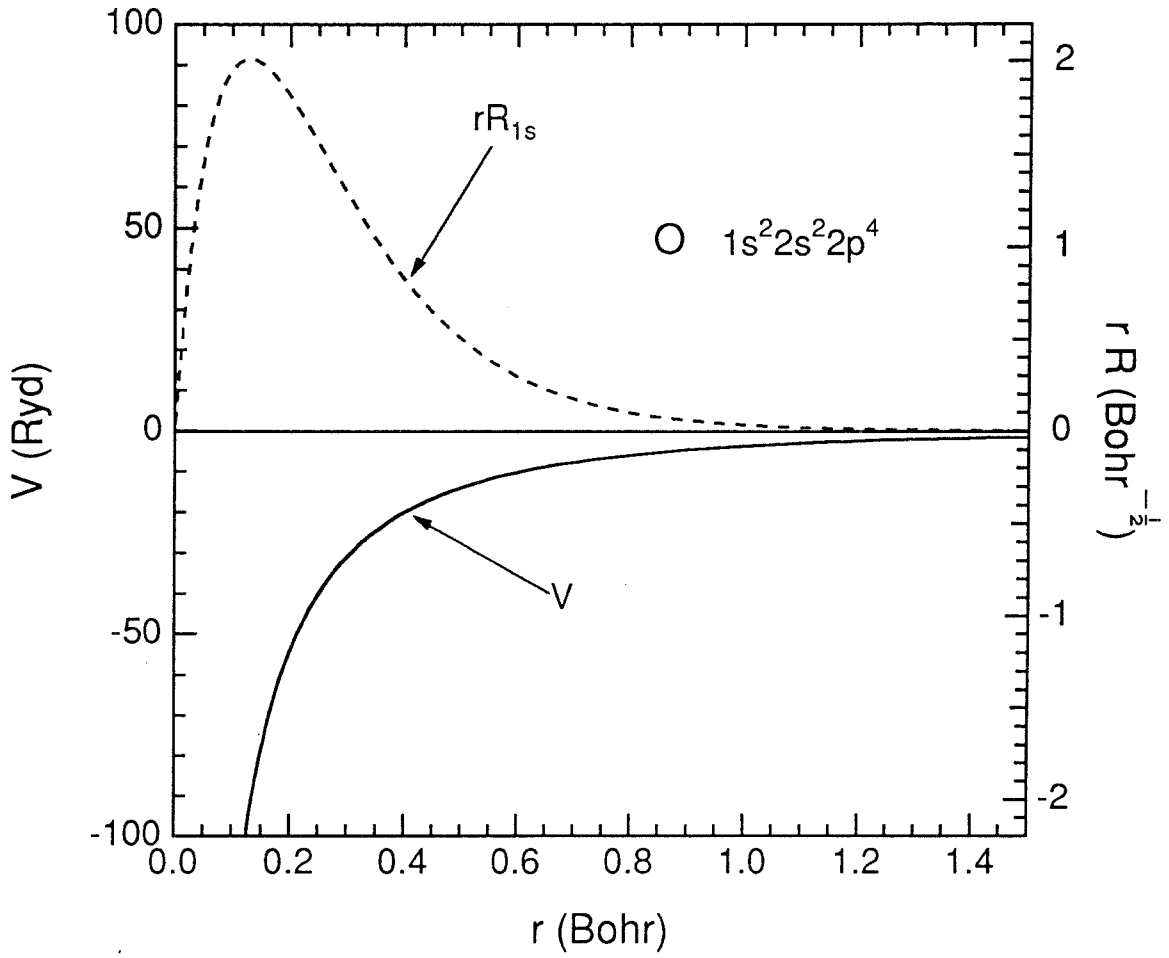

Figure A.1. Hartree-Slater atomic potential and 1s wavefunction for O atom in its ground state.

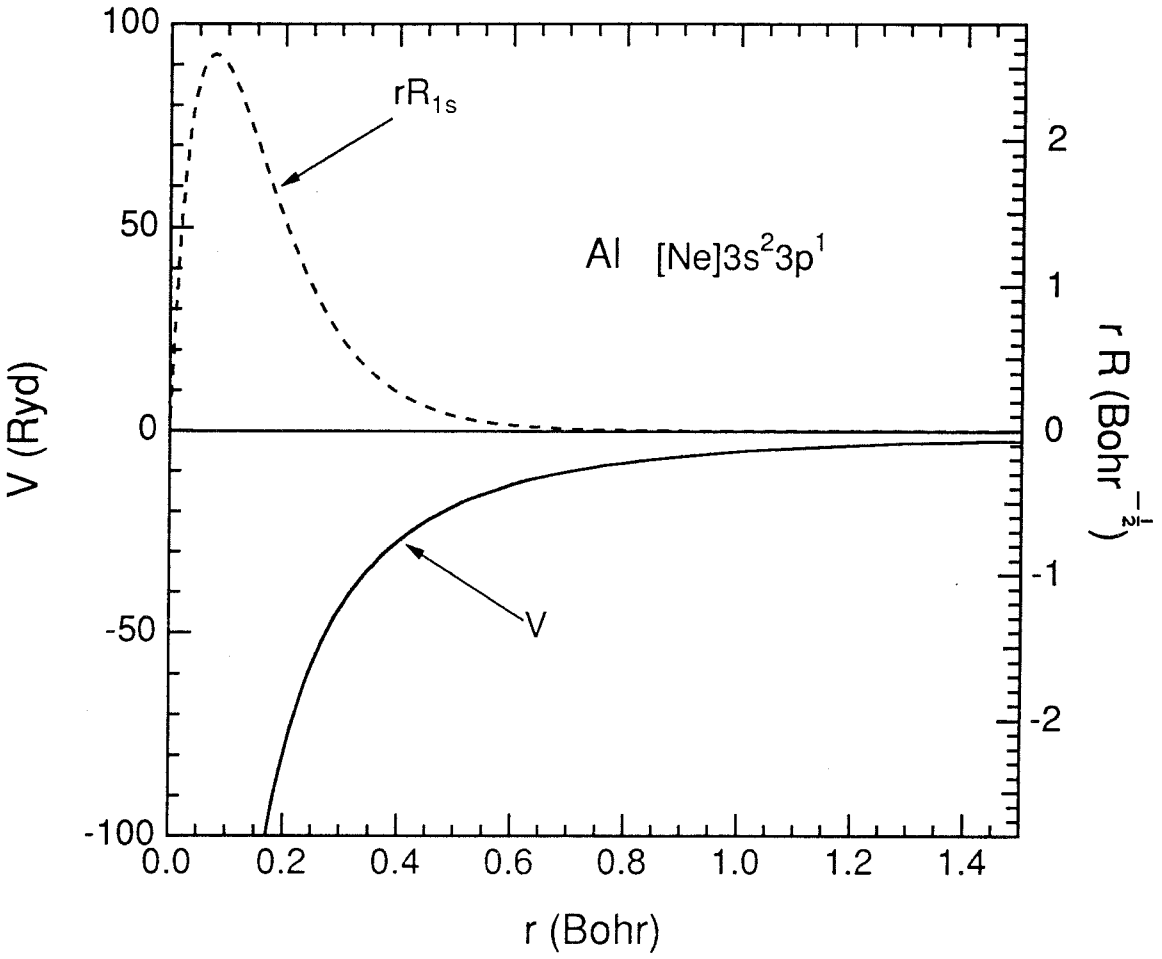

Figure A.2. Hartree-Slater atomic potential and 1s wavefunction for Al atom in its ground state.

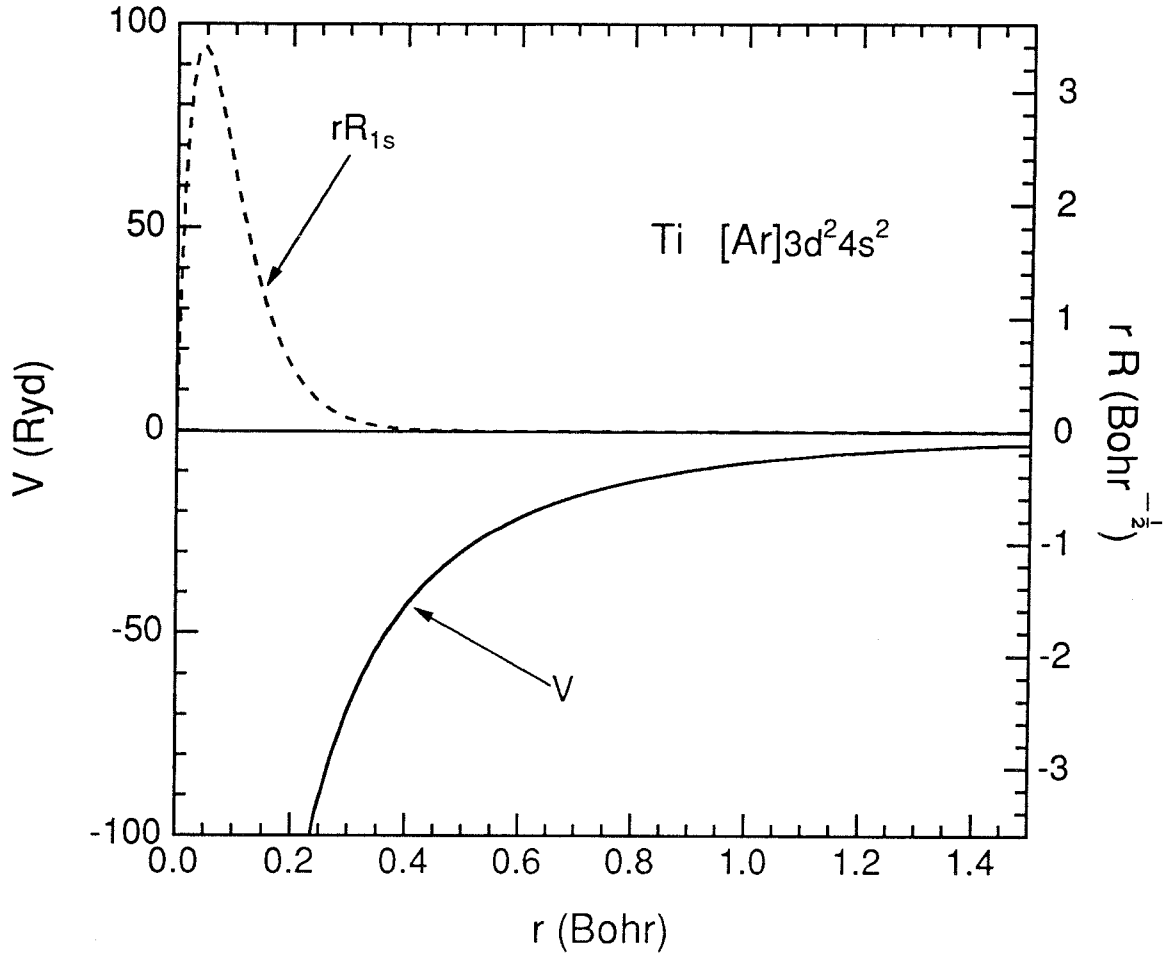

Figure A.3. Hartree-Slater atomic potential and 1s wavefunction for Ti atom in its ground state.

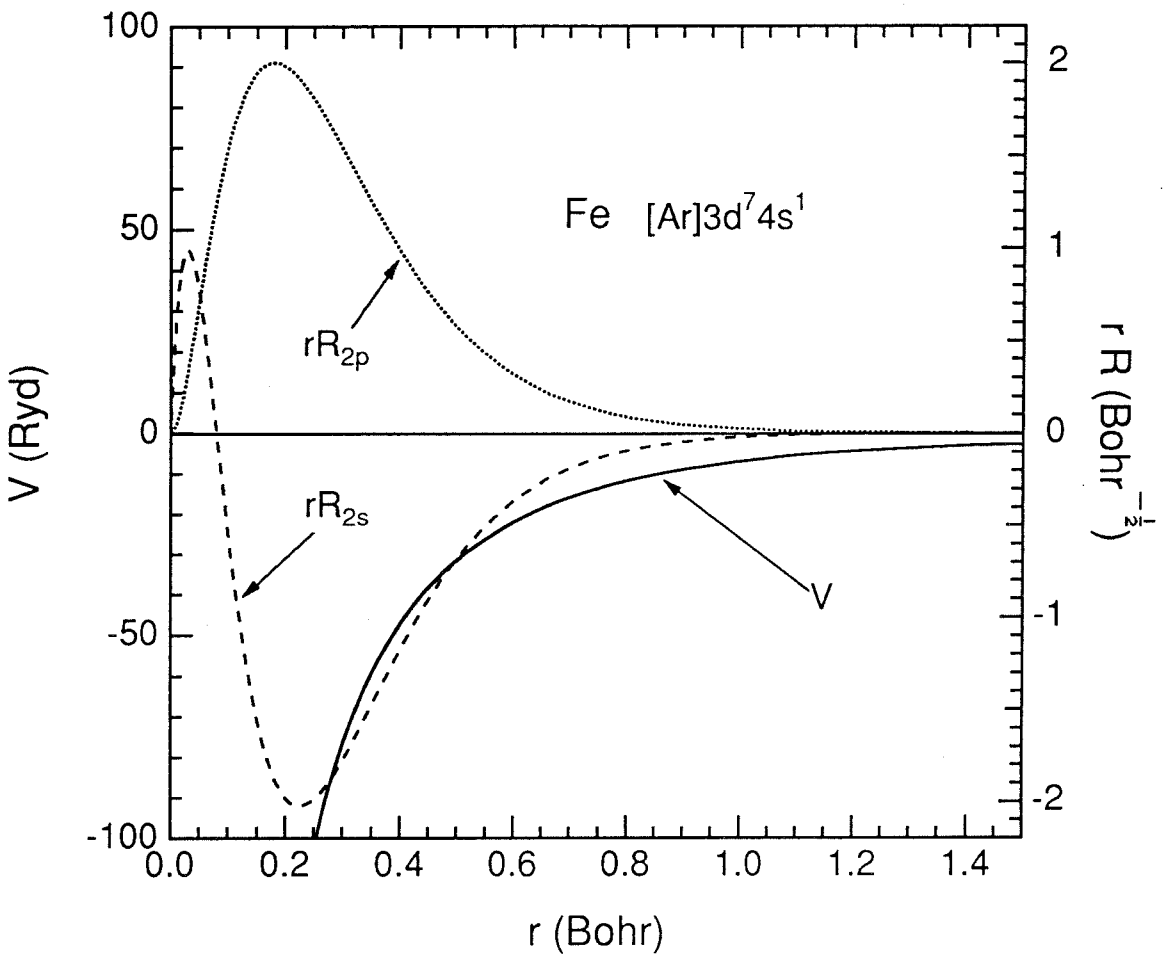

Figure A.4. Hartree-Slater atomic potential along with 2s and 2p wavefunctions for Fe atom in its ground state.

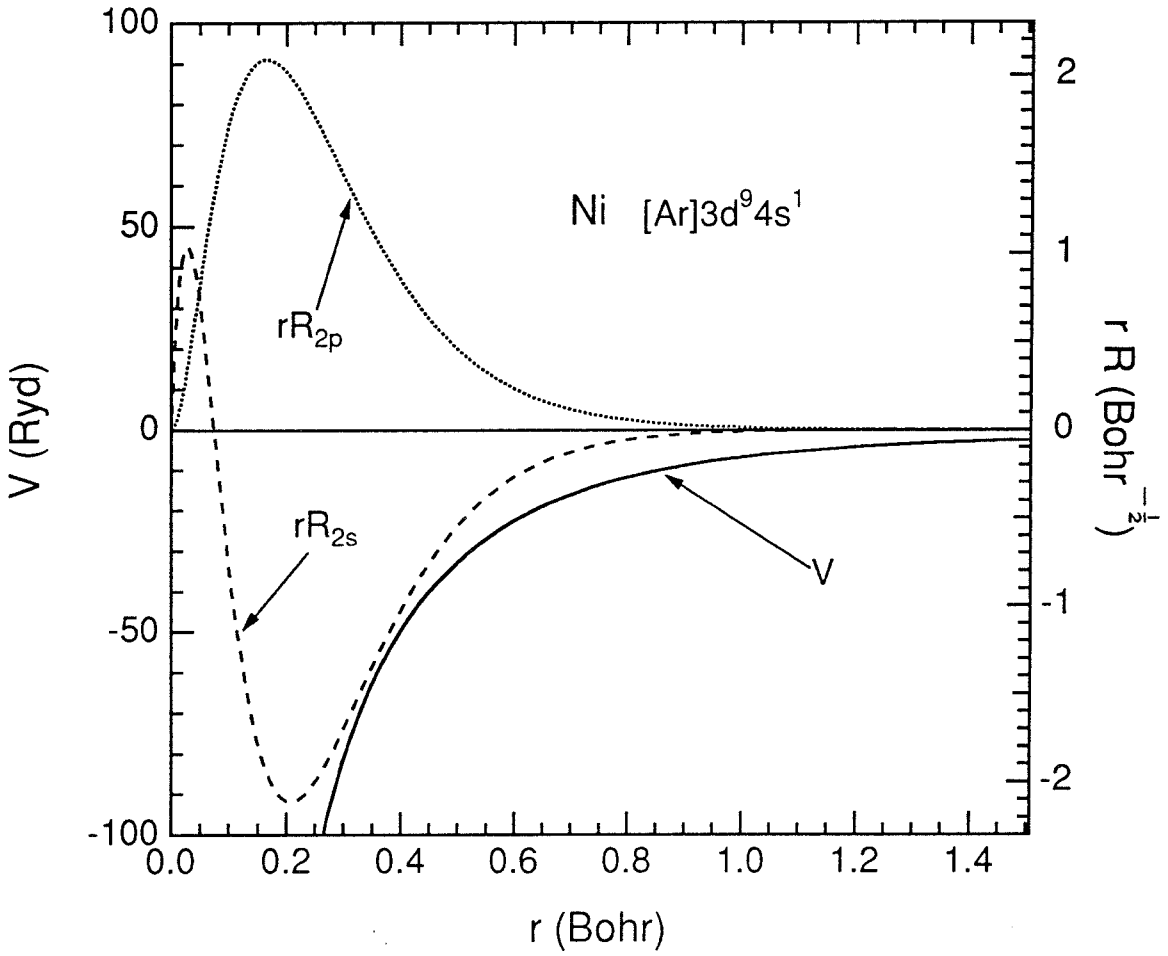

Figure A.5. Hartree-Slater atomic potential along with 2s and 2p wavefunctions for Ni atom in its ground state.

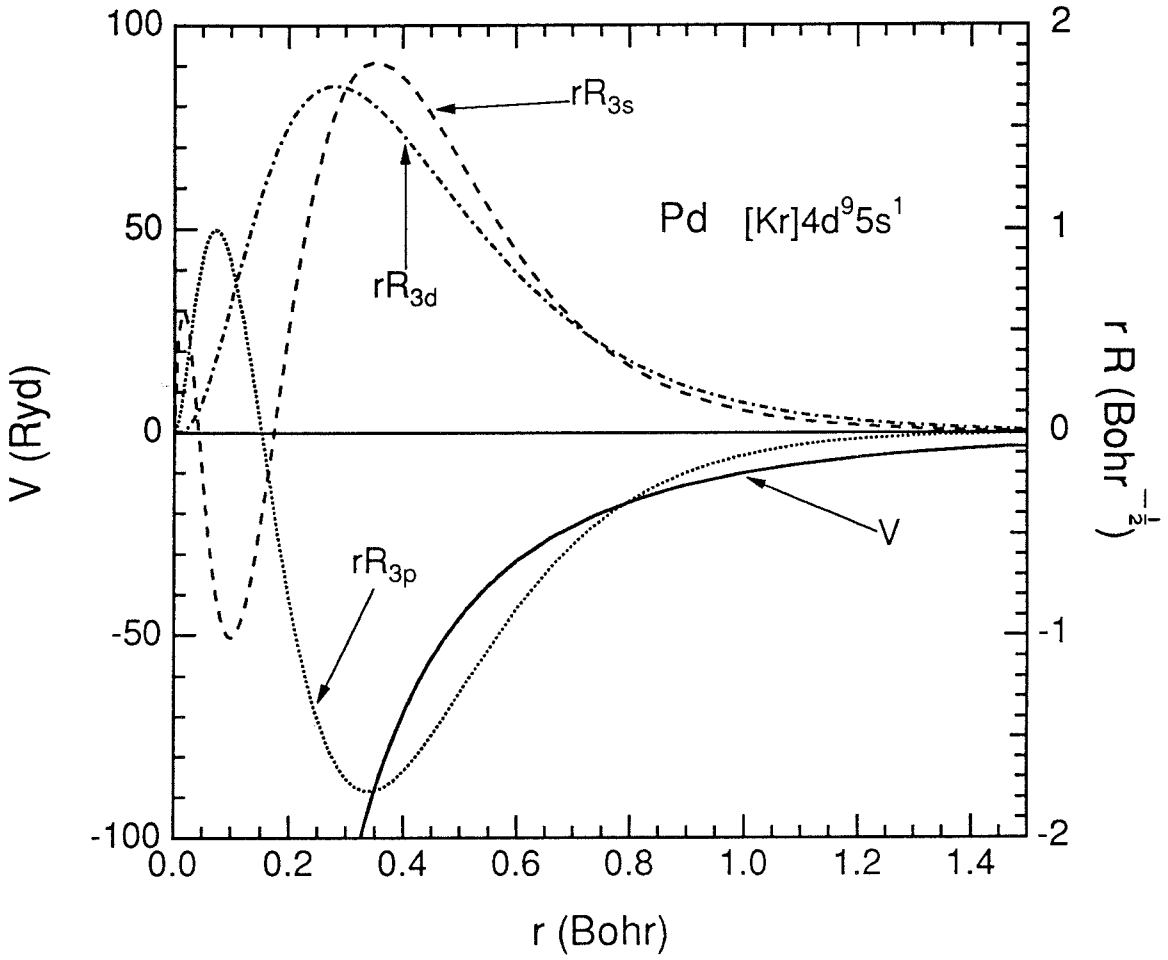

Figure A.6. Hartree-Slater atomic potential along with 3s, 3p, and 3d wavefunctions for Pd atom in its ground state.

Using the Hartree-Slater atomic wavefunctions, energy-differential cross sections for ionization are calcuated using two programs provided by Professor Peter Rez of Arizona State University (Leapman et al., 1980). The first program calculates continuum wavefunctions or partial waves by solving Equation (A.2) with $E > 0$ and uses them, along with the initial atomic wavefunction, to calculate the double-differential cross section via Equation (2.10). The double-differential cross section is a function of both energy loss and momentum transfer. The second program implements Equation (2.11) which integrates the double-differential cross section over the appropriate range of momentum transfer to determine the energy-differential cross section for ionization. Figures A.7 through A.12 display the calculated energy-differential cross sections of the O K, Al K, Ti K, Fe L, Ni L, and Pd M edges. Note that spin-orbit splitting is included in the figures. On the basis of the $(2j + 1)$ degeneracy of the initial core states, the ratio of L_3-to-L_2 or M_3-to-M_2 intensities is assumed to be 2:1, and the ratio of M_5-to-M_4 intensities is assumed to be 3:2.

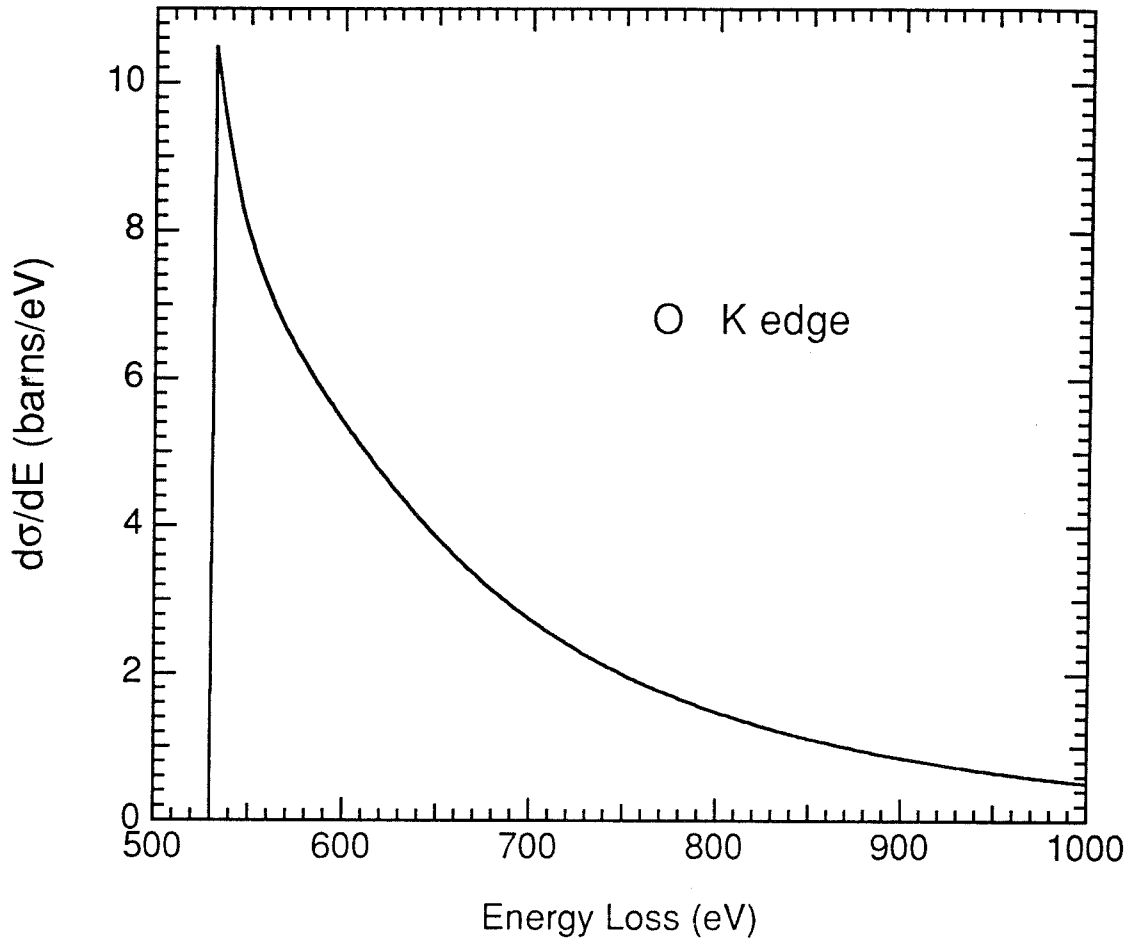

Figure A.7. Energy-differential cross section of O K edge. Energy of incident beam = 200 keV. Collection semiangle = 5 mrad.

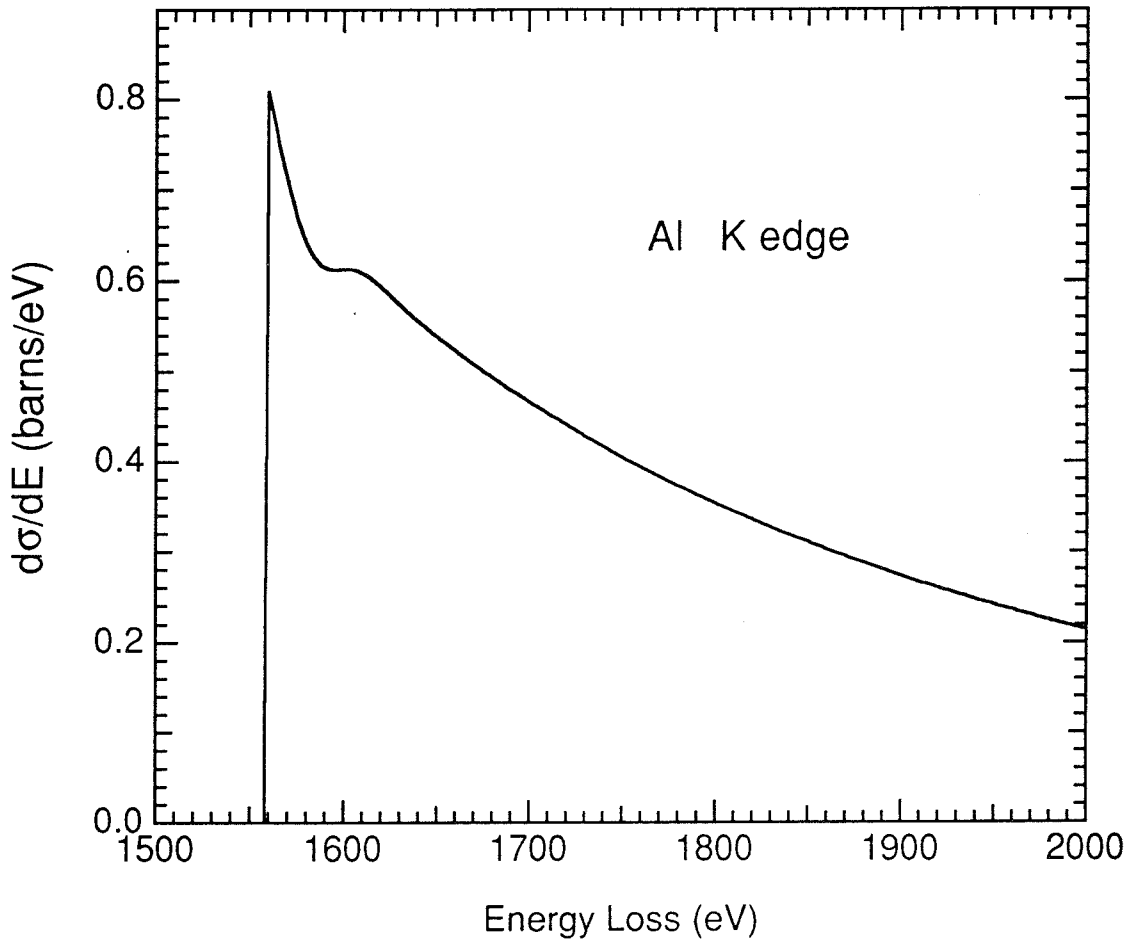

Figure A.8. Energy-differential cross section of Al K edge. Energy of incident beam = 200 keV. Collection semiangle = 10 mrad.

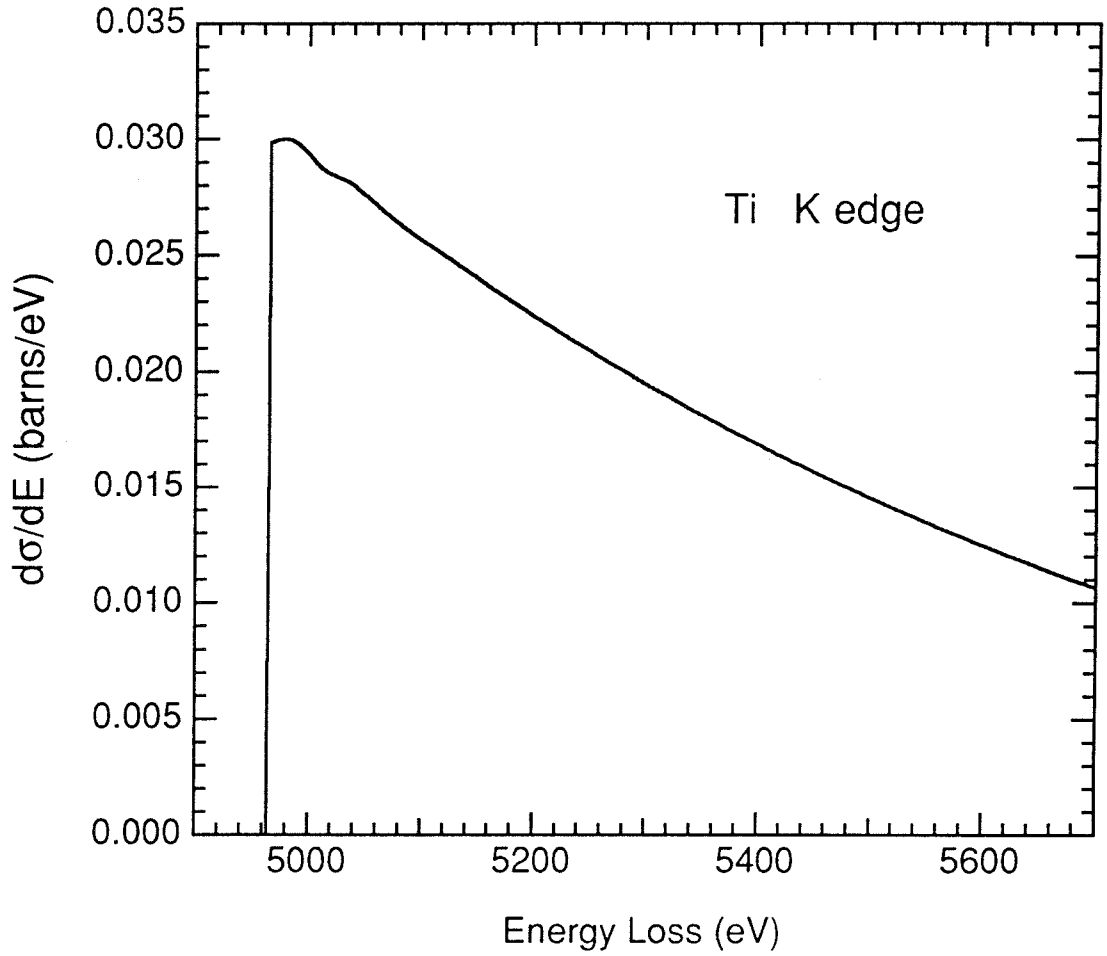

Figure A.9. Energy-differential cross section of Ti K edge. Energy of incident beam = 200 keV. Collection semiangle = 35 mrad.

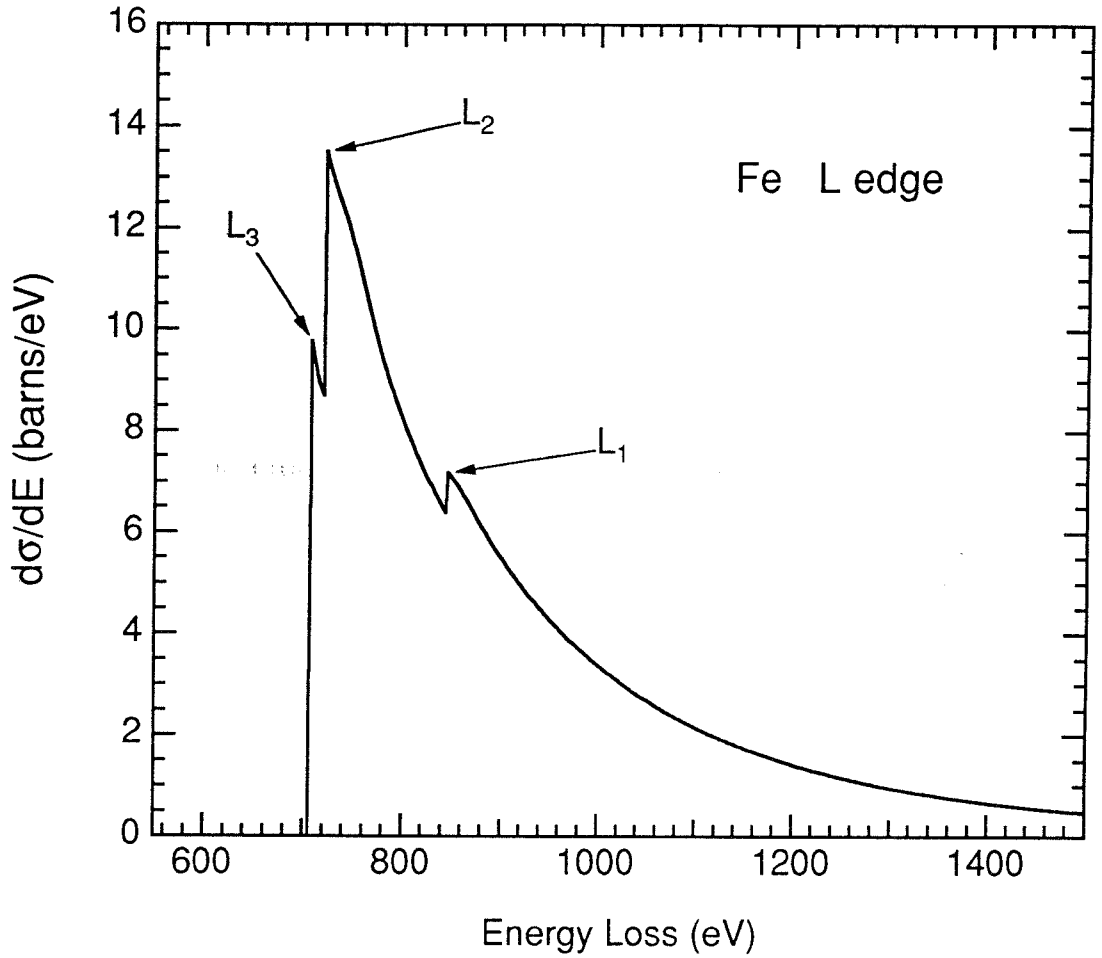

Figure A.10. Energy-differential cross section of Fe L edge. Energy of incident beam = 200 keV. Collection semiangle = 5 mrad.

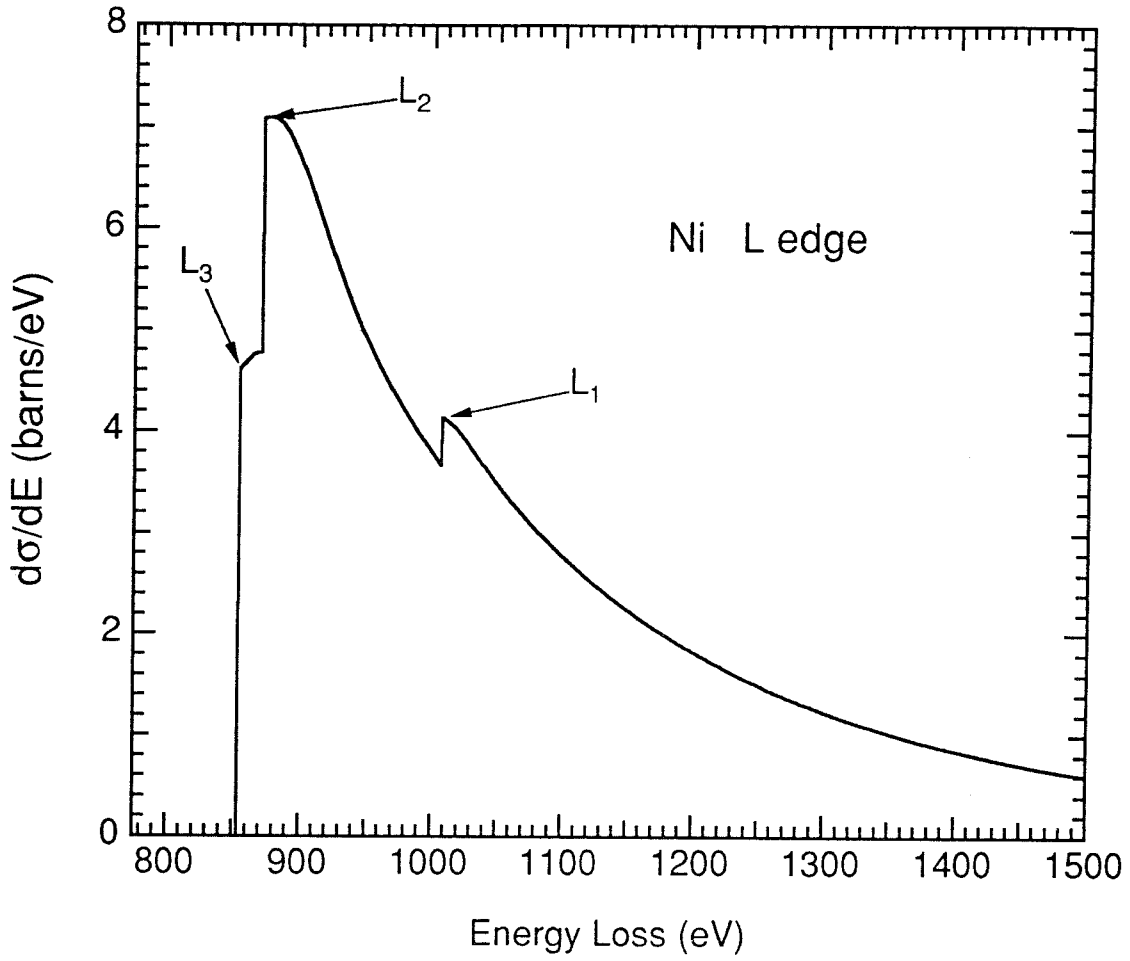

Figure A.11. Energy-differential cross section of Ni L edge. Energy of incident beam = 200 keV. Collection semiangle = 5 mrad.

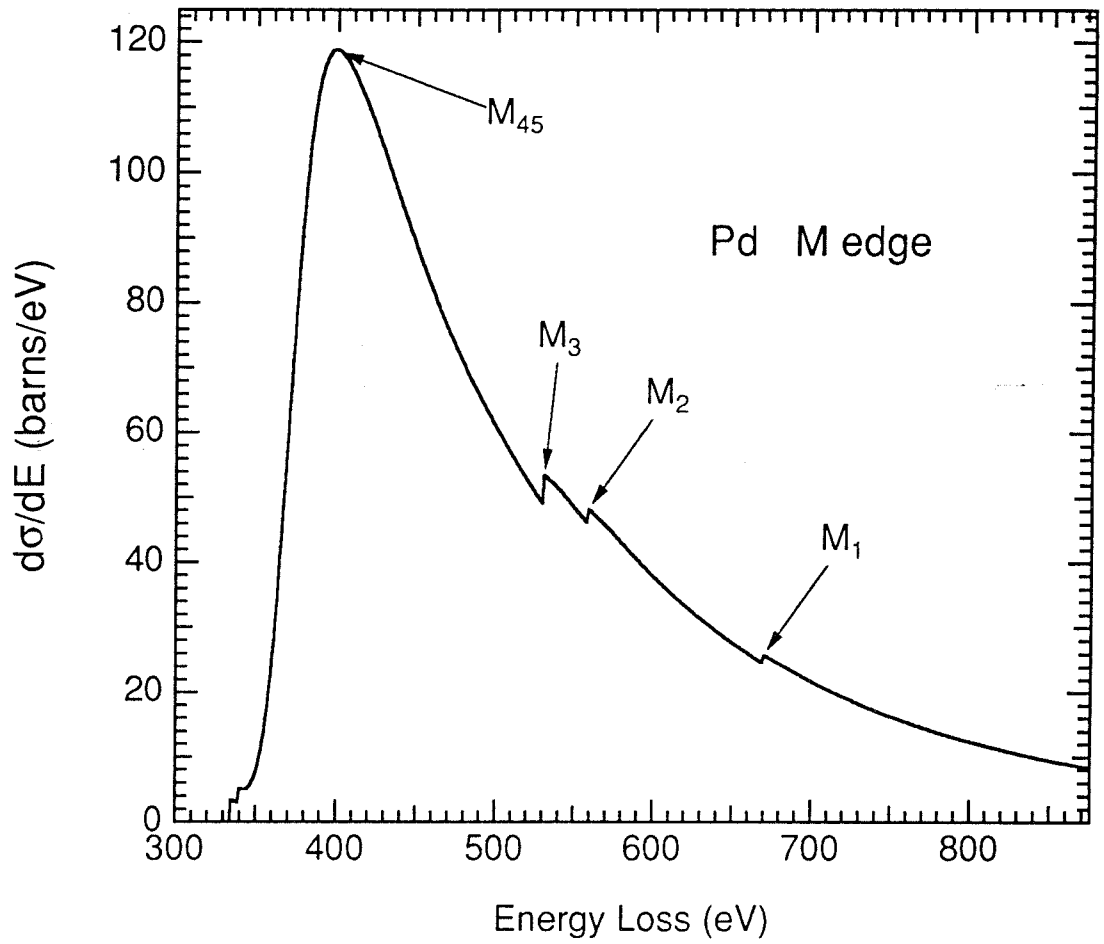

Figure A.12. Energy-differential cross section of Pd M edge. Energy of incident beam = 200 keV. Collection semiangle = 5 mrad.

A.2 Central Atom Phase Shifts and Backscattering Amplitudes

This section contains calculations of central atom phase shifts and backscattering amplitudes for EXELFS. Results relevant to the experiments in this thesis are presented, along with some results which should be useful for future EXELFS experiments. The computer program "PHASE," which I wrote to make the calculations, is given.

My calculations start with Hartree-Slater atomic wavefunctions from a computer program originally written by Herman and Skillman (1963). Hartree-Slater atomic wavefunctions are self-consistent wavefunctions which assume that exchange between atomic electrons can be accounted for by the exchange potential given in Equation (A.1). Here, I assume that exchange between the external electron and the electrons in the scattering atom can also be described by the exchange potential given in Equation (A.1), where $\rho(r)$ is the total charge density of the atomic electrons.

To calculate the central atom phase shift, a completely relaxed central atom with a core-hole was used. The central atom is assumed to be relaxed because the relaxation time ($\sim 10^{-18}$ s) is much shorter than the transit time of the ionized electron as it travels to a neighboring atom and back ($\sim 10^{-17}$ s). The lifetime of the core hole ($\sim 10^{-15}$ s), on the other hand, is much longer than the transit time (Teo, 1986). To calculate the backscattering amplitude, a neutral neighboring atom was assumed. In either case, beyond two times the covalent radius of the atom, the potential was gradually reduced to zero over the distance of 1 Bohr.

Using the Hartree-Slater potential $V(r)$, partial waves $rR_{kl}(r)$ are calculated by solving Equation (A.2) with $E = k^2$. These partial waves are compared with the corresponding free waves $rj_l(kr)$ to determine the phase shifts $\delta_l(k)$, where

$j_l(kr)$ is the spherical Bessel function of the first kind of order l. For the central atom phase shift, only $\delta_{l_0+1}(k)$ needs to be calculated, where l_0 is the orbital angular momentum quantum number of the initial core state. For the backscattering amplitude, all $\delta_l(k)$ which have $l \lesssim kr_{trunc}$ need to be calculated, where r_{max} is the maximum radius of the atomic potential. The backscattering amplitude, $f(\pi,k) = |f(\pi,k)|\exp[i\eta(\pi,k)]$, is then determined using Equation (2.21). Note that multiples of 2π can be added or subtracted from $\eta(\pi,k)$ without changing the physical consequences.

For the purpose of illustration, Figure A.13 presents an example of a partial wave for a relaxed C atom with a 1s core hole, along with the corresponding free wave. The figure shows that the partial wave experiences a phase shift $\delta_{l=1}(k=10\ \text{Å}^{-1})$ of a bit more than $+\pi/2$ with respect to the free wave. In this way, by varying k, the k-dependence of the phase shifts, $\delta_l(k)$, can be determined. Figure A.14 displays the central atom phase shift for the C K edge as calculated both by myself using the Hartree-Slater potential and by Teo and Lee (1979). Teo and Lee's calculation used a simple energy-dependent approximation for the exchange and correlation potentials between the external electron and electrons in the scattering atom (Lee and Beni, 1977). Figures A.15 and A.16 display calculations of the magnitude and phase of the backscattering amplitude from a neutral C atom.

Figures A.14 and A.16 show that my calculations predict slightly larger phase shifts than those calculated by Teo and Lee. The k-dependence of the phase shifts, however, are remarkably similar, and it is this k-dependence which determines the change in peak positions in the Fourier transform of the EXELFS.

This thesis measures and analyzes the EXELFS on the Al K, Ti K, Fe L, Ni L, and Pd M edges. Figures A.17 through A.21 present the central atom phase

shifts for these edges. Figures A.22 through A.25 display the magnitude and phase of backscattering amplitudes from neighboring O, Al, Ti, Fe, Ni, and Pd atoms.

In particular, note the central atom phase shift $\delta_3(k)$ for the Pd M edge in Figure A.21. $\delta_3(k)$ is the phase shift for a partial wave with f-symmetry. Although knowledge of $\delta_3(k)$ is necessary for the EXELFS analysis of M_{45} or N_{45} edges, values for $\delta_3(k)$ are not published in Teo and Lee (1979) because x-ray absorption cannot easily measure those edges.

In principle, EXELFS experiments may be performed using any atomic edge which can be measured by EELS. However, most published calculations of central atom phase shifts are for those atomic edges which can be measured by x-ray absorption spectrometry. To help remedy this situation, Figures A.26 through A.28 present central atom phase shifts for some edges that, while not easily measurable by EXAFS, are possible candidates for EXELFS experiments. Specifically Figure A.26 gives $\delta_1(k)$ for K edges of very light elements. Figures A.27 and A.28 give $\delta_3(k)$ for M_{45} edges of elements with $32 \leq Z \leq 48$. In these calculations, the valence configuration for the 4d transition metal series is assumed to be $4d^{Z-37}5s^1$.

Figures A.27 and A.28 show that, in the region of interest, the central atom phase shifts $\delta_3(k)$ have relatively small k-dependences. This implies that the nearest-neighbor peak positions in the Fourier transform of the EXELFS from M_{45} edges are only slightly changed by the central atom phase shifts. In comparison, the central atom phase shifts $\delta_1(k)$ for K edges have relatively large k-dependences, and thus have greater effect on the peak positions.

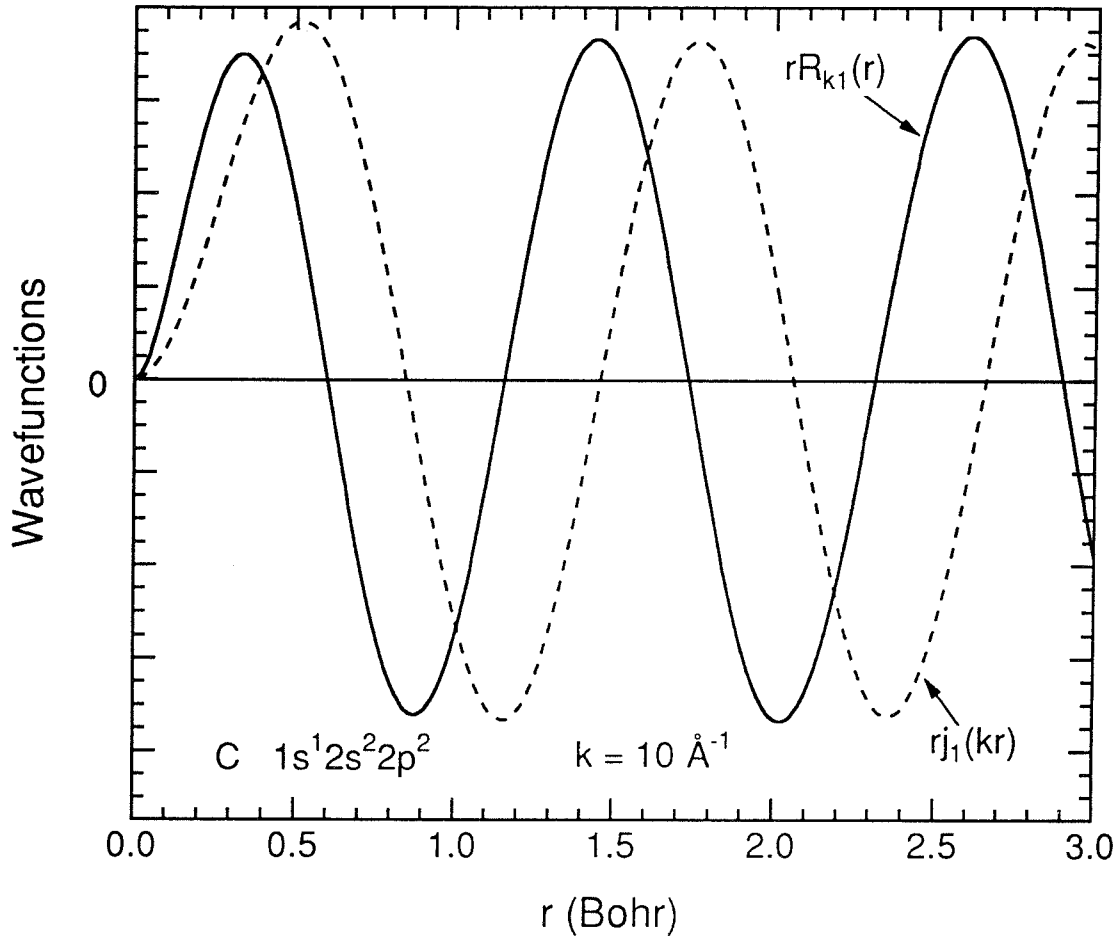

Figure A.13. Partial wave and corresponding free wave for relaxed C atom with 1s core hole.

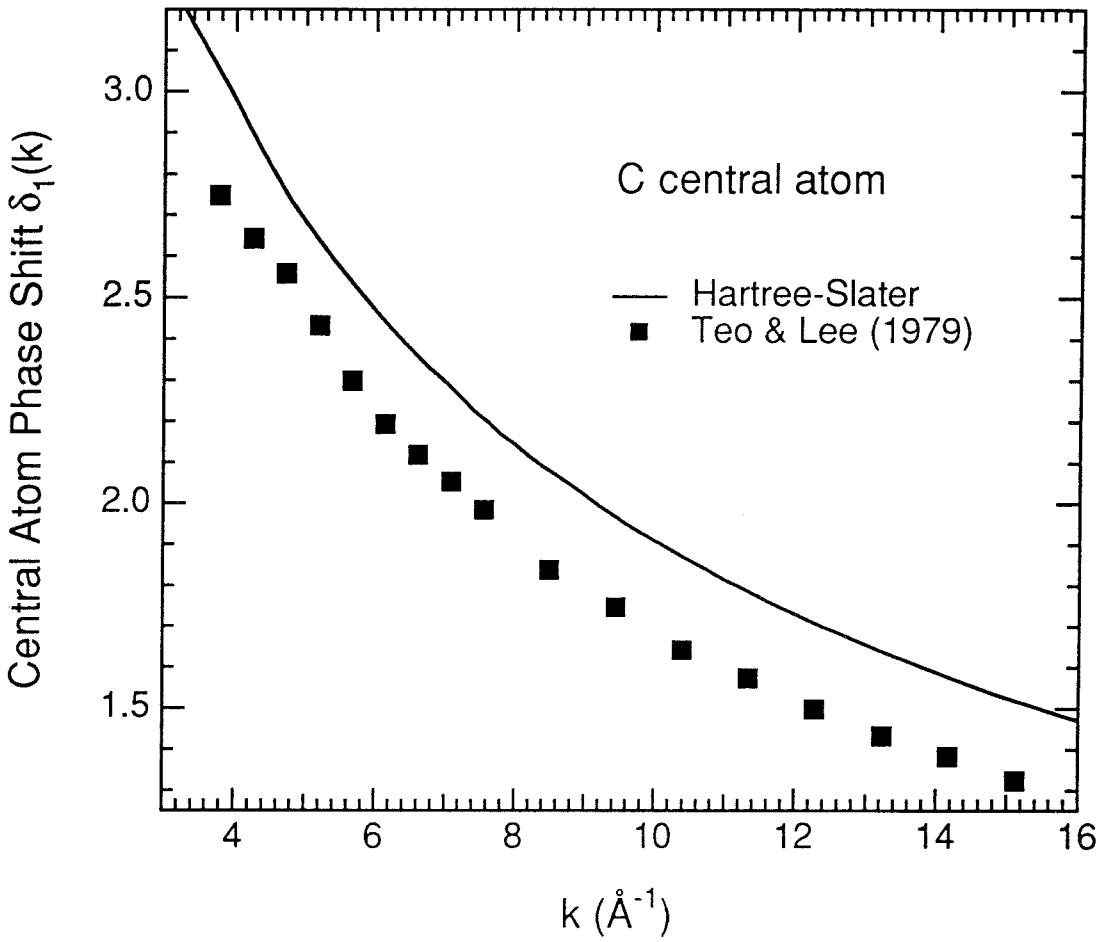

Figure A.14. Central atom phase shift for C K edge.

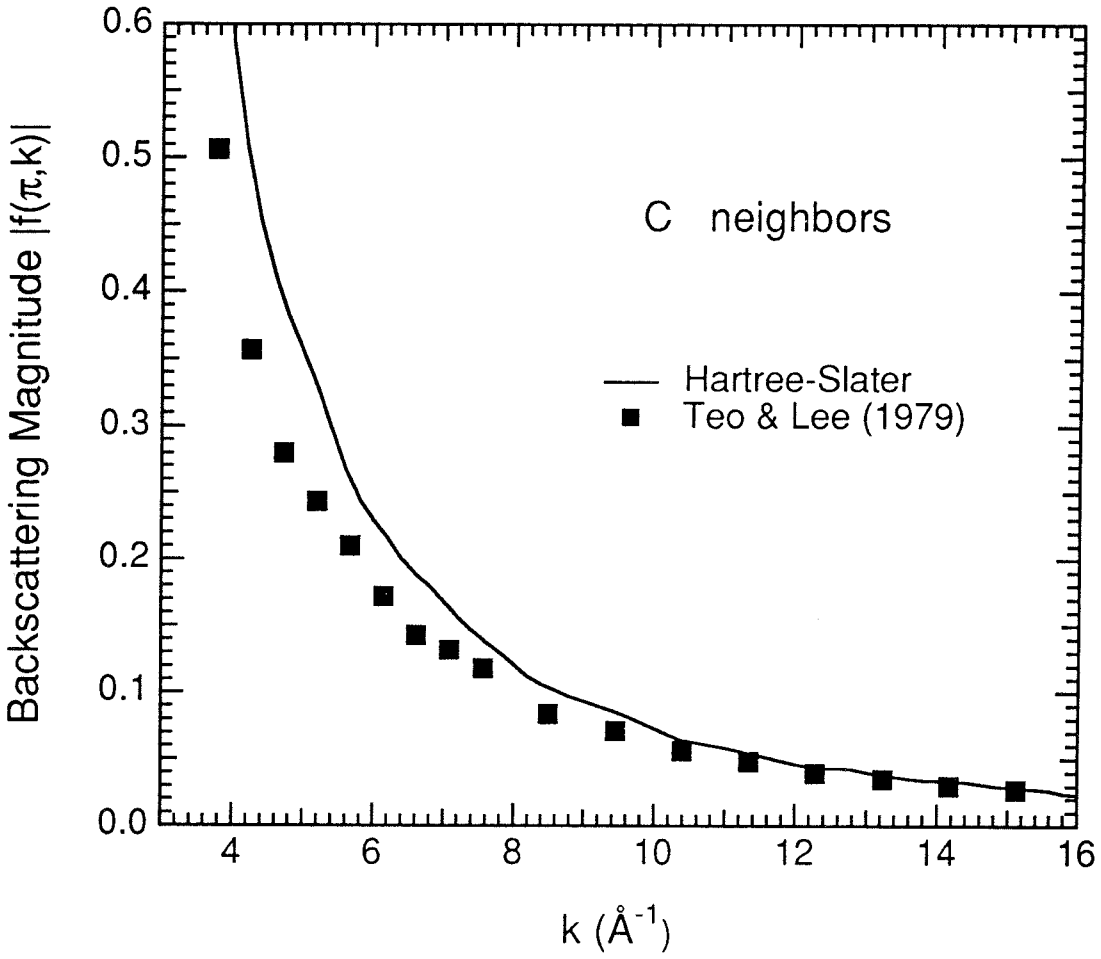

Figure A.15. Magnitude of backscattering amplitude for C neighbors.

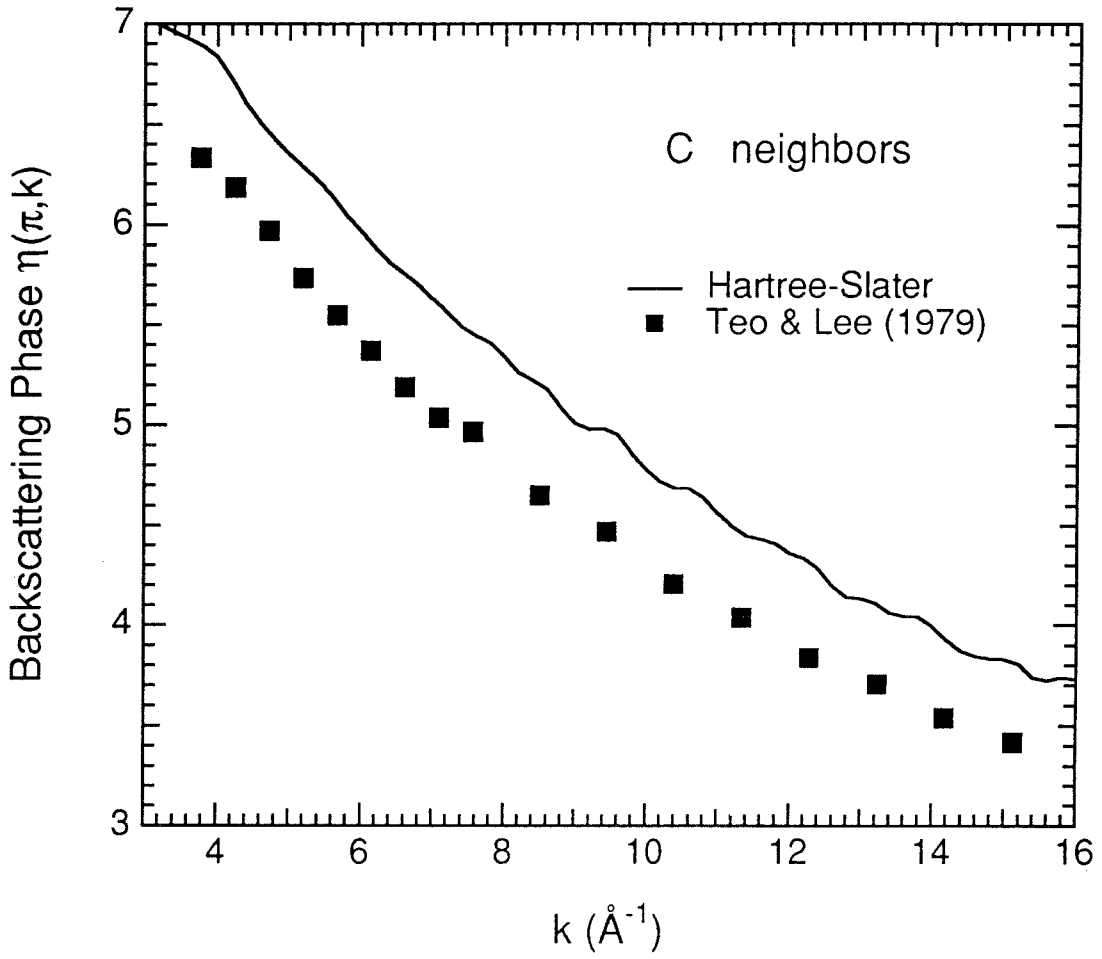

Figure A.16. Phase of backscattering amplitude for C neighbors.

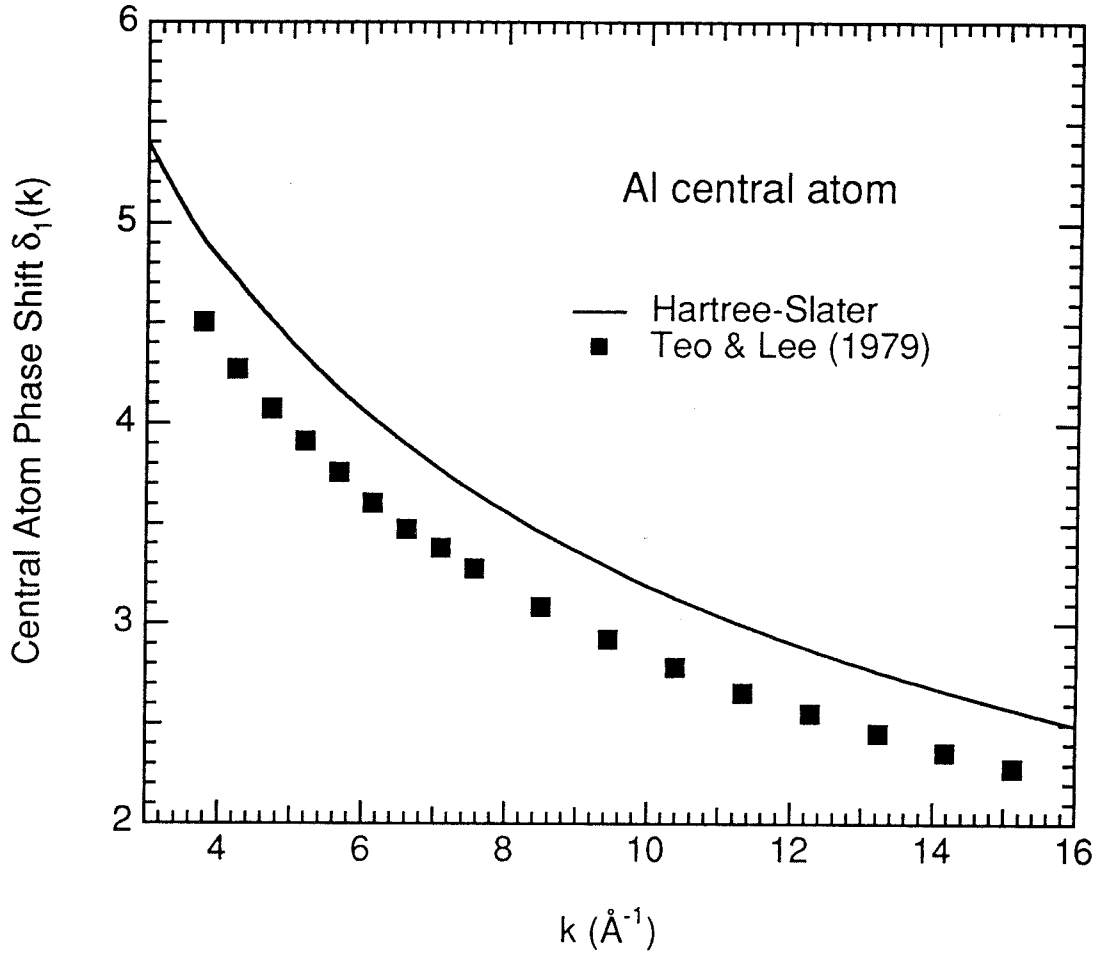

Figure A.17. Central atom phase shift for Al K edge.

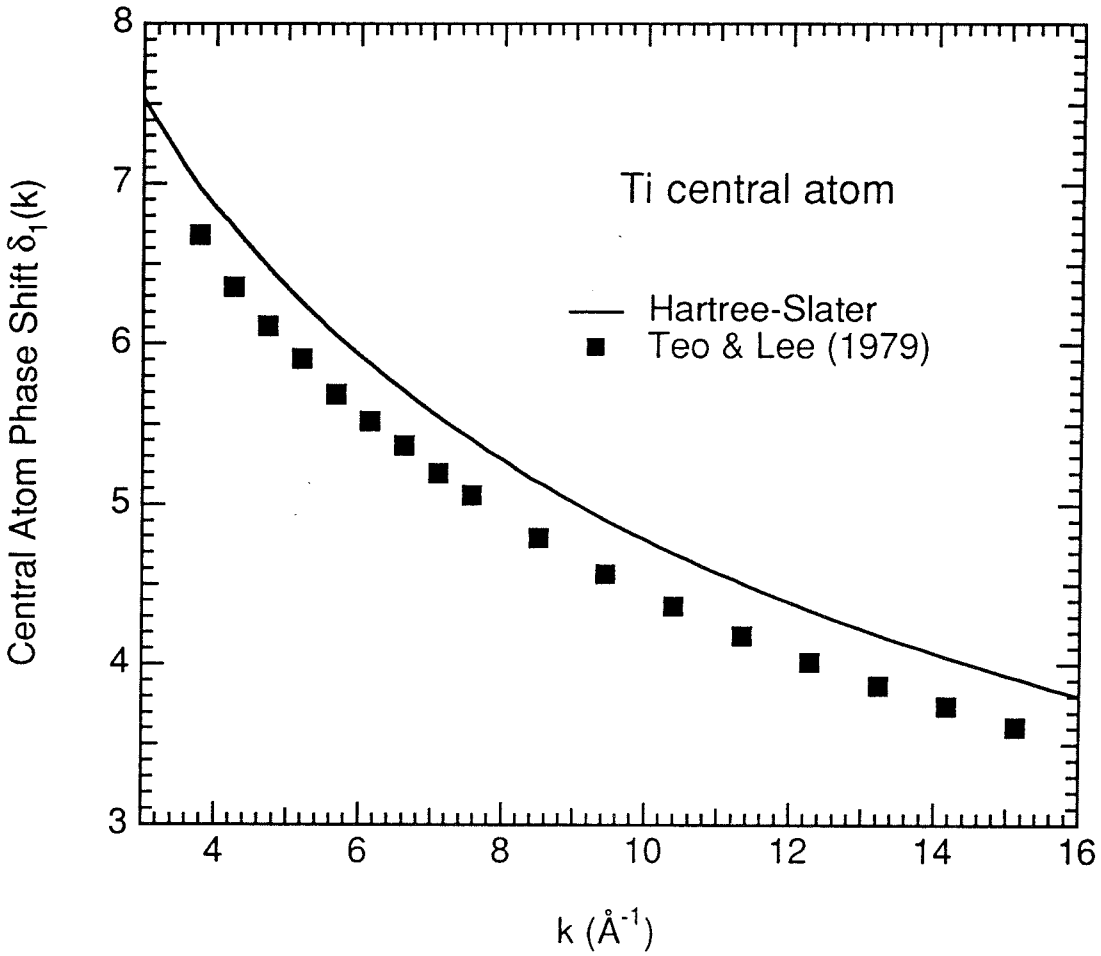

Figure A.18. Central atom phase shift for Ti K edge.

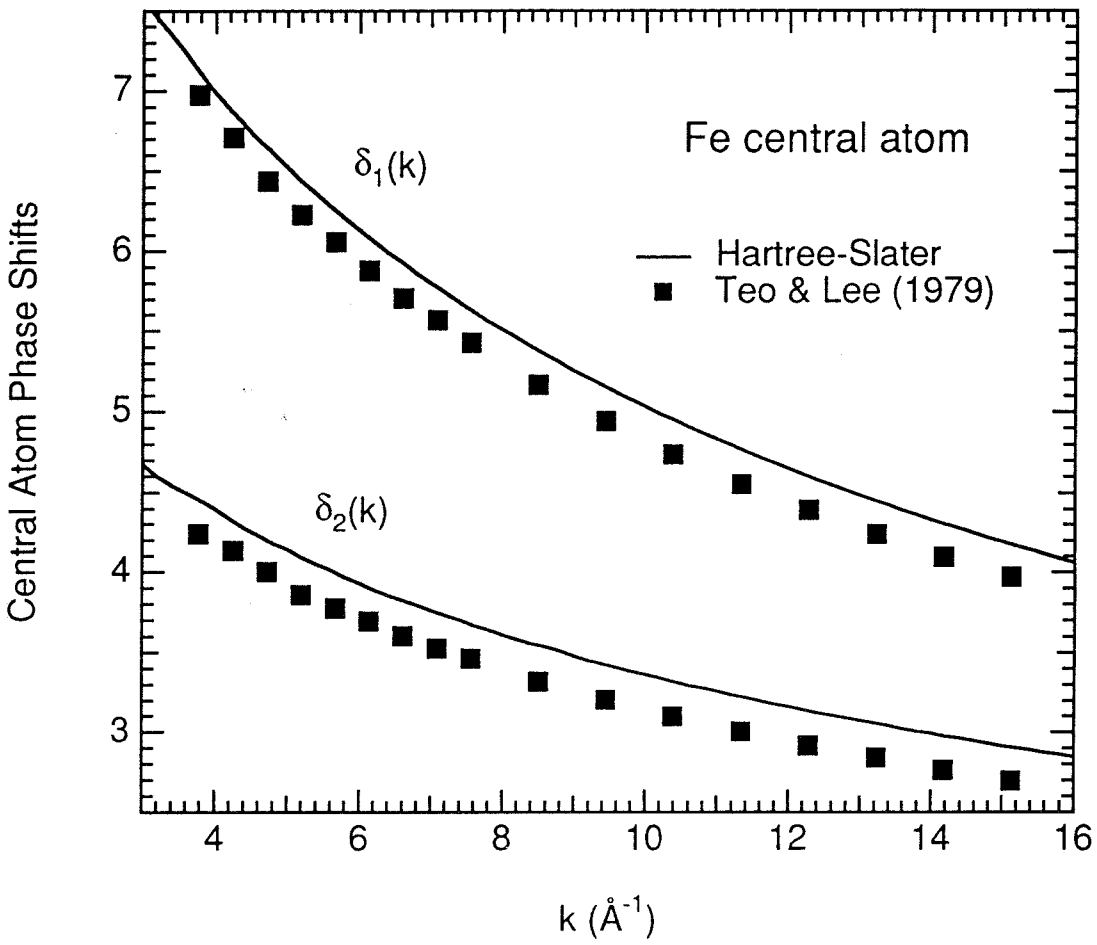

Figure A.19. Central atom phase shifts for Fe L edge.

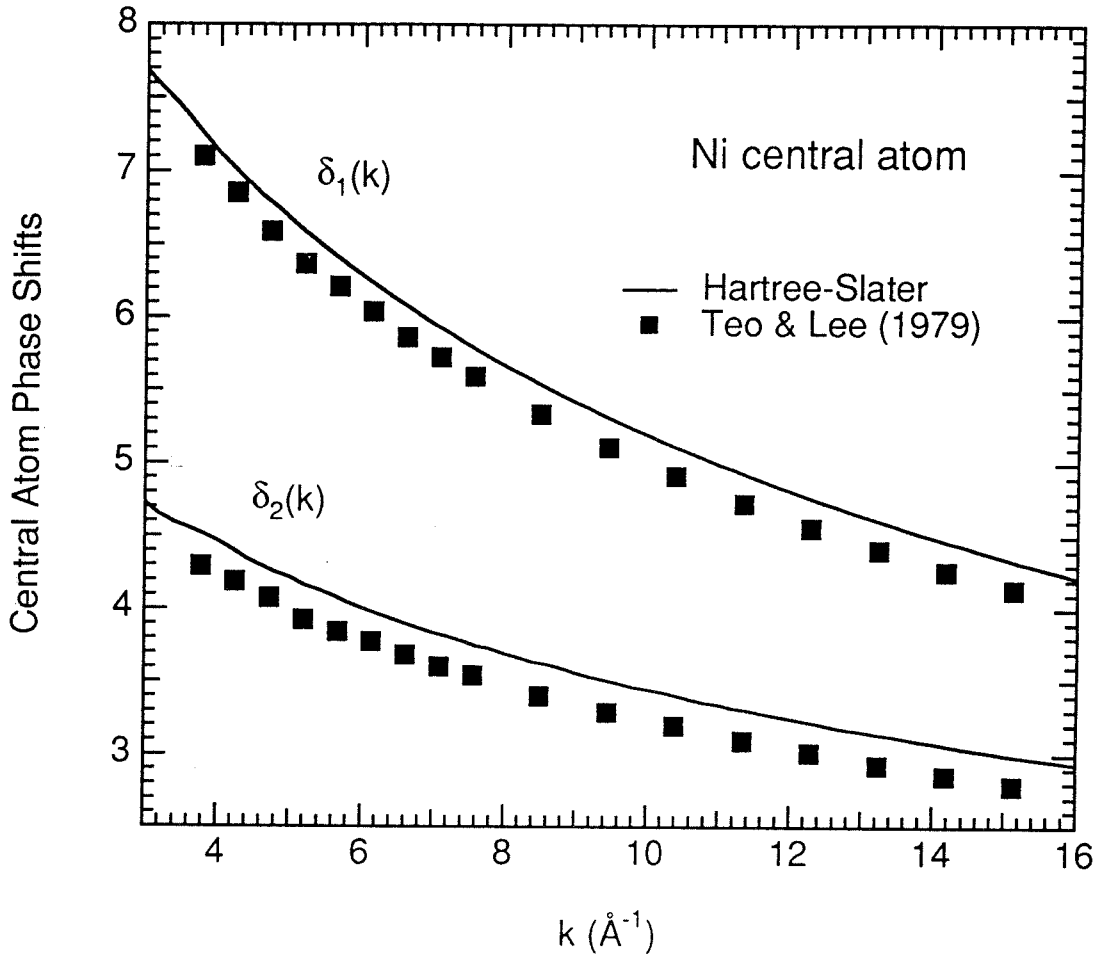

Figure A.20. Central atom phase shifts for Ni L edge.

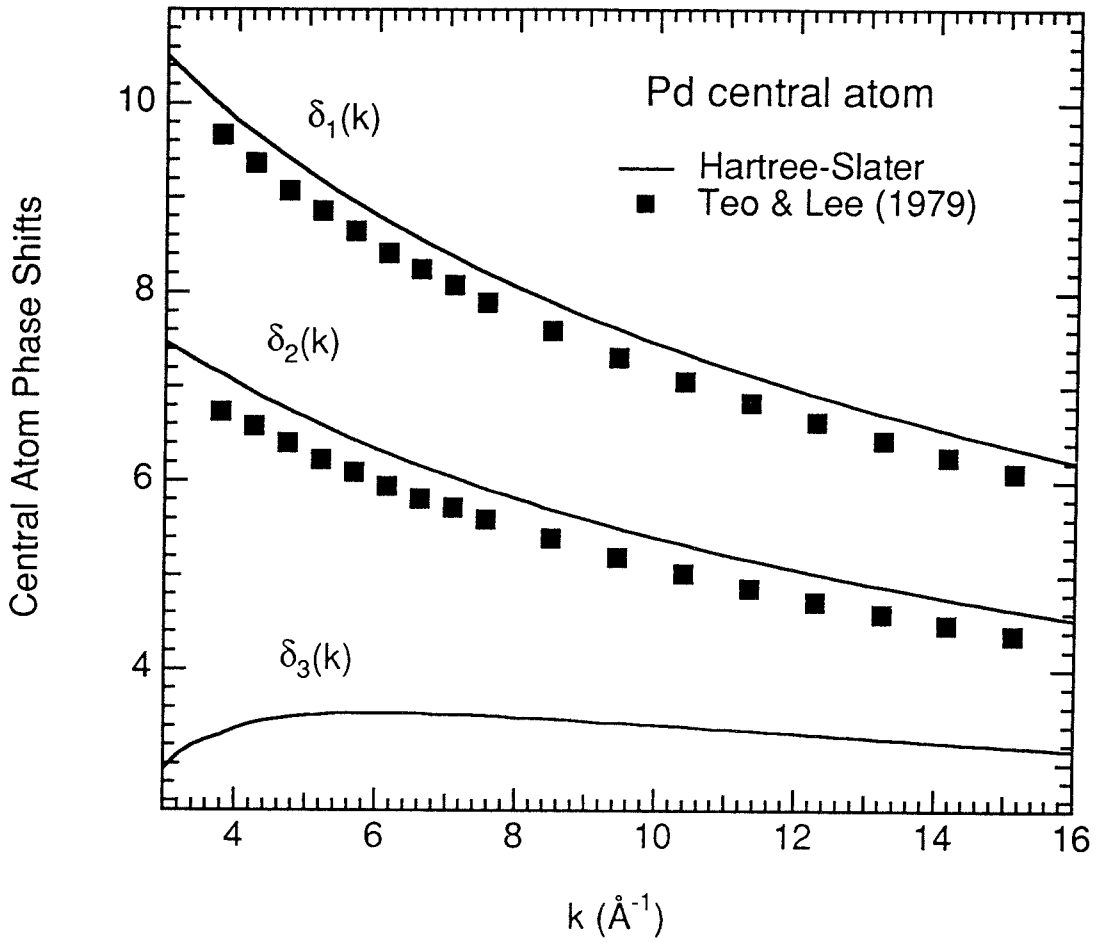

Figure A.21. Central atom phase shifts for Pd M edge.

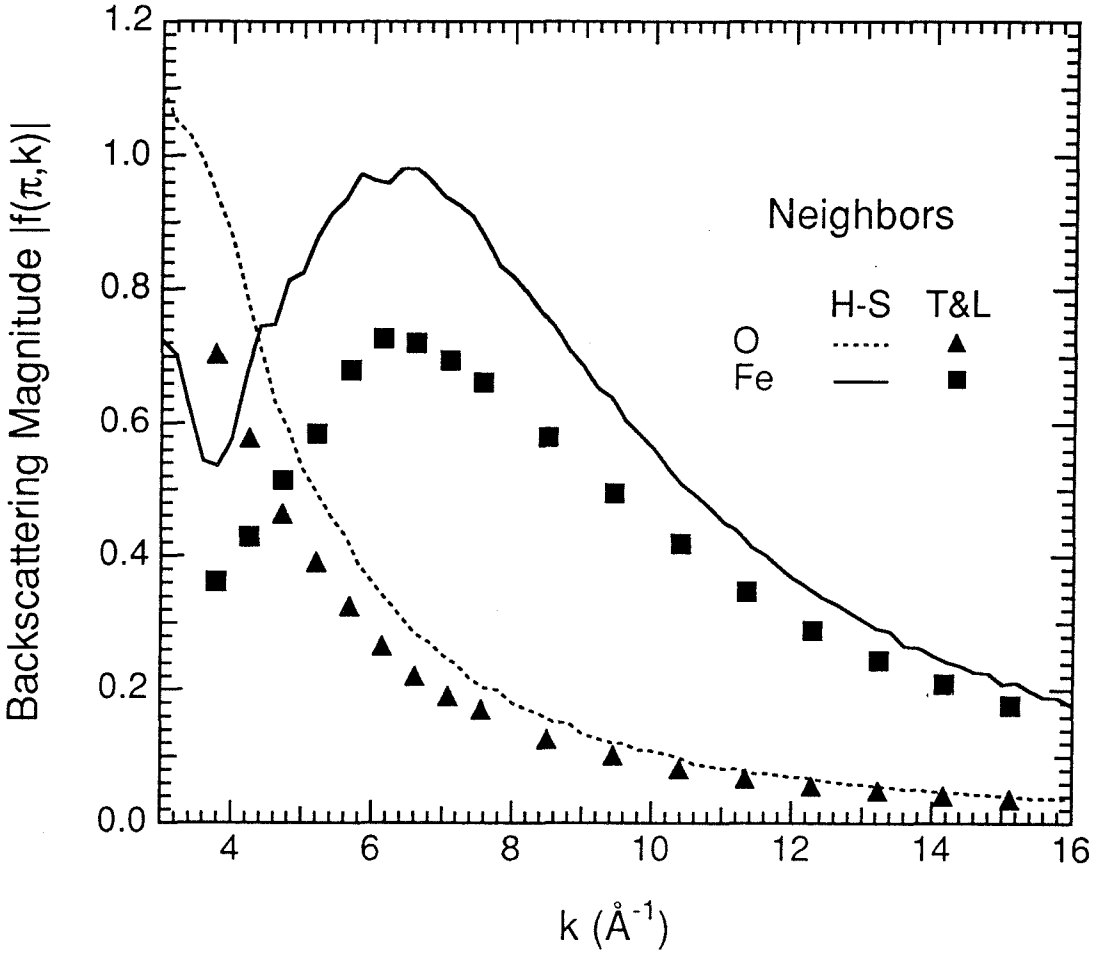

Figure A.22. Magnitude of backscattering amplitude for O and Fe neighbors.

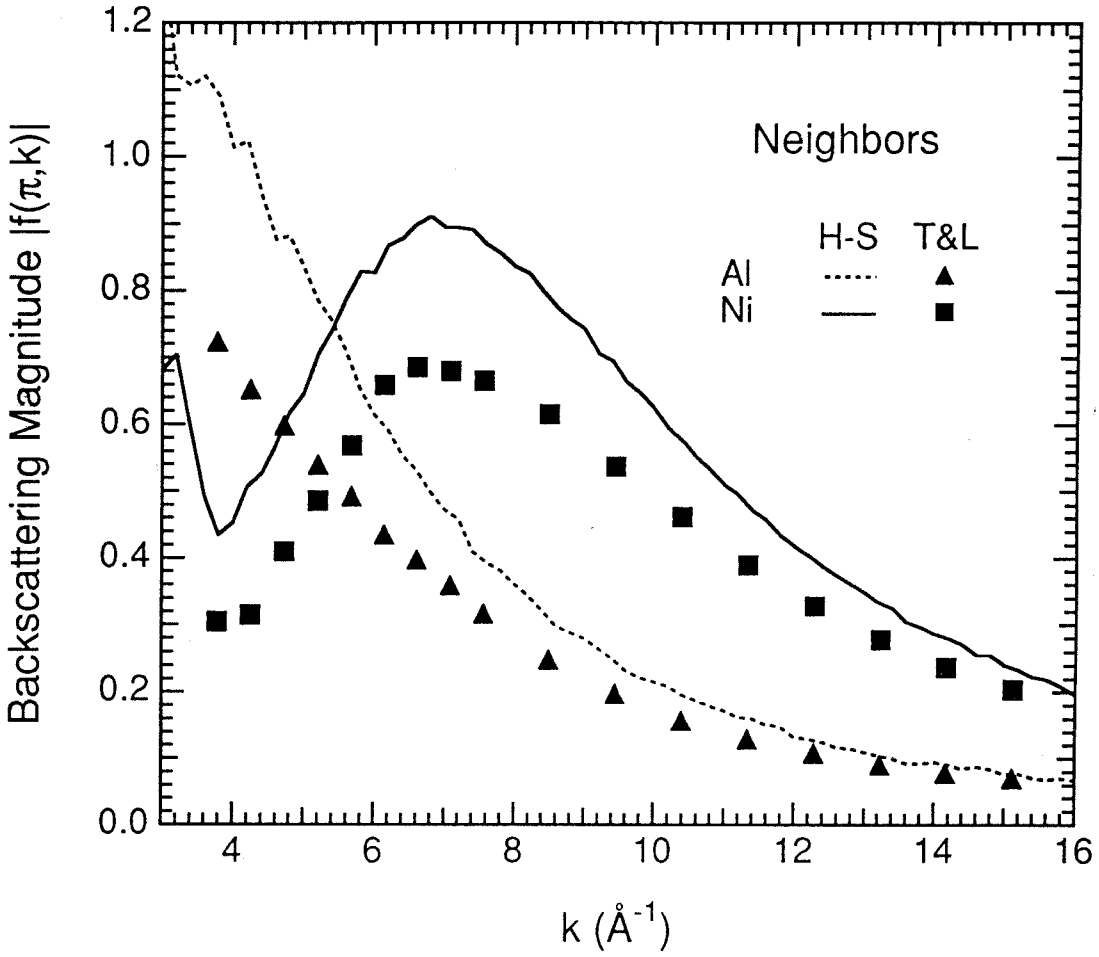

Figure A.23. Magnitude of backscattering amplitude for Al and Ni neighbors.

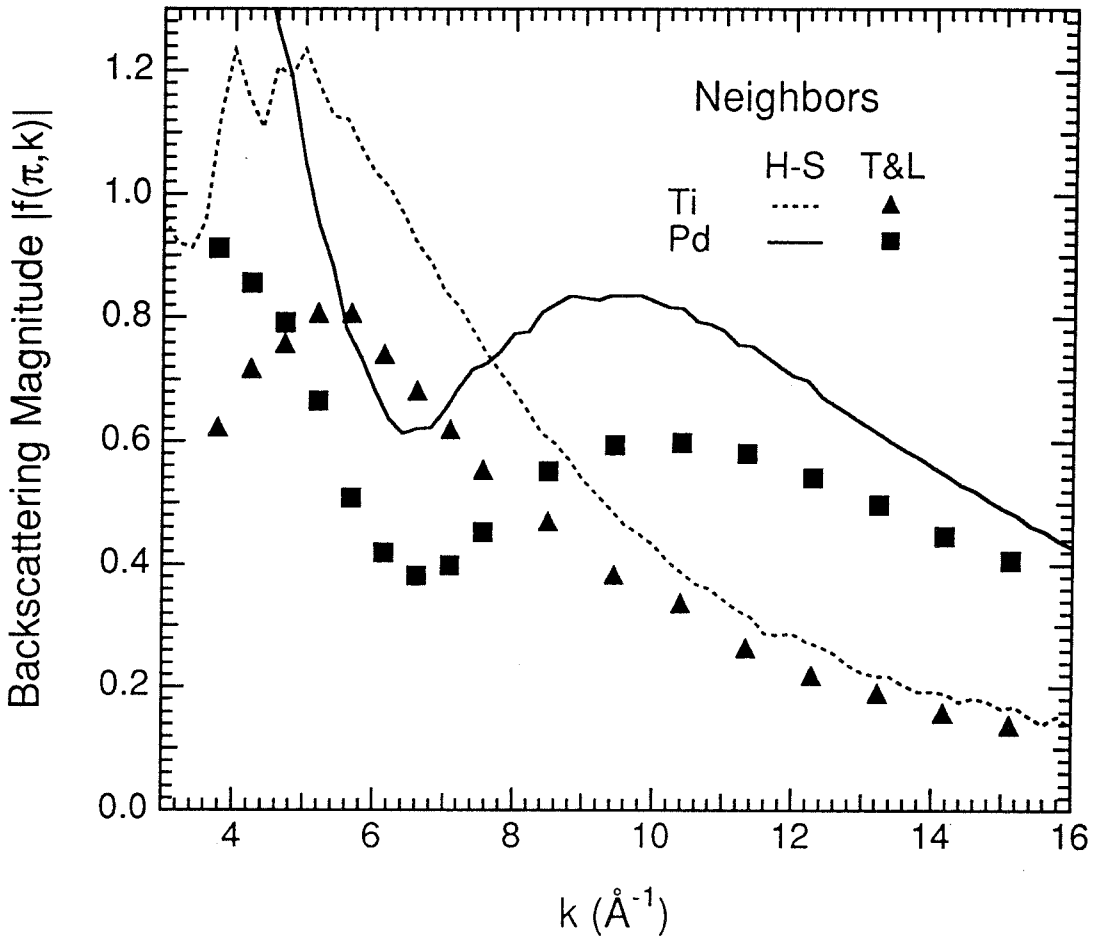

Figure A.24. Magnitude of backscattering amplitude for Ti and Pd neighbors.

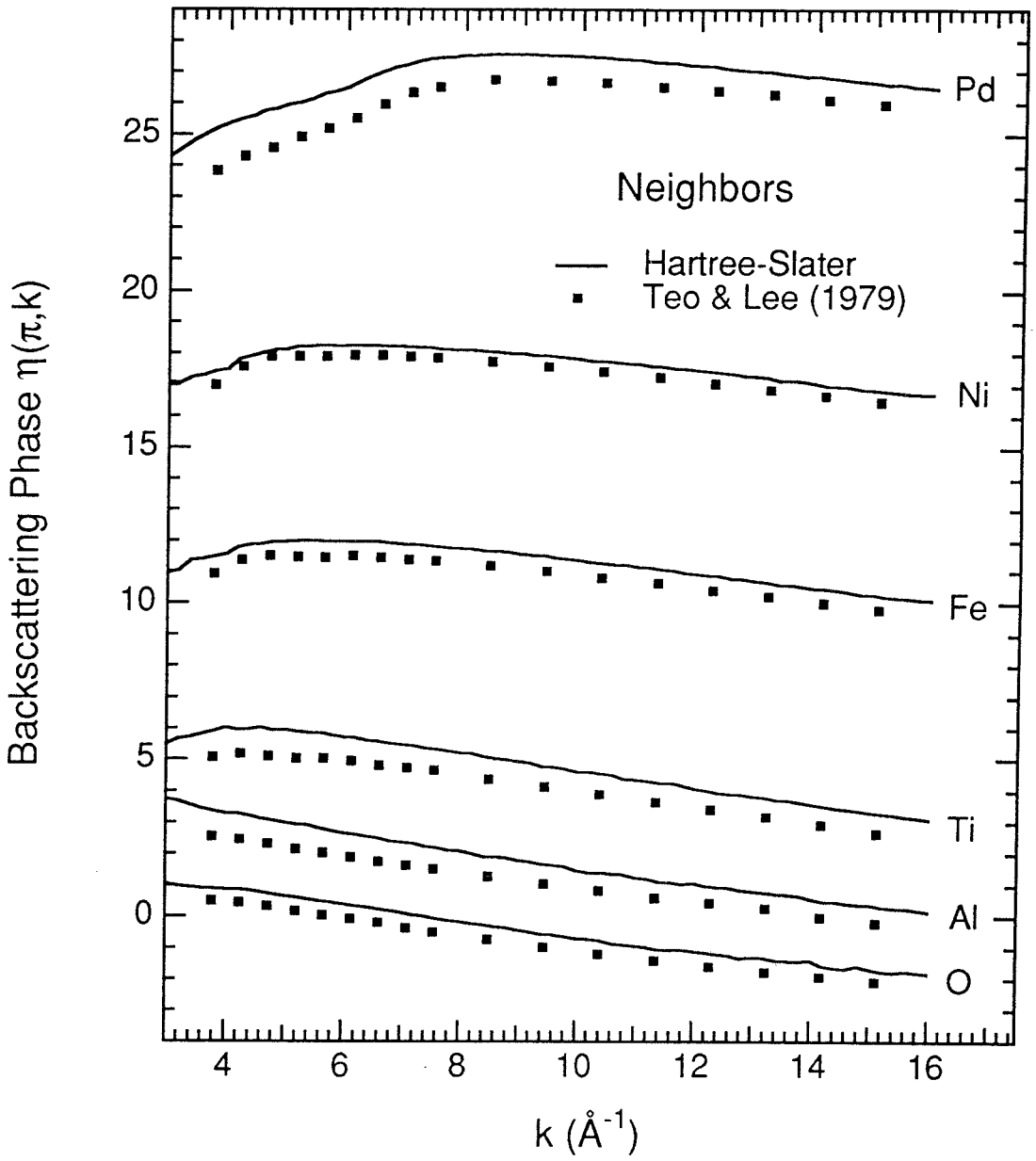

Figure A.25. Phase of backscattering amplitude for O, Al, Ti, Fe, Ni, and Pd neighbors. Note phases plotted as increasing function of Z merely to separate them.

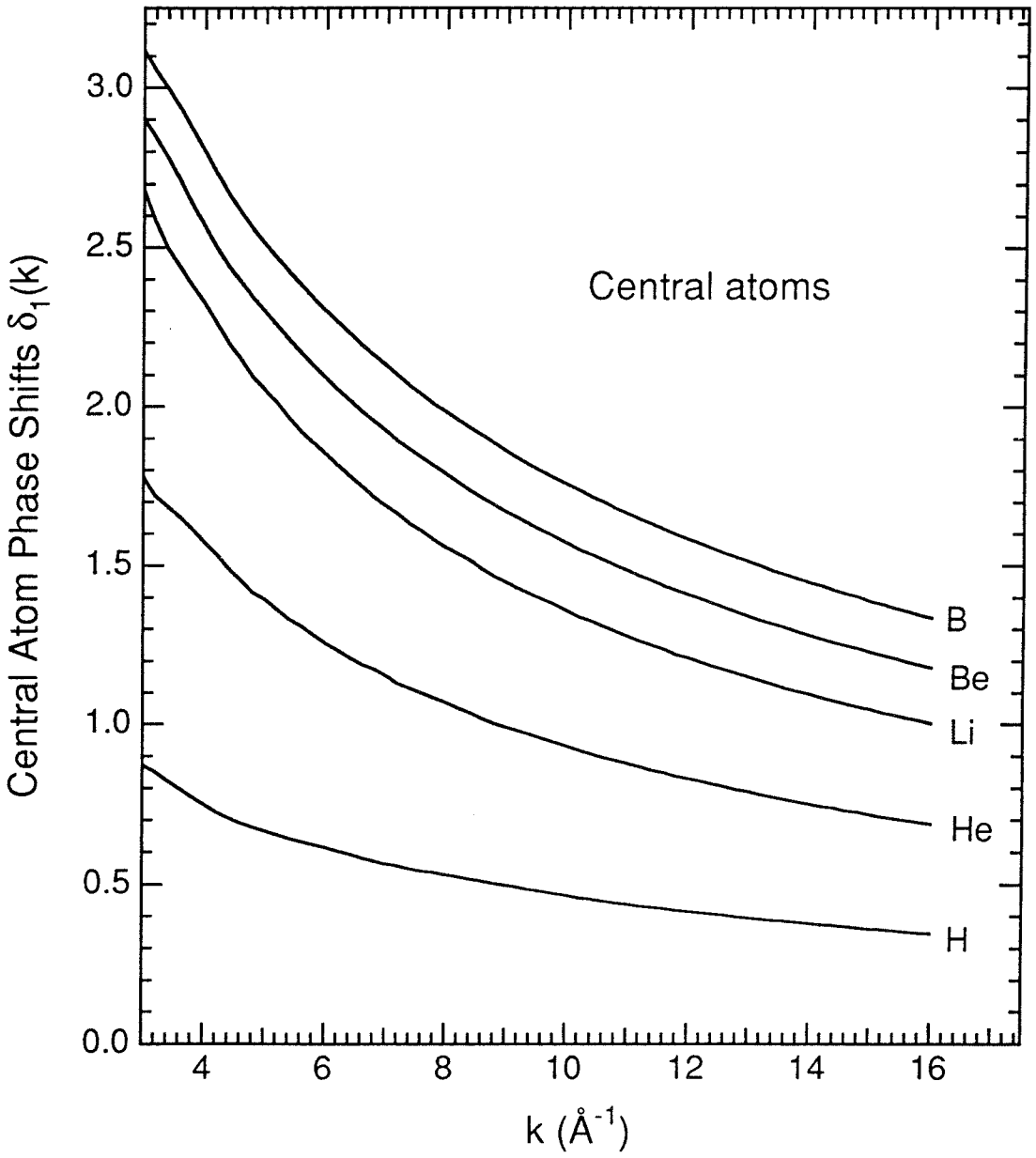

Figure A.26. Hartree-Slater calculations of central atom phase shifts for K edges of very light elements not listed in Teo and Lee (1979).

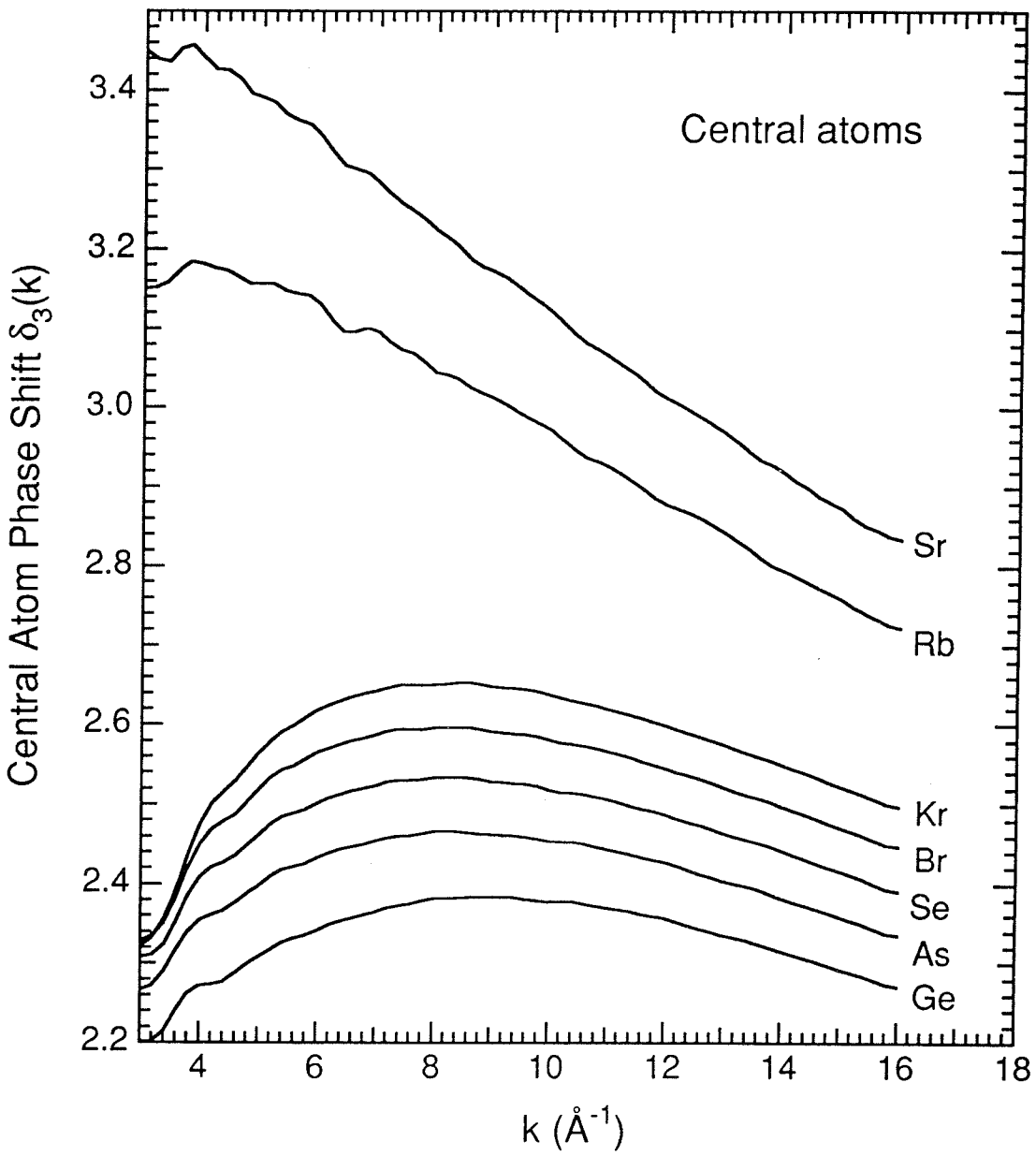

Figure A.27. Hartree-Slater calculations of central atom phase shifts for M_{45} edges of elements with $32 \leq Z \leq 38$.

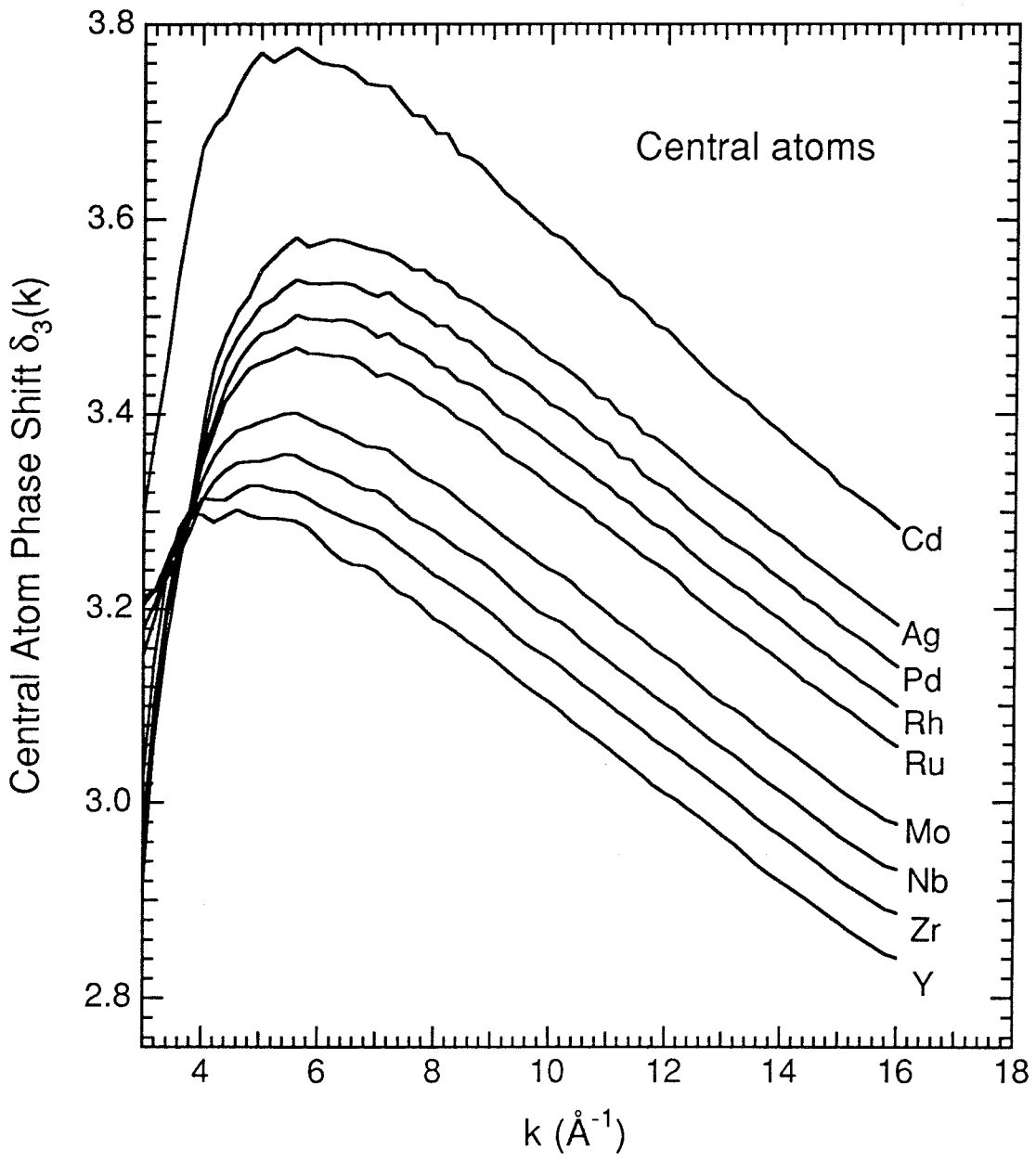

Figure A.28. Hartree-Slater calculations of central atom phase shifts for M_{45} edges of elements with $39 \leq Z \leq 48$.

```
      PROGRAM PHASE

C CALCULATION OF PHASE SHIFTS WHEN PARTIAL WAVES ARE SCATTERED
C   FROM A CENTRAL POTENTIAL.
C READS POTENTIAL FROM HERMAN-SKILLMAN OUTPUT FILE CONVERTED TO
C   "IGOR" FORMAT.

C JAMES K OKAMOTO 02FEB93

C CONSTANTS
      REAL PI
      DATA PI/3.1415927/

C VARIABLES
      CHARACTER*40 TEXT0,TEXT
      REAL Z,R1,H
      INTEGER NDATA,NWAVS
      INTEGER I,M
      REAL A,B,C
      REAL UD(0:512),OCC(20),EORB(20),WAV(20,0:512)
      CHARACTER*3 ORB(20)
      INTEGER ANGMOM(20)

      REAL RHOD(0:512)

      REAL RAD,CUT,RCUT,RAMP,RMAX,DR
      INTEGER I0,I1,I2,NEXTRA,NR

      INTEGER LL

      REAL RD(0:512),RB(5000)
      REAL DK,KA(100),KB(100)

      REAL U(5000),V(5000),RHO(5000)

      INTEGER LK,NK,IK,KK
      REAL X
      INTEGER L,MAXL(100),LHIGH
      REAL N(0:199,2),J(0:399,2),J1,J2
      INTEGER M1,M2,M3,RSIGN,REX,JSIGN,JEX
      REAL F(5000),FJ(5000),RWAV(5000),JWAV(5000)
      REAL RRWAV(5000),JJWAV(5000)
      REAL G,T,D(0:199,100)
      REAL RESUM,IMSUM,REAMP(100),IMAMP(100)
      REAL ABSAMP(100),PHAMP(100),FIX(100)

      DATA DR,CUT,RAMP,NEXTRA/0.002,2.0,1.0,100/
      DATA DK,LK,NK,KK/0.2,15,80,50/

C READ PARAMETERS, U=-RV/2 (BOHR*RYD), AND ORBITALS
      OPEN(UNIT=3,NAME='phase.in',TYPE='OLD')
      READ(3,5) TEXT0
      WRITE(6,5) TEXT0
      READ(3,5) TEXT
      WRITE(6,5) TEXT
5     FORMAT(A20)
      READ(3,10)  Z,R1,H,NDATA,NWAVS
      WRITE(6,10) Z,R1,H,NDATA,NWAVS
      IF (NDATA.EQ.0) STOP
10    FORMAT(F3.0,' ',F6.4,' ',F6.4,' ',I3,' ',I2)
      DO I=0,NDATA-1
       READ(3,50) UD(I)
50     FORMAT(E12.5)
```

```
          ENDDO
          DO M=1,NWAVS
           READ(3,55) TEXT
           IF (M.EQ.1) WRITE(6,55) TEXT
55         FORMAT(A20)
           READ(3,60) ORB(M),ANGMOM(M),OCC(M),EORB(M)
           WRITE(6,60) ORB(M),ANGMOM(M),OCC(M),EORB(M)
60         FORMAT('  ',A2,'    ',I2,'    ',F5.2,' ',F9.2)
           DO I=0,NDATA-1
            READ(3,70) WAV(M,I)
70          FORMAT (E12.5)
           ENDDO
          ENDDO
          CLOSE(3)

C INPUT COVALENT RADIUS, DETERMINE CUTOFF, MAX, AND INTEGRATION RADII
          WRITE(6,*) 'COVALENT RADIUS OF ELEMENT IN ANG (F5.3):'
          READ(5,100) RAD
100       FORMAT(F5.3)
          WRITE(6,105) CUT*RAD
105       FORMAT('CUTOFF RADIUS(ANG)  = ',F5.3)
          RCUT=CUT*RAD*1.89
          RMAX=(CUT)*RAD*1.89 + RAMP
          I0=INT(RCUT/DR)+1
          I1=INT(RMAX/DR)+1
          I2=I1+NEXTRA
          NR=I2

C CREATE RDATA(BOHR), R(BOHR AND ANG), AND K(INV ANG AND INV BOHR)
          DO I=0,NDATA-1
           RD(I)=R1*EXP(H*REAL(I))
          ENDDO
          DO I=1,NR
           RB(I)=REAL(I)*DR
           RA(I)=RB(I)*0.5292
          ENDDO
          DO I=LK,NK
           KA(I)=REAL(I)*DK
           KB(I)=KA(I)*0.5292
          ENDDO
          WRITE(6,200)  RA(I1),RA(I2)
200       FORMAT('RADIUS1(ANG)=',F5.3,' RADIUS2(ANG)=',F5.3)

C INPUT PARTICULAR ANG MOM LL
          WRITE(6,*) 'PARTICULAR ANG MOM L FOR WAVE(I2):'
          READ(5,210) LL
210       FORMAT(I2)

C TOTAL CHARGE DENSITY OF ATOM FROM DATA
          DO I=0,NDATA-1
           RHOD(I)=0.0
           DO M=1,NWAVS
            RHOD(I)=RHOD(I)+OCC(M)*WAV(M,I)*WAV(M,I)
           ENDDO
           RHOD(I)=RHOD(I)/(4.0*PI*RD(I)*RD(I))
          ENDDO

C INTERPOLATE TO DETERMINE ATOMIC POTENTIAL V(RYD)
C   AND TOTAL CHARGE DENSITY OF ATOM RHO(ELECTRONS/BOHR**3)
          WRITE(6,*) 'STARTING INTERPOLATION'
          DO I=1,NR
           U(I)=0.0
           DO M=0,NDATA-1
```

```
            A=UD(M+1)-UD(M)
            B=RB(I)-RD(M)
            C=RD(M+1)-RD(M)
            IF ((RB(I).GE.RD(M)).AND.(RB(I).LT.RD(M+1))) U(I)=UD(M)+A*B/C
           ENDDO
           V(I)=-2.0*U(I)/RB(I)
          ENDDO
          DO I=1,NR
           RHO(I)=0.0
           DO M=0,NDATA-1
            A=RHOD(M+1)-RHOD(M)
            B=RB(I)-RD(M)
            C=RD(M+1)-RD(M)
            IF ((RB(I).GE.RD(M)).AND.(RB(I).LT.RD(M+1))) RHO(I)=RHOD(M)+A*B/C
           ENDDO
          ENDDO

C CUTOFF POTENTIAL
990       DO I=2,NR
           A=RB(I) - RB(I0)
           B=RB(I1) - RB(I0)
           IF (I.GT.I0) V(I)=V(I)*(1.0-A/B)
           IF (I.GE.I1) V(I)=0.0
          ENDDO

CC MAIN LOOP OVER ENERGIES
          WRITE(6,*) 'STARTING MAIN LOOP'
          WRITE(6,1000)
1000      FORMAT('K(INV ANG)  MAXL')
          DO IK=LK,NK
C DETERMINE MAXIMUM L NEEDED TO CALCULATE
           A=KB(IK)*RMAX
           MAXL(IK)=INT(A) + 2
           IF (MAXL(IK).GT.199) MAXL(IK)=199
C WRITE SOME INFO TO SCREEN
           A=REAL((IK-1)/10)
           B=REAL(IK/10)
           IF (A.NE.B) WRITE(6,1010) KA(IK),MAXL(IK)
1010       FORMAT(F4.1,' ',I2)
C CALCULATE SPHERICAL BESSELS AT 2 RADII
           DO I=1,2
            X=KB(IK)*RB(I1)
            IF (I.EQ.2) X=KB(IK)*RB(I2)
            N(0,I)= -COS(X)/X
            N(1,I)= -COS(X)/(X*X) - SIN(X)/X
            DO L=2,MAXL(IK)
             N(L,I)=REAL(2*(L-1)+1)*N(L-1,I)/X - N(L-2,I)
             IF (ABS(N(L,I)).GT.(1.0E5)) THEN
              DO M=0,L
               N(M,I)=N(M,I)*1.0E-5
              ENDDO
             ENDIF
            ENDDO
            LHIGH=INT(X+100.0)
            J2=0.0
            J1=1.0E-25
            DO L=LHIGH,0,-1
             A=REAL(2*(L+1)+1)*J1/X - J2
             IF (L.LE.MAXL(IK)) J(L,I)=A
             J2=J1
             J1=A
             IF (ABS(A).GT.(1.0E5)) THEN
              J2=J2*1.0E-5
```

```
                J1=J1*1.0E-5
                DO M=L,MAXL(IK)
                 J(M,I)=J(M,I)*1.0E-5
                ENDDO
               ENDIF
              ENDDO
              A=J(0,I)/(SIN(X)/X)
              DO L=0,MAXL(IK)
               J(L,I)=J(L,I)/A
              ENDDO
             ENDDO
C ZERO SUMS
             RESUM=0.0
             IMSUM=0.0
C LOOP OVER ANG MOM
             DO L=0,MAXL(IK)
C REAL FUNCTION FROM SCHROD EQN
              DO I=1,NR
               F(I)=-V(I)-REAL(L*(L+1))/(RB(I)*RB(I))+KB(IK)*KB(IK)
               FJ(I)= -REAL(L*(L+1))/(RB(I)*RB(I)) + KB(IK)*KB(IK)
              ENDDO
C INITIAL VALUES FOR NUMEROV ALGORITHM
              RWAV(1)=1.0E-25
              RWAV(2)=(2.0 - DR*DR*F(1))*RWAV(1)
              JWAV(1)=1.0E-25
              JWAV(2)=(2.0 - DR*DR*FJ(1))*JWAV(1)
C INTEGRATE USING NUMEROV ALGORITHM
              RSIGN=0
              REX=0
              JSIGN=0
              JEX=0
              DO I=3,NR
               A=1.0 + DR*DR*F(I)/12.0
               B=2.0*(1.0 - 5.0*DR*DR*F(I-1)/12.0)
               C=1.0 + DR*DR*F(I-2)/12.0
               RWAV(I)=(B*RWAV(I-1)-C*RWAV(I-2))/A
               A=0.0
               M1=1
               M2=1
               IF (RWAV(I).LT.A) M1=-1
               IF (RWAV(I-1).LT.A) M2=-1
               M3=M1*M2
               IF (M3.LT.0) RSIGN=RSIGN + 1
               M1=1
               M2=1
               IF ((RWAV(I)-RWAV(I-1)).LT.A) M1=-1
               IF ((RWAV(I-1)-RWAV(I-2)).LT.A) M2=-1
               M3=M1*M2
               IF (M3.LT.0) REX=REX + 1
               IF (ABS(RWAV(I)).GT.(1.0E5)) THEN
                DO M=1,I
                 RWAV(M)=RWAV(M)*1.0E-5
                ENDDO
               ENDIF
               A=1.0 + DR*DR*FJ(I)/12.0
               B=2.0*(1.0 - 5.0*DR*DR*FJ(I-1)/12.0)
               C=1.0 + DR*DR*FJ(I-2)/12.0
               JWAV(I)=(B*JWAV(I-1)-C*JWAV(I-2))/A
               A=0.0
               M1=1
               M2=1
               IF (JWAV(I).LT.A) M1=-1
               IF (JWAV(I-1).LT.A) M2=-1
```

```
            M3=M1*M2
            IF (M3.LT.0) JSIGN=JSIGN + 1
            M1=1
            M2=1
            IF ((JWAV(I)-JWAV(I-1)).LT.A) M1=-1
            IF ((JWAV(I-1)-JWAV(I-2)).LT.A) M2=-1
            M3=M1*M2
            IF (M3.LT.0) JEX=JEX + 1
            IF (ABS(JWAV(I)).GT.(1.0E5)) THEN
             DO M=1,I
              JWAV(M)=JWAV(M)*1.0E-5
             ENDDO
            ENDIF
           ENDDO
C SAVE RWAV AND JWAV FOR IK=KK AND L.LE.LL
           IF (IK.NE.KK) GOTO 1200
           IF (L.NE.LL) GOTO 1200
           DO I=1,NR
            RRWAV(I)=RWAV(I)
            JJWAV(I)=JWAV(I)
           ENDDO
C USING TWO RADII FOR MATCHING WITH FREE WAVES
1200       G=RB(I1)*RWAV(I2)/(RB(I2)*RWAV(I1))
           T=(G*J(L,1) - J(L,2))/(G*N(L,1) - N(L,2))
           A=ATAN(T)
           B=0.0
           M1=RSIGN+REX-JSIGN-JEX
           M2=M1/2
           IF (A.LE.B) M2=(M1+1)/2
           D(L,IK)=A + REAL(M2)*PI
           A=REAL(2*L+1)
           B=SIN(D(L,IK))
           C=COS(D(L,IK))
           RESUM=RESUM + A*B*C*REAL((-1)**L)
           IMSUM=IMSUM + A*B*B*REAL((-1)**L)
          ENDDO
          REAMP(IK)=RESUM/KA(IK)
          IMAMP(IK)=IMSUM/KA(IK)
          ABSAMP(IK)=(REAMP(IK)**2 + IMAMP(IK)**2)**0.5
          PHAMP(IK)=ATAN(IMAMP(IK)/REAMP(IK))
          IF (PHAMP(IK).GT.(PI/2.0)) WRITE(6,*) 'WARNING: ATAN'
          IF (PHAMP(IK).LT.(-PI/2.0)) WRITE(6,*) 'WARNING: ATAN'
          IF (REAMP(IK).LT.(0.0)) PHAMP(IK)=PHAMP(IK)-PI
         ENDDO
         FIX(NK)=0
         A=5.0
         DO IK=NK-1,LK,-1
          FIX(IK)=FIX(IK+1)
1300      B=PHAMP(IK)+FIX(IK)-PHAMP(IK+1)-FIX(IK+1)
          IF (B.LT.(-A)) FIX(IK)=FIX(IK)+2.0*PI
          IF (B.GT.A) FIX(IK)=FIX(IK)-2.0*PI
          IF ((B.LT.(-A)).OR.(B.GT.A)) GOTO 1300
         ENDDO


C WRITE THE DATA IN IGOR ASCII FORMAT
         OPEN(UNIT=4,NAME='phase.out',STATUS='NEW')
         WRITE(4,*) TEXT0
         WRITE(4,1950) CUT*RAD
1950     FORMAT('CUTOFF RADIUS(ANG) = ',F4.2)
         WRITE(4,*) 'K(INV ANG) AMP(ANG) PHA(RAD)'
         DO IK=LK,NK
          WRITE(4,2000) KA(IK),ABSAMP(IK),PHAMP(IK)+FIX(IK)
```

```
2000     FORMAT(F6.3,' ',F8.4,' ',F8.4)
        ENDDO
        WRITE(4,*) 'DL(RAD): L = 0 1 2 3 4 5'
        DO IK=LK,NK
         WRITE(4,2005) D(0,IK),D(1,IK),D(2,IK),D(3,IK),D(4,IK),D(5,IK)
2005     FORMAT(F8.4,' ',F8.4,' ',F8.4,' ',F8.4,' ',F8.4,' ',F8.4)
        ENDDO
        WRITE(4,2007)  LL,KA(KK)
2007    FORMAT('LL=',I2,'   KK(INV ANG)=',F6.3)
        WRITE(4,*) 'R(BOHR) V(RYD) RWAVLL(BOHR**-1/2) JWAVLL'
        DO I=1,NR
         M1=(I-1)/5
         M2=I/5
         IF (M1.NE.M2)  WRITE(4,2010) RB(I),V(I),RRWAV(I),JJWAV(I)
2010     FORMAT(F5.3,' ',E10.3,' ',E10.3,' ',E10.3)
        ENDDO
        CLOSE(4)
        END
```

Appendix B EXELFS Data Processing Software

The procedures used to extract EXELFS information from the unprocessed PEELS spectra were outlined in §3.4 and §4.1. These procedures are implemented in the computer programs documented in this appendix.

First of all, the PEELS spectra are corrected for gain variations in the parallel-detection system. §B.1 documents my program for direct normalization and gain averaging of PEELS spectra. §B.1 also contains my program which changes the format of the data.

After correcting for gain variations in the parallel detection system, the oscillatory EXELFS data are extracted from the EELS spectrum. §B.2 documents my program which uses polynomial spline fits to extract and normalize the EXELFS oscillations.

After the EXELFS oscillations are isolated, Fourier band-pass filtering is used to select information from a particular nearest-neighbor shell. §B.3 documents my program for Fourier band-pass filtering.

Finally, after data from a particular nearest-neighbor shell has been selected, least-squares fitting is used to determine the difference in backscattering amplitude or mean-square relative displacement between two experimental measurements. §B.4 documents my simple program for least-squares fitting of EXELFS data.

B.1 Correction for Channel-to-Channel Gain Variations

This section has a listing of my program "CORR" for the direct normalization and gain averaging of PEELS spectra. Direct normalization is performed by dividing by a "uniform illumination" spectrum, which is obtained by illuminating the linear diode array with a nearly uniform electron beam. Gain averaging is accomplished by using a common feature to align the spectra, then adding them together.

This section also lists my program, "EIC" (which stands for EL/P to Igor conversion), which converts the data files from "EL/P" format to "Igor" format. EL/P is the data collection program supplied by Gatan with the spectrometer, and Igor is a data analysis program.

```
      PROGRAM CORR

C DIRECT NORMALIZATION AND GAIN AVERAGING OF ENERGY LOSS SPECTRA
C   FOR EXELFS ANALYSIS.
C OPTIONAL TO FIRST SUBTRACT A REPRESENTATIVE NOISE SPECTRUM FROM
C   THE EXPERIMENTALLY OBTAINED SPECTRA.  THE NOISE SPECTRUM MUST
C   BE NAMED "noise."
C DIRECT NORMALIZATION IS PERFORMED BY DIVIDING SPECTRA BY A UNIFORM
C   ILLUMINATION SPECTRUM, COLLECTED USING A SPECIAL MODE ON THE
C   GATAN MODEL 666 PEELS.  THE UNIFORM ILLUMINATION SPECTRUM
C   MUST BE NAMED "uni."
C GAIN AVERAGING IS PERFORMED BY FIRST CHOOSING A REGION IN THE FIRST
C   SPECTRUM WHICH IS TO BE MATCHED.  EACH SUBSEQUENT SPECTRUM IS
C   REALIGNED TO THE FIRST SPECTRUM BY MINIMIZING THE ABSOLUTE VALUE
C   OF THE DIFFERENCE BETWEEN THE TWO SPECTRA.  BEFORE THE COMPARISON
C   BETWEEN THE SPECTRA IS MADE, EACH SPECTRUM IS NORMALIZED BY THE
C   TOTAL NUMBER OF COUNTS IN THE SELECTED REGION.

C JAMES K OKAMOTO 12OCT92

      REAL*4 TEMP(1024),PEELS(22,1024),MAX(22),NORM(1024),ZERO
      REAL*4 NORMLIM,VAR(22),AREA1,AREA
      REAL*8 INTEG,SUMDATA(1024)
      INTEGER NSPECTRA,UNIFORM,NOISE,NFILES,VRSION
      INTEGER UPPER,LOWER,MINSH,MAXSH,SHIFT(22)
      INTEGER I,J,K,N
      CHARACTER*80 CHRBUF
      CHARACTER*14 ELFILE(22),SUMFILE
      DATA MINSH,MAXSH /-99,99/
```

```
      DATA NORMLIM /0.1/
      DATA ZERO /0.0/
      DATA ELFILE / 'noise','uni',
      1 'a.01','a.02','a.03','a.04','a.05',
      2 'a.06','a.07','a.08','a.09','a.10',
      1 'a.11','a.12','a.13','a.14','a.15',
      2 'a.16','a.17','a.18','a.19','a.20'/

C ASK HOW MANY DATA FILES AND IF NOISE SPECTRUM EXISTS
      WRITE(6,10) 'HOW MANY SPECTRA TO ADD (MAX 20): '
      READ(5,15) NSPECTRA
      WRITE(6,10) 'SUBTRACT NOISE SPECTRUM (0=NO, 1=YES) ?'
      READ(5,15) NOISE
      WRITE(6,10) 'DIVIDE BY UNI ILLUM SPECTRUM (0=NO, 1=YES) ?'
      READ(5,15) UNIFORM
      WRITE(6,10) 'LOWEST CHANNEL OF REGION TO MATCH (MIN 100)'
      READ(5,15) LOWER
      IF (LOWER.LE.99) LOWER=100
      WRITE(6,10) 'HIGHEST CHANNEL OF REGION TO MATCH (MAX 900)'
      READ(5,15) UPPER
10    FORMAT(A45)
15    FORMAT(I3)
      IF (UPPER.GE.901) UPPER=900
      IF (UPPER.LE.LOWER) UPPER=900
      NFILES=NSPECTRA+2

C OPEN TAGGED ASCII DATA FILES FROM EL/P
      DO N = 2-NOISE,NFILES
            OPEN(UNIT=7,FILE=ELFILE(N),STATUS='OLD')

C READ PRECEDING TEXT
            READ(7,20) CHRBUF
20          FORMAT(A18)
            IF (CHRBUF.NE.'Tagged ASCII Data') GOTO 120
            READ (7,30) VRSION
30          FORMAT(I2)
35          CONTINUE
                  READ(7,40) CHRBUF
40                FORMAT(A4)
            IF (CHRBUF.NE.'EELS') GOTO 35

C READ EELS DATA
            READ(7,*,END=110) (TEMP(J),J=1,1024)
110         DO J=1,1024
                  IF (TEMP(J).EQ.0) TEMP(J)=1.
                  PEELS(N,J)=TEMP(J)
            END DO
120         CLOSE(7)
            DO J = 1,1024
                  IF (PEELS(N,J).GT.MAX(N)) MAX(N)=PEELS(N,J)
            END DO
            WRITE(6,50) 'FILE = ',ELFILE(N),'MAX DATA = ',MAX(N)
```

```
 50             FORMAT(A8,A15,A12,F10.0)
        END DO

C IF NEEDED THEN SUBTRACT NOISE SPECTRUM
        IF (NOISE.EQ.0) GOTO 130
        DO N = 3,NFILES
                WRITE(6,53) 'SUBRACTING NOISE SPECTRA FROM ',ELFILE(N)
 53             FORMAT(A31,A15)
                DO J = 1,1024
                        PEELS(N,J) = PEELS(N,J) - PEELS(1,J)
                END DO
        END DO


C IF REQUESTED THEN NORMALIZE UNIFORM ILLUMINATION SPECTRUM
 130    IF (UNIFORM.EQ.0) GOTO 140
        INTEG = 0.0
        DO J = 1,1024
                INTEG = INTEG + PEELS(2,J)
        END DO
        WRITE(6,55) 'AVERAGE COUNTS IN UNIFORM SPECTRUM = ',INTEG/1024.0
 55     FORMAT(A38,F16.0)
        DO J = 1,1024
                NORM(J) = PEELS(2,J)*(1024.0/INTEG)
                IF (NORM(J).LT.NORMLIM) NORM(J)=1.0
        END DO

C NORMALIZE ENERGY-LOSS SPECTRA
        DO N = 3,NFILES
        WRITE(6,56) ELFILE(N)
 56     FORMAT('DIRECT NORMALIZATION OF ',A15)
                DO J = 1,1024
                        PEELS(N,J) = PEELS(N,J)/NORM(J)
                END DO
        END DO


C FIND SHIFTS BY MINIMIZING ABS DIFF IN REGION BETWEEN LOWER AND UPPER CHANNELS
 140    AREA1=0.0
        DO J=LOWER,UPPER
                AREA1=AREA1+PEELS(3,J)
        ENDDO
        DO N = 4,NFILES
                VAR(N)=0.0
                DO I=MINSH,MAXSH
                        AREA=0.0
                        DO J=LOWER,UPPER
                                AREA=AREA+PEELS(N,J+I)
                        ENDDO
                        SUM=0.0
                        DO J=LOWER,UPPER
                                SUM=SUM+ABS(PEELS(3,J)/AREA1-PEELS(N,J+I)/AREA)
```

```
                        ENDDO
                        IF ((SUM.LT.VAR(N)).OR.(VAR(N).EQ.ZERO)) SHIFT(N)=I
                        IF ((SUM.LT.VAR(N)).OR.(VAR(N).EQ.ZERO)) VAR(N)=SUM
60              ENDDO
                WRITE(6,65) ELFILE(N),SHIFT(N),VAR(N)
65              FORMAT('FILE:',A10,'  SHIFT=',I3,'  ABS DIFF=',F8.6)
        ENDDO

C SET ANY SHIFTS?
400     WRITE(6,80)
80      FORMAT('SET SHIFT OF WHICH FILE (none=0,a.01=1,...,a.20=20):')
        READ(5,85) J
85      FORMAT(I2)
        IF (J.LE.1) GOTO 500
        IF (J.GT.NSPECTRA) GOTO 500
        WRITE(6,88)'SHIFT:'
88      FORMAT(A7)
        READ(5,89) I
89      FORMAT(I4)
        SHIFT(J+2)=I
        GOTO 400

C SHIFT AND ADD SPECTRA
500     DO J = 1,1024
                SUMDATA(J) = PEELS(3,J)
        END DO
        DO N = 4,NFILES
                WRITE(6,67) 'SHIFTING AND ADDING ',ELFILE(N)
67              FORMAT(A21,A15)
                DO J = 1,1024
                        IF ((J+SHIFT(N).GE.1).AND.(J+SHIFT(N).LE.1024))
        1               SUMDATA(J) = SUMDATA(J) + PEELS(N,J+SHIFT(N))
                END DO
        END DO

C DIVIDE SUMMED SPECTRUM BY NUMBER OF SPECTRA
        DO J = 1,1024
                SUMDATA(J)=SUMDATA(J)/NSPECTRA
        END DO
        WRITE(6,70) 'SUMMED SPECTRA DIVIDED BY ',NSPECTRA
70      FORMAT(A27,I3)

C SAVE SUMMED SPECTRUM
        WRITE(6,75) 'INPUT FILE NAME FOR SUMMED SPECTRUM: '
75      FORMAT(A38)
        READ(5,1010) SUMFILE
1010    FORMAT(A14)
        OPEN(UNIT=9,FILE=SUMFILE,STATUS='NEW')
        WRITE(9,1012)
1012    FORMAT('Tagged ASCII Data')
        WRITE(9,1014)
1014    FORMAT('2')
```

```
      WRITE(9,1015)
1015  FORMAT()
      WRITE(9,1016)
1016  FORMAT('EELS f 1024')

      DO I = 1,8
      DO J = 1,16
            WRITE(9,1050) (SUMDATA(128*(I-1)+8*(J-1)+K),K=1,8)
1050        FORMAT(8F8.0)
      END DO
      WRITE(9,*)
      END DO
      CLOSE (9)

C END
9999  END

*************************************************************

      PROGRAM EIC

C ASCII TO ASCII CONVERSION OF EL/P TEXT DATA TO FORMAT
C   FOR IGOR INPUT.
C THE INPUT FILE BASICALLY HAS DATA IN ROWS OF 8 COLUMNS, AS
C   THE EL/P PROGRAM OUTPUTS, BUT THE HEADER MUST BE EDITED.
C   THE 1ST LINE IN THE HEADER SHOULD CONTAIN INFORMATION
C   ABOUT THE EXPERIMENT.  TO CALIBRATE THE ENERGY SCALE, THREE
C   ADDITIONAL VALUES ARE NEEDED.  THE 2ND AND 3RD LINES MUST HAVE AN
C   ENERGY LOSS VALUE (REAL, EV) AND ITS CORRESPONDING DATA
C   CHANNEL (INTEGER).  THE 4TH LINE MUST HAVE THE DISPERSION (REAL,
C   EV/CH) OF THE SPECTRUM.
C THIS PROGRAM USES "PGPLOT" GRAPHICS WHICH WAS WRITTEN
C   BY THE CALTECH ASTRONOMY DEPARTMENT.  GRAPHICS IMPLEMEN-
C   TATION RESIDES ON A SYSTEM FILE.

C JAMES K OKAMOTO 17OCT92

C VARIABLES
      REAL*4 EL(4096),MAX,B
      REAL*4 C(8),CTS(4096)
      INTEGER I,J,N
      INTEGER CALCH
      REAL*4 EVCH,CALEV
      REAL*4 EOFF
      CHARACTER*40 TEXT1

C READ ENERGY-SCALE AND DATA
      OPEN(UNIT=13,NAME='eic.in',TYPE='OLD')
      READ(13,100) TEXT1
100   FORMAT(A40)
      READ(13,110) CALEV
110   FORMAT(F8.3)
```

```
      READ(13,120) CALCH
 120  FORMAT(I4)
      READ(13,130) EVCH
 130  FORMAT(F5.3)
      EOFF=CALEV-(CALCH-1)*EVCH
      N=0
      DO 500 J=1,512
      READ(13,FMT=*,END=530) (C(I),I=1,8)
       DO 470 I=1,8
        N=N+1
        CTS(N)=C(I)
470    CONTINUE
500   CONTINUE
530   CLOSE(13)
      NCH=N
      WRITE(*,510) NCH
510   FORMAT('READ ',I4,' DATA POINTS.')

C DETERMINE ENERGY SCALE AND MAX NUMBER OF COUNTS
      EL(1)=EOFF
      MAX=CTS(1)
1400  DO 1465 I=2,NCH
       EL(I)=EL(I-1)+EVCH
       IF(CTS(I).LT.(1.0)) CTS(I)=1.0
       IF(MAX.LT.CTS(I)) MAX=CTS(I)
1465  CONTINUE

C PLOT DATA
      B=1.2*MAX
      CALL PGBEGIN(0,'/tek',1,1)
      CALL PGENV(EL(1),EL(NCH),0.,B,0,0)
      CALL PGLABEL('CHANNELS','COUNTS',TEXT1)
      CALL PGLINE(NCH,EL,CTS)
      CALL PGPOINT(1,CALEV,CTS(CALCH),4)
      CALL PGEND

C WRITE THE DATA IN IGOR ASCII FORMAT
      OPEN(UNIT=14,NAME='eic.out',STATUS='NEW')
      WRITE(14,3005) TEXT1
 3005 FORMAT(A40)
      WRITE(14,3007)
 3007 FORMAT('ELOSS   COUNTS')
      DO I=1,NCH
       WRITE(14,3010) EL(I),CTS(I)
 3010  FORMAT(F8.3,F10.0)
      ENDDO
      WRITE(14,3020) 0.0,0.0
 3020 FORMAT(F8.3,F10.0)
      CLOSE(14)

      STOP
      END
```

B.2 Extraction and Normalization of EXELFS Oscillations

After correcting for gain variations in the parallel detection system, the oscillatory EXELFS data is extracted from the EELS spectrum. This section contains a listing of my program "EXT" for the extraction and normalization of the EXELFS oscillations. Utilized in "EXT" is a subroutine called "PSPLIN" from an EXAFS software package developed at the University of Illinois (Scott, 1983). "PSPLIN" fits a polynomial spline function to data.

First, the pre-edge background is subtracted by fitting a relatively stiff polynomial spline to the post-edge region, then subtracting a constant offset from the spline so that it matches the data in the pre-edge region. In practice, this determines an experimental edge jump and removes most of the non-oscillatory curvature in the post-edge data. A polynomial spline fit is then used to extract the EXELFS oscillations from the post-edge data. The experimental edge jump and theoretical edge shapes are used to normalize the oscillations.

```
      PROGRAM EXT

C EXTRACTION AND NORMALIZATION PROGRAM.
C POLYNOMIAL SPLINE FITS TO EXTRACT EXELFS OSCILLATIONS AND
C  DETERMINE EDGE JUMP HEIGHT.  USES EXPERIMENTAL EDGE
C  JUMP HEIGHT AND THEORETICAL EDGE SHAPES TO NORMALIZE
C  EXELFS.
C READS FILE FORMATTED AS AN OUTPUT FILE FROM THE PROGRAM
C  CALLED GIC.F WHICH CONVERTS AND ENERGY-LOSS SPECTRUM
C  FROM "GATAN" FORMAT TO "IGOR" FORMAT.  THE "IGOR"
C  FORMAT IS BASICALLY AN ASCII FILE WITH ENERGY LOSS IN THE
C  1ST COLUMN AND COUNTS IN THE 2ND COLUMN.
C PROGRAM USES SUBROUTINE CALLED PSPLIN.
C PROGRAM ALSO USES PGPLOT GRAPHICS WHICH WAS WRITTEN
C  BY THE CALTECH ASTRONOMY DEPARTMENT.  GRAPHICS
C  IMPLEMENTATION RESIDES ON A SYSTEM FILE.

C JAMES K. OKAMOTO  17OCT92

C VARIABLES:

C GENERIC
      CHARACTER*40 TEXT
```

```
      INTEGER I,J,FINI
      REAL RZERO,A,B,C,D,XX(2),YY(2)
      DATA RZERO /0.0/
C FOR READ DATA
      CHARACTER*40 TEXT1,TEXT2
      INTEGER NPTS
      REAL EL(1025),RCTS(1025),MAXRCTS
C FOR READ SPLINE PARAMETERS
      INTEGER PREREG,PREORD(9)
      INTEGER POSTREG,POSTORD(9)
      REAL PREXL(9),PREXH(9),EPRE
      REAL POSTKL(9),POSTKH(9),ONSET
      REAL POSTXL(9),POSTXH(9)
C FOR READ THEORETICAL EDGE SHAPE
      CHARACTER*40 TEXT3
      INTEGER NTH,LASTTH
      REAL ETH(1025),TH(1025),MAXTH
C FOR DETERMINE CHANNELS
      INTEGER ONSETCH,KNOT(10)
C FOR PRE-EDGE BACKGROUND SUBTRACTION
      REAL BKFIT(1025)
C FOR SUBROUTINE PSPLIN
      INTEGER NREG,NORD(9)
      REAL XL(9),XH(9),WGHT(1025)
      REAL XSPL(1025),YDAT(1025),YSPL(1025)
C COMMONS FOR SUBROUTINE PSPLIN
      COMMON/XY/EL,XSPL,YDAT,YSPL
      COMMON/SPLINE/NREG,XL,XH,NORD,WGHT
C FOR DETERMINE EDGE SHAPE
      REAL J0(1025)
C FOR EDGE JUMP
      REAL JUMP
C FOR (K, UNNORMALIZED FINE STRUCTURE)
      INTEGER NOUT
      REAL K(1025),FS(1025)
C FOR NORMALIZED OF FINE STRUCTURE
      REAL CHI(1025)
C FOR TOTAL SPLINE FIT TO EELS DATA
      REAL FIT(1025)


C READ EELS DATA

      OPEN(UNIT=2,FILE='ext.in',STATUS='OLD')
      READ(2,1005) TEXT1
1005  FORMAT(A40)
      READ(2,1007) TEXT2
1007  FORMAT(A40)
      FINI=0
      I=0
      DO WHILE (FINI.EQ.0)
        I=I+1
```

```
          READ(2,*) EL(I),RCTS(I)
          IF (MAXRCTS.LT.RCTS(I)) MAXRCTS=RCTS(I)
          IF (EL(I).EQ.RZERO) FINI=1
        ENDDO
        NPTS=I-1
        CLOSE(2)

C READ POLYNOMIAL SPLINE PARAMETERS

        OPEN(UNIT=2,FILE='ext.poly',STATUS='OLD')
        READ(2,1060) TEXT2
1060    FORMAT(A40)
        READ(2,1070) PREREG
1070    FORMAT(I1)
        IF (PREREG.EQ.0) GOTO 1100
        NREG=PREREG
        DO I=1,PREREG
          READ(2,1075) PREXL(I)
1075      FORMAT(F8.3)
        ENDDO
        READ(2,1080) PREXH(PREREG)
1080    FORMAT(F8.3)
        DO I=1,PREREG-1
          PREXH(I)=PREXL(I+1)
        ENDDO
        DO I=1,PREREG
          READ(2,1083) PREORD(I)
1083      FORMAT(I1)
        ENDDO
1100    READ(2,1105) EPRE
1105    FORMAT(F8.3)

        READ(2,1110) POSTREG
1110    FORMAT(I1)
        DO I=1,POSTREG
          READ(2,1120) POSTKL(I)
1120      FORMAT(F8.3)
        ENDDO
        READ(2,1130) POSTKH(POSTREG)
1130    FORMAT(F8.3)
        DO I=1,POSTREG
          READ(2,1140) POSTORD(I)
1140      FORMAT(I1)
        ENDDO
        READ(2,1150) ONSET
1150    FORMAT(F8.3)
        DO I=1,POSTREG
          POSTXL(I)=ONSET+3.81*POSTKL(I)*POSTKL(I)
        ENDDO
        POSTXH(POSTREG)=ONSET+3.81*POSTKH(POSTREG)*POSTKH(POSTREG)
        CLOSE(2)
```

```
C READ THEORETICAL EDGE SHAPE

      OPEN (UNIT=2,FILE='ext.shape',STATUS='OLD')
      READ(2,1155) TEXT3
1155  FORMAT(A40)
      FINI=0
      I=0
      DO WHILE (FINI.EQ.0)
         I=I+1
         READ(2,*) ETH(I),TH(I)
        IF (ETH(I).EQ.RZERO) FINI=1
      ENDDO
      CLOSE(2)
      NTH=I-1
      MAXTH=0.0
      DO I=1,NTH
         IF (TH(I).GT.MAXTH) MAXTH=TH(I)
      ENDDO

C DETERMINE CHANNEL OF ONSET ENERGY AND CHANNELS OF
C    POST-EDGE KNOTS

      ONSETCH=0
      DO J=1,NPTS
        IF ((ONSET.GE.EL(J)).AND.(ONSET.LE.EL(J+1))) ONSETCH=J+1
      ENDDO

      DO I=1,POSTREG
         KNOT(I)=0
         DO J=1,NPTS
            IF ( (POSTXL(I).GE.EL(J)).AND.(POSTXL(I).LE.EL(J+1)) )
     1         KNOT(I)=J+1
        ENDDO
      ENDDO
      KNOT(POSTREG+1)=0
      DO J=1,NPTS
        IF ((POSTXH(POSTREG).GE.EL(J)).AND.(POSTXH(POSTREG).LE.EL(J+1)))
     1    KNOT(POSTREG+1)=J+1
      ENDDO
      KNOT(POSTREG+1)=KNOT(POSTREG+1)-1

C PRE-EDGE BACKGROUND SUBTRACTION
C  NOTE THAT LAST STEP REPLACES "YDAT"
C  WITH PRE-EDGE SUBTRACTED DATA.

      IF (PREREG.EQ.0) GOTO 1190

      DO I=1,NPTS
        XSPL(I)=EL(I)
        WGHT(I)=1.0
      ENDDO
      DO I=1,NPTS
```

```
        YDAT(I)=RCTS(I)
      ENDDO
      NREG=PREREG
      DO I=1,PREREG
        XL(I)=PREXL(I)
      ENDDO
      XH(PREREG)=PREXH(PREREG)
      DO I=1,PREREG-1
        XH(I)=PREXL(I+1)
      ENDDO
      DO I=1,PREREG
       NORD(I) = PREORD(I)
      ENDDO

      CALL PSPLIN(NPTS)

      PRECH=0
      DO I=1,NPTS
        IF ((EL(I).GT.EPRE).AND.(PRECH.EQ.0)) PRECH=I
      ENDDO
      OFFSET = YSPL(PRECH) - RCTS(PRECH)
      DO I=1,NPTS
         BKFIT(I) = YSPL(I)-OFFSET
         YDAT(I) = RCTS(I) - BKFIT(I)
         IF (YDAT(I).LT.RZERO) YDAT(I)=1.0
      ENDDO

C DISPLAY EELS DATA AND PRE-EDGE BACKGROUND SUBTRACTION

1190  A=1.1*MAXRCTS
      CALL  PGBEGIN(0,'/tek',1,1)
      CALL  PGENV(XSPL(1),XSPL(NPTS),0.,A,0,0)
      CALL PGLABEL('ENERGY-LOSS (eV)','EELS',TEXT1)
      CALL PGLINE(NPTS,XSPL,RCTS)
      CALL PGPOINT(1,XSPL(ONSETCH),RCTS(ONSETCH),4)

      IF (PREREG.EQ.0) GOTO 1193
      CALL PGLINE(NPTS,XSPL,YSPL)
      CALL PGLINE(NPTS,XSPL,BKFIT)
      DO  I=1,14
          WRITE(*,1192)
1192      FORMAT()
      ENDDO
1193  READ(*,1195)  TEXT
1195  FORMAT(A1)
      CALL PGEND

C POST-EDGE BACKGROUND SUBTRACTION

      NREG=POSTREG
      DO I=1,POSTREG
        XL(I)=POSTXL(I)
```

```
        ENDDO
        XH(POSTREG)=POSTXH(POSTREG)
        DO I=1,POSTREG-1
          XH(I)=POSTXL(I+1)
        ENDDO
        DO I=1,POSTREG
         NORD(I) = POSTORD(I)
        ENDDO

        CALL PSPLIN(NPTS)

C DETERMINE EDGE SHAPE

     FINI=0
    DO I=ONSETCH,NPTS
      IF (EL(I).GT.ETH(NTH)) FINI=1
      IF (FINI.EQ.0) LASTTH=I
    ENDDO

        J=1
        DO I=ONSETCH,LASTTH
            J=J-1
1430        J=J+1
           IF ((EL(I).LE.ETH(J)).OR.(EL(I).GT.ETH(J+1))) GOTO 1430
           IF ((EL(I).GT.ETH(J)).AND.(EL(I).LE.ETH(J+1)))
    1           J0(I)=TH(J)+(EL(I)-ETH(J))*
    2            (TH(J+1)-TH(J))/(ETH(J+1)-ETH(J))
1440      CONTINUE
        ENDDO

C DETERMINE EDGE JUMP

        WRITE(6,1450) YSPL(ONSETCH)
1450    FORMAT('DEFAULT EDGE JUMP HEIGHT = ',E10.4)
        WRITE(6,1460)
1460    FORMAT('INPUT EDGE JUMP HEIGHT, IF DIFFERENT FROM ABOVE:')
        READ(5,1470)  JUMP
1470    FORMAT(E10.4)
        IF (JUMP.LE.(0.0)) JUMP=YSPL(ONSETCH)

C NORMALIZE EDGE SHAPE TO EDGE JUMP TO GET J0

    DO I=ONSETCH,LASTTH
        J0(I)=J0(I)*(JUMP/MAXTH)
    ENDDO

C DISPLAY POST-EDGE SPLINE AND J0

        IF (PREREG.NE.0) A=1.2*OFFSET
        IF (PREREG.EQ.0) A=1.2*MAXRCTS
        CALL  PGBEGIN(0,'/tek',1,1)
        CALL  PGENV(XSPL(1),XSPL(NPTS),0.,A,0,0)
```

```
      CALL PGLABEL('E-LOSS (eV)',
     1   'POST-EDGE DATA, SPLINE, THEORETICAL EDGE SHAPE',
     2    TEXT1)
      CALL PGLINE(NPTS,XSPL,YDAT)
      CALL PGLINE(NPTS,XSPL,YSPL)
      CALL PGLINE(NPTS,XSPL,J0)
      YY(1)=0.0
      DO I=1,NREG+1
         XX(1)=XSPL(KNOT(I))
         XX(2)=XSPL(KNOT(I))
         YY(2)=YDAT(KNOT(I))
        CALL PGLINE(2,XX,YY)
      ENDDO
      READ(*,1400)  TEXT
1400  FORMAT(A1)
      CALL PGEND

C DETERMINE K, UN-NORMALIZED FINE STRUCTURE, FS,
C   AND NORMALIZED FINE STRUCTURE, CHI.
C   ALSO DETERMINE NUMBER OF POINTS OF FINE STRUCTURE
C   DATA, NOUT, BETWEEN FIRST AND LAST KNOTS.
      NOUT=KNOT(POSTREG+1)-KNOT(1)+1
      J=0
      DO I=KNOT(1),KNOT(POSTREG+1)
         J=J+1
           K(J)=0.512*((EL(I)-ONSET)**0.5)
         FS(J)=YDAT(I)-YSPL(I)
        IF (J0(I).LE.RZERO) GOTO 1670
          CHI(J)=FS(J)/J0(I)
1670    CONTINUE
      ENDDO

C DISPLAY CHI VS K
      A=0.0
      B=0.0
      DO I=1,NOUT
         IF (CHI(I).LT.A) A=CHI(I)
        IF (CHI(I).GT.B) B=CHI(I)
      ENDDO
      A=1.1*A
      B=1.1*B
      C=K(1)
      D=K(NOUT)

      CALL  PGBEGIN(0,'/tek',1,1)
      CALL  PGENV(C,D,A,B,0,0)
      CALL PGLABEL('K','CHI',TEXT1)
      CALL PGLINE(NOUT,K,CHI)
      YY(1)=A
      DO I=1,POSTREG+1
        J=KNOT(I)
          XX(1)=0.512*((EL(J)-ONSET)**0.5)
```

```
            XX(2)=XX(1)
              YY(2)=(YDAT(J)-YSPL(J))/J0(J)
            CALL PGLINE(2,XX,YY)
          ENDDO
          CALL PGEND

C WRITE TOTAL SPLINE FIT AND THEN (K,CHI) TO OUTPUT FILE
          OPEN(UNIT=3,FILE='ext.out',STATUS='NEW')
          WRITE(3,1900) TEXT1
1900      FORMAT(A40)
          WRITE(3,1901)
1901      FORMAT('KNOT    ORDER')
          IF (PREREG.EQ.0) GOTO 1906
          DO I=1,PREREG
             WRITE(3,1903) PREXL(I),PREORD(I)
1903         FORMAT(F8.3,I3)
          ENDDO
          WRITE(3,1905) PREXH(PREREG)
1905      FORMAT(F8.3)
1906      DO I=1,POSTREG
             WRITE(3,1907) POSTKL(I),POSTORD(I)
1907         FORMAT(F8.3,I3)
          ENDDO
          WRITE(3,1908) POSTKH(POSTREG)
1908      FORMAT(F8.3)
          WRITE(3,1909) ONSET
1909      FORMAT(F8.3)
          WRITE(3,1910) JUMP
1910      FORMAT('EDGE JUMP=',E10.4)
          WRITE(3,1912) TEXT2
1912      FORMAT(A40)
          WRITE(3,1925)
1925      FORMAT('ELOSS  COUNTS  TOTALSPLINE')
          DO I=1,NPTS
            IF (XSPL(I).LT.EPRE) GOTO 1995
            IF (XSPL(I).GT.XH(NREG)) GOTO 1995
             FIT(I)=BKFIT(I)+YSPL(I)
             WRITE(3,1990) XSPL(I),RCTS(I),FIT(I)
1990         FORMAT(F8.3,2F10.0)
1995       CONTINUE
          ENDDO

          WRITE(3,2000)
2000      FORMAT('K       CHI')
          DO I=1,NOUT
             WRITE(3,2010) K(I),CHI(I)
2010         FORMAT(F8.5,F10.5)
          ENDDO

       CLOSE(3)
       END
```

B.3 Fourier Band-Pass Filtering

After the EXELFS oscillations are isolated and normalized, Fourier band-pass filtering can be used to select information from a particular nearest-neighbor shell. This section contains a listing of my program "FOUR" for Fourier band-pass filtering.

First, an optional polynomial spline fit can be applied to reduce any low frequency curvature remaining after the previous polynomial spline fits. The data is then multiplied by a window whose ends are smoothed to reduce the possibility of false peaks due to "ringing" in the transform. After Fourier transformation, a band-pass window is applied to isolate the EXELFS oscillations from a particular nearest-neighbor shell. These particular nearest-neighbor shell EXELFS oscillations are then contained in the real part of the inverse Fourier transformation.

```
      PROGRAM FOUR

C FOURIER FILTERING.
C SLOW FOURIER TRANSFORM (FT) AND INVERSE FT OF
C   EXELFS DATA.
C READS FILE FORMATTED AS THE OUTPUT FILE FROM THE
C   THE BACKGROUND SUBTRACTION PROGRAM CALLED EXT.F.

C MAIN PROGRAM
C FORTRAN 77
C JAMES K. OKAMOTO  17OCT92

C VARIABLES:

C GENERIC
      CHARACTER*40 TEXT
      INTEGER I,J
      REAL A,B
C FOR READ DATA
      CHARACTER*40 TEXT1
      INTEGER NDATA
      REAL  TEMP(2050),KDATA(1025),CHIDATA(1025)
C FOR K-LIMITS AND WEIGHTING
      REAL KLO,KHI,KHW,KMIN,KMAX,KLT,KRT
      REAL N
```

```
      REAL WCHIDATA(1025)
C FOR (SECONDARY) SPLINE FIT
      INTEGER NREG,NORD(9)
      REAL XL(9),XH(9)
      REAL XSPL(1025),WGHT(1025),YSPL(1025)
C COMMON WITH SPLINE SUBROUTINE
      COMMON/XY/KDATA,XSPL,WCHIDATA,YSPL
      COMMON/SPLINE/NREG,XL,XH,NORD,WGHT
C FOR FOURIER TRANSFORM
      INTEGER NR
      REAL WCHI(1025)
      REAL DK(1025),K(1025),WK(1025)
      REAL WWCHI(1025)
      REAL MAXMAG,MINIMFT
      REAL R(0:160),DR
      REAL REFT(0:160),IMFT(0:160),MAGFT(0:160)
      DATA NR,DR /160,0.05/
C FOR R-LIMITS
      REAL RLO,RHI,RHW,RMIN,RMAX,RLT,RRT
C FOR INVERSE FOURIER TRANSFORM
      INTEGER NKK
      REAL WR(0:160),PLOTWR(0:160)
      REAL DKK,KK(301)
      REAL REIFT(301),IMIFT(301)
      REAL MAXREIFT,MINREIFT
      REAL PI
      DATA NKK,PI /300,3.1415927/

C READ DATA, FIGURE OUT NDATA

      OPEN(UNIT=2,FILE='four.in',STATUS='OLD')

      READ(2,105) TEXT1
105   FORMAT(A40)
108   READ(2,109) TEXT
109   FORMAT(A4)
      IF (TEXT.NE.'K   ') GOTO 108
      READ(2,*,END=115) (TEMP(I),I=1,2050)
115   DO I=1,2050
        A=REAL(I)/2.0
        B=I/2
        IF (A.NE.B) KDATA(I/2+1)=TEMP(I)
        IF (A.EQ.B) CHIDATA(I/2)=TEMP(I)
      END DO
      CLOSE(2)

      NDATA=0
      DO I=1,1025
            IF (KDATA(I).NE.0.0) NDATA=I
      ENDDO
      WRITE(*,117) TEXT1
117   FORMAT(A40)
```

```
      WRITE(*,120)  NDATA
120   FORMAT('NUMBER OF DATA POINTS READ:',I4)

C INPUT (SECONDARY) SPLINE PARAMETERS

      WRITE(*,150)
150   FORMAT('# OF REGIONS FOR SECONDARY SPLINE FIT (I1) ?')
      READ(*,155) NREG
155   FORMAT(I1)
      DO I=1,NREG
        WRITE(*,157) I
157     FORMAT('KNOT #',I1,' (REAL) ?')
        READ(*,160)  XL(I)
160     FORMAT(F8.3)
      ENDDO
      IF (NREG.NE.0) WRITE(*,162) NREG+1
162   FORMAT('KNOT #',I1,' (REAL) ?')
      IF (NREG.NE.0) READ(*,165) XH(NREG)
165   FORMAT(F8.3)
      DO I=1,NREG-1
        XH(I)=XL(I+1)
      ENDDO
      DO I=1,NREG
        WRITE(*,168) I
168     FORMAT('ORDER OF REGION #',I1,' (I1) ?')
        READ(*,170) NORD(I)
170     FORMAT(I1)
      ENDDO

      DO I=1,NDATA
        WGHT(I)=1.0
        XSPL(I)=KDATA(I)
      ENDDO

C INPUT K-LIMITS AND WEIGHTING, WEIGHT CHIDATA

      WRITE(*,180) ' KLO (REAL) ?'
180   FORMAT(A15)
      READ(*,185)  KLO
185   FORMAT(F8.5)
      WRITE(*,180) ' KHI (REAL) ?'
      READ(*,185)  KHI
      WRITE(*,180) ' KHW (REAL) ?'
      READ(*,185)  KHW
      WRITE(*,190) ' WEIGHTING N (REAL) ?'
190   FORMAT(A22)
      READ(*,185)  N

      KMIN=KLO-KHW
      KMAX=KHI+KHW
      KLT=KLO+KHW
      KRT=KHI-KHW
```

```
      DO I=1,NDATA
        WCHIDATA(I)=(KDATA(I)**N)*CHIDATA(I)
      ENDDO

C SECONDARY SPLINE FIT:

C CALL (SECONDARY) SPLINE FIT

      CALL PSPLIN(NDATA)

      DO I=1,NDATA
       WCHI(I)=WCHIDATA(I)-YSPL(I)
      ENDDO

C DISPLAY SECONDARY SPLINE FIT

      A=0.0
      B=0.0
      DO I=1,NDATA
       IF (KDATA(I).LT.KMIN) GOTO 205
       IF (KDATA(I).GT.KMAX) GOTO 205
       IF (WCHIDATA(I).LT.A) A=WCHIDATA(I)
       IF (WCHIDATA(I).GT.B) B=WCHIDATA(I)
205    CONTINUE
      ENDDO
      A=1.1*A
      B=1.1*B
      CALL  PGBEGIN(0,'/tek',1,1)
      CALL  PGENV(KMIN,KMAX,A,B,0,0)
      CALL PGLABEL('K','SECONDARY SPLINE FIT',TEXT1)
      CALL PGLINE(NDATA,KDATA,WCHIDATA)
      CALL PGLINE(NDATA,KDATA,YSPL)
      CALL PGLINE(NDATA,KDATA,WCHI)
      CALL PGEND

      READ(*,220)  TEXT
220   FORMAT(A1)

C FOURIER TRANSFORM:

C DETERMINE K, DK, WINDOW-K FOR EACH DATA INTERVAL

      A=KHW**2/LOG(2.0)
      DO  J=1,NDATA-1
        DK(J)=KDATA(J+1)-KDATA(J)
        K(J)=(KDATA(J)+KDATA(J+1))/2.0
       WK(J)=1.0
       IF  ((K(J).LT.KLT).AND.(K(J).GT.KMIN))
     1        WK(J)=EXP(-(K(J)-KLT)**2/A)
       IF  ((K(J).GT.KRT).AND.(K(J).LT.KMAX))
     1        WK(J)=EXP(-(K(J)-KRT)**2/A)
```

```
          IF ((K(J).LT.KMIN).OR.(K(J).GT.KMAX)) WK(J)=0.0
        ENDDO

C MULTIPLY DATA BY WINDOW

        DO I=1,NDATA
          WWCHI(I)=WK(I)*WCHI(I)
        ENDDO

C PERFORM FT

        MAXMAG=0.
        MINIMFT=0.
        DO I=0,NR
          R(I) = REAL(I)*DR
          DO J=1,NDATA-1
             B=2*K(J)*R(I)
            REFT(I)=REFT(I)+WWCHI(J)*COS(B)*DK(J)
             IMFT(I)=IMFT(I)+WWCHI(J)*SIN(B)*DK(J)
         ENDDO
            MAGFT(I)=(REFT(I)**2.0+IMFT(I)**2.0)**0.5
          IF (MAGFT(I).GT.MAXMAG) MAXMAG=MAGFT(I)
          IF (IMFT(I).LT.MINIMFT) MINIMFT=IMFT(I)
        ENDDO

C DISPLAY FT MAGNITUDE AND IMAGINARY PART

        A=1.1*MINIMFT
        B=1.1*MAXMAG
        CALL PGBEGIN(0,'/tek',1,1)
        CALL PGENV (0.,8.,A,B,0,0)
        CALL PGLABEL('R','FT MAG AND IMAG',TEXT1)
        CALL PGLINE(NR,R,MAGFT)
        CALL PGLINE(NR,R,IMFT)
        WRITE(*,250) KLO,KHI,KHW
250     FORMAT('KLO=',F5.2,'  KHI=',F5.2,'  KHW=',F4.2)
        WRITE(*,260) N
260     FORMAT('WEIGHTED BY K**',F3.1)

C INVERSE FOURIER TRANSFORM:

C ASK FOR R-LIMITS

        WRITE(*,410) ' RLO (REAL) ?'
        READ(*,415) RLO
        WRITE(*,410) ' RHI (REAL) ?'
        READ(*,415) RHI
        WRITE(*,410) ' RHW (REAL) ?'
        READ(*,415) RHW
410     FORMAT(A15)
415     FORMAT(F8.5)
420     FORMAT(A22)
```

```
      RMIN=RLO-RHW
      RMAX=RHI+RHW
      RLT=RLO+RHW
      RRT=RHI-RHW


C DETERMINE DKK AND WINDOW-R, APPEND WINDOW-R
C   TO DISPLAY

      DKK=(KMAX-KMIN)/REAL(NKK)

      A=RHW**2/LOG(2.0)
      DO J=0,NR
        WR(J)=1.0
        IF ((R(J).LE.RLT).AND.(R(J).GE.RMIN))
     1          WR(J)=EXP(-(R(J)-RLT)**2.0/A)
        IF ((R(J).GE.RRT).AND.(R(J).LE.RMAX))
     1          WR(J)=EXP(-(R(J)-RRT)**2.0/A)
        IF ((R(J).LT.RMIN).OR.(R(J).GT.RMAX)) WR(J)=0.0
      ENDDO

      DO J=0,NR
        PLOTWR(J)=WR(J)*B
      ENDDO

      CALL PGLINE(NR,R,PLOTWR)

      CALL PGEND
      READ(*,430)
430   FORMAT()

C PERFORM INVERSE FT

      MAXREIFT=0.
      MINREIFT=0.
      DO I=0,NKK
        A = I
        KK(I) = KMIN+A*DKK
        DO J=0,NR
          B=-2.0*KK(I)*R(J)
          REIFT(I)=REIFT(I)+(REFT(J)*COS(B)-IMFT(J)*SIN(B))
     1     *2.0*DR*WR(J)
          IMIFT(I)=IMIFT(I) + (REFT(J)*SIN(B) + IMFT(J)*COS(B))
     1     *2.0*DR*WR(J)
        ENDDO
        REIFT(I)=REIFT(I)/(2.0*PI)
        IMIFT(I)=IMIFT(I)/(2.0*PI)
        IF (REIFT(I).GT.MAXREIFT) MAXREIFT=REIFT(I)
        IF (REIFT(I).LT.MINREIFT) MINREIFT=REIFT(I)
      ENDDO
```

```
C DISPLAY REAL PART OF INVERSE FT

      A=1.1*MINREIFT
      B=1.1*MAXREIFT
      CALL  PGBEGIN(0,'/tek',1,1)
      CALL  PGENV  (KMIN,KMAX,A,B,0,0)
      CALL PGLABEL('K','INVERSE FT',TEXT1)
      CALL PGLINE(NKK,KK,REIFT)
      CALL PGEND
      WRITE(*,550)  RLO,RHI,RHW
 550  FORMAT('RLO=',F5.2,'   RHI=',F5.2,'   RHW=',F4.2)

C SAVE RESULTS:

      OPEN(UNIT=3,FILE='four.out',STATUS='NEW')

C SAVE INVERSE FT REAL PART

      WRITE(3,600)  TEXT1
 600  FORMAT(A40)
      WRITE(3,602) RLO,RHI,RHW
 602  FORMAT('RLO=',F5.2,'   RHI=',F5.2,'   RHW=',F4.2)
      WRITE(3,603)
 603  FORMAT('K_FILT    CHI_FILT')
      DO I = 0,NKK
        WRITE(3,605)  KK(I),REIFT(I)
 605    FORMAT(F8.5,F10.5)
      END DO

C SAVE FT MAGNITUDE, REAL, IMAGINARY, WINDOW-R

      WRITE(3,640) KLO,KHI,KHW
 640  FORMAT('KLO=',F5.2,'   KHI=',F5.2,'   KHW=',F4.2)
      WRITE(3,650)
 650  FORMAT('R      MAGFT    REALFT   IMAGFT   WINDOW-R')
      DO I = 0,NR
        WRITE(3,660)  R(I),MAGFT(I),REFT(I),IMFT(I),WR(I)
 660    FORMAT(F8.5,3F10.5,F8.5)
      END DO

C SAVE WEIGHTED CHI (AFTER SECONDARY SPLINE,
C   BUT BEFORE WINDOW) AND WINDOW-K

      WRITE(3,672)
 672  FORMAT('KNOT   ORDER')
      DO I=1,NREG
        WRITE(3,674)  XL(I),NORD(I)
 674    FORMAT(2F8.3)
      ENDDO
      IF (NREG.NE.0) WRITE(3,676) XH(NREG)
 676  FORMAT(F8.3)
      WRITE(3,678)  N
```

```
678   FORMAT('K        CHI*K**',F3.1,',  WINDOW-K')
      DO I = 1,NDATA-1
        IF (WK(I).LT.(0.01)) GOTO 690
        WRITE(3,680) K(I),WCHI(I),WK(I)
680     FORMAT(F8.5,F10.5,F8.5)
690    CONTINUE
      END DO

      CLOSE (3)
9999  END
```

B.4 Least-Squares Fitting

After Fourier band-pass filtering, least-squares fitting can be used to quantify the differences between two experimental measurements. This section lists my program "LEAST" for such least-squares fitting.

The edge onset energy, Eo, is variable in the fits. Either the change in MSRD or the change in backscattering amplitude between two sets of data can be determined.

```
      PROGRAM LEAST

C LEAST-SQUARES FIT TO DETERMINE CHANGE IN MSRD
C   OR CHANGE IN AMPLITUDE BETWEEN TWO EXELFS SPECTRA.
C READS FILE IN FORMAT OF OUTPUT FILE FROM THE
C   FOURIER FILTERING PROGRAM CALLED FOUR.
C THE DATA FROM INPUT FILE #1 IS ADJUSTED UNTIL IT
C   BEST FITS THE DATA FROM INPUT FILE #2.

C JAMES K. OKAMOTO   19OCT92

C UNITS: ANGSTROMS, EV.

C VARIABLES:

C GENERIC
      INTEGER L
      INTEGER I,J
      REAL A,B,C,D
C FOR READ DATA
      CHARACTER*40 TEXT(4)
      INTEGER*4 NDATA(2),NDAT
      REAL KDATA(301,2),XDATA(301,2)
      REAL K(301),X(301)
      REAL TEMP(604)
C FOR LEAST-SQUARES FIT
      INTEGER KIND
      INTEGER LL
      REAL DEL
      REAL E(301),DELTAE(40)
      REAL KNEW(301),ENEW(301),X1E(301)
      REAL VARE(301)
      INTEGER LOC(301)
      INTEGER N,NE,MINE(10)
      INTEGER MINS(10)
      REAL X1(301)
      REAL SIGMA2(301),VARS(301)
```

```
      REAL LIMIT,SIGN,UPPER,LOWER
      REAL TOTDELTAE,TOTSIGMA2,TOTUPPER,TOTLOWER
      DATA LL /3/
C FOR ERROR BARS
      REAL PERCEN
      DATA PERCEN /20.0/
C CONSTANTS
      REAL ZERO,HBAR2ME
      DATA ZERO,HBAR2ME /0.0,14.409/

C READ DATA

      DO I=1,2
       IF (I.EQ.1) OPEN(UNIT=2,FILE='least.in1',STATUS='OLD')
       IF (I.EQ.2) OPEN(UNIT=2,FILE='least.in2',STATUS='OLD')
       READ(2,105) TEXT(I)
105    FORMAT(A40)
108    READ(2,109) TEXT(3)
109    FORMAT(A6)
       IF (TEXT(3).NE.'K_FILT') GOTO 108
       READ(2,*,END=115) (TEMP(J),J=1,602)
115    DO J=1,602
         A=J
         A=A/2.0
         B=J/2
         IF (A.NE.B) KDATA(J/2+1,I)=TEMP(J)
         IF (A.EQ.B) XDATA(J/2,I)=TEMP(J)
       ENDDO
       CLOSE(2)
      ENDDO

C DETERMINE NDAT

      DO I=1,2
       NDATA(I)=0
       DO J=1,301
         K(J)=KDATA(J,I)
         IF (KDATA(J,I).NE.ZERO) NDATA(I)=J
       ENDDO
      ENDDO
      NDAT=NDATA(1)

C DISPLAY ORIGINAL DATA

       A=0.
       B=0.
       DO J=1,NDAT
          IF (XDATA(J,1).LT.A) A=XDATA(J,1)
          IF (XDATA(J,1).GT.B) B=XDATA(J,1)
       ENDDO
       A=1.1*A
       B=1.1*B
```

```
          C=K(1)
          D=K(NDAT)
          CALL PGBEGIN(0,'/tek',1,1)
          CALL PGENV(C,D,A,B,0,0)
          CALL PGLABEL('K','ORIGINAL DATA (#1 PLUSES, #2 DOTS)','')
          DO J=1,NDAT
            X(J)=XDATA(J,1)
          ENDDO
          CALL PGPOINT(NDAT,K,X,2)
          DO J=1,NDAT
            X(J)=XDATA(J,2)
          ENDDO
          CALL PGPOINT(NDAT,K,X,1)
          CALL PGEND

C ASK WHETHER TO VARY DELTA MSRD OR AMPLITUDE

200       WRITE(*,205)
205       FORMAT('VARY 1) DELTA MSRD OR 2) AMPLITUDE?')
          READ(*,210) KIND
210       FORMAT(I1)
          IF ((KIND.NE.1).AND.(KIND.NE.2)) GOTO 200

C *** LEAST-SQUARES FIT ***

C INITIALIZE X1 VECTOR

          DO J=1,NDAT
            X1(J)=XDATA(J,1)
          ENDDO

C FOR LL ITERATIONS

          DO L=1,LL

C * LEAST-SQUARES FIT FOR DELTA Eo PARAMETER *
C FOR A RANGE OF DELTA Eo VALUES
          DO I=1,40
            DEL=REAL(I)
            DELTAE(I)=DEL*1.0 - 20.0
C CALCULATE NEW K VECTOR PER Eo
            DO J=1,NDAT
              E(J)=HBAR2ME*K(J)*K(J)/2.0
              ENEW(J)=E(J)+DELTAE(I)
              KNEW(J)=SQRT(2.0*ENEW(J)/HBAR2ME)
            ENDDO
C INTERPOLATE TO FIND NEW EXELFS VECTOR (WHICH
C   CORRESPONDS TO NEW K VECTOR) PER Eo
            NE=NDAT
            DO J=1,NDAT
              X1E(J)=0.0
              LOC(J)=0
```

```
            DO N=1,NDAT
              IF ((K(J).GE.KNEW(N)).AND.(K(J).LT.KNEW(N+1))) LOC(J)=N
            ENDDO
            N=LOC(J)
            IF (N.EQ.0) GOTO 700
            B=(X1(N+1)-X1(N))/(KNEW(N+1)-KNEW(N))
            X1E(J)=X1(N)+(K(J)-KNEW(N))*B
700         CONTINUE
           ENDDO
C CALCULATE SQUARE VARIATION OF FIT PER Eo
           VARE(I)=0.0
           N=NDAT
           DO J=1,NDAT
            IF (LOC(J).EQ.0) N=N-1
            IF (LOC(J).EQ.0) GOTO 750
            VARE(I)=VARE(I)+(X1E(J)-XDATA(J,2))**2.0
750         CONTINUE
           ENDDO
           VARE(I)=VARE(I)/REAL(N)
          ENDDO
C DETERMINE DELTA Eo THAT GAVE BEST FIT
          MINE(L)=1
          A=VARE(1)
          DO I=1,40
           IF (VARE(I).LT.A) MINE(L)=I
           IF (VARE(I).LT.A) A=VARE(I)
          ENDDO
C RECALCULATE KNEW VECTOR FOR BEST FIT
           DO J=1,NDAT
            KNEW(J)=0.0
            E(J)=HBAR2ME*K(J)*K(J)/2.0
            ENEW(J)=E(J)+DELTAE(MINE(L))
            IF (ENEW(J).LT.ZERO) GOTO 770
            KNEW(J)=SQRT(2.0*ENEW(J)/HBAR2ME)
770         CONTINUE
           ENDDO
C REINTERPOLATE TO FIND X1E VECTOR FOR BEST FIT
           DO J=1,NDAT
            X1E(J)=0.0
            LOC(J)=0
            DO N=1,NDAT
              IF ((K(J).GE.KNEW(N)).AND.(K(J).LT.KNEW(N+1))) LOC(J)=N
            ENDDO
            N=LOC(J)
            IF (N.EQ.0) GOTO 800
            B=(X1(N+1)-X1(N))/(KNEW(N+1)-KNEW(N))
            X1E(J)=X1(N)+(K(J)-KNEW(N))*B
800         CONTINUE
           ENDDO

C *** LEAST-SQUARES FIT DELTA MSRD OR AMPLITUDE PARAMETER
```

```
      DO I=1,300
       IF (KIND.EQ.1) SIGMA2(I)=REAL(I)*0.0001 - 0.015
       IF (KIND.EQ.2) AMP(I)=REAL(I)*0.005
      ENDDO
      DO I=1,300
       VARS(I)=0.0
       N=NDAT
       DO J=1,NDAT
        IF (LOC(J).EQ.0) N=N-1
        IF (LOC(J).EQ.0) GOTO 900
        IF (KIND.EQ.1) X1(J)=X1E(J)*EXP(-2.0*K(J)*K(J)*SIGMA2(I))
        IF (KIND.EQ.2) X1(J)=X1E(J)*AMP(I)
        VARS(I)=VARS(I)+(X1(J)-XDATA(J,2))**2.0
900     CONTINUE
       ENDDO
       VARS(I)=VARS(I)/REAL(N)
      ENDDO
C DETERMINE BEST FIT PER ITERATION
      MINS(L)=0
      A=VARS(1)
      DO I=1,300
       IF (VARS(I).LT.A) MINS(L)=I
       IF (VARS(I).LT.A) A=VARS(I)
      ENDDO
      DO J=1,NDAT
       IF (KIND.EQ.1) X1(J)=X1E(J)*EXP(-2.0*K(J)*K(J)*SIGMA2(MINS(L)))
       IF (KIND.EQ.2) X1(J)=X1E(J)*AMP(MINS(L))
      ENDDO
C DISPLAY BEST FIT PER ITERATION
      A=0.
      B=0.
      DO J=1,NDAT
       IF (XDATA(J,1).LT.A) A=XDATA(J,1)
       IF (XDATA(J,1).GT.B) B=XDATA(J,1)
      ENDDO
      A=1.1*A
      B=1.1*B
      C=K(1)
      D=K(NDAT)
      CALL PGBEGIN(0,'/tek',1,1)
      CALL PGENV(C,D,A,B,0,0)
      CALL PGLABEL('K','FITTED DATA #1 (PLUSES), ORIGINAL DATA #2 (DOTS)','')
      CALL PGPOINT(NDAT,K,X1,2)
      DO J=1,NDAT
       X(J)=XDATA(J,2)
      ENDDO
      CALL PGPOINT(NDAT,K,X,1)
      CALL PGEND
      WRITE(6,910) L,DELTAE(MINE(L))
910   FORMAT('ITERATION #',I1,' DEL Eo=',F3.0)
      IF (KIND.EQ.1) WRITE(6,920) L,SIGMA2(MINS(L))
      IF (KIND.EQ.2) WRITE(6,930) L,AMP(MINS(L))
```

```
920     FORMAT('ITERATION #',I1,' DEL SIG=',F7.4)
930     FORMAT('ITERATION #',I1,' FACTOR AMP=',F6.3)

C END ITERATION LOOP
        ENDDO

c DETERMINE TOTAL DEL Eo,
C   AND TOTAL DEL MSRD OR TOTAL AMP CHANGE
        TOTDELTAE=0.0
        TOTSIGMA2=0.0
        TOTAMP=1.0
        DO L=1,LL
          TOTDELTAE=TOTDELTAE+DELTAE(MINE(L))
          IF (KIND.EQ.1) TOTSIGMA2=TOTSIGMA2+SIGMA2(MINS(L))
          IF (KIND.EQ.2) TOTAMP=TOTAMP*AMP(MINS(L))
        ENDDO

c DETERMINE ERROR BAR
        LIMIT=VARS(MINS(LL))*(1.0+PERCEN/100.0)
        DO J=2,300
          SIGN=(VARS(J-1)-LIMIT)*(VARS(J)-LIMIT)
          IF (KIND.EQ.1) GOTO 950
          IF (KIND.EQ.2) GOTO 960
950       IF ((SIGN.LT.ZERO).AND.(J.LT.MINS(LL))) LOWER=SIGMA2(J)
          IF ((SIGN.LT.ZERO).AND.(J.GT.MINS(LL))) UPPER=SIGMA2(J-1)
        GOTO 970
960       IF ((SIGN.LT.ZERO).AND.(J.LT.MINS(LL))) LOWER=AMP(J)
          IF ((SIGN.LT.ZERO).AND.(J.GT.MINS(LL))) UPPER=AMP(J-1)
970     ENDDO
        IF (KIND.EQ.1) TOTLOWER=TOTSIGMA2-SIGMA2(MINS(LL))+LOWER
        IF (KIND.EQ.1) TOTUPPER=TOTSIGMA2-SIGMA2(MINS(LL))+UPPER
        IF (KIND.EQ.2) TOTLOWER=(TOTAMP/AMP(MINS(LL))) * LOWER
        IF (KIND.EQ.2) TOTUPPER=(TOTAMP/AMP(MINS(LL))) * UPPER


C WRITE TO OUTPUT FILE:

C BEST DELTA MSRD (OR  AMPLITUDE), TOTAL MSRD (OR TOTAL AMPLITUDE) VS VARIANCE
C VECTORS,  TOTAL DELTA EO VS VARIANCE VECTORS, AND FINAL X1 VS K

        OPEN(UNIT=3,FILE='least.out',STATUS='NEW')
        DO I=1,2
          WRITE(3,1000) I,TEXT(I)
1000      FORMAT('FILE #',I1,': ',A40)
        ENDDO
        WRITE(3,1002) PERCEN
1002    FORMAT('LIMITS AT ',F4.1,'% LARGER AVE FUNCTIONAL.')
        IF (KIND.EQ.1) WRITE(3,1003) TOTSIGMA2,TOTLOWER,TOTUPPER
        IF (KIND.EQ.2) WRITE(3,1004) TOTAMP,TOTLOWER,TOTUPPER
1003    FORMAT('SIGMA^2:',F7.5,'  LOWER:',F7.4,'  UPPER:',F7.4)
1004    FORMAT('AMP:',F6.3,'  LOWER:',F6.3,'  UPPER:',F6.3)
        IF (KIND.EQ.1) WRITE(3,1006)
```

```
1006   FORMAT('TOT SIGMA^2  VARIANCE')
       IF (KIND.EQ.2) WRITE(3,1007)
1007   FORMAT('TOT AMP  VARIANCE')
       DO I = 1,300
        IF (KIND.EQ.1) WRITE(3,1008) TOTSIGMA2-SIGMA2(MINS(LL))+SIGMA2(I),VARS(I)
        IF (KIND.EQ.2) WRITE(3,1009) (TOTAMP/AMP(MINS(LL))) * AMP(I),VARS(I)
1008    FORMAT(F8.5,' ',E10.4)
1009    FORMAT(F6.3,' ',E10.4)
       END DO
       WRITE(3,1010) TOTDELTAE
1010   FORMAT('DEL Eo:',F4.0)
       WRITE(3,1015)
1015   FORMAT('TOT DEL Eo  VARIANCE')
       DO I=1,40
        WRITE(3,1020) TOTDELTAE-DELTAE(MINE(LL))+DELTAE(I),VARE(I)
1020    FORMAT(F4.0,' ',F8.5)
       ENDDO
       WRITE(3,1100)
1100   FORMAT('BEST FIT: K  X1(K)')
       DO J = 1,NDAT
        WRITE(3,1105) K(J),X1(J)
1105    FORMAT(F8.5,' ',F8.5)
       END DO
       CLOSE (3)

C END
 9999  END
```

Appendix C Software for Calculations of Vibrational MSRD

Various models used to calculate vibrational MSRD were discussed in §5.1. This appendix documents the computer software which implements these calculations.

The Einstein model is a very simple model, but it adequately parameterizes all of the MSRD data presented in this thesis. The software used to fit ΔMSRD vs temperature data to Einstein temperatures is documented in §C.1.

The correlated Debye model is slightly more sophisticated than the Einstein model. The software used to fit ΔMSRD vs temperature data to Debye temperatures is documented in §C.2.

The force constant model uses interatomic force constants to calculate the "projected" density of vibrational modes, which determines the vibrational MSRD. §C.3 contains computer software for such calculations.

C.1 Correlated Einstein Model

This section contains a listing of my program "EIN" which fits ΔMSRD vs temperature data to an Einstein temperature. The reduced mass of the two atoms of interest, i.e., the central and neighboring atoms, must be input. The ΔMSRD data are then fit to predictions of the correlated Einstein model, allowing the value of the lowest-temperature experimental MSRD to float.

```
      PROGRAM EIN

C INPUT DELMSRD (SQ ANGSTROMS) VS TEMPERATURE (KELVIN) DATA.
C OUTPUT EINSTEIN TEMPS WITH VARIANCE AND OFFSET VECTORS
C   ALSO OUTPUT MSRD VS TEMP FOR BEST FIT.

C JAMES K OKAMOTO 20OCT92

C VARIABLES:
      CHARACTER*40 TEXT
      INTEGER NSETS,NPTS(6),I,J,K,N
      REAL T(6,20),DELMSRD(6,20)
      REAL MRED
      REAL LOWEST,HIGHEST
      REAL TEIN(101),OFF(300),TOUT(100)
      REAL SUM,DIFF,CONST,ARG,FUNCT,MSRD
      REAL VAR(6),TOTVAR(101),OFFSET(101,6)
      REAL MINTOTVAR,BESTTEIN,BESTOFFSET(6),MSRDOUT(100)
      REAL PERCEN,LIMIT,SIGN,LOWER,UPPER
      DATA PERCEN /100.0/

C CONSTANTS:
      REAL H2MKA2
      DATA H2MKA2 /48.46/

C READ DATA
      OPEN(UNIT=2,FILE='ein.in',STATUS='OLD')
      READ(2,100) TEXT
100   FORMAT(A40)
      WRITE(*,105) TEXT
105   FORMAT(A40)
      READ(2,107) NSETS
107   FORMAT(I2)
      DO N=1,NSETS
       READ(2,110) NPTS(N)
110    FORMAT(I2)
       DO I=1,NPTS(N)
        READ(2,120) T(N,I),DELMSRD(N,I)
```

```
120         FORMAT(F8.1,F8.4)
           ENDDO
         ENDDO
         CLOSE(2)

C INPUT REDUCED MASS, RANGE OF TEIN
         WRITE(*,150)
150      FORMAT('INPUT AVE REDUCED MASS OF BOND (AMU):')
         READ(5,160) MRED
160      FORMAT(F8.4)
         WRITE(*,170)
170      FORMAT('INPUT LOWEST TEIN TO TRY (K):')
         READ(5,180) LOWEST
180      FORMAT(F6.2)
         WRITE(*,190)
190      FORMAT('INPUT HIGHEST TEIN TO TRY (K):')
         READ(5,200) HIGHEST
200      FORMAT(F6.2)


C SET UP TEIN, OFF, AND TOUT VECTORS
         DO I=1,101
           TEIN(I)=LOWEST+(I-1)*(HIGHEST-LOWEST)/100.0
         ENDDO
         DO I=1,300
           OFF(I)=REAL(I)*0.0001 - 0.0150
         ENDDO
         DO I=1,100
           TOUT(I)=REAL(I)*10.0
         ENDDO

C MAIN LOOPS

C FOR EACH EINSTEIN TEMP
         MINTOTVAR=1.0
         DO I=1,101
           TOTVAR(I)=0.0
           CONST=H2MKA2/(2.0*MRED*TEIN(I))
C FOR EACH SET OF TEMPERATURE-DEPENDENT DATA
           DO N=1,NSETS
             VAR(N)=1.0
             OFFSET(I,N)=0.0
C FOR EACH OFFSET
             DO J=1,300
               SUM=0.0
C FOR EACH TEMPERATURE DATA POINT
               DO K=1,NPTS(N)
C                CALCULATE MSRD, DETERMINE SUM OF SQ DIFF
                 ARG=TEIN(I)/T(N,K)
                 FUNCT=(2.0/(EXP(ARG)-1.0)) + 1.0
                 MSRD=CONST*FUNCT
                 DIFF=(OFF(J)+DELMSRD(N,K)) - MSRD
```

```
            SUM=SUM+DIFF*DIFF
           ENDDO
           IF (SUM.LT.VAR(N)) OFFSET(I,N)=OFF(J)
           IF (SUM.LT.VAR(N)) VAR(N)=SUM
          ENDDO
          TOTVAR(I)=TOTVAR(I)+VAR(N)
         ENDDO
         IF (TOTVAR(I).LT.MINTOTVAR) BESTTEIN=TEIN(I)
         DO N=1,NSETS
          IF (TOTVAR(I).LT.MINTOTVAR) BESTOFFSET(N)=OFFSET(I,N)
         ENDDO
         IF (TOTVAR(I).LT.MINTOTVAR) MINTOTVAR=TOTVAR(I)
        ENDDO

C CALCULATE MSRD VS TEMP FOR BEST TEIN
        DO I=1,100
         CONST=H2MKA2/(2.0*MRED*BESTTEIN)
         ARG=BESTTEIN/TOUT(I)
         FUNCT=(2.0/(EXP(ARG)-1.0)) +1.0
         MSRDOUT(I)=CONST*FUNCT
        ENDDO

C DETERMINE LOWER AND UPPER LIMITS OF ERROR BAR FOR TEIN
        LIMIT=MINTOTVAR*(1.0+PERCEN/100.0)
        DO I=2,101
         SIGN=(TOTVAR(I-1)-LIMIT)*(TOTVAR(I)-LIMIT)
         IF ((SIGN.LT.ZERO).AND.(TEIN(I).LT.BESTTEIN)) LOWER=TEIN(I-1)
         IF ((SIGN.LT.ZERO).AND.(TEIN(I).GT.BESTTEIN)) UPPER=TEIN(I)
        ENDDO


C WRITE OUTPUT
        OPEN(UNIT=3,FILE='ein.out',STATUS='NEW')
        WRITE(3,1000) TEXT
1000    FORMAT(A40)
        DO N=1,NSETS
         DO I=1,NPTS(N)
          WRITE(3,1002) T(N,I),DELMSRD(N,I)
1002      FORMAT(F6.1,'  ',F8.4)
         ENDDO
        ENDDO
        WRITE(3,1004) MRED
1004    FORMAT('REDUCED MASS OF BOND = ',F8.4)
        WRITE(3,1005) PERCEN
1005    FORMAT('LIMITS AT ',F5.1,'% GREATER VARIANCE')
        WRITE(3,1010) BESTTEIN,LOWER,UPPER
1010    FORMAT('TEIN: BEST=',F6.1,' LOWER=',F6.1,' UPPER=',F6.1)
        WRITE(3,1015) (BESTOFFSET(N),N=1,NSETS)
1015    FORMAT('BEST OFFSETS:',6F8.5)
        WRITE(3,1017) MINTOTVAR
1017    FORMAT('MIN TOTAL VARIANCE=',E10.4)
        WRITE(3,1020)
```

```
1020   FORMAT('TEIN    VARIANCE   OFFSETS')
       DO I=1,101
        WRITE(3,1100) TEIN(I),TOTVAR(I),(OFFSET(I,N),N=1,NSETS)
1100    FORMAT(F6.1,X,E10.4,X,6(F8.5,X))
       ENDDO
       WRITE(3,1110)
1110   FORMAT('TEMP    MSRDOUT')
       DO I=1,100
        WRITE(3,1200) TOUT(I),MSRDOUT(I)
1200    FORMAT(F6.1,'  ',F8.6)
       ENDDO
       CLOSE(3)

       END
```

C.2 Correlated Debye Model

This section contains a listing of my program "DEB" which fits ΔMSRD vs temperature data to a Debye temperature. The required inputs are as follows:

1) reduced mass of the central atom and neighbor of interest

2) neighbor distance

3) atomic density of solid

The ΔMSRD data are then fit to predictions of the correlated Debye model, allowing the value of the lowest-temperature experimental MSRD to float.

```
      PROGRAM DEB

C INPUT DMSRDDAT (SQ ANGSTROMS) VS TEMPERATURE (KELVIN) DATA.
C IN GENERAL, CALCULATIONS USE UNITS OF ANG,AMU,PICOSEC,KELVIN.
C OUTPUT CORRELATED DEBYE TEMPS WITH MSRD OFFSET AND LOWEST
C  VARIANCE VECTORS
C ALSO OUTPUT MSRD VS TEMP FOR BEST FIT.

C JAMES K OKAMOTO 05MAR93

C LOOPS:
      INTEGER I,J,K,L,N

C CONSTANTS:
      REAL PI,HBAR,KB
      DATA PI,HBAR,KB /3.14159,6.35,0.831/

C VARIABLES:
      CHARACTER*40 TEXT
      INTEGER NPTS(6)
      REAL TDAT(6,20),DMSRDDAT(6,20)

      REAL MRED,RNN,DENS,KD,LOWEST,HIGHEST

      REAL TDEB(51),WDEB(51),OFF(150),TOUT(100),WOUT(100),DTOUT
      DATA DTOUT/10.0/

      REAL BESTTOTVAR,BESTTDEB,BESTOFFSET(6)
      REAL VAR(6),TOTVAR(51),OFFSET(51,6),C,DW
      INTEGER LMAX
```

```
      DATA DW /0.5/
      REAL SUM
      REAL INTEG
      REAL ARG,W(2000),COTH,WRC,PROJDOS
      REAL MSRD(20),DIFF

      REAL BESTWDEB,MSRDOUT(100)

      REAL PERCEN,LIMIT,SIGN,LOWER,UPPER
      DATA PERCEN /100.0/

C READ DATA
      OPEN(UNIT=2,FILE='deb.in',STATUS='OLD')
      READ(2,100) TEXT
100   FORMAT(A40)
      WRITE(*,105) TEXT
105   FORMAT(A40)
      READ(2,107) NSETS
107   FORMAT(I1)
      DO N=1,NSETS
       READ(2,110) NPTS(N)
110    FORMAT(I2)
       DO I=1,NPTS(N)
        READ(2,120) TDAT(N,I),DMSRDDAT(N,I)
120     FORMAT(F8.1,F8.4)
       ENDDO
      ENDDO
      CLOSE(2)

C INPUT REDUCED MASS, ATOMIC DENS, RANGE OF TDEB
      WRITE(*,140)
140   FORMAT('ALL INPUTS MUST BE FLOATS (NOT INTEGER)')
      WRITE(*,150)
150   FORMAT('INPUT AVE REDUCED MASS OF BOND (AMU):')
      READ(5,160) MRED
160   FORMAT(F8.4)
      WRITE(*,161)
161   FORMAT('INPUT NEIGHBOR DISTANCE (ANG)')
      READ(5,162) RNN
162   FORMAT(F8.4)
      WRITE(*,163)
163   FORMAT('INPUT ATOMIC DENSITY (ANG^-3):')
      READ(5,165) DENS
165   FORMAT(F8.4)
      KD=(6.0*PI*PI*DENS)**0.333
      WRITE(*,170)
170   FORMAT('INPUT LOWEST TDEB TO TRY (K):')
      READ(5,180) LOWEST
180   FORMAT(F6.2)
      WRITE(*,190)
190   FORMAT('INPUT HIGHEST TDEB TO TRY (K):')
      READ(5,200) HIGHEST
```

```
200     FORMAT(F6.2)


C SET UP TDEB,WDEB, OFF,W,TOUT,WOUT VECTORS
        WRITE(*,250)
250     FORMAT('SETTING UP VECTORS')
        DO I=1,51
          TDEB(I)=LOWEST+REAL(I-1)*(HIGHEST-LOWEST)/50.0
          WDEB(I)=TDEB(I)*KB/HBAR
        ENDDO
        DO I=1,150
          OFF(I)=REAL(I)*0.0001
        ENDDO
        DO I=1,2000
          W(I)=(REAL(I)+0.5)*DW
        ENDDO
        DO I=1,100
          TOUT(I)=REAL(I)*DTOUT
          WOUT(I)=TOUT(I)*KB/HBAR
        ENDDO

C MAIN LOOPS
        WRITE(*,300)
300     FORMAT('IN MAIN LOOP')
        WRITE(*,400)
400     FORMAT('TDEB    TOTVAR    OFFSETS')
        BESTTOTVAR=1.0E20
C FOR EACH DEBYE TEMP
        DO I=1,51
          C=KB*TDEB(I)/(HBAR*KD)
          LMAX=INT(WDEB(I)/DW+0.5)
          TOTVAR(I)=0.0
C FOR EACH SET OF TEMP-DEP DATA
          DO N=1,NSETS
            OFFSET(I,N)=0.0
C FOR EACH OFFSET
            DO J=1,150
              SUM=0.0
C FOR EACH TEMPERATURE DATA POINT
C CALCULATE MSRD, DETERMINE SUM OF SQ DIFF
              DO K=1,NPTS(N)
                INTEG=0.0
C   INTEGRATION LOOP OVER PHONON FREQUENCIES
                DO L=1,LMAX
                  ARG=HBAR*W(L)/(KB*TDAT(N,K))
                  COTH=(2.0/(EXP(ARG)-1.0)) + 1.0
                  WRC=W(L)*RNN/C
                    PROJDOS=3.0*W(L)*W(L)*(1.0-SIN(WRC)/WRC)/(WDEB(I)**3.0)
                    INTEG=INTEG + DW*PROJDOS*COTH/W(L)
                ENDDO
                MSRD(K)=INTEG*HBAR/(2.0*MRED)
                DIFF=(OFF(J)+DMSRDDAT(N,K)) - MSRD(K)
```

```
              SUM=SUM+DIFF*DIFF
             ENDDO
             IF (J.EQ.1) VAR(N)=SUM
             IF (SUM.LE.VAR(N)) OFFSET(I,N)=OFF(J)
             IF (SUM.LE.VAR(N)) VAR(N)=SUM
            ENDDO
            TOTVAR(I)=TOTVAR(I)+VAR(N)
           ENDDO
           WRITE(*,490) TDEB(I),TOTVAR(I),(OFFSET(I,N),N=1,NSETS)
490        FORMAT(F6.1,3X,E10.4,6(X,F8.4))
           IF (TOTVAR(I).LE.BESTTOTVAR) BESTTDEB=TDEB(I)
           DO N=1,NSETS
            IF (TOTVAR(I).LE.BESTTOTVAR) BESTOFFSET(N)=OFFSET(I,N)
           ENDDO
           IF (TOTVAR(I).LE.BESTTOTVAR) BESTTOTVAR=TOTVAR(I)
          ENDDO
          WRITE(*,500) BESTTDEB
500       FORMAT('best fit Debye temp: ',F6.1)

C CALCULATE MSRD VS TEMP FOR BEST TDEB
          BESTWDEB=BESTTDEB*KB/HBAR
          LMAX=INT(BESTWDEB/DW+0.5)
          C=KB*BESTTDEB/(HBAR*KD)
          DO I=1,100
           INTEG=0.0
           DO L=1,LMAX
            ARG=W(L)/WOUT(I)
            COTH=(2.0/(EXP(ARG)-1.0)) +1.0
            WRC=W(L)*RNN/C
            PROJDOS=3*W(L)*W(L)*(1.0-SIN(WRC)/WRC)/(BESTWDEB**3)
            INTEG=INTEG + DW*PROJDOS*COTH/W(L)
           ENDDO
           MSRDOUT(I)=INTEG*HBAR/(2.0*MRED)
          ENDDO

C DETERMINE LOWER AND UPPER LIMITS OF ERROR BAR FOR TDEB
          LIMIT=BESTTOTVAR*(1.0+PERCEN/100.0)
          DO I=2,51
           SIGN=(TOTVAR(I-1)-LIMIT)*(TOTVAR(I)-LIMIT)
           IF ((SIGN.LT.ZERO).AND.(TDEB(I).LT.BESTTDEB)) LOWER=TDEB(I-1)
           IF ((SIGN.LT.ZERO).AND.(TDEB(I).GT.BESTTDEB)) UPPER=TDEB(I)
          ENDDO


C WRITE OUTPUT
          OPEN(UNIT=3,FILE='deb.out',STATUS='NEW')
          WRITE(3,1000) TEXT
1000      FORMAT(A40)
          DO N=1,NSETS
           DO I=1,NPTS(N)
            WRITE(3,1002) TDAT(N,I),DMSRDDAT(N,I)
1002        FORMAT(F6.1,'  ',F8.4)
```

```
        ENDDO
       ENDDO
       WRITE(3,1005) PERCEN
1005   FORMAT('LIMITS AT ',F5.1,'% GREATER VARIANCE')
       WRITE(3,1010) BESTTDEB,LOWER,UPPER
1010   FORMAT('TDEB: BEST=',F6.1,' LOWER=',F6.1,' UPPER=',F6.1)
       WRITE(3,1015) (BESTOFFSET(N),N=1,NSETS)
1015   FORMAT('BEST OFFSETS=',6F8.5)
       WRITE(3,1017) BESTTOTVAR
1017   FORMAT('MIN TOTAL VARIANCE=',E10.4)
       WRITE(3,1020)
1020   FORMAT('TDEB  VARIANCE OFFSET')
       DO I=1,51
        WRITE(3,1100) TDEB(I),TOTVAR(I),(OFFSET(I,N),N=1,NSETS)
1100    FORMAT(F6.1,X,E10.4,X,6(F8.5,X))
       ENDDO
       WRITE(3,1110)
1110   FORMAT('TEMP    MSRDOUT')
       DO I=1,100
        WRITE(3,1200) TOUT(I),MSRDOUT(I)
1200    FORMAT(F6.1,'  ',F8.6)
       ENDDO
       CLOSE(3)

       END
```

C.3 Force Constant Model

This section documents my computer software to calculate the "projected" density of vibrational modes from the interatomic force constants of a monatomic Bravais lattice. The program outputs the density of vibrational modes and the projected density of vibrational modes for the three phonon branches: one longitudinal and two transverse.

The particular program presented is tailored for fcc lattices. The program was modified for bcc lattices, but that version of the program is not shown. The program can also be easily modified for other crystal lattice structures and other neighboring shells.

Also included is the program "FCMSRD" which uses the projected density of modes to calculate the vibrational MSRD.

```
/*      projected phonon DOS calculation
        for L,T2,T1 branches
        version fcc, 1nn shell
        James K. Okamoto 1/15/91 */

#include <stdio.h>
#include <math.h>
#include "alforce.h"

#define NQ 50
#define DX 0.02
#define PI 3.14159


main()
{
        int i,j,k;

        int n,x2,nn[25];

        int l,m;
        float s,ctemp;

        int r[730],x[730][4];

        float q[4],q0,q1;
```

```
        float qr,dyn[4][4],d[4][4];
        int thesign;


        int nrot;
        float e[4],v[4][4],test[4][4];
        int iq,ip;
        float tresh,theta,tau,t,sm,h,g,c,b[4],z[4];
        float under;

        int first,longitudinal;
        int origbranch[4],oldbranch[4],koldbranch[4],joldbranch[4],branch[4];
        float olde[4],kolde[4],jolde[4],olddel[4],kolddel[4],jolddel[4];
        float del[4][4],long1,long2,long3,same,reverse;
        float origv[4][4],cross[4],orighand,hand;
        int nfreq[4];
        float polardot[4],freq[4],dot,unnormg[4][100],unnormproj[4][100];
        int nn1[13],i1,i2;

        float areag,normg[4][100],normproj[4][100];

        FILE *fp,*fopen();

/* determines allowed r for fcc lattice up to 8nn shell */

        printf("determining allowed r in fcc lattice\n");
        for (i=1;i<=8;i++)
          nn[i]=0;
        for (i = 39; i <= 689; i++)
        {
          for (j = 1; j <= 3; j++)
          {
            switch (j)
            {
              case 1:
                n=i/81;
                break;
              case 2:
                n=i/9;
                break;
              case 3:
                n=i;
                break;
              default:
                break;
            }
            x[i][j] = (n%9) - 4;          /* x[i][j] is 2 times the jth coordinate of atom i
                                  e.g. if atom i is at 0.5(110) then x[i][1]=1,
                                  x[i][2]=1,x[i][3]=0. */
          }
          x2 = x[i][1]*x[i][1] + x[i][2]*x[i][2] +  x[i][3]*x[i][3];
          if ((x2%2)==0)
```

```
        {
         r[i] = x2/2;            /*atom i is in the r[i]th nearest neigbor shell */
         nn[r[i]]++;
         if (r[i]==1)
            nn1[nn[r[i]]]=i;
        }
        else
         r[i] = 0;
      }
      for (i=1;i<=8;i++)
       printf("nn[%d]=%d\n",i,nn[i]);


/* main loop over all q allowed in 1st BZ needed by symmetry  */

      first=1;
      printf("in main loop\n");
      for (i = 1; i <= NQ; i++)
       for (j = 1; j <= NQ; j++)
        for (k = 1; k <= i; k++)
        {
         q[1]=((float)i - 0.5)*DX;  /* q=(qx,qy,qz) is a wavevector in reciprocal space */
         q[2]=((float)j - 0.5)*DX;
         q[3]=((float)k - 0.5)*DX;
         q0=0.0;
         q1=0.0;
         for (l = 1; l <= 3; l++)
         {
            q0+=q[l]*q[l];       /* distance from origin of recip space */
            q1+=(q[l]-1.0)*(q[l]-1.0); /* distance from recip latt pt at (111) */
         }
         if (q0 < q1)
         {
          if ((j==1) && (k==1))
            printf("i = %d\n",i);
          /* printf("qx=%f qy=%f qz=%f\n",q[1],q[2],q[3]); */

      /* calculate dynamical matrix dyn given q */

            /* printf("calculating dynamical matrix\n"); */
            for (m = 1; m<=3; m++)
               for (n = 1; n<=3; n++)
                  dyn[m][n] = 0.0;
            for (l = 0; l <= 728; l++)
            {
             if (r[l] != 0)
             {
              qr=0.0;
               for (m = 1; m<=3; m++)
                  qr += q[m]*(float)x[l][m];
               s = 2.0*sin(0.5*PI*qr)*sin(0.5*PI*qr);
               for (m = 1; m <= 3; m++)
```

```
for (n = 1; n <= m; n++)
{
 thesign = 1;
 if  (x[l][m]<0)
    thesign = -thesign;
 if (x[l][n]<0)
    thesign = -thesign;
 ctemp = 0.0;
 switch (r[l])
 {
  case 1:
   if (m == n)
   {
    if (x[l][m]==0)
      ctemp = C1ZZ;
    else
      ctemp = C1XX;
   }
   else
    if  ((x[l][m]!=0) && (x[l][n]!=0))
      ctemp = C1XY;
   break;
 case 2:
  if (m==n)
  {
   if (x[l][m]==0)
                          ctemp = C2YY;
    else
      ctemp = C2XX;
  }
  break;
 case 3:
  if (m==n)
  {
   if (abs(x[l][m])==2)
     ctemp = C3XX;
   if (abs(x[l][m])==1)
     ctemp = C3YY;
  }
  break;
 case 4:
  if (m==n)
  {
   if (x[l][m]!=0)
     ctemp = C4XX;
   if (x[l][m]==0)
     ctemp = C4ZZ;
  }
  else
  {
   if ((x[l][m]!=0) && (x[l][n]!=0))
     ctemp = C4XY;
```

```
    }
    break;
  case 5:
    if (m==n)
    {
      if (abs(x[l][m])==3)
        ctemp = C5XX;
      if (abs(x[l][m])==1)
        ctemp = C5YY;
      if (x[l][m]==0)
        ctemp = C5ZZ;
    }
    else
    {
      if ((x[l][m]!=0) && (x[l][n]!=0))
        ctemp = C5XY;
    }
    break;
  case 6:
    if (m==n)
      ctemp = C6XX;
    else
      ctemp = C6XY;
    break;
  case 7:
    if (m==n)
    {
      if (abs(x[l][m])==3)
        ctemp = C7XX;
      if (abs(x[l][m])==2)
        ctemp = C7YY;
      if (abs(x[l][m])==1)
        ctemp = C7ZZ;
    }
    else
    {
      if ((abs(x[l][m])!=3) && (abs(x[l][n])!=3))
        ctemp = C7YZ;
      if ((abs(x[l][m])!=2) && (abs(x[l][n])!=2))
        ctemp = C7XZ;
      if ((abs(x[l][m])!=1) && (abs(x[l][n])!=1))
        ctemp = C7XY;
    }
    break;
  case 8:
    if (m==n)
    {
      if (x[l][m]!=0)
        ctemp = C8XX;
      if (x[l][m]==0)
        ctemp = C8YY;
    }
```

```
            break;
          default:
            ctemp = 0.0;
            break;
        }
        dyn[m][n] += (float)thesign*ctemp*s;
      }
    }
  }
 for (m = 1; m <= 2; m++)
  for (n = m+1; n<=3; n++)
     dyn[m][n] = dyn[n][m];
 for (m = 1; m <= 3; m++)
 {
  for (n = 1; n<=3; n++)
  {
     d[m][n] = dyn[m][n];
     /* printf("dyn[%d][%d] = %e  ",m,n,dyn[m][n]); */
  }
  /* printf("\n"); */
 }

/* find eigenvalues e and eigenvectors v of dynamical matrix d
    section adapted from subroutine jacobi in numerical recipes in c */

        /* printf("in eigen-routine jacobi\n");fflush(stdout); */
        n = 3;

/* Computes all eigenvalues and eigenvectors of a real symmetric matrix
d[1...n][1...n]. On output, elements of a above the diagonal are destroyed.
e[1...n] returns eigenvalues of a. v[1...n(direction)][1...n(eigenvector)]
is a matrix whose columns contain, on output, the normalized eigenvectors of
d. nrot returns the number of Jacobi rotations that were required. */

        for (ip=1;ip<=n;ip++)     /* Initialize identity matrix. */
        {
         for (iq=1;iq<=n;iq++)
           v[ip][iq]=0.0;
         v[ip][ip]=1.0;
        }

        for (ip=1;ip<=n;ip++)
        {
         b[ip]=e[ip]=d[ip][ip];  /* Init b and e to the diagonal of d. */
         z[ip]=0.0;     /* This vector accumulates terms of the form
                           t*d[ip][iq] as in equation (11.1.14). */
        }

        nrot=0;
        l=0;
        under=999.0;
        while (under != 0.0)   /* Exit of loop relies on quadratic
```

```
                                        convergence to machine underflow. */
                    {
                     l++;
                     sm=0.0;
                     for (ip=1; ip<=n-1; ip++)   /* Sum off-diagonal elements. */
                     {
                      for (iq=ip+1;iq<=n;iq++)
                       sm += fabs(d[ip][iq]);
                     }
                     /* printf("sum off-diagonal elements = %e\n",sm);fflush(stdout); */
                     under=sm;
                     if (sm!=0.0)
                     {
                      if (l<4)     /* on the first 3 sweeps ... */
                       tresh=0.2*sm/((float)n*(float)n);
                      else         /* thereafter ... */
                       tresh=0.0;
                      for (ip=1;ip<=n-1;ip++)
                      {
                       for (iq=ip+1;iq<=n;iq++)
                       {
                        g=100.0*fabs(d[ip][iq]);
                        if
((l>4)&&((fabs(e[ip])+g)==fabs(e[ip]))&&((fabs(e[iq])+g)==fabs(e[iq])))
                         d[ip][iq]=0.0;
                        else if (fabs(d[ip][iq]) > tresh)
                        {
                         h=e[iq]-e[ip];
                         if ((fabs(h)+g) == fabs(h))
                          t=(d[ip][iq])/h;
                         else
                         {
                          theta=0.5*h/(d[ip][iq]);
                          t=1.0/(fabs(theta)+sqrt((1.0+theta*theta)));
                          if (theta < 0.0)
                              t = -t;
                         }
                         c=1.0/sqrt(1+t*t);
                         s=t*c;
                         tau=s/(1.0+c);
                         h=t*d[ip][iq];
                         z[ip] -= h;
                         z[iq] += h;
                         e[ip] -= h;
                         e[iq] += h;
                         d[ip][iq]=0.0;
                         for (m=1;m<=ip-1; m++)
                         {
                          g=d[m][ip]; h=d[m][iq]; d[m][ip]=g-s*(h+g*tau);
                          d[m][iq]=h+s*(g-h*tau);
                         }
                         for (m=ip+1;m<=iq-1;m++)
```

```
            {
              g=d[ip][m]; h=d[m][iq]; d[ip][m]=g-s*(h+g*tau);
              d[m][iq]=h+s*(g-h*tau);
            }
            for (m=iq+1;m<=n;m++)
            {
              g=d[ip][m]; h=d[iq][m]; d[ip][m]=g-s*(h+g*tau);
              d[iq][m]=h+s*(g-h*tau);
            }
            for (m=1;m<=n;m++)
            {
              g=v[m][ip]; h=v[m][iq]; v[m][ip]=g-s*(h+g*tau);
              v[m][iq]=h+s*(g-h*tau);
            }
            ++nrot;
          }
        }
      }
      for (ip=1;ip<=n;ip++)
      {
        b[ip] += z[ip];
        e[ip]=b[ip];
        z[ip]=0.0;
      }
    }
  }

/*

  for (m=1;m<=3;m++)
  {
     for (n=1;n<=3;n++)
     {
        test[n][m]=0.0;
        for(l=1;l<=3;l++)
           test[n][m] += dyn[n][l]*v[l][m];
     }
  }

  for (m=1;m<=3;m++)
     printf("e[%d] = %e  ",m,e[m]);
  printf("\n");

  for (n=1;n<=3;n++)
  {
     for (m=1;m<=3;m++)
        printf("v[%d][%d] = %f  ",n,m,v[n][m]);
     printf("\n");
  }

  for (n=1;n<=3;n++)
  {
     for (m=1;m<=3;m++)
```

```
                printf("test[%d][%d] = %f  ",n,m,test[n][m]/e[m]);
            printf("\n");
        }
*/


    /* determining to which branch each eigenvector belongs */

        /* calculate how parallel to the q vector */
        n=0;
        for (l=1;l<=3;l++) /* for each eigenvector */
        {
            polardot[l]=0.0;
            for (m=1;m<=3;m++) /* for each direction */
              polardot[l]+=v[m][l]*q[m]/sqrt(q0);
        }

        /* assign original branches 1=L,2=T1,3=T2 */
        if (first==1)
        {
         first=0;
         n=0;
         for (l=1;l<=3;l++)
         {
            if ((polardot[l]>0.95)&&(polardot[l]<1.01))
               origbranch[1]=l;
            else
            {
               origbranch[2+n]=l;
               n++;
             }
            for(m=1;m<=3;m++)
              origv[l][m]=v[l][m];
         }
         /* set olde,kolde,jolde,oldbranch,...,olddel,...*/
         for (l=1;l<=3;l++)
         {
            olde[l]=kolde[l]=jolde[l]=e[l];
            oldbranch[l]=koldbranch[l]=joldbranch[l]=origbranch[l];
            olddel[l]=kolddel[l]=jolddel[l]=0.0;
         }
         /* determine original handedness */
/*        for (l = 1; l <= 3; l++)
         {
            cross[l]=0.0;
            for (m = 1; m <= 3; m++)
              for (n = 1; n <= 3; n++)
                if ((l!=m)&&(m!=n)&&(n!=l))
                    cross[l]+=pow(-1.0,(m-l+2)%3)*origv[m][2]*origv[n][3];
         }
         orighand=0.0;
         for (l=1;l<=3;l++)
```

```
                orighand+=cross[l]*origv[l][1];
*/
            }

            /* assign new branches */
            if (k==1)
            {
               for (l=1;l<=3;l++)
               {
                  if (j==1)
                  {
                     olde[l]=jolde[l];
                     oldbranch[l]=joldbranch[l];
                     olddel[l]=jolddel[l];
                  }
                  else
                  {
                     olde[l]=kolde[l];
                     oldbranch[l]=koldbranch[l];
                     olddel[l]=kolddel[l];
                  }
               }
            }
            n=0;
            longitudinal=0;
/*
            for (l=1;l<=3;l++)
              printf("polardot[%d] = %f ",l,polardot[l]);
            printf("\n");
*/
            for (l = 1; l <= 3; l++)  /* for each eigenvector */
               if ((polardot[l]>0.95)&&(polardot[l]<1.01))
               {
                  branch[1]=l;
                  longitudinal++;
               }
               else
               {
                  branch[2+n]=l;
                  n++;
               }
            if (longitudinal!=1)
            {
             printf("warning: %d longitudinal modes\n",longitudinal);

             /* check for min change in derivs of long branch */
             for (l = 1; l <= 3; l++)  /* for each possible long branch */
                del[l][1]=e[branch[1]]-olde[oldbranch[1]];
             long1=fabs(del[1][1]-olddel[1]);
             long2=fabs(del[1][2]-olddel[1]);
             long3=fabs(del[1][3]-olddel[1]);
             if ((long1 < long2) && (long1 < long3))
```

```
    {
     branch[1]=1;
     branch[2]=2;
     branch[3]=3;
    }
    if ((long2 < long1) && (long2 < long3))
    {
     branch[1]=2;
     branch[2]=1;
     branch[3]=3;
    }
    if ((long3 < long1) && (long3 < long2))
    {
     branch[1]=3;
     branch[2]=1;
     branch[3]=2;
    }
  }

  /* check for minimum change in derivatives of trans branches */
  for (l = 2; l <= 3; l++)  /* for each transverse branch */
     for (m=2;m<=3;m++) /*for each new transverse branch */
        del[l][m]=e[branch[m]]-olde[oldbranch[l]];
  same=fabs(del[2][2]-olddel[2])+fabs(del[3][3]-olddel[3]);
  reverse=fabs(del[2][3]-olddel[2])+fabs(del[3][2]-olddel[3]);
  if (reverse < same)
  {
     l=branch[2];
     branch[2]=branch[3];
     branch[3]=l;
  }

  /* check handedness */
/*
  for (l = 1; l <= 3; l++)
  {
     cross[l]=0.0;
     for (m = 1; m <= 3; m++)
        for (n = 1; n <= 3; n++)
           if ((l!=m)&&(m!=n)&&(n!=l))
              cross[l]+=pow(-1.0,(m-l+2)%3)*v[m][2]*v[n][3];
  }
  hand=0.0;
  for (l=1;l<=3;l++)
     hand+=cross[l]*v[l][1];
  if ((hand*orighand) < 0.0)
  {
     l=branch[2];
     branch[2]=branch[3];
     branch[3]=l;
  }
*/

  /* assign olde,kolde,jolde,oldbranch,...,olddel,... */
```

```
        for (l=1;l<=3;l++)
        {
           olde[l]=e[l];
           oldbranch[l]=branch[l];
           olddel[l]=del[l][branch[l]];
           if (k==1)
           {
              kolde[l]=e[l];
              koldbranch[l]=branch[l];
              kolddel[l]=del[l][branch[l]];
           }
           if (j==1)
           {
              jolde[l]=e[l];
              joldbranch[l]=branch[l];
              jolddel[l]=del[l][branch[l]];
           }
        }



/* from each dynamical matrix, find 3(eigenvectors)*12(1nns)
   = 36 projections and put them into histogram, unnormg(nfreq) */

        for (l = 1; l <= 3; l++)  /* for each branch */
        {
          freq[l] = 1.0e-12 * sqrt(e[branch[l]]/MASS) / (2.0*PI);
                                  /* eigenfrequency in THz */
          /* printf("freq(in THz) = %f  ",freq[l]); */
          nfreq[l] = (int)(freq[l]*10.0);
          if ((nfreq[l]> 0) && (nfreq[l]<100))
          {
             unnormg[l][nfreq[l]]+=1.0;
             for (m = 1; m <= 12; m++) /* for each of 12 1nn */
                 {
                    qr=0.0;
                    for (n = 1; n<= 3; n++)  /* for each direction */
                       qr += PI*q[n]*x[nn1[m]][n];
                    dot=0.0;
                    for (n = 1; n <= 3; n++)  /* for each direction */
                       dot += v[n][branch[l]]*(float)x[nn1[m]][n]/sqrt(2.0);
                    if (dot>1.01)
                       printf("error:  dot>1 in code.\n");

                    unnormproj[l][nfreq[l]]+=dot*dot*(1.0-cos(qr))/12.0;
                    }
          }

        }
        /* printf("\n"); */
 }
```

```
        }

/* write output to file "proj.out" */
/* contains 7 columns: freq in 10^-13 rad/sec, 3 norm phonon dos,
   3 proj norm phonon dos */

        areag=0.0;
        for (l=1; l<=3; l++)
           for (m=0;m<=99;m++)
              areag += (float)unnormg[l][m]*0.01*2.0*Pl;
        printf("areag = %f\n",areag);
        for (l=1; l<=3; l++)
           for (m=0; m<=99; m++)
           {
              normg[l][m] = (float)unnormg[l][m]/areag;
              normproj[l][m] = 3*unnormproj[l][m]/areag;
           }
        printf("writing output to proj.out\n");fflush(stdout);
        fp = fopen("proj.out", "w");
        for (m=0; m<=99; m++)
           fprintf(fp, "%f\t%f\t%f\t%f\t%f\t%f\t%f\n",
                    ((float)m+0.5)*0.01*2.0*Pl,normg[1][m],normg[2][m],
                    normg[3][m],normproj[1][m],normproj[2][m],normproj[3][m]);

}
```

****

The following is a listing of the file "alforce.h" which is "included" in the C program above. This file contains the atomic mass in kg and the force constants in dyn/cm for the first 8 nn shells. These particular force constants were obtained from a fit by Cowley (1974) to inelastic neutron scattering data taken by Stedman et al. (1967):

```
#define MASS 4.48e-26

#define C1XX 10.4578
#define C1ZZ -2.6322
#define C1XY 10.3657

#define C2XX 2.4314
#define C2YY -0.1351

#define C3XX 0.0986
#define C3YY -0.2366
```

```
#define C3YZ -0.2862
#define C3XZ -0.1819

#define C4XX 0.1363
#define C4ZZ 0.1854
#define C4XY 0.3753

#define C5XX -0.3003
#define C5YY 0.1842
#define C5ZZ 0.2603
#define C5XY -0.3239

#define C6XX -0.1412
#define C6XY 0.1990

#define C7XX 0.1828
#define C7YY -0.2207
#define C7ZZ -0.0173
#define C7YZ -0.0214
#define C7XZ -0.0747
#define C7XY 0.0397

#define C8XX -0.0681
#define C8YY -0.0202

**********************************************************

        PROGRAM FCMSRD

C PROGRAM TO DETERMINE MSRD FROM PROJECTED DOS.

C JAMES K. OKAMOTO  24MAR93

C VARIABLES:
C GENERIC
        INTEGER I,J
C CONSTANTS (AMU, ANG, 10^-13 SEC,KELVIN)
        REAL HBAR,KB
        DATA HBAR,KB /0.635,0.00831/
C FOR READ DATA
        INTEGER NPTS
        DATA NPTS /100/
        REAL W(200),G1(200),G2(200),G3(200),P1(200),P2(200),P3(200)
C FOR INPUT
        REAL M
C FOR SETUP
        REAL T(100),DW
        REAL G(200),P(200),GNORM,PNORM
C FOR DETERMINE MSRD
        REAL SUM,ARG,COTH,MSRD(100)

C READ DATA
```

```
      OPEN(UNIT=2,FILE='fcmsrd.in',STATUS='OLD')
      DO I=1,NPTS
       READ(2,1010) W(I),G1(I),G2(I),G3(I),P1(I),P2(I),P3(I)
1010   FORMAT(7(F8.6,X))
      ENDDO
      CLOSE(2)

C SETUP TEMPERATURE VECTOR, DW,PROJDOS VECTOR
      DO I=1,100
       T(I)=REAL(I)*10.0
      ENDDO
      DW=W(2)-W(1)
      GNORM=0.0
      PNORM=0.0
      DO I=1,NPTS
       G(I)=G1(I)+G2(I)+G3(I)
       P(I)=P1(I)+P2(I)+P3(I)
       GNORM=GNORM+G(I)*DW
       PNORM=PNORM+P(I)*DW
      ENDDO
      WRITE(6,1200) GNORM,PNORM
1200  FORMAT('GNORM=',F8.6,' PNORM=',F8.6)

C INPUT ATOMIC MASS
      WRITE(6,1300)
1300  FORMAT('INPUT ATOMIC MASS (AMU):')
      READ(5,1310) M
1310  FORMAT(F8.4)

C DETERMINE MSRD FROM PROJECTED DOS, DOUBLE LOOP
      DO I=1,100
       SUM=0.0
       DO J=1,NPTS
        ARG=HBAR*W(J)/(2.0*KB*T(I))
        COTH=(EXP(ARG) + EXP(-ARG))/(EXP(ARG) - EXP(-ARG))
        IF (ARG.GT.(10.0)) COTH=1.0
        SUM=SUM + DW*P(J)*COTH/W(J)
       ENDDO
       MSRD(I)=HBAR*SUM/M
      ENDDO

C WRITE TO OUTPUT FILE
      OPEN(UNIT=3,FILE='fcmsrd.out',STATUS='NEW')
      WRITE(3,2000)
2000  FORMAT('Temp(K)    Vibr MSRD(ANG^2)')
      DO I=1,100
        WRITE(3,2010) T(I),MSRD(I)
2010    FORMAT(F6.1,X,E10.4)
      ENDDO

      CLOSE(3)
      END
```

References

Ahn, C.C. and Krivanek O.L. (1983) *EELS Atlas,* Center for Solid State Science, Arizona State University, Tempe, Arizona 85287.

Anthony, L., Okamoto, J.K., and Fultz B. (1993) "Vibrational Entropy of Ordered and Disordered Ni_3Al," *Phys. Rev. Lett.* **70,** 1128-1130.

Ashcroft, N.W. and Mermin, N.D. (1976) *Solid State Physics,* Holt, Rhinehart & Winston, New York.

Ashley, C.A. and Doniach, S. (1975) "Theory of extended x-ray absorption edge fine structure (EXAFS) in crystalline solids," *Phys. Rev. B* **11,** 1279-1288.

Atwater, H.A. and Ahn, C.C. (1991) "Reflection electron energy loss spectroscopy during initial stages of Ge growth on Si by molecular beam epitaxy," *Appl. Phys. Lett.* **58,** 269-271.

Azaroff, L.V. (1963) "Theory of extended fine structure of x-ray absorption edges," *Rev. Mod. Phys.* **35,** 1012-1022.

Becker, J.A. (1924) "Velocity distribution of secondary electrons," *Phys. Rev.* **23,** 664.

Beni, G. and Platzman, P.M. (1976) "Temperature and polarization dependence of extended x-ray absorption fine-structure spectra," *Phys. Rev. B* **14,** 1514-1518.

Bethe, H. (1930) "Zur Theorie des Durchgangs schneller Korpuskularstrahlen durch Materie," *Ann. Phys.* **5,** 325-400.

Birringer, R., Gleiter, H., Klein, H-P., and Marquardt, P. (1984) "Nanocrystalline materials: An approach to a novel solid structure with gas-like disorder," *Phys. Lett.* **102A**, 365-369.

Bohm, D. and Pines, D. (1951) "A collective description of electron interactions: II. Collective vs. individual particle aspects of the interactions," *Phys. Rev.* **85,** 338-353.

Boland, J.J., Crane, S.E., and Baldeschwieler, J.D. (1982) "Theory of extended x-ray absorption fine structure: Single and multiple scattering formalisms," *J. Chem. Phys.* **77,** 142-153.

Cohen-Tannoudji, C., Diu, B., and Laloë, F. (1977) *Quantum Mechanics,* Wiley, New York and Hermann, Paris.

Colliex, C. (1984) "Electron energy-loss spectroscopy in the electron microscope" in *Advances in Optical and Electron Microscopy,* ed. by V.E. Cosslett and R. Barer, Academic Press, London, vol. 9, pp. 65-177.

Colliex, C., Cosslett, V.E., Leapman, R.D., and Trebbia, P. (1976) "Contribution of electron energy-loss spectroscopy to the development of analytical electron microscopy," *Ultramicroscopy* **1,** 301-315.

Cowley, E.R. (1974) "A Born-von Karman Force Constant Model for Aluminum," *Can. J. Phys.* **52,** 1714-1715.

Crozier, E.D., Rehr, J.J., and Ingalls, R. (1988) "Amorphous and liquid systems," chap. 9 in *X-ray Absorption*, ed. by D.C. Koningsberger and R. Prins, Wiley, New York, pp. 373-442.

Csillag, S., Johnson, D.E., and Stern, E.A. (1981) "EXELFS analysis--the useful data range," *Analytical Electron Microscopy--1981*, ed. by R.H. Geiss, San Francisco Press, San Francisco, pp. 221-224.

Disko, M.M., Meitzner, G., Ahn, C.C., and Krivanek, O.L. (1989) "Temperature-dependent transmission extended electron energy-loss fine-structure of aluminum," *J. Appl. Phys.* **65,** 3295-3297.

Disko, M.M., Ahn C.C., and Fultz B., eds. (1992) *Applications of Transmission EELS in Materials Science,* The Minerals, Metals & Materials Society, Warrendale, Pennsylvania 15086.

Egerton, R.F. (1986) *Electron Energy-Loss Spectroscopy in the Electron Microscope*, Plenum Press, New York and London.

Egerton, R.F. and Wang, Z.L. (1990) "Plural-scattering deconvolution of electron energy-loss spectra recorded with an angle-limiting aperture," *Ultramicroscopy* **32,** 137-148.

Eisenberger and Lengeler (1980) "Extended x-ray absorption fine-structure determinations of coordination numbers: Limitations,"*Phys. Rev. B* **22,** 3551-3562.

Franck, J. and Hertz G. (1914) *Verhandl. Phys. Ges.* **16,** 457.

Fricke, H. (1920) "The K-characteristic absorption frequencies for the chemical elements magnesium to chromium," *Phys. Rev.* **16,** 202-215.

Gao, Z.Q. and Fultz, B. (1993) "Transient B32-like order during the early stages of ordering in undercooled Fe_3Al," *Phil. Mag.* (in press).

Gleiter, H. (1989) "Nanocrystalline materials," *Prog. Mat. Sci.* **33,** 223-315.

Gottfried, K. (1966) *Quantum Mechanics,* Benjamin, New York.

Gurman, S.J. (1982) "Review, EXAFS studies in materials science," *J. Mat. Sci.* **17,** 1541-1570.

Gurman, S.J., Binsted, N., and Ross, I. (1984) "A rapid, exact curved-wave theory for EXAFS calculations," *J. Phys. C* **17,** 143-151.

Harris, S.R., Pearson, D.H., and Fultz, B. (1991) "Chemically disordered Ni_3Al synthesized by high vacuum evaporation," *J. Mater. Res.* **6,** 2019-2021.

Haubold, T., Birringer, R., Lengeler, B., and Gleiter, H. (1989) "Extended x-ray absorption fine structure studies of nanocrystalline materials exhibiting a new solid state structure with randomly arranged atoms," *Phys. Lett.* **135,** 461-466.

Hayes, T.M. and Boyce, J.B. (1982) "Extended x-ray absorption fine structure spectroscopy," *Solid State Phys.* **37,** 173-351.

Herman, F. and Skillman, S. (1963) *Atomic Structure Calculations,* Prentice Hall, Englewood Cliffs, New Jersey.

Hertz, G. (1920) "Über die Absorptionsgrenzen in der L-Serie," *Z. Phys.* **3,** 19-25.

Inokuti, M. (1971) "Inelastic collisions of fast charged particles with atoms and molecules--The Bethe theory revisited," *Rev. Mod. Phys.* **43,** 297-347.

Johnson, D.W. and Spence, J.C.H. (1974) "Determination of the single-scattering probability distribution from plural-scattering data," *J. Phys. D* **7,** 771-780.

Kepert, D.L. (1972) *The Early Transition Metals,* Academic Press, London and New York.

Kincaid, B.M. and Eisenberger, P. (1975) "Synchrotron radiation studies of the K-edge photoabsorption spectra of Kr, Br_2, and $GeCl_4$: A comparison of theory and experiment," *Phys. Rev. Lett.* **34,** 1361-1364.

Kincaid, B.M., Meixner, A.E., and Platzman, P.M. (1978) "Carbon K-edge in graphite measured using electron energy-loss spectroscopy," *Phys. Rev. Lett.* **40,** 1296-1299.

Kohn, W. and Sham, L.J. (1965) "Self-consistent equations including exchange and correlation effects,"*Phys. Rev.* **140,** A1133-A1138.

Koningsberger, D.C. and Prins, R., eds. (1988) *X-ray Absorption*, Wiley, New York.

Kossel, W. (1920) "Zum Bau der Röntgenspektren," *Z. Phys.* **1,** 119-134.

Krivanek, O.L., Ahn, C.C., and Keeney R.B. (1987) "Parallel detection electron spectrometer using quadrupole lenses," *Ultramicroscopy* **22,** 103-115.

Kronig, R. de L. (1931) "Zur Theorie der Feinstruktur in den Röntgenabsorptionsspektren," *Z. Phys.* **70,** 317-323.

Kronig, R. de L. (1932) "Zur Theorie der Feinstruktur in den Röntgenabsorptionsspektren. III," *Z. Phys.* **75,** 468-475.

Kruit, P. (1986) "Pushing toward the limits of detectability in electron energy loss spectrometry," in *Microbeam Analysis--1986,* pp. 411-416.

Landau, L.D. and Lifshitz, E.M. (1965) *Quantum Mechanics; Non-Relativistic Theory,* vol. 3 of *Course of Theoretical Physics,* second edition, Pergamon, Oxford and New York.

Leapman, R.D. and Cosslett, V.E. (1976) "Extended fine structure above the x-ray edge in electron energy-loss spectra," *J. Phys. D* **9,** L29-L32.

Leapman, R.D., Rez, P., and Mayers, D.F. (1980) "K, L, and M shell generalized oscillator strengths and ionization cross sections for fast electron collisions," *J. Chem. Phys.* **72,** 1232-1243.

Leapman, R.D., Grunes, L.A., and Fejes, P.L. (1982) "Study of the L_{23} edges in 3d transition metals and their oxides by electron-energy-loss spectroscopy with comparisons to theory," *Phys. Rev. B* **26,** 614-635.

Le Caër, G. and Dubois, J.M. (1979) "Evaluation of hyperfine parameter distributions from overlapped Mössbauer spectra of amorphous alloys," *J. Phys. E* **12,** 1083-1090.

Lee, P.A. (1976) "Possibility of absorbate position determination using final-state interference effects," *Phys. Rev. B* **13,** 5261-5270.

Lee, P.A. and Beni, G. (1977) "New method for the calculation of atomic phase shifts: Application to extended x-ray absorption fine structure (EXAFS) in molecules and crystals," *Phys. Rev. B* **15,** 2862-2883.

Lee, P.A. and Pendry, J.B. (1975) "Theory of extended x-ray absorption fine structure," *Phys. Rev. B* **11,** 2795-2811.

Lee, P.A., Citrin, P.H., Eisenberger, P., and Kincaid, B.M. (1981) "Extended x-ray absorption fine structure--its strengths and limitations as a structural tool," *Rev. Mod. Phys.* **53,** 769-806.

Manson, S.T. (1972) "Inelastic collision of fast charged particles with atoms: Ionization of the aluminum L shell," *Phys. Rev. A* **6,** 1013-1024.

Martin, R.L. and Davidson, E.R. (1977) "Halogen atomic and diatomic 1s hole states," *Phys. Rev. A* **16,** 1341-1346.

Marton, L., Leder, L.B., and Mendlowitz, H. (1955) "Characteristic energy losses of electrons in solids" in *Advances in Electronics and Electron Physics VII,* Academic Press, New York, pp. 183-238.

Massalski, T.B., ed. (1986) *Binary Alloy Phase Diagrams,* American Society for Metals, Metals Park, Ohio 44073.

Mayo, M.J., Siegel, R.W., Narayanasamy, A., and Nix, W.D. (1990) "Mechanical properties of nanophase TiO2 as determined by nanoindentation," *J. Mater. Res.* **5,** 1073-1082.

Miiler, A.P. and Brockhouse, B.N. (1971) "Crystal dynamics and electronic specific heats of palladium and copper," *Can. J. Phys.* **49,** 704-723.

Minkiewicz, V.J., Shirane, G., and Nathans R. (1967) "Phonon dispersion relation for iron," *Phys. Rev.* **162,** 528-531.

Pearson, D.H. (1992) "Measurements of White Lines in Transition Metals and Alloys using Electron Energy Loss Spectrometry," doctoral dissertation, California Institute of Technology, Pasadena, California 91125.

Pearson, D.H., Ahn, C.C., and Fultz B. (1988) "Measurements of 3d state occupancy in transition metals using electron energy loss spectrometry," *Appl. Phys. Lett.* **53,** 1405-1407.

Pearson, D.H. (1992) "Measurements of White Lines in Transition Metals and Alloys using Electron Energy Loss Spectrometry," doctoral dissertation, California Institute of Technology, Pasadena, California.

Penn, D.R. (1976) "Electron mean free paths for free-electron-like materials," *Phys. Rev. B* **13,** 5248-5254.

Powell, C.J. (1974) "Attenuation lengths of low-energy electrons in solids," *Surface Sci.* **44,** 29-46.

Ritsko, J.J., Schnatterly, S.E., and Gibbons, P.C. (1974) "Simple calculation of $L_{II,III}$ absorption spectra of Na, Al, and Si," *Phys. Rev. Lett.* **32,** 671-674.

Rudberg, E. (1930) "Characteristic energy losses of electrons scattered from incandescent solids," *Proc. R. Soc. London* **A127,** 111-140.

Ruthemann, G. (1941) "Diskrete Energieverluste schneller Elektronen in Festkörpern," *Naturwissenschaften* **29,** 648.

Ruthemann, G. (1942) "Elektronenbremsung an Röntgenniveaus," *Naturwissenschaften* **30,** 145.

Sayers, D.E., Stern, E.A., and Lytle, F.W. (1971) "New technique for investigating noncrystalline structures: Fourier analysis of the extended x-ray absorption fine structure," *Phys. Rev. Lett.* **27,** 1204-1207.

Sayers and Bunker (1988) "Data Analysis" in *X-ray Absorption*, ed. by Koningsberger, D.C. and Prins, R., Wiley, New York.

Schiach, W. (1973) "Comment on the Theory of Extended X-Ray-Absorption Fine Structure," *Phys. Rev. B* **8,** 4028-4032.

Schiach, W.L. (1984) "Derivation of single-scattering formulas for x-ray-absorption and high-energy electron-loss spectroscopies," *Phys. Rev. B* **29,** 6513-6519.

Schoone, R.D. and Fischione, E.A. (1966) "Automatic unit for thinning transmission electron micrograph specimens of metals," *Rev. Sci. Inst.,* **37,** 1351.

Scott, R.A. (1983) "EXAFS Software Documentation," School of Chemical Sciences, University of Illinois.

Seah, M.P. and Dench, W.A. (1979) "Quantitative electron spectroscopy of surfaces: A standard data base for electron inelastic mean free paths in solids," *Surf. Inter. Anal.* **1,** 2-11.

Seitz, F. and Turnbull, D., eds. (1956) *Solid State Physics,* vol. 2, Academic Press, New York.

Sevillano, E., Meuth, H., and Rehr J.J. (1979) "Extended x-ray absorption fine structure Debye-Waller factors. I. Monatomic crystals," *Phys. Rev. B* **20,** 4908-4911.

Shuman, H. and Somlyo, A.P. (1981) "Energy filtered 'conventional' transmission imaging with a magnetic sector spectrometer," in *Analytical Electron Microscopy--1981,* ed. R.H. Geiss, San Francisco Press, San Francisco, California, pp. 202-204.

Siegel, R.W., Ramasamy, S., Hahn, H., Li, Z., Lu, T., and Gronsky, R. (1988) "Synthesis, characterization, and properties of nanophase TiO_2," *J. Mater. Res.* **3,** 1367-1372.

Spence, J.C.H. (1979) "Uniqueness and the inversion problem of incoherent multiple scattering," *Ultramicroscopy* **4,** 9-12.

Stearns, D.G. and Stearns, M.B. (1986) "Extended x-ray absorption fine structure," chap. 6 in *Microscopic Methods in Metals*, ed. by U. Gonser, vol. 40 of *Topics in Curent Physics*, Springer, Berlin, pp. 153-192.

Stedman, R., Almqvist, L., and Nilsson, G. (1967) "Phonon-frequency distributions and heat capacities for aluminum and lead," *Phys. Rev.* **162,** 549-557.

Stern, E.A. (1974) "Theory of extended x-ray-absorption fine structure," *Phys. Rev. B* **10,** 3027-3037.

Stern, E.A., Bunker, B.A., and Heald, S.M. (1980) "Many-body effects on extended x-ray absorption fine structure amplitudes," *Phys. Rev. B* **21,** 5521-5539.

Teo, B.K. and Lee, P.A. (1979) "Ab initio calculations of amplitude and phase functions for extended x-ray absorption fine structure spectroscopy," *J. Am. Chem. Soc.* **101,** 2815-2832.

Teo, B.K. and Joy, D.C., eds. (1981) *EXAFS spectroscopy, techniques and applications,* Plenum Press, New York and London.

Teo, B.K. (1986) *EXAFS: Basic Principles and Data Analysis,* Springer-Verlag, Berlin and New York.